UNIVERSITY OF CALIFORNIA, SAN DIEGO

High Power Waveguide Photodiodes - Analysis, Design and Demonstration

A dissertation submitted in partial satisfaction of the

requirements for the degree Doctor of Philosophy

in

Electrical Engineering (Applied Physics)

by

Dingbo Chen

Committee in charge:

Professor Paul K. L. Yu, Chair
Professor William S. C. Chang, Co-Chair
Professor Michael Heller
Professor Ying S. Meng
Professor Deli Wang

2016

The Dissertation of Dingbo Chen is approved, and it is acceptable in quality and form for publication on microfilm and electronically:

_____

_____

_____

_____
Co-Chair

_____
Chair

University of California, San Diego

2016

Dedication

Finishing this Dissertation was a challenging work for me. I made it with the guidance and encouragement from people who were close to my heart.

I dedicate this dissertation to

Professor Chang & Yu,

Along with My family members.

Epigraph

十年树木

百年树人

《管子•权修》

Growing trees is a ten-year project,

educating people is a life-long one.

Table of Contents

List of Figures

List of Tables

Acknowledgements

I am deeply indebted to two important people in my UCSD time and in my life. One is Professor Paul Yu. The guidance and challenges from Professor Yu allowed me to grow as a researcher. His knowledge and experiences gave me the foundation to start exploring the research area; his patience and support gave me the driving force to move forward with the graduate study. To me, Professor Yu is not only an academic advisor, but also a life mentor. The other one is Professor William Chang. He has spent countless hours teaching and advising me with the waveguide study, the work presentation, and dissertation writing. He is one of the best mentors. Regrettably, the only sources I can keep learning from him are his books, the notes, and all the memories. I wish I can be a person like him in the professional field in the future. This dissertation would have been definitely impossible, without the advising and support from the two people.

My gratitude also goes to my other dissertation committee members, Professor Michael Heller, Professor Ying S. Meng, and Professor Deli Wang, for all their time and effort to make my graduation happen.

I would also like to thank Dr. Chen Kuo Sun. He has provided support, expertise and a great environment for me to finish my final years of work. His help in finishing the chapter 4 of my dissertation are greatly appreciated.

I would like to extend my gratitude to the rest of Professor Paul Yu's research group for their help and advice each week. I would like to specially mention a few names, they are Jeffery Bloch, Meredith Draa, Winnie Chen, Wei Lu, Rui Wang, Jianzhi Wu, and Kangwei Wang.

I am grateful for the financial support I have received throughout my time at UCSD. The research in this dissertation was funded by Defense Advanced Research Projects Agency (DARPA), National Science Foundation, and University of California Discovery Program. I am also grateful for other financial support I received, including funding from Space and Naval Warfare Systems

Command (SPAWAR), Lockheed Martin Corporation, Archcom Technology Inc., Photonics System Inc. (PSI), and Multiplex Inc.

Portions of chapter 4 appear in “Cascaded Optical Band Pass Filters in Radio-over-Fiber Link”, IEEE EDSSC, Hongkong (2013), Dingbo Chen, Chen-Kuo Sun and Paul K. L. Yu, and “Optical Band Pass Filters in High Linearity Radio-over-Fiber Link”, IEEE AVFOP, San Diego (2013), Dingbo Chen, Chen-Kuo Sun and Paul K. L. Yu.

Vita

2005	Bachelor of Science, Hunan University, P. R. China
2008	Master of Engineering, Institute of Semiconductors, Chinese Academy of Sciences, P. R. China
2014	Optical Engineer, Titan Photonics, Inc.
2016	Doctor of Philosophy, Electrical Engineering (Applied Physics), University of California, San Diego

Publications

- **Dingbo Chen,** Jeffery Bloch, Rui Wang, Paul K. L. Yu, "Absorption Density Control in Waveguide Photodiode – Analysis, Design, and Demonstration," Frontiers of Optoelectronics, vol. 7, no. 3, pp. 385-392 (2014).

- **Dingbo Chen**, Chen-Kuo Sun and Paul K. L. Yu, "Cascaded Optical Band Pass Filters in Radio-over-Fiber Link", IEEE EDSSC, Hongkong (2013).

- **Dingbo Chen**, Chen-Kuo Sun and Paul K. L. Yu, "Optical Band Pass Filters in High Linearity Radio-over-Fiber Link", IEEE AVFOP, San Diego (2013).

- Meredith N. Draa, Jeffery Bloch, **Dingbo Chen**, David C. Scott, Nong Chen, Steven Bo Chen, Xuecai Yu, William S. C. Chang, and Paul K. L. Yu, "Novel directional coupler waveguide photodiode-concept and preliminary results," Optics Express, vol. 18, no. 17, pp. 17729-17731 (2010).

ABSTRACT OF THE DISSERTATION

High Power Waveguide Photodiodes - Analysis, Design and Demonstration

by

Dingbo Chen

Doctor of Philosophy in Electrical Engineering (Applied Physics)

University of California, San Diego, 2016

Professor Paul K. L. Yu, Chair

Professor William S. C. Chang, Co-Chair

Large optical power at the photodiode is especially beneficial to the high speed fiber optic link that is demanded by the exponential internet traffic growth. The power handling capability of waveguide photodiode (WGPD) has been limited by one of its intrinsic feature, which is the lack of uniform absorption distribution in the absorber in the longitudinal direction. As the required bandwidth kept increasing, an increasing photocurrent is needed in a reduced absorber length, which challenges the traditional WGPD designs for high power fiber optic link.

In order to study absorption uniformity in a high speed high power WGPD, supermode analysis is developed to replace the traditional WGPD analysis, which optimizes the absorption profile via adjusting the waveguide confinement factor. It is point out that the waveguide confinement factor has opposite effects on the bandwidth and power handling of a WGPD, and

makes the traditional WGPD analysis ineffective for the high speed high power WGPD design. the supermode analysis focuses on finding out the features of supermodes that improve the absorption uniformity. The designs of the waveguide structure and the layer structure are guided by the supermode analysis to improve the absorption uniformity in a WGPD.

The supermode analysis is applied to improve the absorption uniformity in a traditional WGPD. Traditional WGPD with the optimized structure experimentally demonstrates power handling capability higher than most of the reported WGPD with similar bandwidth. A layer structure with diluting layer is proposed to increases the power handling capability by 30% in the demonstrated WGPD. The supermode analysis also points out that the traditional WGPD has a trade-off of absorption uniformity and bandwidth-efficiency product.

The supermode analysis is applied to re-design the directional coupler photodiode (DCPD), which is pre-studied in our group. With the optimization of absorption uniformity in a DCPD that has RC time limited bandwidth being close to 50 GHz, the re-designed DCPD shows better power handling capability than that of any other traditional WGPDs with similar bandwidth.

Finally, we have proposed and demonstrated the incorporation of cascaded optical bandpass filters in a fiber optic link can significantly improve the link performance.

Chapter 1 Introduction

Fiber optic links are used in both analog and digital applications to transfer signal through optical fiber over distance ranging from meters to thousands of kilometers. Comparing to transferring signal through other mediums, such as air, Ethernet cable, and coaxial cable, fiber optic link is favored largely because of two characteristics, low loss and high bandwidth. The main goal of an analog fiber optic link is to reproduce the input signal at the output as close to identical as possible, where the link gain, noise, and distortion are critical parameters. There is a much larger demand of fiber optic link in the digital applications, including the telecommunication and data center. Because the input signal is digitally encoded, the main goal of a digital fiber optic link is to make the input signal delivered to the output and be decodable, where the bit error rate is a critical parameter. Traditionally, fiber optic link is mainly used for long distance signal transmission, and is less popular for distance less than 10 meters. Recently, as the digital data speed goes beyond 40 Gbps for the inter-server and inter-rack connections in data centers, the coaxial cables, which was dominantly used for distance less than 10 meters, are gradually replaced by active optical cables (AOC). In the above case, AOC, which applies fiber optic link to high speed short distance transmission, is favored because of its two traditional advantages over coaxial cable on bandwidth and propagation loss, as well as its low production cost, which becomes important as the connection units in data center are deployed in a large quantity.

High power fiber-optic link, which has the boosted optical power reaching at the detection side, not only has the advantage of higher tolerance of link optical loss and longer transmission distance, but also brings other advantages. For the analog applications, such as cable television network, high link optic power helps increase the link gain and the spur free dynamic range [1]. In digital applications, high link optical power can increase the detected electrical signal at the receiver to a level that can directly drive the digital logic circuits, and eliminates the needs for electrical

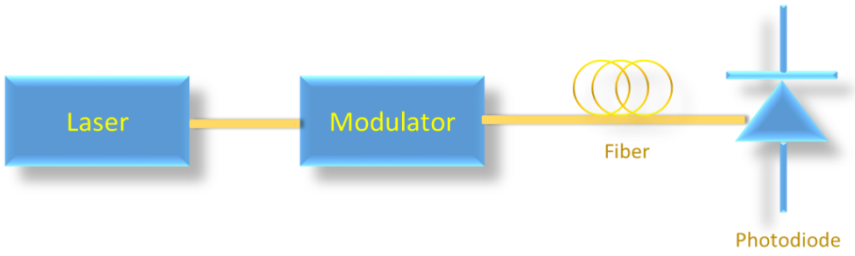

Figure 1-1 Schematic of a typical analog fiber optical link, in which a laser is used as an optical source, and an external modulator is used.

amplification. In this case, high power photodiode, which can deliver the required electrical power without degrading other link performances, becomes essential. In the following discussion, both the analog and digital fiber optic link will be briefly discussed, along with the introduction of benefits brought by increasing the link optical power and using high power photodiode.

1.1 High Power Photodiode and Analog Fiber Optic Link

Analog optical links transmit electrical signals in analog form through fibers, and provide a multitude of advantages when compared to electronic links, including low transmission loss, immunity to electromagnetic radiation, low cost, and small size. As shown in Figure 1.1, a typical analog optical link consists of an optical transmitter and an optical receiver, which are connected using optical fiber. In the optical transmitter, an optical source generates an optical carrier, usually it is a laser that emitting at a single wavelength or multiple wavelengths. A modulator imposes the microwave signal in analog form onto the optical carrier. In some cases, such as a laser diode, the microwave signal is applied to the laser, and the generated optical carrier is also modulated. In these cases, the laser is also a modulator. This modulation is called direct modulation. In some other cases, the optical modulation in a modulator is separated from the optical carrier generation in a laser, and this modulation is called external modulation. There are some other optical components in the optical transmitter, such as optical isolator and optical coupler. When multiple lasers are present in an optical transmitter and are coupled into one single fiber,

there is optical multiplexer in the optical transmitter. The modulated optical carrier from the optical transmitter is coupled into optical fiber, which serves as the transmission channel between the optical transmitter and receiver. An optical fiber can be made of glass, plastic, polymer, or other materials, and can have single or multiple propagation modes. Different fibers serve for different applications. Sometimes, Erbium-doped fiber amplifier (EDFA), or other kinds of optical amplifiers, are selectively placed in the fiber optic link, in order to compensate the link optical loss or achieve certain power level at the receiver. There is a receiver at the other end of the fiber, in which a photodiode regenerates the microwave signals from the detected optical signal, and a microwave amplifier is optionally used to boost up the regenerated microwave signal.

The following is a brief introduction of three figures of merit of an analog optic link: RF link gain, noise, distortions, and dynamic range. As we shall find out later, they are not independent parameters from both link and device perspectives, and they are more or less related to the link optical power.

1.1.1 RF Link Gain

The link RF gain g is defined as the ratio of the RF output power $P_{RF,\,OUT}$ dissipated at the receiver load resistor R_L to the RF input power from the RF source $P_{RF,IN}$ [1],

$$g = \frac{P_{RF,OUT}}{P_{RF,IN}} \qquad 1.1$$

When a circuit of an impedance is connected and matched to a signal source Vs, according to the maximum power transfer theorem [2], the $P_{RF,IN}$ is represented as the maximum power the RF source can dissipate to the circuit impedance, which is reached when the circuit impedance equals to the complex conjugate of the source impedance R_S. Therefore,

$$P_{RF,IN} = (\frac{V_S}{2R_S})^2 \times R_S = \frac{V_S^2}{4R_S} \qquad 1.2$$

where V_S is the root mean square (RMS) value of the source voltage amplitude.

The link output RF power is given by

$$P_{RF,OUT} = i_d^2 R_L \qquad 1.3$$

where i_d is the RMS value of the ac current flowing through the receiver load resistor R_L.

Therefore, the link RF gain can be expressed as:

$$g = \frac{P_{RF,OUT}}{P_{RF,IN}} = \frac{4 i_d^2 R_L R_S}{V_S^2} \qquad 1.4$$

Although in most cases an analog fiber optical link experiences a power loss instead of gain, the term RF link gain is widely used. A negative gain is used to represent the loss. The loss in a traditional coaxial cable link is mainly determined by the transmission loss, as a typical commercial coaxial cable exhibits loss of 56 dB/km at 2.4 GHz, and this loss increases rapidly with the transmitted microwave signal frequency. However, the transmission loss in typical optical fiber is only about 0.2 dB/km at 1.55 μm wavelength, and this loss is constant over the transmitted microwave signal frequency. Therefore, the fiber optical link has an advantage of low loss for long transmission distance and high transmission speed. The loss in an analog optical link is primarily the RF/optical conversion loss at the modulators and photodetectors, and depends on the link optical power. On the one hand, the required RF input power is determined by the optical modulator efficiency, and is independent of the optical power in popular modulators such as electro-absorption modulator (EAM) and Lithium Niobate ($LiNbO_3$) Mach-Zehnder modulator (MZM). On the other hand, the RF output power has a square dependence on the optical power received by the photodiode. When the optical power arrives at the receiver is small, the link RF loss can be very large. For example, when the optical modulator has a half-wave voltage of 2.5 V, at 100% modulation depth, the peak-to-peak RF input voltage is 2.5 V, which corresponds to RF input power of 18 dBm at a 50 ohm load. According to Equation 1.4, when the optical photodiode has a

responsivity of 1 A/W, at 1 mW receiver optical power, the RF output power will be -16 dBm, which corresponds to a RF link loss of 34 dB, or RF link gain of -34 dB.

According to Equation 1.4, the link RF gain/loss has a square dependence on the generated ac photocurrent at the receiver. For example, in the above case, the RF link gain will be increased from -34 dB to +6 dB, when the receiver optical power is increased from 1 mW to 100 mW. Therefore, high optical power at the receiver is favorable to achieve large link gain in an analog optical link.

1.1.2 Noise

Noise is an important parameter in the analog fiber optic link as it determines the minimum signal level that can be transmitted. There are three dominant noise sources in photonic links: thermal, shot and relative intensity noise. The noise sources are taken to be statistically independent, so the total noise power from all these sources is simply the sum of the independent noise powers.

Thermal noise arises from the thermally induced, random movement of electrical carriers in conductors and resistors [2]. The thermal noise power P_{th} in a resistor at an absolute temperature T as measured in a small bandwidth Δf is given by

$$P_{th} = 4\,\mathrm{kT}\,\Delta\mathrm{f} \qquad 1.5$$

where k is the Boltzmann's constant, its numerical value is 1.38×10^{-23} Joules/K, T is temperature, whose unit is Kelvin, and Δf is the RF bandwidth in Hz.

Where there is a load matched to the impedance, according to the maximum power transfer theorem shown in section 1.1.1, the noise power of the impedance delivered to the load is kTΔf. Thermal noise power depends on the signal bandwidth. For example, at 1 MHz bandwidth, N_T = -114 dBm, at 1 GHz bandwidth, N_T = -84 dBm, and at 50 GHz bandwidth, N_T = -67 dBm.

Relative intensity noise (RIN) is commonly used to specify the random fluctuations of a laser's output power. RIN is defined as [3]

$$\text{RIN} = \frac{< \delta p1^2 > \Delta f}{< P_L^2 >} \qquad 1.6$$

where $< \delta p1^2 >$ denotes the mean of the squared spectral density intensity fluctuations, and $< P_L^2 >$ is the average laser power squared.

The RIN noise can be reduced at higher laser emitting optical power level in a direction modulated laser diode, at the expense of smaller extinction ratio or larger driving current.

Shot noise gives another fundamental limit to the optical intensity noise in a fiber optic link. In general, shot noise exists in both electronic circuit and optic link, because the current and light consist of the movement of discrete particle, which is electron and photon [3]. The photodetector current in an optical link arises from a series of independent, random events, due to the statistical arrival of photons on the photodetector. Consequently, there is a shot noise current superimposed on the average photodetector current. Shot noise becomes a real issue only at fairly low optical power level, as the quantum fluctuations become much more noticeable.

The power of shot noise can be represented as [3]

$$P_{shot} = 2\text{q}i_d R_L \Delta f \qquad 1.7$$

Besides using noise power to characterize the absolute magnitude of noise, the effects of noise on the signal in a component and a link are also characterized by Noise Figure (NF), which specifies the degree of degradation of signal-to-noise ratio (SNR) of a component or a link. It is defined as the ratio of input SNR to the output SNR.

$$NF = {SNR_{IN}}/{SNR_{OUT}} = \frac{{S_{IN}}/{N_{IN}}}{{S_{OUT}}/{N_{OUT}}} = \frac{S_{IN}}{S_{OUT}}\frac{N_{OUT}}{N_{IN}} = 1 + \frac{1}{g}\frac{N_{ADD}}{N_{IN}} \qquad 1.8$$

where g is the gain of a component or a link of interest, N_{IN} and N_{ADD} are the input noise and the additive noise, respectively.

From Equation 1.8, the NF of a fiber optic link relates to two factors, one is the link gain g, the other one is the ratio of N_{ADD} to N_{IN}, N_{ADD}/N_{IN}. On the one hand, NF can be reduced by increasing the link optical power, as the RF link gain g has a square dependence on the link optical power, as shown in Equation 1.4. This statement is based on an assumption that the increase of link gain is not at the price of large increase of N_{ADD}/N_{IN}. On the other hand, NF can be reduced by reducing N_{ADD}/N_{IN}, which is usually achieved by reducing N_{ADD} of each link component.

Each noise source obeys a different law with respect to the amount of receiver optical power in a given system. Therefore, when the laser RIN noise and photodiode shot noise are added together with receiver thermal noise, as shown in Figure 1-2, SNR shows different dependence on the receiver optical power in several different cases. It indicates that within a certain range, the increase of the optical power at the receiver helps improve the link output SNR. In a thermal noise and shot noise limited fiber optic link, the link output SNR increase linearly with the increase of the receiver optical power. In a RIN limited fiber optic link, the link output SNR is set by the laser optical output at the transmitter side, and is independent on the receiver optical power. When all three kinds of noise are present in a fiber optic link, the link output SNR will increase along with the increase of receiver optical power, and approach the SNR limit set by RIN. This SNR limit goes

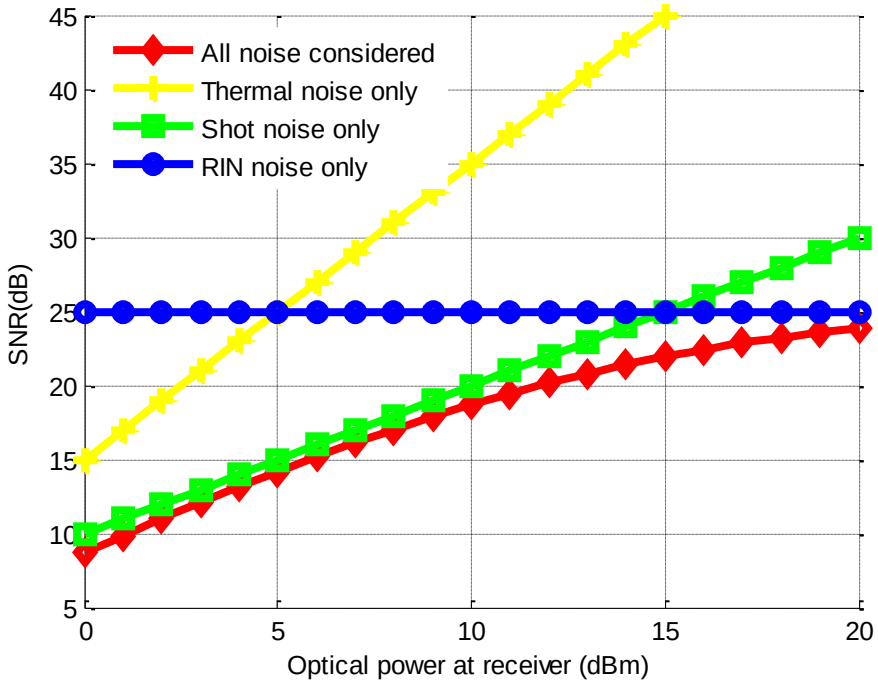

Figure 1-2 Plot of SNR vs. optical power reached at the receiver for a fiber optic link with various noises. The RIN noise density is -170 dB/Hz. The thermal noise density is 10 pA/Hz$^{1/2}$, and the signal bandwidth Δf is 50 GHz. N_{ADD} is assumed to be negligible.

up with the reduced RIN. In the simulated case in Figure 1-2, when the RIN noise density is -170 dB/Hz, the improvement of the link output SNR occurs up to 20 dBm receiver optical power. Therefore, a high power fiber optic link and a high power photodiode is favorable to achieve high SNR in an analog optical link.

1.1.3 Distortions and Dynamic Range

For links with sub-octave applications, the third-order intercept point is frequently used to characterize the link linearity, as the second-order distortions are usually out of the band of interest, and other higher order distortions have smaller magnitude than the third-order distortions [1]. If the transmitted optical power in the fiber-optic link is modulated by two equal level sinusoidal tones at frequency f1 and f2, third-order intermodulation distortion (IMD3) products, which are generated

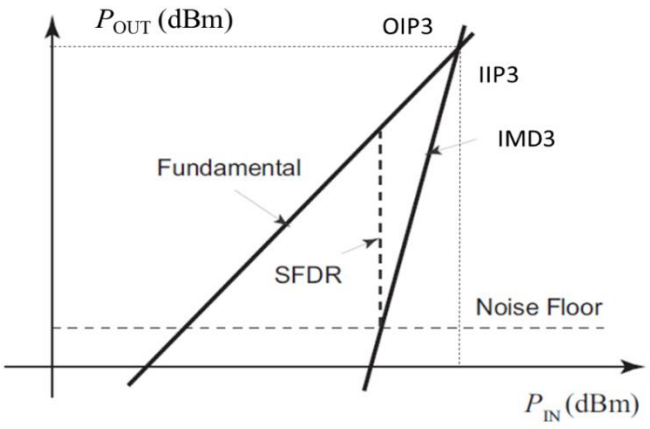

Figure 1-3 Fundamental and IMD3 as a function of input RF power, and an illustration of third-order spurious-free dynamic range (SFDR), IIP3 and OIP3 [1].

at frequency 2f1– f2 and 2f2 – f1, are of interest, as they appear close to the fundamental tones f1 and f2 and cannot be filtered out. As shown in Figure 1-3, when plotted against the link input RF power expressed in dBm, the magnitude of these IMD3 distortions expressed in dBm has a slope of three, and the magnitude the fundamental tones expressed in dBm has a slope of one. In this case, when the link input RF power increases, the magnitude of IMD3 distortions increases at a rate larger than that of the fundamental tones, and will exceed that of the fundamental tones at certain input RF power level. To quantify this effect, the slopes of the fundamental tones and IMD3 distortions are extrapolated to higher power until they intercept. The input RF power corresponding to this intersection is defined as the input third-order intercept point (IIP3), and the output RF power corresponding to this intersection is defined as the output third-order intercept point (OIP3). Therefore, IIP3 or OIP3 is a quantitative measurement of the linearity of a component or a link, and greater IIP3 or OIP3 indicates higher linearity of a component or a link.

While the generated distortions limit the maximum signal magnitude that can be transmitted, the noise floor determines the minimum signal detectable in a given link. The dynamic range defined by distortions and noise, in which the output fundamental tone power is above the

noise floor and the dominant intermodulation distortion (IMD) is below the noise floor, is called spurious free dynamic range (SFDR). In a super linear and noiseless world, SFDR of an ideal link is infinite. However, in a realistic link, the SFDR is usually limited by the noise at the low power side and by the nonlinearities at the high power side. Therefore, SFDR is a measure of combined effect of the link nonlinearity and the link noise.

In a traditional analog fiber optic link, a RF amplifier, which is used for increase the link gain, contributes to the raising of the link noise floor and the SNR degradation. A RF amplifier not only equally amplifies the input signal and the input noise, but also adds additional noise and degrades the SNR. In a RF amplifier, there are three major noise sources for the additional noise, the shot noise, the thermal noise and the Flicker noise [4]. As discussed in Equation 1.8, NF of an amplifier is used to specify the degree of degradation of SNR due to the additional amplifier noise. Therefore, ΔN_f, which is the raising of the noise floor at the output of an amplifier, equals to the sum of the amplifier gain and the amplifier's noise figure NF, as shown in Equation 1.9.

$$\Delta N_f = Gain(dB) + NF(dB) \qquad 1.9$$

In Equation 1.9, the Gain (dB) of an amplifier is determined by the link gain requirement, the NF (dB) is determined by the design, manufacturing, and operation of the amplifier itself. For example, when the input RF power and the gain are the same, different RF amplifiers made by different companies may have different NF. For a given RF amplifier, the NF will also be different at different operation conditions, such as the input RF power level, amplification gain, and temperature.

In a high power optic link, the large link gain is achieved by optical amplifier instead of RF amplifier. When the optical wavelength is in the Conventional band (C-band, from approximately 1525 nm to 1565 nm) or in the Long band (L-band, from approximately 1570 nm to 1610 nm), the erbium-doped fiber amplifier (EDFA) is widely used. Besides, semiconductor optical

amplifier (SOA) is also used for applications having the optical wavelength in between 850 nm and 1610 nm. The performance of SOA is not quite comparable with the EDFA, as the SOA has higher noise, lower gain, moderate polarization dependence and high nonlinearity with fast transient time. SOA is usually used when EDFA is not available for the wavelength, and will not be discussed in this dissertation. In an EDFA, the pump laser generates spontaneous emission noise, which is subsequently amplified becomes so-called amplified spontaneous emission (ASE) noise. ASE noise is the dominant noise element in an EDFA [5]. The characterization of noise in an EDFA can also be done using Noise Figure, as shown in Equation 1-9, which relates to the design, manufacturing, and operation of the EDFA itself.

The location of the EDFA relative to the optical modulator makes difference to the link noise floor, as hence the SFDR. When the EDFA is placed after the modulator, although the requirement for the power handling capability of the modulator is less stringent, both the noise from the optical carrier and the electrical signal will be amplified by the EDFA. When the EDFA is placed before the modulator, only the noise from the optical carrier is amplified by the EDFA, but large power handling capability of the modulator is required.

The optical amplification has several advantages over the RF amplification, such as better gain flatness over the signal spectrum, and more cost effective for high frequency signal amplification. Increasing the link optical power can be a cost effective solution for transmitting broadband analog signal in a fiber optic link.

1.1.4 Summary

In this section, with the increase of the receiver optical power, the potential improvements of link performances of an analog fiber optic link are discussed. Through the introduction of several critical link parameters, including the RF link gain, the noise, the distortions, and the SFDR, it is found out that increasing the receiver optical power helps improve the RF link gain, which in turn

make it feasible for replacing the RF amplifier at the receiver with an optical amplifier, such as an EDFA. This replacement will bring advantages such as better gain flatness over the signal spectrum, and more cost effective for high frequency signal amplification. Therefore, increasing the receiver optical power is a good approach of transmitting broadband analog signal in a fiber optic link.

The increase of the receiver optical power requires improved power handling capability for the photodiode in the receiver, while maintain good performance of low noise, linearity, and large frequency response at the raised optical power level. Therefore, high power photodiode becomes important research subject for the high performance broadband analog fiber optic link.

1.2 High Power Photodiode in Digital Fiber Optic Link

The way digital fiber optic links are built and are accessed is fundamentally changing again. On the one hand, the traditional Multiple Service Operators (MSOs) are facing the challenge from rapid internet traffic growth in their digital fiber optic link in the past decade, which is largely due to video streams to millions of display screens. Meanwhile, those MSOs are also facing the competition from the new internet technology companies, such as Google Fiber, who provides 10 to 100 times faster broadband internet access services to the customer. Therefore, how to re-construct the digital fiber optic network architectures, in order to meet the customer's larger bandwidth needs for now and for the future, as well as increasing their own competitiveness, is very important to the MSOs. On the other hand, numerous data centers are built worldwide in the past decade, in order to meet the fast growing needs for cloud-based services from both enterprises and individual consumers. Data centers have brought profound changes and impacts to the industry of digital fiber optic link. In the traditional fiber optic link deployed by MSOs, there are only a few thousands of optical transceivers (an assembly of optical transmitter and receiver) are installed in a city, and mostly in an outdoor environment. In contrast, there are hundreds of thousands (if not millions) of optical transceivers in a middle-size data center, which covers only a few acres. Therefore, the speed and cost of these optical components, as well as energy expenditure, become

very important concerns in the data center market. These changes remake the network architectures of the service providers, and in turn reshape the component supplying market.

When the digital fiber optic links are widely and rapidly deployed for the next generation high speed Ethernet in both Telecom and Datacom, reducing the cost and increasing the speed are two critical approaches to reduce the bandwidth cost. As discussed in section 1.1.1, increasing the incident optical power into the large bandwidth photodiodes can increase the output RF power. When the output RF power is large enough to directly drive the digital logic circuits, high power photodiode can replace the large bandwidth RF amplifier, which brings issues like cost and complications. Therefore, a high power fiber optic system, which adopts high power photodiode, becomes an affordable and well-performed solution for the next generation high speed Ethernet.

In the following discussion, two of the most important applications, cloud computing and web services, which drive the needs for high speed Ethernet are described, followed by the issues exist in the development of next generation Ethernet. After that, a high power fiber optic system, which adopts high power photodiode, is proposed to solve these issues.

1.2.1 Cloud Computing

Cloud computing is a general term for anything that involves delivering hosted services over the internet, the name cloud computing was inspired by the cloud symbol that is often used to represent the internet in flow charts and diagrams [7]. Traditional businesses have always been very complicated and expensive. The amount and variety of hardware and software required to run Traditional business applications are huge. As shown in Figure 1-4, with cloud computing, it eliminates those headaches because the customer is not managing hardware and software, which is

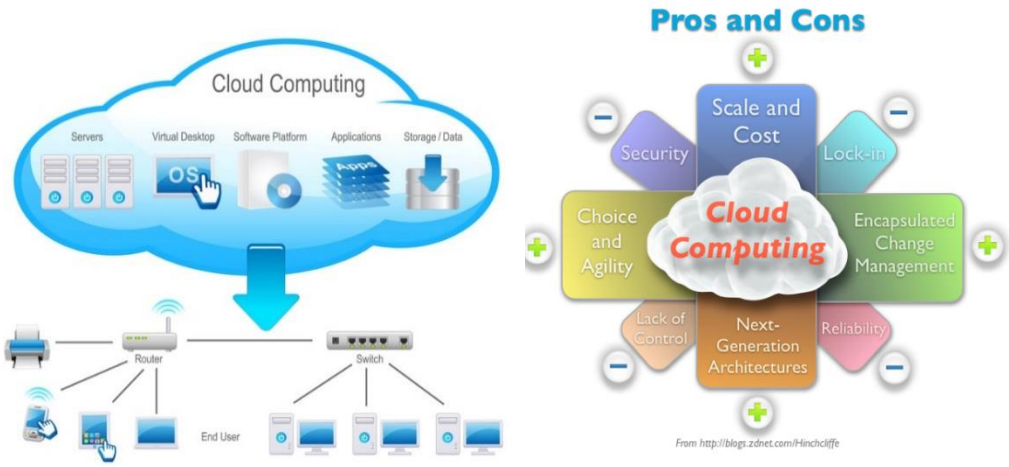

Figure 1-4 An illustration of cloud computing and its Pros and Cons. (Picture source: www.zdnet.com)

the responsibility of an experienced vendor. The shared infrastructure means it works like a utility: Customer only pay for what they need, upgrades are automatic, and scaling up or down is easy [8]. There are still distinct disadvantages of Cloud Computing, such as issue of security and privacy, and limited control over the function and execution of their hosting infrastructure. As the technology, market, and ecosystem continue to grow, those issues will be tackled and the cloud computing will be more widely adopted.

The rise of cloud computing is not just changing the traditional business applications; it is also changing the nature of competition within the computer industry. Since the invention of computer, technological developments have pushed the computing power away from central hubs to the very distributed end computer units, such as personal computers and servers. Now a combination of cheaper processors and faster networks is pushing the computing power back to the center in some respects. The cloud's data centers are actually supersize public computing center.

At the same time, the PC is being pushed aside by a host of smaller, often wireless devices, such as laptops, tablets, smartphones, and wearable devices.

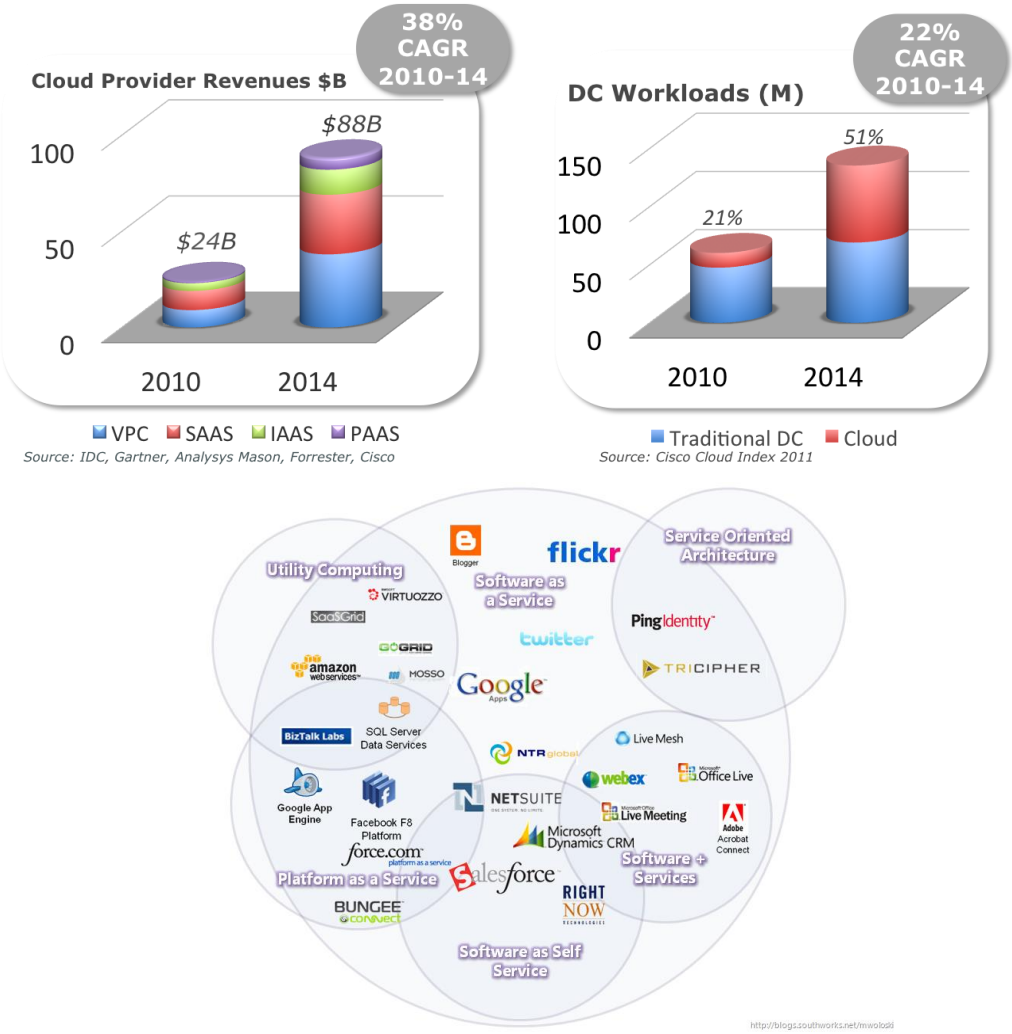

Figure 1-5 The comparison of cloud provider revenues and data center (DC) workloads in year 2010 and 2014 (a). A list of companies that provide various cloud computing based services (b). (Picture source: [9]).

Cloud computing has experienced serious growth in recent years, and more and more companies put in investments to improve their cloud services, as shown in Figure 1-5. By the end of 2014, the value of cloud services boosts from $24 billion in 2010 to $88 billion, and the workload percentage of the data centers that is from the cloud service increases from 21% in 2010 to 51% [9].

There are several challenges for the optical transceivers in a data center. First, the optical transceiver speed has to keep pace with the rapidly growing data traffic in a data center. As shown

Table 1-1 Progression of Optical Networking. (Source: [6])

Stage	Time frame	Applications
Initial optical networks	1980-1995	Telephony, voice traffic, dial-up modem traffic
10 G	1995-2005	Internet traffic ramps
40 G	2005-2012	FTTx broadband, video, Netflix, Facebook, YouTube
100 G/400 G	2013-2020	Cloud computing, widespread video, mobile broadband, yet-to-be invented apps

in Table 1-1, during the last 10 years, major innovation in the network has been moving to the last mile and the data centers, in which the speed requirement increases from up to 10 Gbps per fiber to up to 400 Gbps per fiber for the interconnection between two optical transceivers. In this case, the optical transceivers have to be upgraded to provide enough bandwidth for the new internet applications [6]. Second, as the number of optical transceivers a data center uses are very large number, the above upgrade should be done with the additional cost and complication minimized. However, the current development of 100 Gbps (4 x 25 Gbps/λ) optical transceivers shows much greater cost and complication than the 40 Gbps (4 x 10 Gbps/λ) version, due to the required upgrade of the optics (the laser chips and the photodetector) and the electronics (the laser driver and the RF amplifier in the receiver). Internet giants who largely rely on high speed and wide coverage internet to provide services, such as Google, Facebook, Apple, and Microsoft, are building their own supersize data center and are longing for low cost solution of upgrading the optical transceiver speed. As shown in Figure 1-6, currently the 100 Gbps optical transceivers are over 10 times more expensive than the 40 Gbps version, and the time for the price per Gbps dropping to the current level will be so long that Facebook hopes to use its buying power and relaxed specs to drive down by an order of magnitude projected 2016 costs of 100 G optical Ethernet transceivers. Cloud is

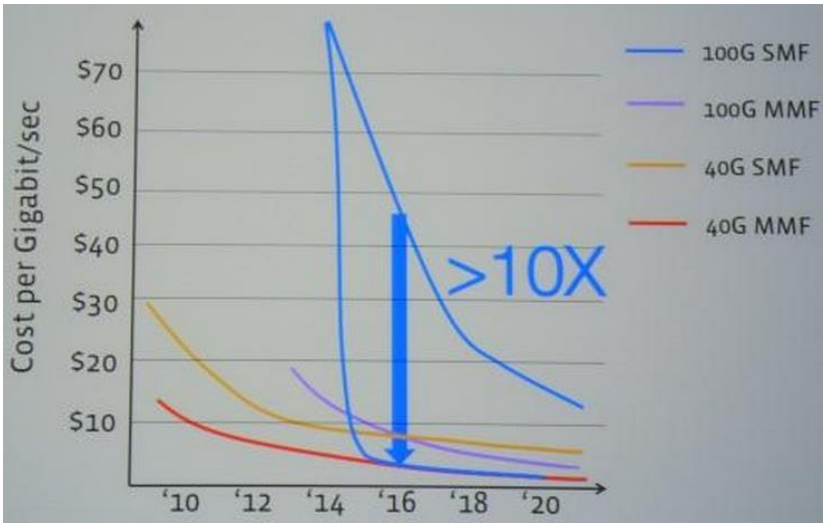

Figure 1-6 The price of 40G (4 x 10 Gbps/λ) and 100G (4 x 25 Gbps/λ) optical transceiver currently in use in datacenter, and the price of those optical transceivers is expected to be in the future. There are two blue curves representing the price trend of 100G SMF optical transceiver used for data center. The one on top is a prediction based on the past experiences. The one on bottom is the trend Facebook would like to see for the use in its own data center. The price is in per Gbps. SMF and MMF stand for single mode fiber and multimode fiber, which are two major types of fiber used for the optical transceiver. (Picture source: EE times [10])

reshaping global data traffic and cannot be ignored. The industry needs to provide a low cost solution preparing for the fast internet traffic growth driven by the cloud computing.

1.2.2 Web Applications

Global internet traffic has been growing rapidly. A critical challenge facing the industry is how to supply more traffic annually while keep the bandwidth cost low. Before discussing the reduction in bandwidth cost, first the major factors contributing to internet traffic growth are discussed.

As indicated in Figure 1-7, internet traffic growth is largely due to video streams to millions of display screens, including television, laptops, tablets, and smartphones. For the year 2014, the

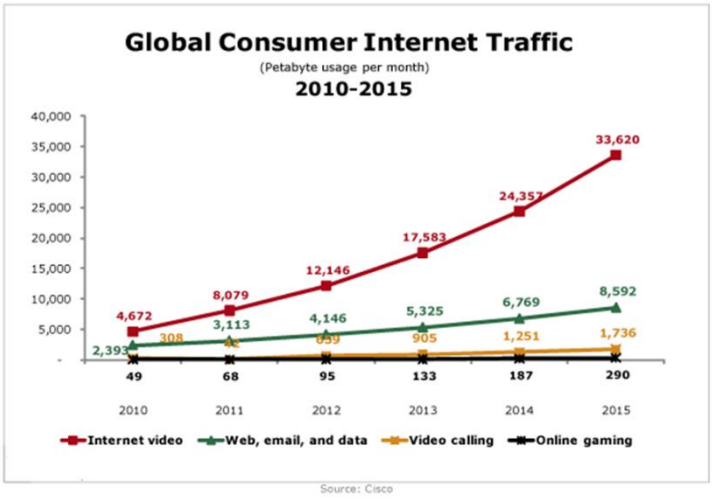

Figure 1-7 The growth trend of global consumer internet traffic. (Source: Cisco 2013)

worldwide smartphone market totals a 1.3 billion units. This is a 27.7% growth from the 1.0 billion units in 2013, according to data from the International Data Corporation (IDC) Worldwide Quarterly Mobile Phone Tracker [11]. These devices will make the internet more accessible than ever, and make users stay online from more places for longer periods of time. The user base of the internet is also expanding rapidly, as the cost to connect declines and the ease of connecting increases. According to the Cisco visual networking index [12], the internet user base is growing at about 5% per year from 1.7 billion users in 2010 to 2.2 billion users in 2015. The combination of high-definition videos and billons of access devices creates exponential traffic growth in various digital fiber optic links, such as the local area network (LAN), metropolitan area network (MAN), and the wide area network (WAN). As shown in Figure 1-7, we're seeing a continuous increase in data traffic with a growth rate of about 30 percent every year, an increase that shows no signs of slowing down. To meet this enormous surge in data, large speed upgrade is required in the digital fiber optic link.

Although the market of LAN, MAN and WAN use less optical transceivers and has lower cost sensitivity than the data center market, it has more stringent requirement for the speed and

other performances. This is because the optical transceivers are dispersively installed in the field, and hence the upgrade cost per unit will be much higher than that in a data center. In order to extend the upgrade period in LAN, MAN and WAN, 400 Gbps (4 x 100 Gbps/λ or 8 x 50 Gbps/λ) optical transceivers are demanded, with higher speed required for each wavelength than the 100 Gbps version. In this case, considering the various challenges 100 Gbps optical transceiver development is facing [13] [14] [15], even higher cost and more complications are expected for both development and production of 400 Gbps optical transceiver. The industry need to provide a low cost and reliable solution preparing for the fast internet traffic growth driven by the web applications.

1.2.3 Current Progress of Development for The Next Generation Digital Fiber Optic Link

Over the past few years, the exponential increase of the internet traffic, mainly driven by emerging cloud computing and web applications, has created the need for connection speed per optical transceiver to be upgraded from the current 10 Gbps and 40 Gbps to 100 Gbps or higher in the data center and in the core networks, such as LAN, MAN and WAN. When the data rate is 10 Gbps per wavelength, the required bandwidth for the post electrical amplifier in the receiver is usually no more than 10 GHz. The current electronics and optics in the industry are already mature to support the needs of 10 Gbps Ethernet. However, when the transmitted data rate per wavelength reaches 25 Gbps or higher, there are many challenges for the electronics and optics, including the technology, cost, and manufacturing. Both the standard creation and the product development are actively in progress right now for the next generation digital fiber optic link.

The effort to create specifications for 400 Gigabit Ethernet (100 Gbps x 4) has reached a major milestone with the formal creation of the IEEE P802.3bs Task Force in May 2014 [16]. The standard will include the creation of Physical Medium Dependent Sublayers (PMDs) for such applications as 100 m over multimode fiber and 500 m, 2 km, and 10 km via single mode fiber. Several middle stages, such as 25 Gbps and 50 Gbps, are specified. Formed in March 2014, The

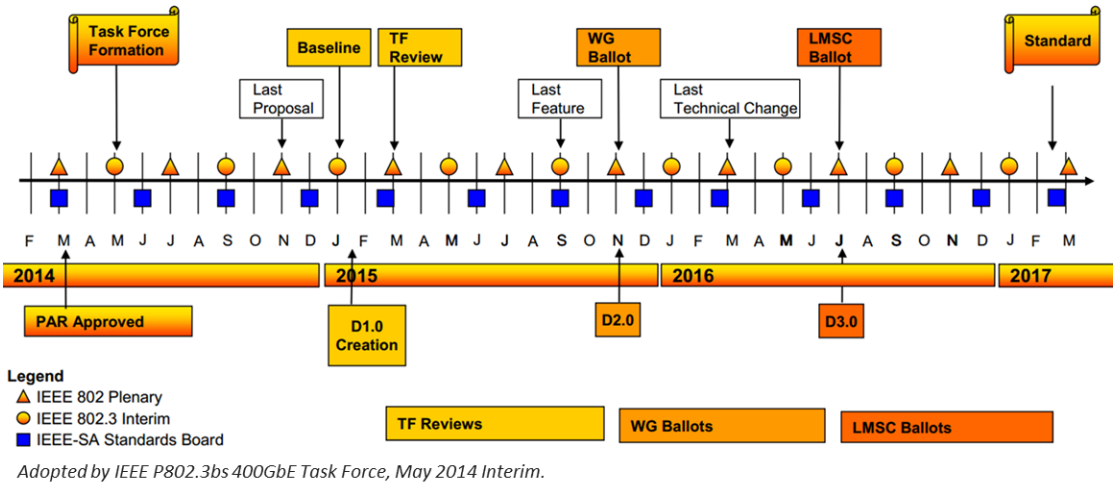

Figure 1-8 IEEE P802.3bs 400GbE Task Force Agenda

CWDM4 MSA (Coarse Wavelength Division Multiplexed 4x25G Multi-Source Agreement) consortium released the first detailed specification (revision 1.0), which targets a common specification for 4 x 25 Gbps optical interfaces that addresses data communication links up to 2 kilometers in the data center. However, specifications for 8 x 50 Gbps and 4 x 100 Gbps are in the middle of negotiating with very slow progress, due to the lacking of convincing and clear solution for the higher speed system [17].

The product development is also actively in progress right now for the 100 Gbps optical transceiver. Several module companies have released 100 Gbps CWDM4 transceiver product of their own versions, including Finisar, Avago, Source Photonics, Skorpios Technologies, Inc., and NeoPhotonics Corporation, etc. At the time of the writing, the price of 100 Gbps CWDM4 transceiver module is more than 20 times of that of the 40 Gbps transceiver module [10], because of the complication of the optics and electronics. Moreover, for the same reason, at the time of the writing, there is not one single company being able to make reliable 400 Gbps transceiver.

From the above introduction, it can be seen that for the next generation digital fiber optic link, both the standard creation and the product development fall behind the application needs, due

to the complication of the optics and electronics make it difficult for the development of the low cost and high reliability solution.

1.2.4 High Power Photodiode for The Next Generation Digital Fiber Optic Link

In an optical transceiver for the digital fiber optic link, there is a photodetector for optical to electronic conversion. In a traditional digital fiber optical link, the receiver optical power is usually lower than 0 dBm. Assume the responsivity of the receiver is 1 A/W, then peak-to-peak voltage of the detected electrical signal in the photodetector will be less than 0.05 V in a 50 Ω system. In order to drive the digital logic circuit for signaling and clock recovery, the peak-to-peak voltage level of the electrical signal is usually between 0.2 V and 1.0 V [18]. Therefore, a trans-impedance amplifier (TIA), which is used for boosting up the signal, is usually added after the photodetector. A good TIA must meet the requirements for bandwidth, phase response, gain, noise figure, and cost. As the data rate goes higher and higher, the design and manufacturing of the TIA becomes more and more complex and costly. Many works on TIA design with speed up to 40 Gbps have been published in recent years [19] - [24]. However, no existing design of 100 Gbps TIA has achieved the similar performance of gain, noise, phase response as the 40 Gbps version, not to mention the cost. Therefore, it is expected that at the stage of 50 Gbps and 100 Gbps per wavelength, the complication and cost issue of the receiver will become severe in a digital fiber optic link.

It is pointed out in section 1.1 that increasing the receiver optical power can eliminate the needs for the RF amplifier in an analog fiber optic link. Similarly, the elimination of the TIA in the receiver, via increasing the receiver optical power, can be realized in a digital fiber optic link. As the optical amplification is much less affected by the data rate than the electrical amplification, the proposal of increasing the receiver optical power naturally fits the next generation high speed digital fiber optic link.

The receiver optical power level required for eliminate the TIA depends on several factors, including the coupling efficiency between the fiber and the receiver, the responsivity of the photodiode, the optical modulation index, and the required voltage level of the electrical signal. It is mentioned at the beginning of this section, in order to drive the digital logic circuit for signaling and clock recovery, the peak-to-peak voltage level of the electrical signal is usually between 0.2 V and 1.0 V. In this case, assuming the coupling efficiency is 1, the responsivity is 1 A/W, and the optical modulation index is 100%, then 20mW receiver optical power is required for generating an electrical signal with peak-to-peak voltage of 1.0 V. At this power level, with the assumed -170 dB/Hz RIN noise density, the noise is not dominated by RIN yet, and the SNR can still be improved by the increasing of optical power, as shown in Figure 1-2. With reduced coupling efficiency and optical modulation index, the actual required receiver optical power will be greater.

In summary, high power photodiode, which can do broadband O-E conversion and generate the required microwave signal power, can replace the TIA in the receiver, and eases the design of the next generation high speed digital fiber optic link. Because of that, the research of high power photodiode becomes a valuable topic for the digital fiber optical link.

1.3 The Motivation and Scope of Dissertation

For the study of a high power photodiode in this dissertation, the performance of power handling capability is focused, as large receiver optical power benefits the performances of both analog and digital fiber optic link. However, other performances, such as bandwidth, noise, and linearity, are equally critical for a photodiode, and are not purposely compromised to trade for better power handling capability.

The study in this dissertation focuses on waveguide type photodiode, which attracts many interests from both academia and industry, especially when photonic integrated circuits (PIC) are widely adopted nowadays. The power handling capability of waveguide photodiode (WGPD) has been limited by one of its intrinsic feature, which is the lack of uniform absorption distribution in

the propagation direction. The power handling capability of WGPD has been improved over the past decade, but is still not comparable to that of the ideal photodiode, due to the fact that the way WGPD is designed traditionally does not provide good solutions to effectively reduce the large absorption near the absorber front end and improve the overall absorption uniformity. In order to further improve the power handling capability of WGPD, in this dissertation, a different approach of analyzing and simulating WGPD, which is based on supermode analysis, is presented, and is utilized to re-design the traditional WGPD structure and directional coupler photodiode (DCPD).

In chapter 2, the re-design of traditional WGPD is focused. First, the cause of absorption crowding near the absorber front end in a traditional WGPD is studied using supermode analysis, which is followed by the solution to reduce this absorption crowding in a re-designed traditional WGPD. Besides, the overall absorption uniformity of a traditional WGPD is also studied using supermode analysis. Finally, the improvement of the power handling capability in the re-designed traditional WGPD is examined and verified by simulation and experiments. The work in this chapter is not only a demonstration of the improvement of an existing design, but also and more important, it is a demonstration of another angle to understand and design WGPD by using supermode analysis.

The chapter 2 is a starting point for the supermode analysis to shows its utility in deep understanding of the waveguide structure. However, the improvement of the re-designed traditional WGPD's power handling capability is still limited, due to the inevitable absorption crowding near the absorber front end. Because of the limitation of traditional WGPD, the supermode analysis is applied to DCPD, which is novel design developed in our group [25], [26], and has shown some potential of having great power handling capability.

In chapter 3, the goal is discovering more potential of DCPD's high power handling capability, via the study and re-design using supermode analysis. First, the study of DCPD reveals one of its intrinsic differences from the traditional WGPD, which is the intrinsic suppression of the

absorption crowding near the absorber front end. Next, the effects of DCPD waveguide parameters on the power handling capability are studied more substantially, with the help of supermode analysis. Last, a re-designed DCPD is presented to show much improved power handling capability.

In chapter 4, a novel cascaded optical bandpass filter is proposed to assist the long distance transmission of signal in a dispersive fiber. As the high power fiber optic link enables the signal transmit in a fiber for long distance, the fiber dispersion, which causes the fading effect of the transmitted signal [27]- [30], becomes an important issue. Traditional optical bandpass filter reduces the RF signal fading effect in the long distance optical channel at the price of increased magnitude of IMD3 [29] [30]. In comparison, this novel cascaded filter can effectively reduce the RF signal fading effect, without increasing the magnitude of IMD3.

Finally, chapter 5 summarizes the key contributions from each of the previous chapters and presents future work.

1.4 References

[1] C. H. Cox, *Analog Optical Links: Theory and Practice,* NY: Cambridge, New York (2004).

[2] H.W. Jackson, *Introduction to Electronic Circuits,* Prentice-Hall, New York (1959).

[3] D. Kleinfeld, *Summary on Noise and Signal-to-Noise in Photodetector Systems,* University of California, San Diego (1979).

[4] K. K. Asparuhova, E. D. Gadjeva, "Noise analysis of operational amplifier circuits using MATLAB," *Electronics Technology: Meeting the Challenges of Electronics Technology Progress,* vol. 4, pp. 471 – 475 (2007).

[5] I. P. Kaminow, T. Li, A. E. Willner, *Optical Fiber Telecommunications V A: Components and Subsystems,* Academic Press, Waltham (2008).

[6] A. Schmitt, "The fast approaching 100G Era," Infonetics Research White Paper (2011).

[7] Splunk Inc., "Splunk for the cloud," *www.splunk.com*.

[8] Association of Modern Technologies Professionals, "Cloud computing", *www.itinifo.am*.

[9] D. Standridge, P. Minasian, F. Seelbach, J. Reich, "Seeing Through the Clouds Navigating the Evolving Technology Ecosystem," *Booz & Company Inc.* (2011).

[10] R. Merritt, "Facebook likes 100G at $1/G: Web giant plans 2016 Ethernet upgrade," *EE Times* (2015).

[11] IDC Corporate, "Worldwide Quarterly Mobile Phone Tracker, Q4 2014," (2015).

[12] Cisco, "VNI Global IP Traffic Forecast, 2014 – 2019".

[13] B. Weisinger, B. Microsystems, "Facing the Challenges of Developing 100 Gbps Platforms," *www.ethernetalliance.org* (2010).

[14] Y. LeMaitre, "Challenges and Solutions for Optical Networks at 100Gbps and beyond," *ECOC Market Focus,* (2012).

[15] M. Shipon Ali, "The Challenges of Data Transmission toward Tbps Line rate in DWDM System for Long Haul Transmission," *International Journal of Future Generation Communication and Networking,* vol.7, no.1, pp.209-216 (2014).

[16] D. Lewis, C. Cole, "100G CWDM4 MSA Technical Specifications: 2 km Optical Specifications," *www.cwdm4-msa.org* (2013).

[17] S. Hardy, "IEEE P802.3bs Task Force adopts serial 100G for 400 Gigabit Ethernet," *Lightwave Online* (2015).

[18] "Continuous Rate 10 Mbps to 2.7 Gbps Clock and Data Recovery ICs", *Analog Devices, Inc.*

[19] J. D. Jin and S. H. Hsu, "A 40-Gb/s Transimpedance Amplifier in 0.18-μm CMOS Technology," *IEEE Journal of Solid-State Circuits*, vol. 43, no. 6, pp. 520-5123, (2008).

[20] C. F. Liao and S. L. Liu, "40 Gb/s Transimpedance-AGC Amplifier and CDR Circuit for Broadband Data Receivers in 90 nm CMOS", *IEEE Journal of Solid-State Circuits*, vol. 43, no. 3, pp. 642 - 655 (2008).

[21] J. Kim and J. F. Buckwalter, "Bandwidth Enhancement with Low Group-Delay Variation for a 40-Gb/s Transimpedance Amplifier," *IEEE Transactions on Circuits and Systems—I: Regular Papers*, vol. 57, no. 8, pp. 1964-1972, (2010).

[22] S. Bashiri, C. Plett, J. Aguirre and P. Schvan, "A 40 Gb/s Transimpedance Amplifier in 65 nm CMOS," *International Symposium on Circuits and Systems (ISCAS*), pp 757-760 (2010).

[23] J. Kim and J. F. Buckwalter "A 40-Gb/s Optical Transceiver Front-End in 45 nm SOI CMOS," *IEEE Journal of Solid-State Circuits*, vol. 47, no. 3, pp. 1-4, (2012).

[24] S. T. Chou, S. H. Huang, Z. H. Hong, and W. Z. Chen "A 40 Gbps Optical Receiver Analog Front-End in 65 nm CMOS," *International Symposium on Circuits and Systems (ISCAS)*, pp.1736-1739, (2012).

[25] M. N. Draa, J. Bloch, D. Chen, D. C. Scott, N. Chen, S. B. Chen, X. Yu, W. S. C. Chang, and P. K. L. Yu, "Novel directional coupler waveguide photodiode-concept and preliminary results," *Optics Express*, vol. 18, no. 17, pp. 17729-17731 (2010).

[26] M. N. Draa, *High Power High Linearity Waveguide Photodiodes: Measurement, Modeling, and Characterization for Analog Optical Links*, University of California, San Diego (2010).

[27] G. H. Smith and D. Novak, "Broad-band millimeter-wave fiber-wireless transmission system using electrical and optical SSB modulation," *IEEE Photon. Technol. Lett*., vol. 10, no. 1, pp.141-143 (1998).

[28] C. Lim, M. Attygalle , A. Nirmalathas , D. Novak, and R. Waterhouse, "Analysis of optical carrier-to-sideband ratio for improving transmission performance in fiber-radio links," *IEEE Trans. Microw. Theory Technol*., vol. 54, no. 5, pp.2181-2187 (2006).

[29] E. Vourc'h, B. Della, D. L. Berre, and D. Herve, "Millimeter-wave power –fading compensation for WDM fiber-radio transmission using a wavelength-self-tunable single-sideband filter," *IEEE Trans. Microwave Theory Tech*., vol. 50, no. 12, pp. 3009-3015, (2002).

[30] A. Narasimha, X. Meng, C. F. Lam, M. C. Wu, and E. Yablonovitch, "Maximizing spectral utilizing in WDM systems by microwave domain filtering of tandem single sidebands", *IEEE Trans. Microwave Theory Tech*., vol. 49, no. 10, pp. 2042-2047, (2001).

Chapter 2 High Power Traditional Waveguide Photodiode: Analysis, Design, and Demonstration

2.1 Introduction

Photodiode is an important component of the receiver in both digital and analog links. Its high power performance is important to the overall characteristics of the links [1, 2]. There are two configurations of photodiode, the surface normal photodiode (SNPD), and the waveguide photodiode (WGPD). Designing WGPD with high power performance has been very challenging, due to the non-uniform power distribution in WGPD. In the past, most of the analyses of high power WGPD have focused on direct calculation or simulation of how the incident optical power propagates and distributes in the absorber [3-9]. This kind of analysis has evolved around waveguide configurations and multi-layer structure, without a clear physical explanation of power distribution pattern in WGPD. In this chapter, supermode analysis is applied to traditional WGPD, and provides a clear and meaningful explanation of power distribution in WGPD. Armed with these understandings, traditional WGPD with better uniformity of power distribution can be designed and demonstrated.

2.2 The Operation of Photodiode

Traditionally, due to the format difference of data modulation, the operation of photodiode is different in digital and analog fiber optic links. The transmitted binary data in the traditional digital fiber optic link only has two amplitude states, and thus requires a highly sensitive photodiode that is able to detect a weak signal from a noisy background. The transmitted RF signal in the analog fiber optic link has continuously varying transient power and specific frequency, and thus requires a high power linear photodiode, which helps detect a signal in a link with high dynamic range, as discussed in section 1.2.

During the past few years, the boundary between digital and analog fiber optic links becomes blurred, due to the deployed higher order modulation (HOM) formats [10] for transmitting much higher data rate than that in a traditional digital fiber optic link. The modulation order is determined by the number of the different symbols that a digital communication scheme can transmit. The modulation order is 2 in traditional binary modulation, while it is 4 and above in HOM. HOM helps reduce the required channel bandwidth, due to the high spectral efficiency. For example, when transmitting 100 Gbps/λ data in a digital fiber optic link, the required link bandwidth is about 25 GHz using 16 quadrature amplitude modulation (16-QAM), while it is close to 100 GHz using traditional binary modulation. As the spectral efficiency in the HOM formats increases, some of the metrics for both broadband digital link and analog link, such as the dynamic range and link gain, become identical. Therefore, high power linear photodiode, which helps improve the dynamic range and link gain, becomes more attractive in the digital fiber optic link.

Photodiode is an optic-electronic converter. The incident light gets absorbed in the photodiode's absorber, in which the photon energy hν is larger than the bandgap of the absorber material. The absorption generates electron-hole pairs, which are collected in an external circuit in

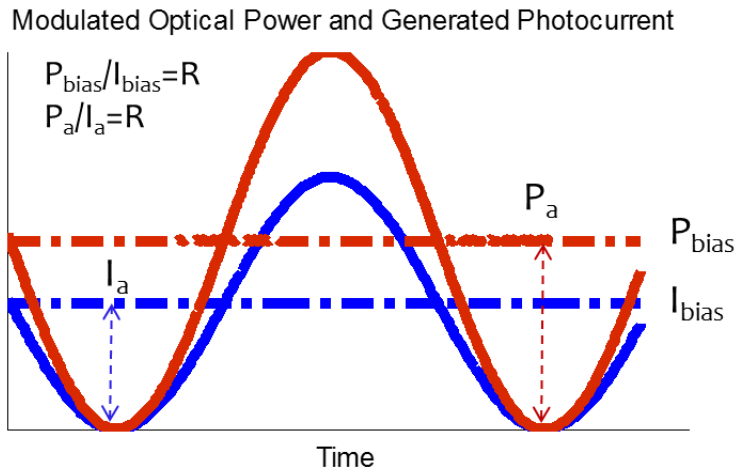

Figure 2-1 The relationship between incident optical power and photocurrent.

the form of photocurrent. External quantum efficiency η_e is defined as the number ratio of collected photo-generated carriers to the incident photons. This definition takes care of the optical coupling loss, incomplete absorption of the coupled optical power, and the photo-absorption generated carrier loss/gain during the transition. Responsivity R is defined as the ratio of the output photocurrent to the input optical power, and can be expressed as:

$$\mathrm{R} = \eta_e \frac{q}{h\upsilon} \quad (A/W) \tag{2.1.}$$

where q is the charge of an electron.

In the analog fiber optic link, as well as the modern broadband digital fiber optic link with higher order modulation (HOM) format, the incident optical power is modulated at certain bias point P_{bias} with certain amplitude P_a. Accordingly, the generated photocurrent is also modulated at certain bias point I_{bias} with certain amplitude I_a. The bias and amplitude of photocurrent relate to the bias and amplitude of input optical power P_{opt} by R, as shown in Figure 2-1. In order to avoid nonlinear device performance, I_{bias} has to be no less than I_a in the photodiode's operation.

$$I_{bias} \geq I_a \tag{2.2.}$$

Linear performance also sets certain requirements for the magnitude of the reverse bias voltage V_{bias}. First, a voltage drop V_s across the depletion region is required to maintain the saturated drift velocity of designed photo-generated carriers, so that when there is a small change of the electrical field in the depletion region, the number of carrier reached the external circuit will be relatively constant per unit time. Second, the circuit feedback voltage, which reduces the voltage drop across the depletion region, has to be considered. The photocurrent generated from the absorption of modulated optical power has two components, DC current and rf current. As shown in Figure 2-2, the rf current flows through the external load and results in a voltage swing in parallel with the bias voltage. The more rf photocurrent generated, the more voltage swing occurs. In this

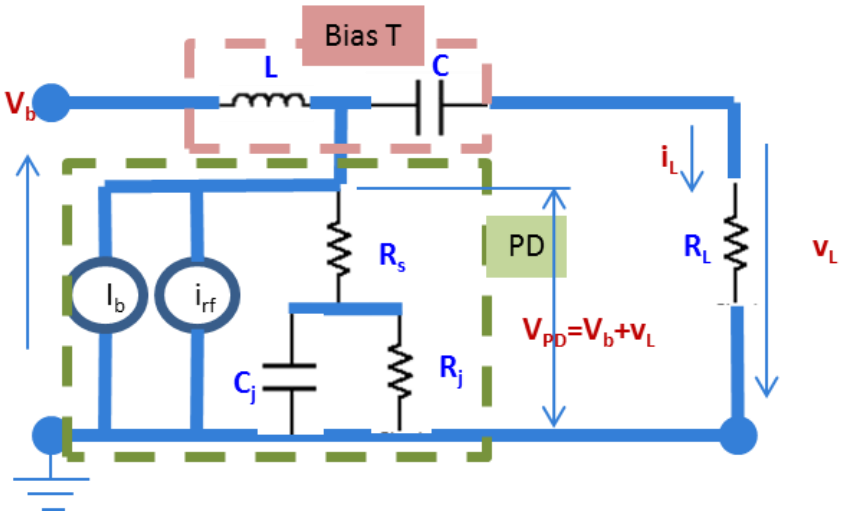

Figure 2-2 Equivalent circuit of photodiode with an external load resistance R_L. low rf frequencies is assumed, when the rf wavelength is much larger than the dimension of the detector structure. Here, i_{rf} is the rms RF photocurrent, I_b is the DC photocurrent. V_{bias} is the DC bias voltage. V_L is the rms output voltage. C_j is the junction capacitance. R_j is the junction leakage resistance. R_s is the series contact resistance of the electrode. In actual applications, matching circuit may be used instead of R_L.

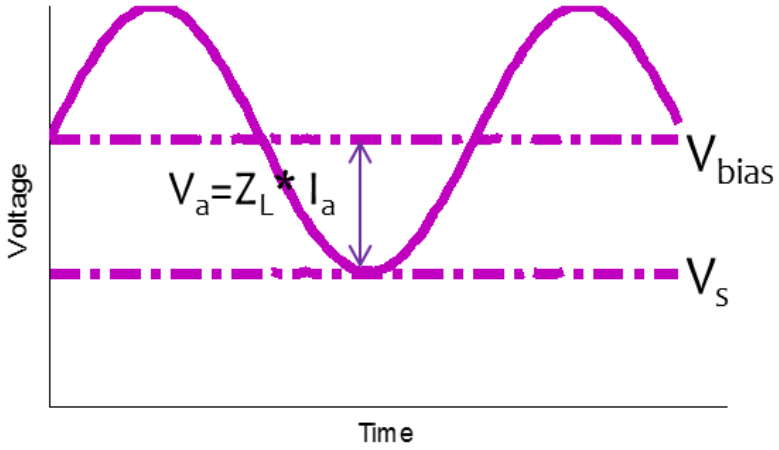

Figure 2-3 The bias voltage for photodiode with modulated incident optical power. V_s is the voltage required for carrier saturated drift velocity, V_a is the amplitude of voltage swing, I_a is the amplitude of the rf photocurrent, Z_L is the load impedance.

case, for linear operation of photodiode, as the rf current changes, the bias voltage has to be adjusted to maintain the saturated carrier drift velocity, as shown in Equation 2.3 and Figure 2-3.

$$V_a = \sqrt{2} i_{rf} \frac{Z_L}{1 + \frac{Z_L\left(1 + jR_j\omega C_j\right)}{R_j + R_s\left(1 + jR_j\omega C_j\right)}} \approx \sqrt{2} i_{rf} Z_L$$
$$V_b \geq V_{sat} + V_a \qquad 2.3.$$

where V_a is reduced to the last expression in Equation. 2.3, as R_j is in the order of MΩ, and is much larger than Z_L and R_s, which are usually less than 100 Ω.

2.3 Thermal dissipation power

As current flows through the photodiode under certain DC bias voltage, heat generates and becomes one of the important factors limiting photodiode's high power performance [11, 12, 13]. For the widely observed junction thermal failure, the thermal power related to heat generation in the p-i-n junction equals to the product of voltage dropped across the junction and the photocurrent flowing through the junction [13]. Because of the finite thermal conduction coefficient of the semiconductor [9], when the photodiode operates under high power, the heat will accumulate in the junction and finally damage the semiconductor's crystalline structure, and cause device thermal failure. There are two ways to represent the heat generated in a photodiode, one uses Instantaneous Power, and the other one uses Averaged Power. The two types of power are expressed as

$$\text{Instantaneous Power} = \left(I_{bias} + I_a * \sin\left(\mathrm{t} * \frac{2\pi}{\mathrm{T}}\right)\right)\left(V_{bias} + V_a * \sin\left(\mathrm{t} * \frac{2\pi}{\mathrm{T}} + \pi\right)\right)$$

$$\text{Averaged Power} = \frac{\int_0^T (I_{bias} + I_a * \sin(\mathrm{t} * \frac{2\pi}{\mathrm{T}}))(V_{bias} + V_a * \sin(\mathrm{t} * \frac{2\pi}{\mathrm{T}} + \pi))}{T}$$

$$= I_{bias} * V_{bias} + \frac{I_a V_a}{2}$$
$$= DC\ power + rms\ RF\ power \qquad 2.4.$$

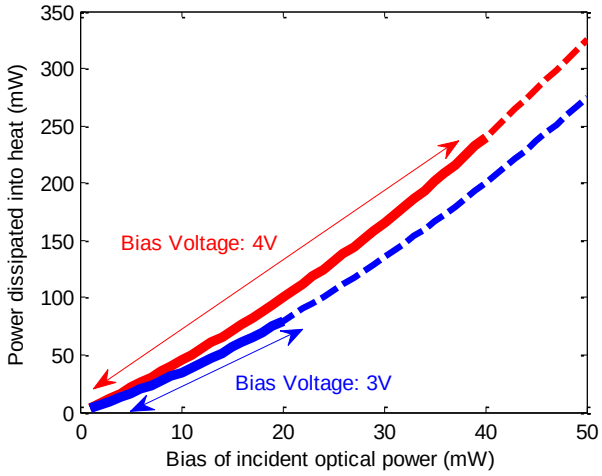

Figure 2-4 The plot of power dissipated into heat in a photodiode versus the bias of the incident optical power. The i_{rf} reduces the voltage drop at the depletion region, the solid line corresponds to when the voltage in the depletion region is always larger than voltage for carrier saturated drift velocity V_S, while the dashed line corresponds to the voltage in the depletion region drops below V_S when the bias voltage is reduced by V_a. The modulation index MI is 1, V_S is 2 V, external load impedance Z_L is 50 Ω, photodiode responsivity is 1 A/W.

where T is the period of the modulated optical signal, I_a and V_a are the amplitude of the rf current and the feedback voltage swing.

For photodiode used in the link with GHz order modulation frequency, the characteristic time of an instantaneous signal oscillation is in the order of ns, while the characteristic time of the heat generation and thermal dissipation is in the order of μs. Due to the orders of difference between the characteristic times, the heat generation and conduction will not respond to the instantaneous signal oscillation. In this sense, Average Power would be the better way to represent the heat generation and thermal dissipation, which are treated as time and frequency independent physical phenomena.

2.4 Limitations of electrical power dissipated at the load

There are several factors limiting the maximum i_{rf} that a photodiode can dissipate at the external load. First, the maximum i_{rf} is limited by the bias of the incident optical power and hence the bias of the generated photocurrent, as the amplitude of the rf current should not be larger than the bias current. Second, the maximum $i_{rf}*Z_L$ is limited by the bias voltage V_b, as shown in section 2.3. Third, the maximum i_{rf} is limited by the photodiode's power handling capability. Although increasing the bias of incident optical power and bias voltage can alleviate the constraints on achieving high i_{rf}, the resulted large thermal dissipation power will finally exceed what a photodiode can handle and cause device thermal failure. As shown in Equation 2.5, the thermal dissipation power depends on I_{bias}, V_{bias}, I_a and V_a, all of which are functions of the bias of incident optical power. In this case, with given V_{bias} and modulation index (MI) of the incident optical power, the thermal dissipation power in a photodiode can be plotted as a function of the bias of the incident optical power, as shown in Figure 2-4.

At a given bias voltage V_{bias} and modulation index, i_{rf} increases when the bias of the incident optical power goes up. The voltage drop in the photodiode due to the circuit feedback effects, which is proportional to the i_{rf}, also varies. The transient voltage drop varies in time, and the maximum voltage drop V_a is $P_{bias}R\frac{MI}{2-MI}Z_L$, as shown in Equation 2.5.

$$P_{heat} = I_{bias} * V_{bias} + \frac{I_a V_a}{2}$$

In which:

$$I_{bias} = R * P_{bias}$$

$$I_a = P_{bias} R \frac{MI}{2-MI} \qquad \text{2.5.}$$

$$V_a = I_a Z_L = P_{bias} R \frac{MI}{2-MI} Z_L$$

$$V_{bias} \geq V_S + V_a = V_S + i_{rf} * Z_L$$

$$= V_S + I_a/\sqrt{2} * Z_L$$

$$= V_S + \frac{P_{bias} R \frac{MI}{2-MI}}{\sqrt{2}} * Z_L$$

$$P_{bias,\,max} = \sqrt{2}(V_{bias} - V_S) \Big/ (\frac{MI}{2-MI} R Z_L)$$

where R is the photodiode's responsivity, Z_L is the impedance of the external load, V_S is the voltage required for carrier drifting at saturated velocity in the depletion region, and $P_{bias,max}$ is the bias of incident optical power that make the transient voltage start dropping below V_S.

In order to maintain the saturated carrier drift velocity, the bias of the incident optical power has an upper limit $P_{bias,max}$ so that V_{bias}- V_a can be kept above V_S, which corresponds to the solid line region in Figure 2-4. When the bias of the optical incident optical power is larger than $P_{bias,max}$, the photodiode operation becomes nonlinear, as V_{bias} drops below V_S. In this case, a larger V_{bias} is required to restore the linear operation.

The thermal failure point in a photodiode, which has an InP substrate and an InGaAs absorber, and has the majority part of the thermal power dissipated through the substrate, is related to the heat dissipation and semiconductor material characteristics. InP has a fairly low thermal conductivity (0.68 W/cm/K) and InGaAs is even worse (0.05W/cm/K). The thermal failure in photodiode usually occurs when the average power density is less than 1 mW/ μm^2 [11, 12, 13], upon which the material in and near the intrinsic region melts. However, most of photodiodes reported a thermal failure power density $P_{fail\ density}$ much less than 1 mW/ μm^2 [3-9], which can be attributed to many factors, including the thermal power distribution, heat dissipation, and material quality, etc. The early discussion of Figure 2-4 shows that larger bias voltage benefits the linear operation of a photodiode. However, a larger bias voltage also results in more heat generation in the photodiode. In this case, for a photodiode with given active area size A, it is important to

increase $P_{fail\ density}$, in order to prevent it from thermal failure at high power level. One major goal of this dissertation is to analyze and improve the optical power distribution in a photodiode, as it directly relates to the thermal power distribution and hence $P_{fail\ density}$. Other issues, such as material conductivities and heat sinking, are also important. However, in this dissertation, the discussion of improvement of thermal failure power density, as well as its comparison to the thermal failure power density in an ideal WGPD, will be in the scope of utilizing the average, instead of the best, performance of material conductivities and heat sinking etc. Therefore, the comparison emphasizes the same thermal dissipation even in the presence of different thermal generation.

2.5 Photodiode Layer Structure

P-I-N layer structure, instead of p-n layer structure, is widely used in photodiode, to increase the response speed. When a photon with sufficient energy reaches the absorber in the photodiode, it can be absorbed and creates an electron-hole pair. Depends on the location of absorption occurrence, the photodiode layer structure is classified into two major types, PIN and Uni-Carrier-Traveling (UTC).

2.5.1 PIN

The absorber in a conventional PIN photodiode is part of the intrinsic region. Photodiodes with a PIN structure are widely used for optical communication because they have simple structures and relatively high responsivity. However, PIN photodiodes cannot sustain high photocurrent levels for several reasons. One main reason is that PIN photodiodes are particularly susceptible to space-charge induced current saturation [14, 15]. In a PIN photodiode, the electron drift velocity is higher than that of holes, which causes spatial imbalance of the photo-generated carrier density in the intrinsic region [16], with more holes accumulated in the intrinsic absorber region. As the optical power increases, the electric field in the intrinsic region is gradually screened by the unbalanced carrier density distribution, with the total electrical field started to reduce in magnitude

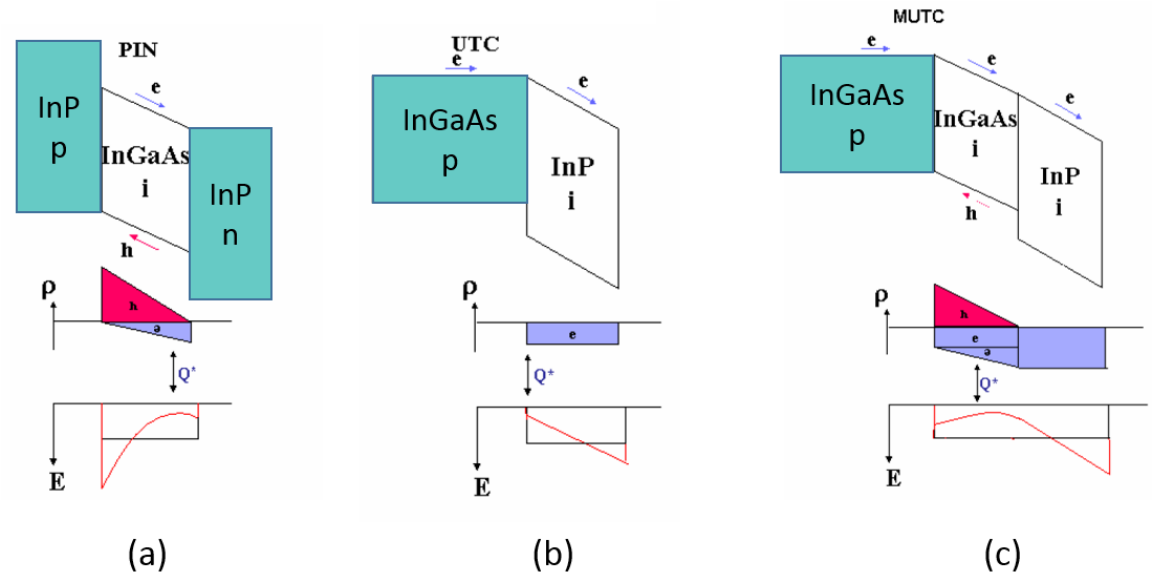

Figure 2-5 Schematic of PIN (a), UTC (b), and MUTC (c) photodiodes, and the corresponding electric field distribution [5].

and finally collapses near the n side, as shown in Figure 2-5(a). When the electrical field drops and carriers drift at below saturation velocity, the carrier transit time increases and the output current saturates. This is referred as the space charge effect [16], which affects photodiode's linearity and bandwidth performances at high incident power level. Besides, PIN photodiodes are very susceptible to thermal failure. On one hand, the electric field in the intrinsic InGaAs absorber is responsible for most of the heat generation in PIN photodiode. On the other hand, InGaAs is a narrow-bandgap semiconductor, and its critical temperature for thermal runaway is relatively low. Therefore, thermal failure is expected to occur at a relatively small photocurrent level in PIN photodiodes.

2.5.2 UTC

Several photodiode structures have been developed to mitigate the space charge effect. The uni-traveling-carrier (UTC) photodiode as shown in Figure 2-5(b), which utilizes an undepleted p-type layer to absorb light and inject electrons into a wide-bandgap depleted drift region, has shown

improved bandwidth and power performances [17, 18]. T. Ishibashi et al first demonstrated the potential of achieving high bandwidth and high power [17, 18]. In UTC, the carriers are photo-generated in the p-type absorber layer, and minority electrons diffuse/drift into the collection layer. A diffusion-blocking layer is on the p-contact side of the absorption layer, so the electrons have net motion toward the collection layer. Since holes are the majority carriers, their transport is a collective motion, and thus the absorption layer response is primarily determined by the electron transport. Although the response of hole current is limited by the dielectric relaxation time (τ_R), it is short enough in a typical design. (e.g., $1/2\pi\tau_R$ = 1.2 THz for p-InGaAs = 1 x 10^{18} /cm^3). In a UTC structure, the high mobility and high drift velocity of electrons are essential for minimizing the absorption layer traveling time (τ_A). The depleted collection layer traveling time (τ_d) is a time delay of the induced current, and it will not affect the frequency response, if a frequency independent delay is assumed. The UTC structure has three advantages. First, there is only electrons transit in the depleted region, so the space charge effect is greatly suppressed. Second, a wide bandgap, high thermal conductivity III-V material is used in the drift region, which renders the photodiode less susceptible to thermal failure. However, there is one issue for the UTC structure utilized in SNPD, that is the performance tradeoff associated with the thickness of the absorber. If the layer is very thick, a high fraction of the incident light can be absorbed, which will yield high responsivity. In this case, thick absorber is favored for yielding high responsivity, however, it also results in large probability of recombination, and more importantly, it reduces the transit time limited bandwidth, as the time required for the photo-generated electrons to diffuse into the wide-bandgap collector becomes long. This issue becomes less critical in a waveguide photodiode, which utilize long absorber rather than thick absorber to achieve high responsivity. In order to circumvent this problem in SNPD, the modified UTC (MUTC), which is another variation of original UTC structure, is developed. As shown in Figure 2-5(c), the MUTC narrow-bandgap absorber has an undepleted p-type region and a depleted layer, as well as a wide-bandgap depleted drift region next

to the absorber. In this structure, space charges generated in the intrinsic InGaAs layer is relatively small, owing to the fact that the absorber is thin. Also, there is no heterobarrier to impede the transport of holes toward the p-region. The thickness of the undepleted absorber, depleted absorber and the electron drift layer can be adjusted separately to achieve required bandwidth, responsivity and power handling capability. This dissertation will focus on UTC-type photodiodes owing to their high bandwidth and excellent power handling capability.

2.6 Photodiode Device Structure

Depending on the direction that light is illuminated into the photodetector, there are two major types of photodiode device structure, surface normal photodetector (SNPD) and waveguide photodetector (WGPD). The structure in Figure 2-6 (a) is a conventional surface normal illuminated p-i-n photodetector (SNPD). In this geometry, light is illuminated into the photodiode either from the top or from the substrate side. When the absorber layer gets thicker, the absorption efficiency will go up. However, the increased thickness of the intrinsic layer results in a longer transit time for photo-generated carriers. To overcome the tradeoff between absorption efficiency and carrier transit time in the SNPD, an edge-illuminated photodetector, also called waveguide photodetector (WGPD), is developed, as shown in Figure 2-6 (b). In this structure, the absorption length is determined by the absorber length in the longitudinal direction, and the transit time is determined by the thickness of the absorber and intrinsic layers in the vertical direction. Consequently, these two quantities become independent of each other, and wide bandwidth and high absorption efficiency can be obtained simultaneously in a WGPD. However, when light is illuminated into this device, most of the optical power will be absorbed at the forward section of the absorber. As a result, the induced high absorption density in this section restricts the device performances at high power. This dissertation will focus on studying how to control the overall absorption distribution

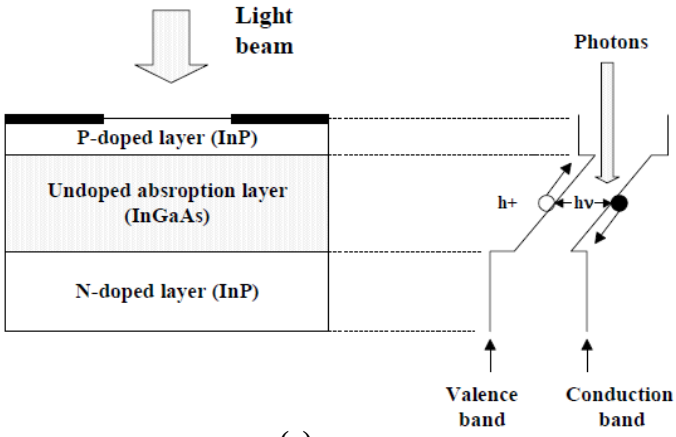

(a)

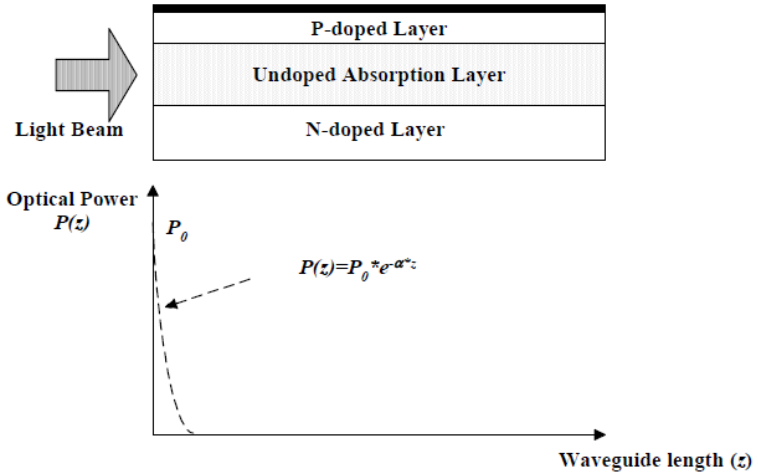

(b)

Figure 2-6 Surface normal illuminated p-i-n photodetector (SNPD) and its band diagram (a), Edge-illuminated waveguide photodetector (WGPD) and its power distribution profile (b) [5].

in WGPD.

2.7 General Discussions of Ideal WGPD

Now that we have briefly discussed photodiode types and layer structures, we will outline the general considerations for designing a high power WGPD: bandwidth, responsivity, and power handling capability. Understanding the tradeoffs between those performances is critical for

designing a high power WGPD with optimized bandwidth and responsivity. A realistic WGPD has non-uniform absorption profile, which will make the discussion of such a design very complicated. Therefore, an ideal WGPD is used for the discussion first, which will be followed by the discussion of a realistic WGPD with added feature of non-uniform absorption profile.

2.7.1 Assumptions for ideal WGPD

A few assumptions are made for an ideal WGPD in the following discussion.

First, the power distribution and absorption in the absorber is uniform in the longitudinal and lateral directions. As discussed before, the incident optical power goes to the absorber layer perpendicularly in SNPD but in parallel to the waveguide in WGPD, which induces large difference of absorption uniformity in the two types of photodiodes. As we will discuss later, the non-uniform distribution of absorbed power limits the power handling capability of the WGPD. Therefore, we assume uniform longitudinal and lateral power distribution in ideal WGPD. In contrast, this condition already exists in SNPD in the first order approximation.

Second, the transit time limited bandwidth is negligible in an ideal WGPD. In a UTC-WGPD, the absorber usually has a graded doping profile, which generates a built-in electrical field and reduces the transit time. The required absorber thickness in WGPD is usually much smaller than in SNPD. For example, in a UTC-WGPD with 0.5 μm intrinsic InGaAsP and 300 μm^2 active layer size, when it is connected to a 50 Ω load, f_{RC} is about 50 GHz. When the absorber is 0.3 μm thick and when it is properly doped, the transit time limited bandwidth f_T can be as high as 180GHz. Hence, the device bandwidth is dominated by the RC time constant, and it is OK to assume that the transit time limited bandwidth is negligible in an ideal WGPD.

Third, we assume that all of the generated thermal power dissipates through the bottom substrate, and the thermal dissipation capability per unit area is independent of the structure and

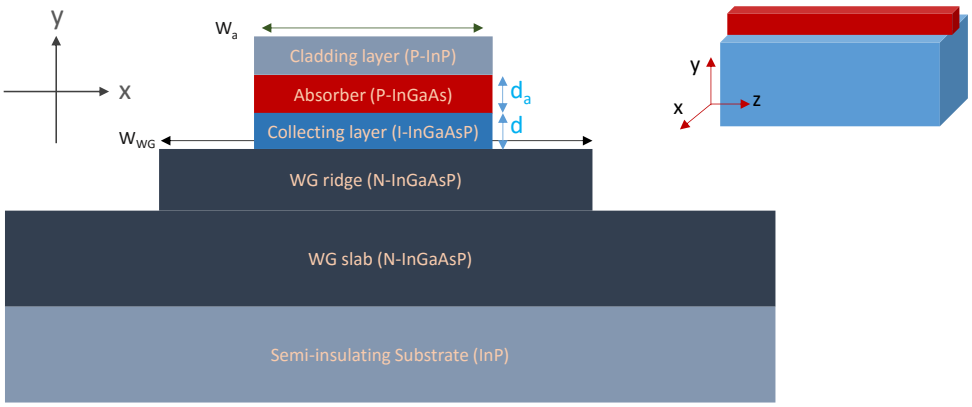

Figure 2-7 A cross-section view of a UTC-WGPD. The inset picture is a schematic of 3-D plot of the WGPD. W_a and W_{WG} are the width of absorber and waveguide ridge, respectively. d_a and d are the thickness of absorber and intrinsic collecting layer, respectively.

the area of the device on the substrate. Therefore, all of the WGPD's in different lateral configurations has the same limit of absorbed power per unit area due to thermal failure.

Fourth, we assume that an ideal WGPD will have the same fraction of the incident power absorbed, which is independent of the lateral configuration.

After making the above assumptions, it is ready to have some general discussion of an ideal WGPD by using the UTC layer structure shown in Figure 2-7.

2.7.2 Bandwidth

In a UTC-photodiode, there is an absorber layer that is doped with p-type dopant, and an electron collecting layer that is unintentionally doped. The generated electrons diffuse in the doped absorber, when they reach the interface between the absorber and the collecting layer, they will drift through the collecting layer and reach the highly n-doped semiconductor, which connects to device's cathode. The carrier transit time in a UTC- photodiode usually refers to the electron's transit time, which is the time an electron takes from generation in the doped absorber to transit through the collecting layer. Therefore, it is related to the absorber region thickness T_a, collecting layer thickness T_c and transit velocity. It can be expressed as [19]:

$$1/t_{transit} = 1\Big/\frac{T_a{}^2}{D_e} + 1\Big/\frac{T_a}{v_{th}} + 1\Big/\frac{T_c}{v_{drift}} \qquad 2.6.$$

where D_e (<300 cm^2/s in InGaAs) is the diffusive constant of electrons, v_{th} is the thermionic emission velocity (~ 2.5 $\times 10^7$ cm/s in InGaAs), v_{drift} is the electron drift velocity in the i-InGaAsP (~1 x 10^7 cm/s).

The transit time limited bandwidth is:

$$f_T = \frac{3.5}{2\pi t_{transit}} \qquad 2.7.$$

Another factor that limits frequency response is the junction capacitance charging time constant, which can be expressed by the RC time constant. The RC time constant describes how rapidly the junction capacitance of the photodiode can be charged and discharged through the effective load resistance, which is approximately the sum of the internal series resistance Rs, and the external load resistance, R_L. The RC limited bandwidth directly relates to the RC time constant, and is given by:

$$f_{RC} = \frac{1}{2\pi C_{PD}(R_L + R_S)} \qquad 2.8.$$

where C_{PD} is the junction capacitance.

$$\mathrm{C} = \frac{\varepsilon A}{T_c} \qquad 2.9.$$

where ε is the dielectric constant, and A is the device active area size.

The total bandwidth of the photodiode is related to a combined effect of transit time limitation and RC circuit time limitation, and it can be expressed as [19]:

$$\frac{1}{f_{3dB}^2} = \frac{1}{f_T^2} + \frac{1}{f_{RC}^2} \qquad 2.10.$$

As have shown in section 2.7.1, the transit time is negligible in a UTC-WGPD, and is smaller than the RC time. In contrast, the transit time in a UTC-SNPD is usually not negligible. In order to achieve large absorption efficiency in a UTC-SNPD, the doped absorber thickness is much

larger than that in a UTC-WGPD. Therefore, it takes much longer time for the photo-absorption generated electrons to diffuse and reach the collecting layer in UTC-SNPD, and the transit time is usually comparable to the RC time constant.

2.7.3 The Fraction of Optical Power within Absorber

A cross-section view of a WGPD is shown in Figure 2-7. In the WGPD, the optical power is confined in two directions (the x direction and y direction in our notation), as it travels in the z direction. The fraction of optical power confined in the waveguide cross-section that is within the absorber is defined as confinement factor Gamma Γ, which is unitless.

In an ideal WGPD, the power distribution is assumed to be uniform not only in the direction, but also in the x direction. Therefore, Gamma per width, which is Gamma divided by the absorber width, is constant along absorber width, and is with unit 1/ μm.

2.7.4 Absorption efficiency

The absorption efficiency η of photodiode is defined as the ratio of the absorbed optical power to the incident optical power:

$$\eta = \frac{P_{absorbed}}{P_{incident}} \qquad 2.11.$$

where η is the absorption efficiency, $P_{absorbed}$ is the incident optical power, and $P_{absorbed}$ is the absorbed optical power. In an ideal WGPD, η is proportional to the absorber length L. In contrast, in a realistic photodiode, the expression of η will be dependent on the absorption method, with two general cases for surface normal and waveguide presented below:

$$\eta_{SN} = (1 - R_L)\left(1 - e^{-\alpha d}\right) \qquad 2.12.$$

$$\eta_{WG} = (1 - R_L)(1 - e^{-\Gamma \alpha L}) \qquad 2.13.$$

where R_L is the reflectivity of the coupling facet, α is the absorption coefficient, d is the absorption layer thickness of the surface normal device, Γ and L are the confinement factor and absorber length, respectively.

As shown in Equation 2.13, the absorption efficiency in a WGPD is an exponential function of the absorber length L. Figure 2-8 plots the absorption efficiency η as a function of L/Lh, where Lh is the absorber length at which η of 0.5 is achieved. As L increases, the increase of η slows down, which indicates that extending the absorber length does not increase η substantially when it is already close to 1. Instead, it comes at a price of reduced bandwidth due to the increased active

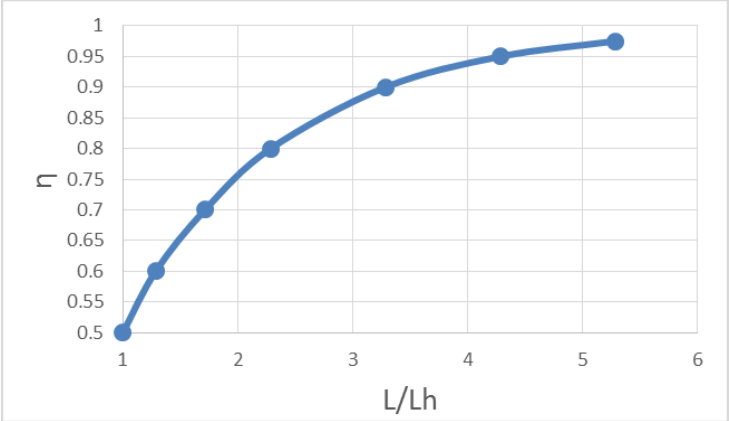

Figure 2-8 The absorption efficiency η plotted as a function of L/Lh in a realistic WGPD, according to equation 2.13. The reflectivity R_L is assumed to be 1. Lh is the absorber length at which η of 0.5 is achieved.

Table 2-1 The effects of reducing active area size in an ideal WGPD. The layer structure is as shown in Figure 2 7.

Active area size	A	½ *A
Bandwidth	1/(2πRC)	2 * 1/(2πRC)
Thermal power density	(I_{bias} * Vbias+I_a*V_a/2)/A	2 * (I_{bias} *V_{bias}+I_a*V_a/2)/A
Minimum Gamma/area	η/A	2*η/A

area size. Therefore, in the following discussion, the design goal of absorption efficiency is usually set around 0.8 instead of 1.

2.7.5 Performances Tradeoff In An Ideal WGPD

In an ideal WGPD, the active area size A is the product of width W_a and length L. The device performances, such as bandwidth, thermal power density, and minimum Gamma/width required for obtaining certain absorption efficiency η, as well as the trade-off between those performances in WGPD design, can be evaluated under different circumstances. In this section, how the design of WGPD's waveguide configuration and layer structure affects the three performances is elaborated by using several examples.

First, the active area size A closely relates to all three performances, as shown in Table 2-1. In the design of WGPD, the active area size A is one of the important parameters that needs to be determined at the beginning. On one hand, an ideal WGPD with smaller A not only has smaller device size, but also and more importantly, has larger bandwidth, as discussed in section 2.7.2. On the other hand, when the total heat generation is the same, an ideal WGPD with smaller A will have higher thermal power density, and reach the thermal failure power density at lower input power. Besides, if the absorption efficiency η needs to be kept the same, the minimum Gamma/width in

Table 2-2 The effects of increasing the intrinsic absorber thickness in an ideal WGPD

Intrinsic absorber thickness	d_i	**2** $*d_i$
Bandwidth	$1/(2\pi RC)$	**½** $* 1/(2\pi RC)$
Minimum Bias voltage V_{bias}	V_s+V_a	$2V_s+V_a$
Thermal power density	$(I_{bias} * (V_s+V_a)+I_a*V_a/2)/A$	$(I_{bias} *(2V_s+V_a)+I_a*V_a/2)/A$

Table 2-3 The effects of reducing the doped absorber thickness in an ideal WGPD

Doped absorber thickness	d_a	2 *d_a
Bandwidth	$1/(2\pi RC)$	$1/(2\pi RC)$
Minimum Bias voltage V_{bias}	V_s+V_a	V_s+V_a
Thermal power density	$(I_{bias} * (V_s+V_a)+I_a*V_a/2)/A$	$(I_{bias} *(V_s+V_a)+I_a*V_a/2)/A$

an ideal WGPD with smaller A has to be increased, which requires redesign of either waveguide configuration or layer structure.

Second, the optimization of the absorber thickness usually comes along with the considerations of active area size A. Once A is determined, an expected absorption efficiency η requires certain adjustment of the Gamma/area, which can be realized by tuning the InGaAs absorber thickness, as it has the largest refractive index among the layers in a WGPD on InP substrate. In a UTC-WGPD, the absorber is p-doped, as shown in Figure 2-7. In contrast, there is intrinsic absorber layer in WGPD with PIN or MUTC structure, as shown in Table 2-2. The effects of adjusting the thickness of doped absorber and intrinsic absorber are different, as shown in Table 2-2 and Table 2-3. The thickness change of the intrinsic absorbing layer affects the bandwidth and power handling capability, due to the change of required voltage for saturated carrier drift velocity. The thickness change of the doped absorbing layer does not affect those performances. However, this is only true for the ideal WGPD. Because of the low thermal conductivity of InGaAs, the thickness change of the doped absorbing layer will affect the thermal dissipation capability in a realistic WGPD, and hence its power handling capability. The thickness change of the doped absorbing layer will have additional effects on the carrier transit time in a realistic SNPD. Thicker absorber reduces SNPD's bandwidth. However, it is a minor concern in a realistic WGPD, as it requires a much thinner absorber than SNPD.

2.7.6 Goals and Limitations of WGPD Designs

Due to the fast increase of internet bandwidth consumption, as discussed in chapter 1, there is high demand of upgrading the currently 10 Gbps per wavelength Ethernet to 100 Gbps at the system level. More research groups are studying the realization of 100 Gbps Ethernet from either components or system aspects [20] [21]. With the deployment of HOM, Pulse amplitude modulation (PAM) 4 with 2 bits/symbol, for instance, it requires the transmission channel bandwidth of 25 GHz in the intermediate stage and 50 GHz at the final stage [22]. Therefore, the system designers' targeted photodiode bandwidth ranges from 25 GHz to 50 GHz, which will also be the PD bandwidth range emphasized in this dissertation.

In this dissertation, for the discussion of UTC-WGPD operating at 1550 nm wavelength, when the UTC layer structure has 0.4 μm thick intrinsic InGaAsP and less than 0.3 μm thick p type InGaAs with grading dopant profile, >100 GHz transit time limited bandwidth is expected, The photodiode's active area size can be easily calculated by using the given bandwidth. For WGPD with bandwidth between 25 GHz and 50 GHz, the active area size will be between 560 μm^2 and 280 μm^2 in a 50 Ω loaded InP-based photodiode with negligible parasitic capacitance.

Once the active area size is determined, the power handling capability in an ideal WGPD can be calculated, with the assumed thermal failure power density of 1 mW/ μm^2. According to

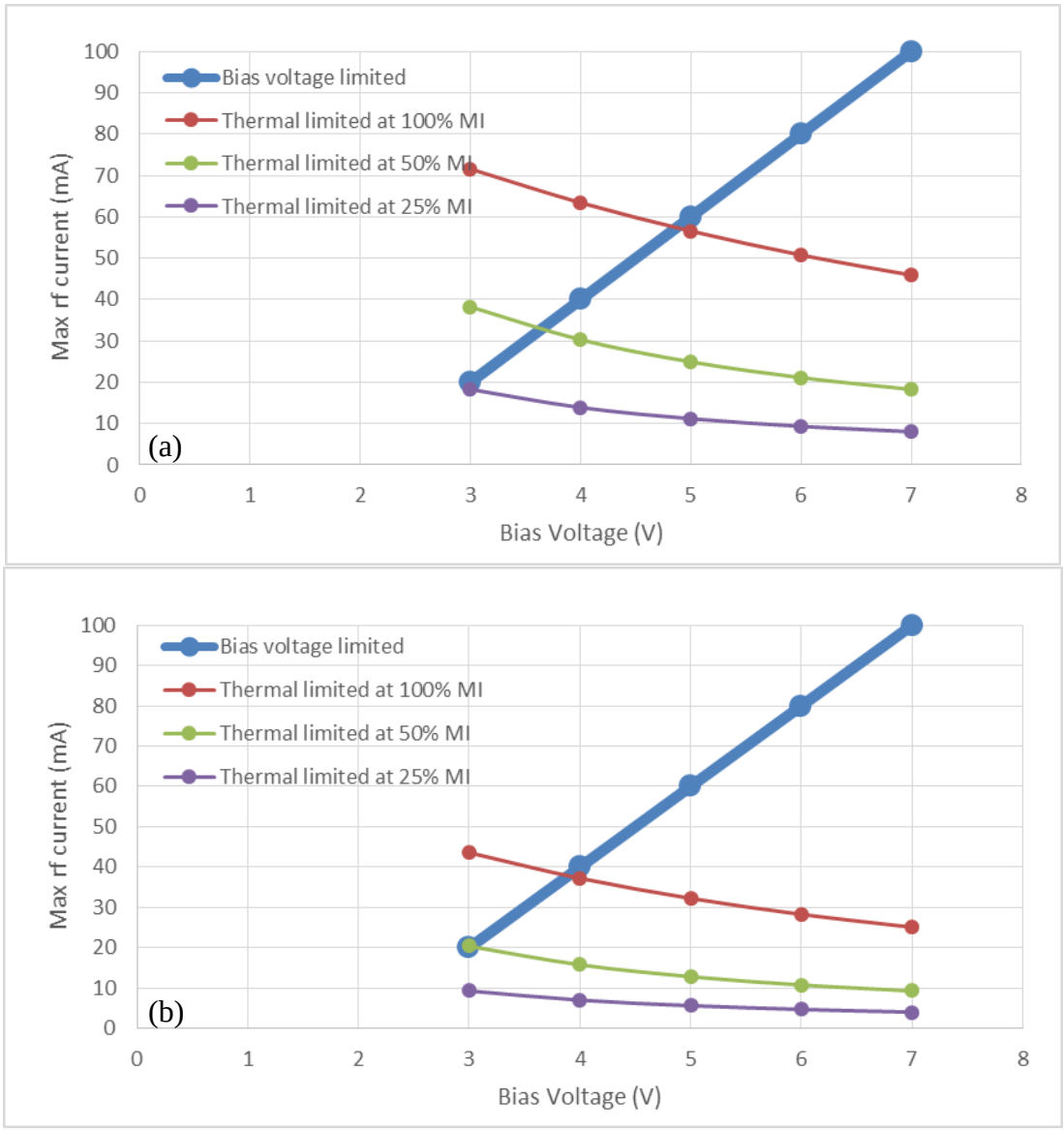

Figure 2-9 The maximum allowed rf photocurrent (rms value) in the 25 GHz (a) and 50 GHz (b) bandwidth photodiodes shown in with bandwidth between 25 GHz and 50 GHz, the active area size will be between 560 μm2 and. The voltage for saturated carrier drift velocity V_S is assumed to be 3 V, the load impedance Z_L is assumed to be 50 Ω.

Equation 2.5, several other important parameters related to photodiode's power handling limit can also be deduced. with bandwidth between 25 GHz and 50 GHz, the active area size will be between 560 μm^2 and is generated to summarize the goals and limitations of 25 GHz and 50 GHz photodiode.

Table 2-4 The list of parameters for 25 GHz and 50 GHz WGPD.

Parameters	**25 GHz**	**50 GHz**
Transit time limited bandwidth f_T	>100 GHz	>100 GHz
Active area size A	560 μm^2	280 μm^2
Absorption efficiency η	0.8	0.8
Minimum Gamma/ area	1.43e-3	2.86e-3
Thermal failure power density	1 mW/ μm^2	1 mW/ μm^2

As discussed in section 2.4, the maximum allowed rf photocurrent in an ideal WGPD is limited by three factors, the bias voltage, the bias current, and the thermal failure power. For a given modulation index (MI) and bias voltage V_{bias}, the maximum allowed rf photocurrent can be calculated, which is shown in Figure 2-9.

$$\begin{aligned} &I_a/\sqrt{2} \le \frac{V_{bias} - V_S}{Z_L} \\ &I_a \le I_{bias} \\ &P_{heat} = I_{bias} * V_{bias} + \frac{I_a V_a}{2} \le I_{bias} * V_{bias} + \frac{1}{2} I_a (V_S + I_a/\sqrt{2} * Z_L) \end{aligned} \quad 2.14.$$

As shown in Figure 2-9, the bias voltage and thermal failure set different limits to the maximum rf photocurrent. As the bias voltage increases, the change of the maximum rf photocurrent limited by the two factors goes to different directions. The optimized bias voltage for testing the power handling capability of a WGPD is the one when bias voltage and thermal failure limit the photocurrent at the same level. While the bias voltage limited photocurrent is the same in both 25 GHz and 50 GHz bandwidth ideal WGPDs, the thermal failure limited photocurrent is at different levels, due to the active area size difference.

2.7.7 The effects of non-uniform power distribution

The power distribution in a realistic WGPD is not as uniform as in an ideal WGPD. In order to discuss the effects of non-uniform power distribution in WGPD, an ideal WGPD and a realistic WGPD are compared, whose absorption profile are shown in Figure 2-10. It is assumed that in the two WGPDs, the layer structure, the active area size A, the absorption efficiency η, and the external load impedance are the same. Moreover, it is assumed that the two WGPD are operated under the same condition, as the incident optical power, and dc bias voltage V_{bias} are the same. Therefore, the two WGPDs will have the same bandwidth, generated photocurrent (I_{bias} and I_a), and voltage feedback (V_a).With the above assumptions, although the average thermal power density is the same, the two WGPDs differ in the peak thermal power density. The average thermal power density depends on parameters such as the total photocurrent (I_{bias} and I_a), bias voltage (V_{bias}), voltage feedback (V_a), and the active area size (A). As those parameters are the same in the two WGPDs, the average thermal power density will also be the same. However, the local thermal power density differs from the average thermal power density in that the former depends on the local photocurrent density instead of the total photocurrent. In a realistic WGPD with non-uniform power distribution, even though the total photocurrent is the same as that in an ideal WGPD, the local photocurrent density varies at different locations, as shown in Figure 2-10.

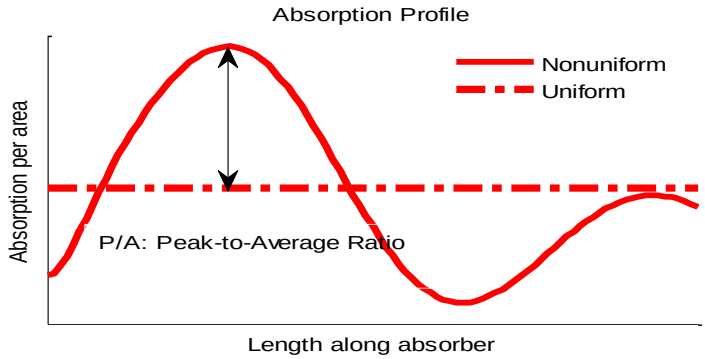

Figure 2-10 Uniform absorption profile in an ideal WGPD, and non-uniform absorption profile in a realistic WGPD.

$$P_{heat} = I_{bias} * V_{bias} + \frac{I_a V_a}{2}$$

$$P_{local\ heat\ density} = I_{bias,local} * V_{bias,local} + {}^{1}/_{2} \times I_{a,local} V_{a,local} \quad 2.15.$$

As shown in Equation 2.15, the local thermal power density $P_{local\ heat\ density}$ can be expressed similarly with the total thermal power P_{heat}, as a sum of the DC power density and the rms of rf power density. The local bias voltage is determined by the DC bias voltage V_{bias} and circuit feedback voltage V_a, so the local bias voltage $V_{bias,local}$, as well as the voltage swing due to circuit feedback $V_{a,local}$, are the same with V_{bias} and V_a, respectively. However, when the absorption density peak to average ratio P/A goes above 1 due to the non-uniform power distribution, the local current density's bias and amplitude $I_{bias,\ local}$ and $I_{a,\ local}$ vary, so does $P_{local\ heat\ density}$. Assume the P/A increases from 1 in an ideal WGPD to 2 in a realistic WGPD, the peak $I_{bias,\ local}$ and $I_{a,\ local}$ in the realistic WGPD will be twice of that in the ideal WGPD, which results in a doubling of the peak thermal power density in the realistic WGPD, as shown in Table 2-5.

The increase of the peak thermal power density causes early thermal failure of WGPD and limits the power handling capability. As the peak thermal power density goes up proportionally with the absorption distribution P/A, the study of controlling absorption profile in a WGPD with

Table 2-5 The performance comparison between ideal WGPD and realistic WGPD. The power distribution peak-to-average ratio P/A is 1 in the former one, and 2 in the latter one.

	Ideal WGPD	Realistic WGPD
P/A	1	2
Absorption efficiency	η	η
Bandwidth	1/(2πRC)	1/(2πRC)
Total Thermal power	$(I_{bias} * V_{bias}+I_a*V_a/2)$	$(I_{bias} *V_{bias}+I_a*V_a/2)$
Peak thermal power density	$(I_{bias} * V_{bias}+I_a*V_a/2)/A$	$2*(I_{bias} * V_{bias}+I_a*V_a/2)$

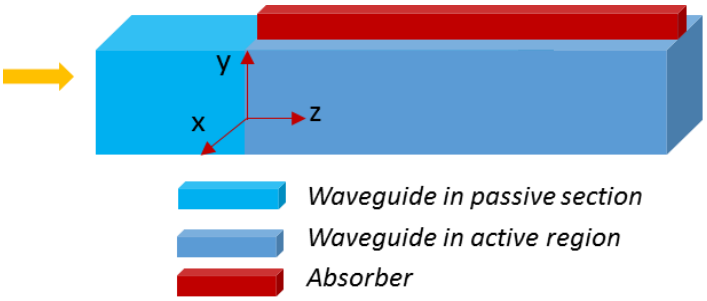

Figure 2-11 Schematic of traditional WGPD for high power applications.

small P/A becomes important for high power applications, and it will be the major study topic in the following sections.

2.8 Progress of Study of the High Power Traditional WGPD

For high power operations at 1.55 μm wavelength, one type of traditional waveguide integrated photodiode structure is widely reported [3], [4], [5], [7], [8], which includes a passive section and an active section. A schematic of this type of traditional WGPD is shown in Figure 2-11. In the passive section, an input waveguide transfers the incident optical radiation into desired modes, which then excite multiple modes in the active section, where an absorber structure sits on top of the waveguide. At the front end of the active section, the optical power is confined in the waveguide and little is in the absorber. It results in smaller absorption near the absorber front end than in the conventional straightforward WGPD, which does not have the passive input waveguide. This is one of the major reasons that the traditional WGPD structure shown in Figure 2-11 is preferred in high power WGPD designs.

The overall absorption profile and hence the power handling capability depends on the specific device layer structure and waveguide design. The maximum average power density that can be achieved in the reported traditional WGPDs in the literature are compared to that in SNPD and the ideal WGPD, as shown in Figure 2-12. The average power density at which a traditional WGPD fails is generally smaller than that in SNPDs and in the ideal WGPD. As the non-uniform

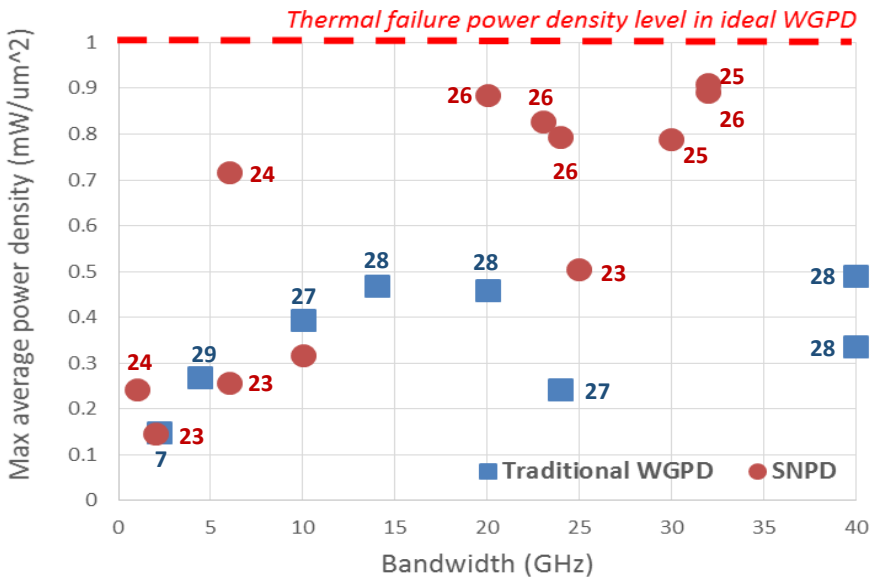

Figure 2-12 The comparison of reported maximum power density between the traditional WGPD, SNPD, and the ideal WGPD. The bandwidth is calculated by the RC time constant, the maximum average power density is calculated by dividing the product of maximum photocurrent. The number next to the points are the respective references.

absorption distribution is one of the major causes of limited power handling capability in the traditional WGPDs, many groups proposed different designs in order to improve the absorption distribution uniformity in the traditional WGPD structure [3-9]. Therefore, the design approach becomes very important. Currently, most of the reported designs are based on a traditional approach, which relies on direct calculation and/or simulation of the absorption distribution of a specific waveguide configuration. In this kind of traditional approach, the WGPD design usually starts with an initial waveguide configuration. Once the absorption distribution profile is calculated/simulated, the initial waveguide configuration can be further adjusted, and the absorption distribution is re-calculated/simulated. The process is repeated until an optimized WGPD design is obtained. There are several drawbacks in this kind of design approach. First, it is an inefficient design process, as there are many parameters in the waveguide structure and layer structure that can affect the absorption profile. Second, this approach simulates and designs waveguide photodiode directly

based on the monitoring of absorption profile simulation, without the interpretation of the physical characteristics of waveguide structure. Considering the numerous parameters of waveguide and layer structure, this approach not only becomes inefficient for waveguide design, but also does not help us to physically understand the power and absorption distribution. Moreover, without physical understanding of the causes of high power limitation, by repeating the calculation/simulation, the optimization of various waveguide parameters may still be a local specialized one.

2.9 Supermode analysis of traditional waveguide absorption profile

The absorption distribution in a WGPD is the result of simultaneous excitation and propagation of multiple supermodes, studying the behavior of WGPD by using supermodes should provide a unique perspective to understand the absorption distribution in a WGPD. In order to achieve better high power performance in a WGPD, the WGPD has been progressed into the one with complicated waveguide structure. Supermodes are the Eigen solutions of an integrated optical waveguide system [33, 34, 35], which makes it a useful tool for analyzing complicated waveguide structure. In this study, in order to find out the supermodes and their excitation coefficient under certain excitation, software FIMMWAVE is used to simulate a WGPD. From the simulated supermodes, analytical expression of the absorption distribution in a WGPD is developed, and the design of a high power WGPD is studied.

In the supermode analysis, first the optical power distribution in waveguide cross-section in “modal form”, which are called supermodes, is simulated. Then the excitation of supermodes in a WGPD with certain optical incident pattern in a WGPD is simulated. Each supermode has different excitation coefficient and propagation constant, the total field pattern at different longitudinal positions is the vector summation of the field pattern of all the excited supermodes, from which the absorption profile in a WGPD is obtained. Based on the analysis of “mode

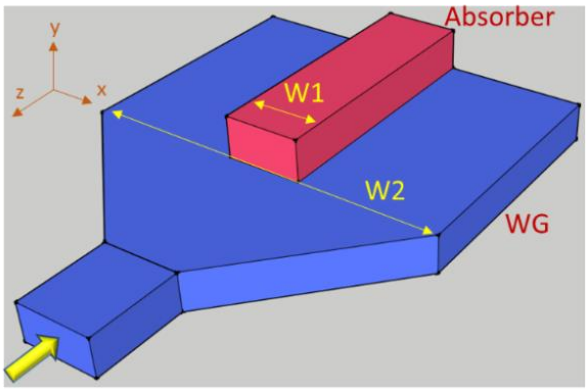

(a)

Layer	Material	Thickness (um)	Index	Type
P-Contact Cap	InGaAs	0.05	3.56	P++
Diffusion Block	InP	0.229	3.17	P+
Absorber	InGaAs	0.2	3.56	P+
Waveguide/MMI	InGaAsP	0.4	3.33	U.I.D
Waveguide/MMI	InGaAsP	0.70	3.33	N
N-Plateau	InGaAsP	0.80	3.33	N+
Substrate	InP			S.I.

absorber

cap

wave guide

(b)

Figure 2-13 The waveguide structure (a) and layer structure (b) of WGPD used for supermode discussion.

excitation" and its effect on absorption profile of WGPD, the design WGPD with more optimized absorption profile for high power operations is discussed.

The waveguide structure and layer structure of the simulated traditional WGPD are shown in Figure 2-13. In the traditional WGPD, the passive section is composed of a straight waveguide and a tapered waveguide. The straight waveguide is for coupling with the external incident radiation. A tapered waveguide is used to connect the straight waveguide and the active section, in order to minimize the excitation of unwanted modes in the passive input waveguide, and make sure most of the power of the incident radiation pattern is in the fundamental mode of the input passive

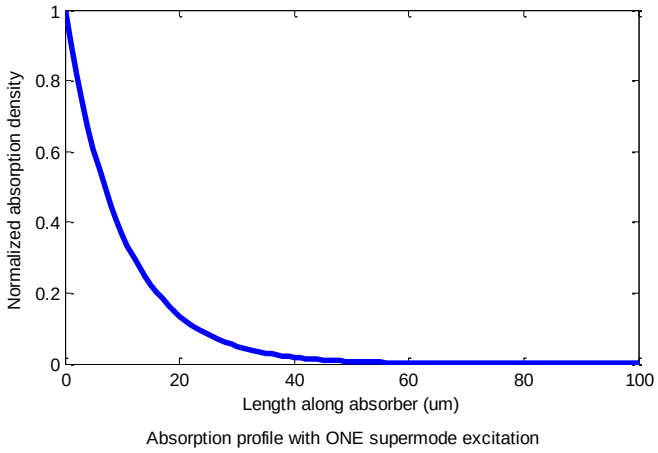

Figure 2-14 The calculated absorption profile of WGPD with only one dominant supermode excitation.

waveguide. In the active section, an absorber structure is added on top of the waveguide, the upper absorber width is W1, and the lower waveguide ridge width is W2.

Although mathematically there are a large number of supermodes existed in a WGPD model, there are only a few supermodes physically excited in a traditional WGPD. The number of excited supermodes and their excitation coefficients are influenced by the waveguide structure and the incident optical pattern. As there are only a few supermodes excited significantly in a traditional WGPD, and other supermodes are excited with negligible excitation coefficient, it becomes feasible to analytically represent the absorption profile in terms of a few supermodes in a WGPD.

2.9.1 WGPD with one supermode

When there is only one supermode $\Phi_0(x, y)$ excited, assuming the excitation coefficient is $|\chi_0|e^{i\theta_0}$, the propagation constant is β_0, the absorption coefficient is α_0, and the absorber confinement factor is Γ, then the optical field distribution $\Phi(x, y, z)$, as well as the absorption profile $P_{absorber}(z)$, can be analytically expressed, as shown in Equation 2.16. This case corresponds to the conventional straightforward WGPD, in which the shape of the absorption

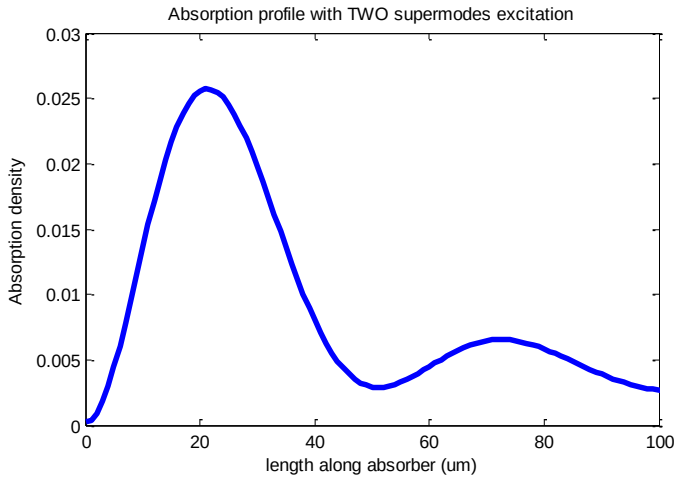

Figure 2-15 The calculated absorption profile of WGPD with two dominant supermode excitation.

profile is exponential, as shown in Figure 2-14. The waveguide structure of this kind of WGPD differs from what is shown in Figure 2-13 in that it does not have the passive input waveguide. It has the simplest mode excitation and can achieve large absorption efficiency with a short active section. However, the absorption uniformity is very poor with the highest absorption at the front end of the absorber, which results in low thermal failure power, according to the discussion in section 2.7.7.

$$\Phi(x,y,z) \approx |\chi_0| e^{i\theta_0} \Phi_0(x,y) e^{-\beta_0 z}$$
$$P_{absorber}(z) = \iint_{absorber} \Phi\Phi^* dxdy = |\chi_0|^2 e^{-\alpha_0 z} \iint_{absorber} \Phi_0\Phi_0^* dxdy = |\chi_0|^2 \Gamma_0 e^{-\alpha_0 z} \quad 2.16.$$

in which β is the propagation constant, α is the characteristic attenuation coefficient, and $\alpha=\Gamma\alpha_{InGaAs}$. α_{InGaAs} is the InGaAs's material absorption coefficient. At λ=1550 nm, $\alpha_{InGsAs}=0.81\ \mu m^{-1}$.

2.9.2 WGPD with two supermodes

When there are two supermodes, the 0th order and the 1st order supermode, excited, the optical field distribution $\Phi(x,y,z)$ and the absorption distribution $P_{absorber}(z)$ can be analytically represented. As the two modes propagate, they interfere with each other in the waveguide, causing

absorption density oscillations. Mathematically, $P_{absorber}(z)$ is the sum of power represented in three terms, as shown in Equation 2.17. The first two terms, which carry an exponential function, represent the power of the 0^{th} order and 1^{st} order modes in the absence of interference, whereas the third term, which carries a cosine function, represents the interference between the two modes. As the interference modifies the exponential decay of the power distribution in a WGPD, it is the key to improve the absorption uniformity. The two-supermode case appears in a traditional WGPD with a passive input waveguide. For the traditional WGPD in Figure 2-13, when W1 is 2 μm and W2 is 4 μm, there are two dominant supermodes excited. A plot of the absorption profile curve of this WGPD is shown in Figure 2-15. Only the straight traditional waveguide PD with a constant cross section is analyzed here. One major difference from the one supermode case is that the absorption density starts from zero in the two-supermode case, instead of starting from its maximum as in the one-supermode case. This difference effectively suppresses the early thermal failure in a two-supermode traditional WGPD. This is the reason the traditional WGPD designs, which have more than one supermode, are more preferred than the one-supermode conventional WGPD for high power operations.

When the characteristic attenuation coefficient of one supermode is much larger than that of the other one, the power of the supermode with large characteristic attenuation coefficient will attenuates much faster than the power of the other supermode. In this case, the absorption profile shape of the two supermode case will be similar with that of the one supermode case.

2.9.3 WGPD with three supermodes and above

While a two-supermode traditional WGPD has better power performance than the one-supermode conventional WGPD, traditional WGPD with more than two supermodes is expected to perform even better at high power. The longitudinal power distribution non-uniformity in a WGPD

$$\Phi(x,y,z) \approx |\chi_0| e^{i\theta_0}\Phi_0(x,y)e^{-\beta_0 z} + |\chi_1| e^{i\theta_1}\Phi_1(x,y)e^{-\beta_1 z}$$

$$P_{absorber}(z) = \iint_{absorber} \Phi\Phi^* dxdy = |\chi_0|^2 e^{-\alpha_0 z} \iint_{absorber} \Phi_0\Phi_0^* dxdy + |\chi_1|^2 e^{-\alpha_1 z} \iint_{absorber} \Phi_1\Phi_1^* dxdy$$

$$+ 2|\chi_0\chi_1|\cos(\mathrm{Re}(\beta_0-\beta_1)z+\varphi)e^{-(\alpha_0+\alpha_1)z/2} \iint_{absorber} \Phi_0(x,y)\Phi_1^*(x,y)dxdy \quad \text{Note}: \varphi = \theta_0 - \theta_1$$

$$= |\chi_0|^2\Gamma_0 e^{-\alpha_0 z} + |\chi_1|^2\Gamma_1 e^{-\alpha_1 z} + 2|\chi_0\chi_1|\cos(\mathrm{Re}(\beta_0-\beta_1)z+\varphi)e^{-(\alpha_0+\alpha_1)z/2}$$

$$* \iint_{absorber} \Phi_0(x,y)\Phi_1^*(x,y)dxdy$$

$$As: P_{absorber}(z=0) = 0, \; Note: \varphi(z=0) = \pi$$

$$\Rightarrow |\chi_0|^2\Gamma_0 + |\chi_1|^2\Gamma_1 - 2|\chi_0\chi_1| \iint_{absorber} \Phi_0(x,y)\Phi_1^*(x,y)dxdy = 0 \qquad \text{(a)}$$

$$As: \Phi(x,y)\big|_{absorber,z=0} = |\chi_0| e^{i\theta_0}\Phi_0(x,y)\big|_{absorber,z=0} + |\chi_1| e^{i\theta_1}\Phi_1(x,y)\big|_{absorber,z=0} = 0 \qquad \text{2.17.}$$

$$|\chi_0| e^{i\theta_0}\Phi_0(x,y)\big|_{absorber,z=0} = -|\chi_1| e^{i\theta_1}\Phi_1(x,y)\big|_{absorber,z=0}$$

$$So: |\chi_0|^2 * \iint_{absorber} \Phi_0(x,y)\Phi_0^*(x,y)dxdy = |\chi_1|^2 * \iint_{absorber} \Phi_1(x,y)\Phi_1^*(x,y)dxdy$$

$$\Rightarrow |\chi_0|^2\Gamma_0 = |\chi_1|^2\Gamma_1 \qquad \Rightarrow \chi_0\sqrt{\Gamma_0} = \chi_1\sqrt{\Gamma_1} \qquad \Rightarrow (\chi_0\sqrt{\Gamma_0} - \chi_1\sqrt{\Gamma_1})^2 = 0$$

$$\Rightarrow |\chi_0|^2\Gamma_0 + |\chi_1|^2\Gamma_1 - 2|\chi_0\chi_1|\sqrt{\Gamma_0\Gamma_1} = 0 \qquad \text{(b)}$$

Combine (a) and (b), one can get :

$$\iint_{absorber} \Phi_0(x,y)\Phi_1^*(x,y)dxdy = \sqrt{\Gamma_0\Gamma_1}$$

$$\text{And}: P_{absorber}(z) = |\chi_0|^2\Gamma_0 e^{-\alpha_0 z} + |\chi_1|^2\Gamma_1 e^{-\alpha_1 z} - 2|\chi_0\chi_1|\cos(\mathrm{Re}(\beta_0-\beta_1)z)e^{-(\alpha_0+\alpha_1)z/2}\sqrt{\Gamma_0\Gamma_1}$$

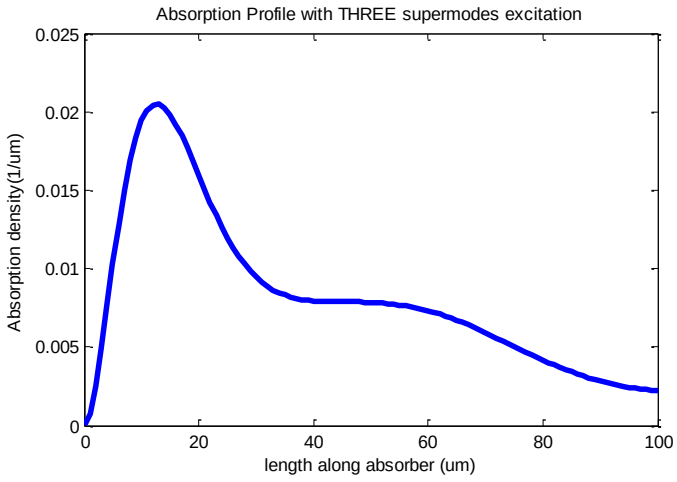

Figure 2-16 The calculated absorption profile of WGPD with three dominant supermode excitation.

mainly results from the attenuation of power available for absorption in the longitudinal direction. One important design goal for waveguide photodiode is improving the power distribution uniformity, which relies on the interference between the excited supermodes. According to Equation 2.17, there is only one beating term in the power distribution expression in a two-supermode traditional WGPD. In this case, the power distribution uniformity is limited for two reasons. First, the single interference term itself introduces additional non-uniformity due to the included cosine function. Second, the power in the interference term also carries an exponential function. In the case of fast attenuation of the interference power, the absorption profile will quickly return to the exponential shape. When the number of supermodes is three or more, there will be more interference terms, and the absorption uniformity will be less limited by the above two issues. For a properly designed traditional WGPD, the inclusion of more supermodes will be able to improve the overall absorption distribution uniformity.

When there are three supermodes, the optical field $\Phi(x, y, z)$, as well as the absorption profile $P_{absorber}(z)$, can also be analytically expressed, as shown in Equation 2.18. The simulation shows that the WGPD structure will have more than two supermodes excited in a WGPD structure when the waveguide itself is wide enough to support multiple modes. For the WGPD in Figure 2-13, when W1 is 2 μm and W2 is 7 μm, there are three dominant supermodes simultaneously excited. The absorption profile curve of this WGPD is shown in Figure 2-16. Similarly, the absorption starts from zero at the absorber front end. However, the multiple interferences results in less oscillation of the absorption density, and hence better absorption uniformity.

In summary, the above discussion goes through the supermode analysis and obtains the analytical expression of absorption distribution in a WGPD, in which the number of dominantly excited supermodes varies. With the interference modifies the exponential decay of the power of each individual supermode, WGPD with larger number of supermodes is expected to distribute the

$$\Phi(x,y,z) \approx |\chi_0| e^{i\theta_0}\Phi_0(x,y)e^{-\beta_0 z} + |\chi_1| e^{i\theta_1}\Phi_1(x,y)e^{-\beta_1 z} + |\chi_2| e^{i\theta_2}\Phi_2(x,y)e^{-\beta_2 z}$$

at z = 0, there is no E field in the absorber, which means :

$$\Phi(x,y)\big|_{absorber,z=0} = |\chi_0| e^{i\theta_0}\Phi_0(x,y)\big|_{absorber,z=0}$$

$$+ |\chi_1| e^{i\theta_1}\Phi_1(x,y)\big|_{absorber,z=0} + |\chi_2| e^{i\theta_2}\Phi_2(x,y)\big|_{absorber,z=0} = 0$$

$$\Rightarrow |\chi_0| e^{i\theta_0}\Phi_0(x,y)\big|_{absorber,z=0} = -(|\chi_1| e^{i\theta_1}\Phi_1(x,y)\big|_{absorber,z=0} + |\chi_2| e^{i\theta_2}\Phi_2(x,y)\big|_{absorber,z=0})$$

$$So: |\chi_0|^2 * \iint_{absorber}\Phi_0(x,y)\Phi_0^*(x,y)dxdy = |\chi_1|^2 * \iint_{absorber}\Phi_1(x,y)\Phi_1^*(x,y)dxdy$$

$$+ |\chi_2|^2 * \iint_{absorber}\Phi_2(x,y)\Phi_2^*(x,y)dxdy + 2|\chi_1\chi_2| \iint_{absorber}\Phi_1(x,y)\Phi_2^*(x,y)dxdy$$

$$\Rightarrow |\chi_0|^2\Gamma_0 = |\chi_1|^2\Gamma_1 + |\chi_2|^2\Gamma_2 + 2|\chi_1\chi_2| \iint_{absorber}\Phi_1(x,y)\Phi_2^*(x,y)dxdy$$

$$\Rightarrow \iint_{absorber}\Phi_1(x,y)\Phi_2^*(x,y)dxdy = \frac{|\chi_0|^2\Gamma_0 - (|\chi_1|^2\Gamma_1 + |\chi_2|^2\Gamma_2)}{2|\chi_1\chi_2|}$$

Similarly :

$$\iint_{absorber}\Phi_0(x,y)\Phi_2^*(x,y)dxdy = -\frac{|\chi_1|^2\Gamma_1 - (|\chi_0|^2\Gamma_0 + |\chi_2|^2\Gamma_2)}{2|\chi_0\chi_2|}$$

$$\iint_{absorber}\Phi_0(x,y)\Phi_1^*(x,y)dxdy = -\frac{|\chi_2|^2\Gamma_2 - (|\chi_0|^2\Gamma_0 + |\chi_1|^2\Gamma_1)}{2|\chi_0\chi_1|}$$

$$P_{absorber}(z) = \iint_{absorber}\Phi\Phi^* dxdy = |\chi_0|^2\Gamma_0 e^{-\alpha_0 z} + |\chi_1|^2\Gamma_1 e^{-\alpha_1 z} + |\chi_2|^2\Gamma_2 e^{-\alpha_2 z} \qquad 2.18.$$

$$+ 2|\chi_0\chi_1|\cos(\mathrm{Re}(\beta_0 - \beta_1)z + \pi)e^{-(\alpha_0+\alpha_1)z/2} \iint_{absorber}\Phi_0(x,y)\Phi_1^*(x,y)dxdy$$

$$+ 2|\chi_0\chi_2|\cos(\mathrm{Re}(\beta_0 - \beta_2)z + \pi)e^{-(\alpha_0+\alpha_2)z/2} \iint_{absorber}\Phi_0(x,y)\Phi_2^*(x,y)dxdy$$

$$+ 2|\chi_1\chi_2|\cos(\mathrm{Re}(\beta_1 - \beta_2)z + 0)e^{-(\alpha_1+\alpha_2)z/2} \iint_{absorber}\Phi_1(x,y)\Phi_2^*(x,y)dxdy$$

$$= |\chi_0|^2\Gamma_0 e^{-\alpha_0 z} + |\chi_1|^2\Gamma_1 e^{-\alpha_1 z} + |\chi_2|^2\Gamma_2 e^{-\alpha_2 z}$$

$$- 2|\chi_0\chi_1|\cos(\mathrm{Re}(\beta_0 - \beta_1)z)e^{-(\alpha_0+\alpha_1)z/2}(-\frac{|\chi_2|^2\Gamma_2 - (|\chi_0|^2\Gamma_0 + |\chi_1|^2\Gamma_1)}{2|\chi_0\chi_1|})$$

$$- 2|\chi_0\chi_2|\cos(\mathrm{Re}(\beta_0 - \beta_2)z)e^{-(\alpha_0+\alpha_2)z/2}(-\frac{|\chi_1|^2\Gamma_1 - (|\chi_0|^2\Gamma_0 + |\chi_2|^2\Gamma_2)}{2|\chi_0\chi_2|})$$

$$- 2|\chi_1\chi_2|\cos(\mathrm{Re}(\beta_1 - \beta_2)z)e^{-(\alpha_1+\alpha_2)z/2}(+\frac{|\chi_0|^2\Gamma_0 - (|\chi_1|^2\Gamma_1 + |\chi_2|^2\Gamma_2)}{2|\chi_1\chi_2|})$$

absorption more evenly, and is a better candidate for high power applications. The focus of the rest of this chapter will be studying the characteristics of each individual supermodes, as well as the interference among them. Those knowledge about the supermodes is utilized to understand their effects on the absorption distribution, and finally obtain more uniform absorption profile in a traditional WGPD.

2.9.4 Comparison of Power Distribution between Power-based and supermode-based analysis

The accuracy of supermode analysis of the absorption profile is examined by comparing with the absorption profile simulated by Beam Propagation Method (BPM), which is used in traditional power based waveguide analysis. BPM simulation is selected for the comparison as it simulates the total power propagation and distribution, without differentiating and separating supermodes from each other. Figure 2-17 compares the absorption profile obtained by the supermode analysis with that simulated by BPM simulation, in which the two are very close in the general shape and magnitude, except more details are included in the BPM simulated curve. This difference arises from the fact that many higher order modes are neglected in the supermodes analysis.

The absorber layer structure and waveguide structure used for this comparison are the same with those shown in Figure 2-13. In this comparison, W1 is 2 μm, and W2 is 9 μm. For the supermode analysis, only three supermodes are considered, and it already achieves good agreement with the BPM simulation. As shown in Figure 2-18, the three supermodes, which are excited by

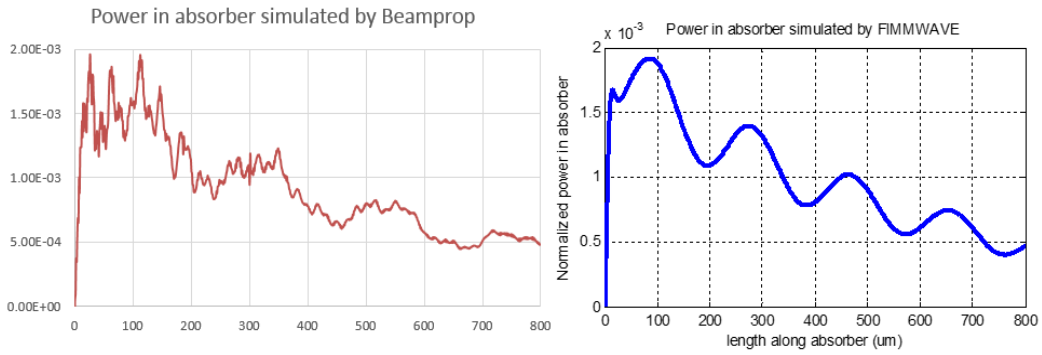

(a) (b)

Figure 2-17 The comparison of absorption profile in WGPD obtained by using Beamprop (a) and supermode analysis (b).

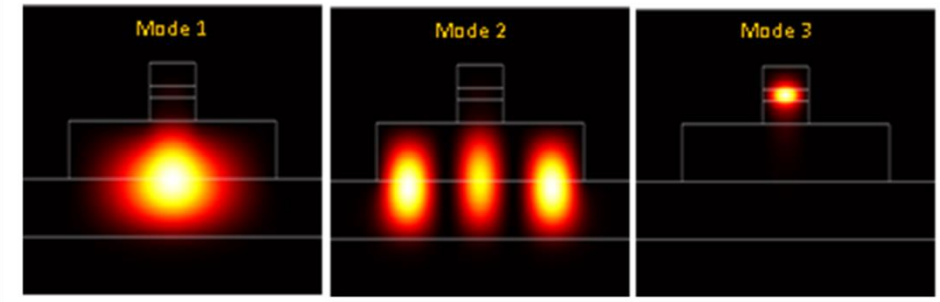

	$Re(n_{eff})$	$Im(n_{eff})$	χ	χ^2
Mode 1	3.3099	0.008	0.9795	0.9596
Mode 2	3.2979	0.004	0.1522	0.0231
Mode 3	3.2719	0.021	0.1056	0.0111
				Sum=0.9938

Figure 2-18 The FIMMWAVE simulated three dominantly excited supermodes and several of their physical parameters. Mode 1 is the 0^{th} order supermode, mode 2 is one of the higher order supermodes, and mode 3 is the 1^{st} order supermode. $Re(n_{eff})$ and $Im(n_{eff})$ are the real part and imaginary of the effective index of each supermode, which is a complex number with the existence of absorption. χ is the excitation coefficient of the supermode. χ^2 is the normalized power of supermode. The total incident power is 1.

the 0^{th} mode of input waveguide, accounts for 99.38% of the total power. This is the major reason why supermode analysis has good agreement with BPM simulation. The above comparison demonstrates the accuracy of representing the absorption distribution with limited number of supermodes.

2.9.5 Supermodes excitation in WGPD

By using the WGPD structure built on the layer structure shown in Figure 2-13, in the following sections the supermode analysis of high power traditional WGPD will be presented. The first discussion is about the supermode excitation, including the discussion about what kinds of supermodes are usually excited, and what are the features of those excited supermodes.

Before discussion, it is worthwhile to define clearly two terms: the confinement factor of a waveguide structure of a WGPD, and the confinement factor of a supermode excited in the same WGPD. The confinement factor of a supermode is defined as the fraction of the optical power of a supermode that is confined and guided in the interested region of a waveguide, whereas the confinement factor of a waveguide is defined as the fraction of the total optical power that is confined and guided in the interested region of a waveguide. As the power distribution in a waveguide is the result of simultaneous propagation of multiple supermodes, the confinement factor of a waveguide structure is the weighted sum of all the excited supermodes' confinement factor. The default interested region in the definition of the two terms is the absorber, unless it is specified differently.

In the traditional WGPD devices, the waveguide and absorber are two main areas that the optical power is confined in, as shown in Figure 2-18. Therefore, the 0^{th} order supermode and the 1^{st} order supermode, which have the power confined primarily in the waveguide and absorber with the least power variations, are the two primarily concerned modes in the supermode analysis. Besides, there are higher order supermodes, which have radiation patterns that have more variations

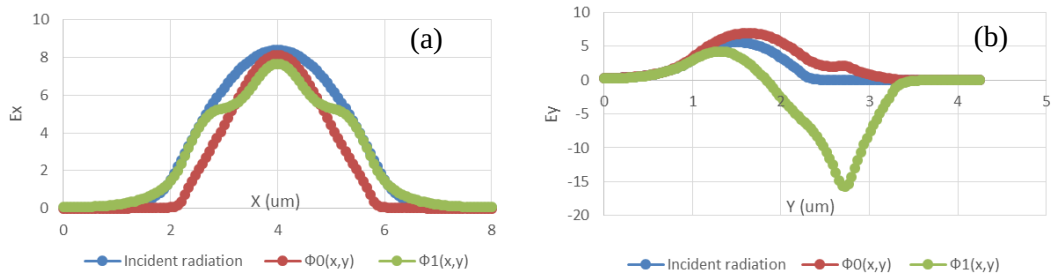

Figure 2-19 The plot for the electric field of the 0th and 1st order modes at the center of waveguide along x direction (a) and y direction (b) for the WGPD shown in Figure 2.13.

in the x or y direction. The radiation pattern and the confinement factors of these supermodes depend on the dimensions of the absorber and the waveguide in the x and y direction, as well as the WGPD's layer structure. For example, when the waveguide is very wide, the supermodes with more than one local power density peak in the waveguide may be excited, which corresponds to one of the higher order supermodes. Because those characteristics affect the power distribution differently, for high power WGPD, some supermodes with certain characteristics are preferred, and some should be suppressed. For example, some higher order supermodes have complex field pattern in the absorber or waveguide in the y direction. When they propagate, they interfere with other supermodes and cause spatial oscillation of optical power in the y direction. As the absorber is usually very thin, this power spatial oscillation will result in large variation of the absorption density. Therefore, such kind of higher order supermodes should be suppressed.

The total number of supermodes that will be excited depends on the waveguide structure, layer structure, and the optical incident radiation pattern. In general, WGPD with large dimension in the x or y direction will support a large number of supermodes. The incident radiation pattern determines which ones to be excited and how large is the excitation coefficient. Among all the excited modes, the 0^{th} order mode and the 1^{st} order mode, $\Phi_0(x,y)$ and $\Phi_1(x,y)$, are of special interest. As shown in Figure 2-19, on the one hand, the two modes' shape is close to that of the incident radiation in the x direction. On the other hand, the two modes are very different from each other in

the y direction, which makes them two very different supermodes. $\Phi_0(x,y)$ is more confined in the waveguide, whereas $\Phi_1(x,y)$ is more confined in the absorber. In this case, the confinement factor of $\Phi_1(x,y)$ is much larger than that of $\Phi_0(x,y)$, and $\Phi_1(x,y)$ is also called the large gamma supermode. The large gamma supermode usually has the least field variations in both x and y directions, and with much more power confined in the absorber. The large gamma supermode usually excites significantly in a traditional WGPD, because of its large field overlap in the x direction with the incident radiation pattern.

The 0^{th} order supermode, which has the power confinement primarily in the waveguide with only one local peak, is usually excited most significantly. The supermode excitation closely relates to the overlap between the supermode and the incident radiation pattern. The 0^{th} order mode and the incident field pattern have very similar field pattern in both x and y direction, with some minor difference that comes from the absorber perturbation to the waveguide. In this case, it is reasonable that the 0^{th} order supermode will have larger excitation coefficient than the large gamma supermode, and is the most significantly excited supermode in a traditional WGPD. The 0^{th} order supermode is also called the fundamental supermode. The fundamental supermode usually is the mode which has the least field variations in both x and y directions, and with much more power confined in the waveguide.

Besides the fundamental supermode and the large gamma supermode, there are higher order supermodes, which have radiation patterns with more variations in the x or y direction than the fundamental supermode and the large gamma supermode, may also be excited in a traditional WGPD. Those higher order supermodes may have different confinement factor, mainly depend on the field distribution in the y direction.

In a traditional WGPD, both the fundamental supermode and the large gamma supermode will be excited significantly, and some higher order supermodes may be excited in some cases. The excitation coefficient of a supermode relates to field overlap between this supermode and the

incident radiation pattern. In this chapter, the input passive waveguide is gently tapered, and the incident radiation pattern of a traditional WGPD is the 0^{th} order mode of the waveguide, whose field pattern is confined in the waveguide, and has only one peak in both x and y direction. As the fundamental supermode and the large gamma supermode also has only one peak in both x and y direction in the waveguide, these two supermodes usually excite significantly in a traditional WGPD. Moreover, the fundamental supermode usually excites more significantly than the large gamma supermode, due to the field distribution difference of the two in the y direction. With more power confined in the waveguide in the y direction, when the field overlap with the incident pattern is considered, the fundamental supermode usually has larger field overlap than the large gamma mode, and hence has greater excitation coefficient. The excitation coefficient of the higher order modes depends on the waveguide structure. For a higher order supermode, the more variations of field pattern in the waveguide it has, the smaller its excitation coefficient will be. Usually the excitation coefficient of the higher order modes is smaller than that of the fundamental supermode, due to the existence of more field variations.

2.9.6 Summary

The Supermode analysis applied here starts from how to describe the absorption profile with the excited supermodes in a traditional WGPD. The representation of the absorption profile in the supermode analysis is reasonably accurate, with the comparison between the supermode analysis and the BPM simulation. The characteristics of several major supermodes are also discussed. In the following sections, the discussion of high power WGPD by supermode analysis includes two parts, one is the supermodes' effect on the power distribution in a traditional WGPD, and the other one is the relationship between supermode excitation and the waveguide structure. The goal is, by using supermode analysis in a traditional WGPD, finding out how certain waveguide

structure limits the power distribution uniformity, and how the waveguide structure can be adjusted for better power distribution uniformity.

2.10 Traditional WGPD design with the supermode analysis

The absorption uniformity is a key parameter in the design of any high power WGPD, as discussed in section 2.7.7. In this section, the discussion of high power traditional WGPD design will focus on the absorption uniformity with the supermode analysis. The goal of the discussion is using supermode analysis to find out the physical reasons behind the absorption nonuniformity in a traditional WGPD, and then propose solutions to improve the absorption uniformity by adjusting the WGPD structure.

2.10.1 General discussions of the absorption uniformity in a traditional WGPD

As discussed in section 2.9.5, the fundamental supermode and the large gamma supermode are two major supermodes in any traditional WGPD. Higher order supermodes may also be present, depending on the waveguide structure. The excited supermodes propagate together and interact with each other, which determine the absorption profile. In order to optimize the absorption profile, the characteristics of mode propagation and interaction, as well as their effects on the absorption profile, are thoroughly studied here. In this section, the discussion object is not limited to two-supermode traditional WGPD.

As discussed in section 2.9.2 and 2.9.3, the absorption profile of all kinds of traditional WGPD can be analytically expressed by the summing of two kinds of terms, one relates to the absorption contributed by the individual supermodes, which describes how each individual supermode propagates and distributes its power in the WGPD. This kind of terms is called the propagation term in this dissertation. The other kind of terms relates to the inter-modal interference between two different supermodes, and it is called the interference term in this dissertation. The propagation terms and the interference terms work together to determine the absorption profile.

In order to achieve more uniform absorption profile in a traditional WGPD, it requires the interference terms to modify the exponential decay of the propagation terms. In a traditional WGPD, the dominant propagation term is the one represents the excited fundamental mode, and the dominant interference terms are the ones that represent the interference between the fundamental supermode and other major supermodes. The linear coefficient of those terms are proportional to the χ_0, which is the excitation coefficient of the fundamental supermode. As the fundamental supermode is usually excited most significantly, as discussed in section 2.9.5, those terms will have larger linear coefficient than other terms that is not related to the fundamental supermode. Although the large gamma supermode and the higher orders supermodes are less excited than the fundamental supermode, they can modify the exponential decay shape of the power in the fundamental mode via the inter-modal interference, and finally reshape the WGPD's absorption profile. Moreover, because of the different modal features of the large gamma mode and the higher order modes, the inter-modal interference between the two modes and the fundamental mode will be very different, and will affect the WGPD's absorption profile differently. Those modal features include the characteristic attenuation coefficient, the effective index, the excitation coefficient, etc. For example, when the large gamma mode has much larger characteristic attenuation coefficient than the higher order modes, then the large gamma mode will affect the absorption profile much more locally than the higher order modes.

Before theoretically analyzing how different the large gamma supermode and the higher order supermodes affect the absorption profile, simulation of a sample traditional WGPD is used to visualize the difference. The layer structure and waveguide structure of the sample WGPD are the same with what are already shown in Figure 2-13. When W1 is 2 μm, and W2 is 9 μm, the Fimmwave simulation shows that there are three major supermodes excited and account for 99.38% of the total guided power in the waveguide at the front end of the active section, as shown in Figure 2-18. The three modes have different excitation coefficient. The fundamental mode, which is the

mode 1, has much larger excitation coefficient than the other two modes. The large gamma mode, which is the mode 3, has similar excitation coefficient with mode 2. A higher order mode, which is the mode 2, has more variations of the field pattern in the waveguide in the x direction than the other two modes. The three modes also have different imaginary part of the effective index, $Im(n_{eff})$, which is proportional to the characteristic attenuation rate of the power of the individual mode. While the fundamental mode and the higher order mode have similar $Im(n_{eff})$, the large gamma mode's $Im(n_{eff})$ is much larger.

According to section 2.9.3, the analytical expression of a three-supermode traditional WGPD absorption profile has six terms, including three propagation terms and three interference terms. However, as discussed earlier in this section, the propagation term that represents the fundamental supermode, as well as the interferences terms that involves the fundamental supermode, are dominant terms and are more important. Therefore, there are three terms that need to be specially considered in a three-supermode case. The first one is the propagation term represents the fundamental supermode. The second one is the interference term represents the interference between the fundamental supermode and the large gamma supermode, and is called the large gamma mode interference term. The third one is the interference term represents the interference between the fundamental supermode and the higher order supermode, and is called the higher order mode interference term. In Figure 2-20, these three terms are visualized in the WGPD described in the last paragraph. As expected, the power of propagation term representing the fundamental supermode attenuates exponentially. Without the inter-modal interference, the absorption profile of the traditional WGPD will be very similar with the exponential decay of the fundamental supermode power, as it accounts for the majority part of the total guided power in the waveguide. However, due to the interference between the fundamental supermode and the other two modes, the picture changes. As shown in Figure 2-20, although the power of the large gamma mode and the higher order mode is much smaller than that of the fundamental mode, the amplitude

of the interference is comparable to the power of the fundamental mode. In this case, the shape of the absorption profile can be very different from the power distribution profile of the fundamental mode. In taking a closer look at the two kinds of interference, we found that they affect the absorption profile very differently, due to the different amplitudes of the two interferences, as shown in the following discussion.

As shown in Equation 2-18, these two interference terms carry a cosine function, whose amplitude is proportional to three items: the product of the two supermodes' excitation coefficient, the field overlap of the two supermodes at the absorber, and an exponential attenuation function, whose characteristic attenuation coefficient is proportional to the sum of that of the two supermodes. (Note: the "two supermodes" mentioned here for a specific interference term refer to the two modes that interfere with each other. For example, for the large gamma mode interference term, the two supermodes are the fundamental supermode and the large gamma supermode. Smililarly, for the higher order mode interference term, the two supermodes are the fundamental supermode and the higher order supermode.) Assuming the higher order mode and the large gamma mode have similar excitation coefficient, the amplitudes of both interference terms depend on the field overlap between the two modes in the absorber, as well as the exponential attenuation function. In a traditional WGPD, there will be higher order modes with different modal features, which interferes differently with the fundamental supermode. The following discussion studies two general cases, one is the higher order mode with the majority of the power confined in the waveguide, the other one is the higher order mode with the majority of the power confined in the absorber.

When the higher order mode has the majority of the power confined in the waveguide, the confinement factor of this higher order mode is much smaller than that of the large gamma mode. An example of this kind of higher order mode is the mode 2 shown in Figure 2-18. In this case, at the absorber, the field distribution of the higher order mode is much smaller than that of the large

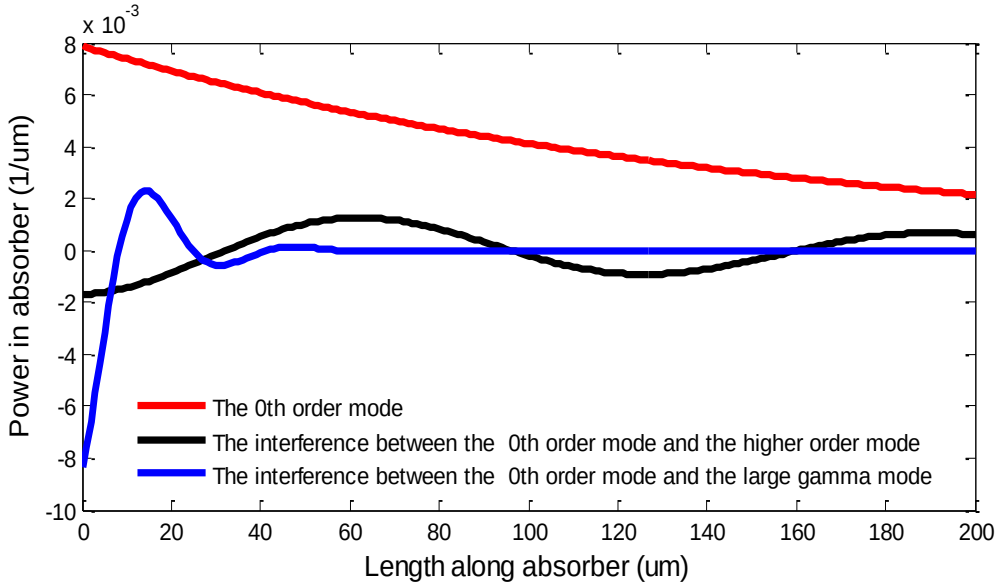

Figure 2-20 The plot of power distribution in the absorber of the excited fundamental mode, and its interference with the large gamma mode and the higher order mode. The plot is based on the supermode simulation of the sample traditional WGPD by Fimmwave.

gamma mode. As a result, the field overlap between the fundamental mode and the higher order mode is smaller than that between the fundamental mode and the large gamma mode. This results in greater amplitude of the large gamma mode interference than that of the higher order mode interference at the absorber front end, before the exponential attenuation function coming into effect. An example is shown in Figure 2-20. In this particular case, even the excitation coefficient of the higher order mode is 1.5 times of that of the large gamma mode, which is shown in Figure 2-18, the amplitude of the higher order mode interference is less than ¼ of that of the large gamma mode interference at the front end of the absorber. Because of the large initial amplitude, in the forward section, much stronger interference exists between the large gamma mode and the fundamental mode, instead of existing between the higher order mode and the fundamental mode. Moreover, the interference between the large gamma mode and the fundamental mode affects the absorption profile much more locally than the interference between the higher order mode and the fundamental mode, due to the different attenuation rates of the two interference terms. As

mentioned in the last paragraph, the amplitude of an interference term has an exponential attenuation function, whose characteristic attenuation coefficient is proportional to the sum of that of the two supermodes in interference. As mentioned in section 2.9.1, the characteristic attenuation coefficient α of a supermode is proportional to the confinement factor of the supermode Γ, which is $\alpha=\Gamma\alpha_{InGaAs}$. Therefore, in the case when the large gamma mode has much larger confinement factor than both the higher order mode and the fundamental mode, the large gamma mode interference attenuates much faster than the higher order mode interference. As a result, it is concluded that the interference between the large gamma mode and the fundamental mode plays a more important role affecting the absorption uniformity in the forward section, and the interference between the higher order mode and the fundamental mode plays a more important role affecting the absorption uniformity in the rest of the absorber.

The above discussion and conclusion are based on an assumption that the higher order mode and the large gamma mode have similar excitation coefficient. When the excitation of the large gamma mode is much larger than that of the higher order mode, the above conclusion still stands. However, when the excitation of the large gamma mode is much smaller than that of the higher order mode, then the amplitude of the large gamma mode interference may be much smaller than that of the higher order mode interference in the forward section. In this case, the absorption profile in both the forward section and the rear section is mainly affected by the higher order mode, instead of by the large gamma mode. In a traditional WGPD, as discussed in section 2.9.5, the large gamma mode excitation is usually significant, and the case mentioned above is very unlikely to happen. However, the large gamma mode excitation is largely suppressed in a novel WGPD developed in our group, and results in very different effects on the absorption profile. This novel WGPD will be discussed in Chapter 3.

When the higher order mode has the majority of the power confined in the absorber, the confinement factor of this higher order mode is comparable to that of the large gamma mode. When

the two supermodes have similar excitation coefficient, the interference between the fundamental supermode and these two modes will have some similar features, such as large amplitude of the interference at the absorber front end, and fast attenuation rate of the interference. As discussed in section 2.9.3, the fast attenuation of all interference terms causes the absorption profile to go back to the exponential decay shape, and it is not preferred in the traditional WGPD designs. Therefore, in this dissertation, only the traditional WGPD with higher order mode that has the majority of the power confined in the waveguide will be discussed.

A simple case with two-supermode, the fundamental supermode $\Phi_0(x,y)$ and the large gamma supermode $\Phi_1(x,y)$, is used for discussing the relationship between supermode features and non-uniform absorption profile in a traditional WGPD, before moving to the discussion of a more general and complex three-supermode traditional WGPD. There are two reasons of using this simple case. First, these two supermodes excite significantly in the traditional WGPD, as discussed in section 2.9.5. Second, these two supermodes represent two distinctive mode types, and other higher order supermodes belong to one of the two mode types. The fundamental supermode represents one type of mode that has the power localizes predominantly in the lower passive waveguide, and the large gamma supermode represents the other type of mode that has the power localizes predominantly in the upper absorber. In the following discussion, the first mode type is named mode type A, and the second mode type is named mode type B. The two mode types have very different mode confinement factor the fundamental supermode $\Phi_0(x,y)$ and the large gamma supermode $\Phi_1(x,y)$ are good examples of the two different mode types. Other higher order supermodes also belong to one of the two mode types, only with more variations of the field distribution in x or y direction.

According to Equation 2.17, in a two-supermode traditional WGPD, the total field $\Phi(x,y,z)$, the total optical power $P(z)$ in the waveguide, and the optical power in the absorber $P_{abs}(z)$ can be written as:

$$\begin{aligned}
&\Phi(x,y,z) = \chi_0\Phi_0(x,y)e^{-i\beta_0 z}e^{i\theta_0} + \chi_1\Phi_1(x,y)e^{-i\beta_1 z}e^{i\theta_1} \\
&P(z) = |\chi_0|^2 e^{-\alpha_0 z} + |\chi_1|^2 e^{-\alpha_1 z} \\
&+ 2|\chi_0\chi_1|\cos(\mathrm{Re}(\beta_0-\beta_1)z+\varphi)\iint_S \Phi_0(x,y)\Phi_1^*(x,y)dxdy e^{-(\alpha_0+\alpha_1)z/2} \\
&= |\chi_0|^2 e^{-\alpha_0 z} + |\chi_1|^2 e^{-\alpha_1 z}
\end{aligned} \qquad 2.19.$$

$$\begin{aligned}
&P_{abs}(z) = {\chi_0}^2\Gamma_0 e^{-\alpha_0 z} + {\chi_1}^2\Gamma_1 e^{-\alpha_1 z} \\
&+ 2\chi_0\chi_1\cos(\mathrm{Re}(\beta_0-\beta_1)z+\pi)\iint_{absorber} \Phi_0(x,y)\Phi_1^*(x,y)dxdy e^{-(\alpha_0+\alpha_1)z/2} \\
&= |\chi_0|^2\Gamma_0 e^{-\alpha_0 z} + |\chi_1|^2\Gamma_1 e^{-\alpha_1 z} + 2|\chi_0\chi_1|\sqrt{\Gamma_0\Gamma_1}\cos(\mathrm{Re}(\beta_0-\beta_1)z+\pi)e^{-(\alpha_0+\alpha_1)z/2}
\end{aligned} \qquad 2.20.$$

where

$$\alpha_0 = 2Im(\beta_0) = \frac{4\pi \times Im(n_{eff0})}{\lambda} = \Gamma_0\alpha_{InGaAs}$$
$$\alpha_1 = 2Im(\beta_1) = \frac{4\pi \times Im(n_{eff1})}{\lambda} = \Gamma_1\alpha_{InGaAs} \qquad 2.21.$$

where α_0 and α_1 are the effective attenuation coefficient of the 0th and 1st order supermode, and α_{InGaAs} is the InGaAs's material absorption coefficient. At λ=1550 nm, α_{InGsAs}=0.81 μm^{-1}.

The total field $\Phi(x,y,z)$ is the sum of two terms, the 0th order mode $\Phi_0(x,y)$ and the 1st order mode $\Phi_1(x,y)$. The two modes propagate in the WGPD at different phase velocity, which results in interference. In the expression of the power in the absorber $P_{abs}(z)$ in Equation 2.20, there are two propagation terms, which represent the power of the 0th and 1st order modes propagating in the WGPD, and one interference term, which represents the variance in the total power due to the interference. The propagation terms and the interference term affect the absorption profile from different angle.

From Equation 2.20, the power goes to the two propagation terms is proportional to the square of the two mode excitation coefficients, which attenuates exponentially, as the two terms carry an exponential function $\exp(-\alpha_0 z)$ and $\exp(-\alpha_1 z)$. In a conventional one-supermode WGPD, the characteristic attenuation length L_a is used to describe the propagation length required for

attenuating the initial power to its 1/e, where e is the Euler's number. Similarly, in the traditional WGPD with two supermodes, L_{a0} and L_{a1} are used to describe the characteristic attenuation length of the two supermodes, as defined in Equation 2.22.

$$L_{a0} = \frac{1}{\alpha_0} = \frac{1}{\Gamma_0 \alpha_{InGaAs}} = \frac{\lambda}{4\pi \times Im(n_{eff0})}$$
$$L_{a1} = \frac{1}{\alpha_1} = \frac{1}{\Gamma_1 \alpha_{InGaAs}} = \frac{\lambda}{4\pi \times Im(n_{eff0})} \qquad 2.22.$$

From Equation 2.20, the interference terms carry a cosine function, and results in periodical fluctuation of the power from the propagation terms. The amplitude of the interference term is proportional to three items: the product of the two supermodes' excitation coefficient, the overlap between the two modes' field in the absorber, and an exponential attenuation function, whose characteristic attenuation coefficient is proportional to the sum of that of the two modes. The period of the interference is inversely proportional to the difference of the two modes' propagation constant. Coupling length Lc is used to describe the propagation length required for the two modes' phase difference changed by 180 degree, and can be written as:

$$L_c = Re\left(\frac{\pi}{\beta_0 - \beta_1}\right) = \frac{\lambda}{2} Re\left(\frac{1}{n_{eff0} - n_{eff1}}\right) \qquad 2.23.$$

In the above discussion, the analytical expression of the absorption distribution in a two-supermode traditional WGPD is studied. Based on the above analysis, in the following discussion, the absorption uniformity of a two-supermode traditional WGPD will be studied from various aspects.

First, by designing a traditional WGPD with L_{a0}, the characteristic attenuation length of the fundamental supermode, being comparable to the absorber length L, it helps to obtain relatively large absorption efficiency. The interference itself does not increase or decrease the absorption efficiency, it only adjusts the absorption distribution. Therefore, the absorption efficiency of a

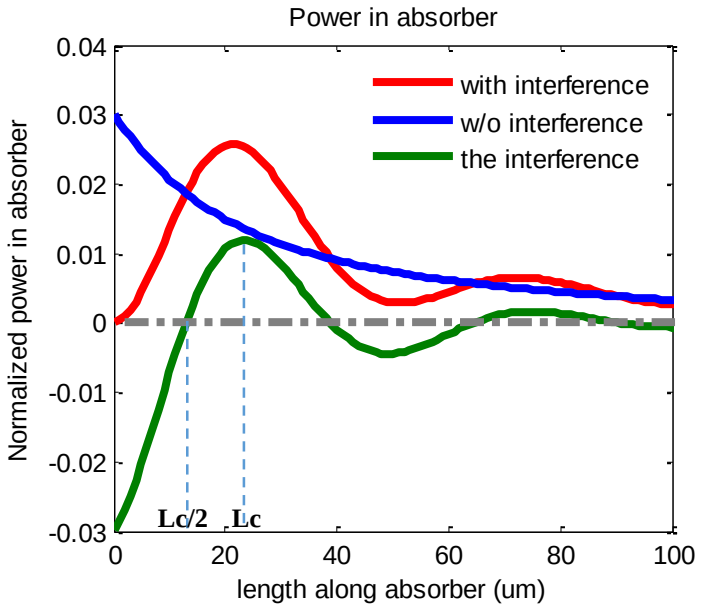

Figure 2-21 The effects of interference on the power distribution in the absorber of a traditional WGPD. The WGPD parameters are shown in Figure 2.13, W1 is 2 um, W2 is 6 um. Lc is the coupling length defined in Equation 2.21. The power distribution is plotted by using Equation 2.17, with the simulation of the fundamental mode and the large gamma mode.

WGPD largely depends on how much power of the dominant supermode is absorbed. When L_{a0} is comparable to L, most of the optical power from the fundamental supermode, which is the dominant supermode, will be absorbed and ensures large absorption efficiency. This applies to all kind of traditional WGPD, including the two-supermode case.

In section 2.7.6, it is mentioned that the discussion scope of this dissertation is about WGPD with RC time limited bandwidth around 50 GHz, and with absorption efficiency around 0.8. For a 50 GHz RC bandwidth p-i-n junction WGPD with 0.4 μm thick intrinsic layer, as shown in Table 2-4, the active area size is ~280 μm^2. The absorber width is usually chosen to be less than 4 μm to reduce the wide absorber related higher order supermodes, and to be more than 2 μm to reduce the optical scattering loss at the rough ridge sidewall. In this case, the absorber length L in a 50 GHz two-supermode traditional WGPD is usually between 70 μm and 140 μm. In order to meet the requirement of having L_{a0} close to L, from Equation 2.22, the confinement factor of the

fundamental supermode Γ_0 should be between 0.0088 and 0.0176, and Im($neff_0$) should be between 0.00088 and 0.00176 for λ at 1.55 μm. When Γ_0 and Im($neff_0$) is too large, more absorption will happen in the forward section and less absorption will happen in the rear section, which results in degraded absorption uniformity. When Γ_0 and Im($neff_0$) is too small, the absorption efficiency of a 50 GHz bandwidth WGPD will be reduced.

Second, the interference is critical for improving the absorption uniformity in any traditional WGPD. A shown in Figure 2-21, due to the existence of the interference between the fundamental mode and the large gamma mode, the power in the absorber $P_{abs}(z)$ starts from zero, instead of starting from its maximum value. Moreover, the interference term changes the exponential decay of the two propagation terms, and is capable of obtaining much better absorption uniformity than the case without interference. As shown in Equation 2.20, the interference term relates to various factors, which affect the amplitude, the period, and the attenuation of the interference power. The relation between the interference and the absorption profile will be a important study subject of the designing of a high power traditional WGPD, and is discussed from section 2.10.3 to section 2.10.5.

Third, in the discussion of absorption uniformity of a traditional WGPD, by using 2Lc, the absorber is divided into two sections in the longitudinal direction, which are the forward section and the rear section. The physical reason of using 2Lc is that the interference have very different strength in these two sections, as mentioned at the beginning of this section. In the forward section, the interference between the fundamental supermode and the large gamma supermode is so strong that it is the dominant factor affecting the absorption profile. Because of the interference, the power in the absorber rises up from z=0, then reaches its first maximum at z=Lc, and drops down to a certain point at z=2Lc. Beyond this point, the interference between the two supermodes becomes very weak, and the absorption uniformity is no longer determined by this interference. Therefore, in a traditional WGPD, considering the strength of interference between the fundamental

supermode and the large gamma supermode, the forward section of the absorber is from the front end to z=2Lc, and the rest of absorber is the rear section of the absorber. This applies to all kinds of traditional WGPD, including the two-supermode case. In the two sections, because of the strength difference of the interference between the fundamental supermode and the large gamma supermode, the absorption uniformity depends on very different factors, which will be discussed separately later.

Fourth, the improvement of the absorption uniformity in the forward section relies on the reduction of the first absorption peak. As shown in Figure 2-21, the interference spatially oscillates along z direction and its sign switches. Mathematically, an interference term with a negative sign helps reduce $P_{abs}(z)$. At z=Lc, the interference power reaches its maximum, and it results in a maximum absorption density $P_{abs,max}$, which can be expressed as:

$$\begin{aligned} P_{abs,\max} &= P_{absorber}(z = Lc) \\ &= {\chi_0}^2\Gamma_0 e^{-\alpha_0 Lc} + {\chi_1}^2\Gamma_1 e^{-\alpha_1 Lc} + 2\chi_0\chi_1\sqrt{\Gamma_0\Gamma_1}\,e^{-(\alpha_0+\alpha_1)Lc/2} \\ &= (\chi_0\sqrt{\Gamma_0}\,e^{-\alpha_0 Lc/2} + \chi_1\sqrt{\Gamma_1}\,e^{-\alpha_1 Lc/2})^2 \end{aligned} \qquad 2.24.$$

Since $|\chi_0|^2\Gamma_0 = |\chi_1|^2\Gamma_1$, Equation 2.24 can be re-written as:

$$P_{abs,\max} = {\chi_0}^2\Gamma_0(e^{-\alpha_0 Lc/2} + e^{-\alpha_1 Lc/2})^2 \qquad 2.25.$$

As $\alpha_0 << \alpha_1$, combine Equation 2.22 and Equation 2.25,

$$\begin{aligned} P_{abs,\max} &\approx {\chi_0}^2\Gamma_0 e^{-\alpha_0 Lc} = {\chi_0}^2 \frac{1}{\alpha_{\mathrm{InGaAs}}}\frac{1}{L_{a0}} e^{-Lc/L_{a0}} \\ &= {\chi_0}^2 \frac{1}{\alpha_{\mathrm{InGaAs}} \times Lc}\frac{Lc}{L_{a0}} e^{-Lc/L_{a0}} \end{aligned} \qquad 2.26.$$

According to Equation 2.26, $P_{abs,max}$ is dependent on χ_0, Lc, and Lc/L_{a0}. In the next sections, how the reduction of $P_{abs,max}$ can be achieved without sacrificing other performances will be discussed. The above discussion uses a two-supermode WGPD, which has the fundamental supermode and the large gamma supermode, to calculate $P_{abs,max}$. For traditional WGPD with higher order modes,

as the interference in the forward section is dominated by the interference between the fundamental supermode and the large gamma supermode, Equation 2.26 is still a good approximation. Therefore, the above results apply to all kinds of traditional WGPD.

Fifth, theoretically, by having 2Lc close to the absorber length L, it helps to obtain a relatively uniform absorption profile in a two-supermode traditional WGPD. As mentioned in the last paragraph, beyond z=2Lc, the power goes into what is called the rear section of the absorber, where interference becomes very weak, and the absorption uniformity is no longer affected by the interference. Therefore, in a two-supermode traditional WGPD, the absorption uniformity in the rear section is very poor. In this sense, by having $2Lc \approx L$, the absorption uniformity only need to be considered in the forward section of the absorber, which can be improved by reducing the $P_{abs,max}$, as discussed earlier in this section. Note, this approach is only true for the two-supermode case, and the feasibility of having $2Lc \approx L$ without sacrificing other performances will be discussed in the following discussion.

In summary, the above discussions cover the design considerations of a traditional WGPD for uniform absorption distribution and large absorption efficiency. The design of a traditional WGPD by supermode analysis involves the understanding of relationship between the supermodes and the devices performances. From the consideration of the bandwidth, in any traditional WGPD, certain absorber length L is required. From the consideration of the absorption efficiency, in any traditional WGPD, the absorber length L should be comparable to the characteristic attenuation length of the fundamental supermode L_{a0}. From the consideration of the absorption uniformity in the forward section of the absorber, in any traditional WGPD, $P_{abs,max}$ has to be reduced to be close to the average power density. Moreover, the absorption uniformity in a two-supermode traditional WGPD can be improved by having the absorber length L be close to 2Lc. In the next section, the implementation of the above design considerations in a traditional WGPD will be discussed.

2.10.2 The absorption uniformity limitation in a two-supermode traditional WGPD

As discussed in the last section, in a two-supermode traditional WGPD, in order to obtain relatively uniform absorption profile, reducing $P_{abs,max}$, as well as having 2Lc close to the absorber length L, is very critical. Meanwhile, having the characteristic attenuation length of the fundamental supermode L_{a0} close to the absorber length L is critical for obtaining large absorption efficiency. In this section, how to design a two-supermode traditional WGPD meeting the above requirements is discussed.

As mentioned at the beginning of this section, uniform absorption and large absorption efficiency require the absorber length L meet two conditions, $L \approx 2Lc$ and $L \approx L_{a0}$. According to Equation 2.22 and Equation 2.23, Lc and L_{a0} are two very different parameters. Therefore, having the numerical value of the two parameters being close to each other, as well as to the absorber length L, might be difficult. In the following discussion, simulation will be used to show more details about the relationship between L, L_{a0}, and Lc in a two-supermode traditional WGPD.

In the simulation, the waveguide structure is based on what is shown in Figure 2-13. The absorber is 2 μm wide, and 150 μm long. The adjustments of the absorber thickness and the waveguide width is used to largely change the fundamental supermode's confinement factor Γ_0, as well as L_{a0}. Meanwhile, the numerical value of 2Lc is simulated and compares to L_{a0}. The adjustments of the absorber thickness and the waveguide width are used for two reasons. First, the adjustment of these two parameters is widely used in the traditional WGPD optimization. Second, the adjustment of these two parameters gives large tuning range of L_{a0}, and benefits the study in this section.

In the first set of simulations, the absorber thickness is adjusted. In order to construct a two-supermode case, the waveguide width W2 is set at 4 μm, and the absorber width W1 is 2 μm. With the narrow waveguide width, as well as the similar width of the waveguide and the absorber, the simulation shows large suppression of the excitation of the higher order supermodes. As shown

in Figure 2-22, when the absorber thickness varies from 0.1 μm to 0.2 μm, it results in significant variation of the imaginary part of the effective index of the fundamental supermode Im(n_{eff0}), and hence large change of L_{a0}. In contrast, the change of 2Lc is much smaller due to the small variation of the Re($1/(n_{eff0}-n_{eff1})$). From Equation 2.22, it is expected that the change of the absorber thickness, or any other measures changing Γ_0 and Im(n_{eff0}), will result in large change of L_{a0}. In contrast, it is more difficult to predict the change of the 2Lc along with the change of Γ_0 and Im(n_{eff0}), as Lc depends on Re($1/(n_{eff0}-n_{eff1})$). It is not the intension of this dissertation to put in lots of analysis for the change of 2Lc, instead, I will only describe the change of 2Lc and compare it to L_{a0}. In this simulation, it shows the two parameters has very different dependence on the absorber thickness variation. With the adjustment of the absorber thickness, while it is easy to have L_{a0} be close to L, it is very difficult to have 2Lc be comparable to L.

In the second set of simulations, the change of waveguide width W2 also changes L_{a0}. Adjusting W2 is another common approach in the waveguide design. This set of simulations differs from the first set in that the simulated WGPDs are not limited to two-supermode case. For example, when W2 is larger than 4 μm, there will be higher order supermodes excited. However, in the forward section of the absorber, as discussed in the last section, the absorption uniformity is dominantly affected by the fundamental supermode and the large gamma supermode. Therefore, the two supermodes can still be used to characterize the absorption uniformity and absorption efficiency in the forward section of the absorber, no matter the discussion subject is a two-supermode or a three-supermode WGPD. In this simulation, the definition of L_{a0} and Lc are kept the same with what are used in the last set of simulations. As shown in Figure 2-23, as the

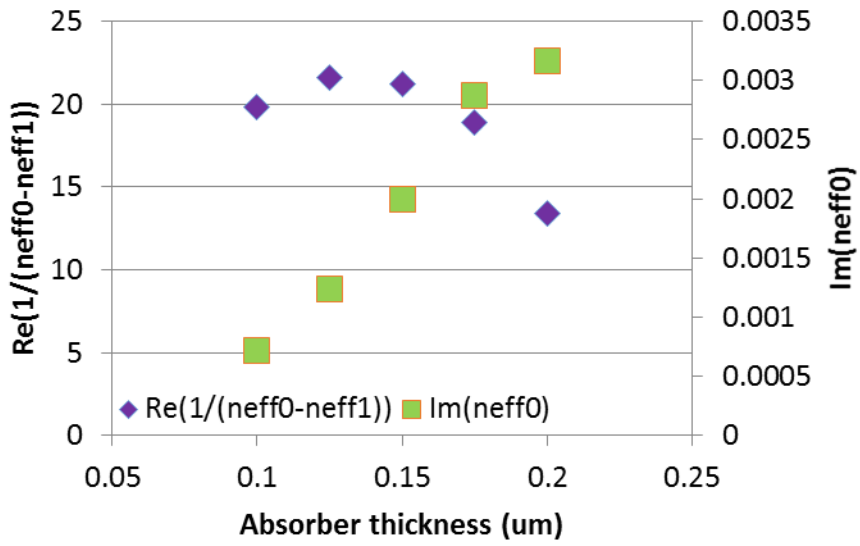

(a)

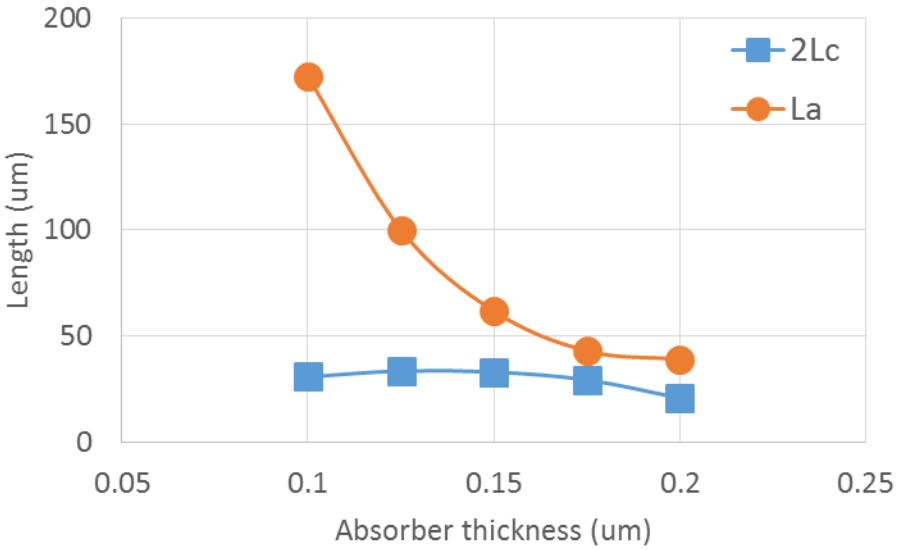

(b)

Figure 2-22 In a two-supermode traditional WGPD with various absorber thickness, the plot of the real part of the inverse of two supermodes' effective index difference Re(1/(n_{eff0}-n_{eff1})), and the imaginary part of the fundamental supermode's effective index Im(n_{eff0}) (a); the plot of the 2Lc and La0 (b). The WGPD structure is shown in Figure 2-13, with the absorber thickness varies. W1 is 2 μm, W2 is 4 μm.

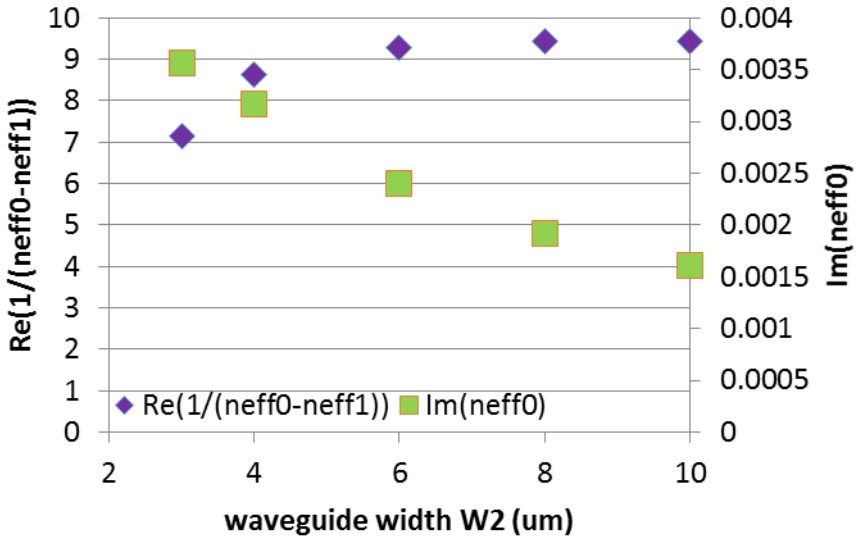

(a)

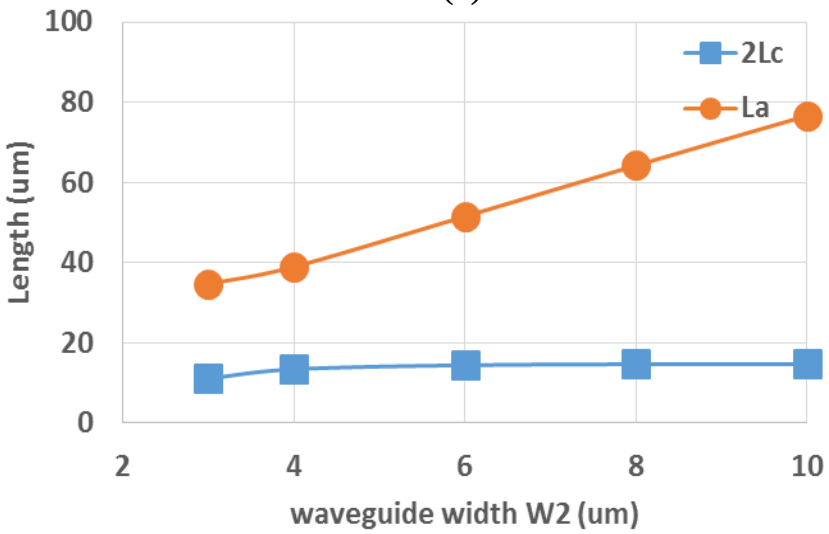

(b)

Figure 2-23 In a two-supermode traditional WGPD with various waveguide width, the plot of the real part of the inverse of two supermodes' effective index difference Re(1/(n_{eff0}-n_{eff1})), and the imaginary part of the fundamental supermode's effective index Im(n_{eff0}) (a); the plot of the 2Lc and La0 (b). The WGPD structure is shown in Figure 2-13, with the absorber thickness varies. W1 is 2 μm.

waveguide gets wider, the waveguide width variation results in more significant variation of $Im(n_{eff0})$ than $Re(1/(n_{eff0}-n_{eff1}))$. As a result, similar with what are observed in the first set of simulations, by adjusting the waveguide width, it is easy to have L_{a0} be close to L, while it is very difficult to have 2Lc be comparable to L.

The above two cases represent two widely used approaches adjusting the waveguide for better power performances. Both cases show that L_{a0} is more sensitive than 2Lc to the change of the these two parameters. While it is relatively easy to have the right L_{a0} being close to L for large absorption efficiency, it is very difficult to adjust the waveguide structure to have 2Lc be comparable to L. Moreover, in the current study, 2Lc is found to be much smaller than the absorber length, which will result in the appearance of high absorption peak near the front end of the absorber. For example, Lc in the both cases shown above is less than 20 μm. Therefore, for a WGPD with 100 μm long absorber, the absorption peak will appear at less than one fifth of the total absorber length from the front end of the absorber, and results in large absorption within a short section.

In summary, the above simulations show the comparison between L_{a0}, 2Lc, and L, which show that 2Lc is usually much smaller than L. This result in a limitation in a two-supermode traditional WGPD. In the rear section of the absorber, which is between z=2Lc and z=L, the interference between the fundamental supermode and the large gamma supermode is very weak. Because of the lacking of other higher order supermodes, the absorption in the rear section of the absorber is not uniform. According to the above simulations, the forward section of the absorber is usually less than 40 μm, which is usually shorter than the rear section length in a 50 GHz WGPD. Therefore, the issue of absorption uniformity in both the forward section and the rear section of a traditional WGPD is equally important. As the two-supermode traditional WGPD does not have the capability of having uniform absorption in the rear section, the traditional WGPD with more than two supermodes is studied with supermode analysis in the following sections, in order to achieve better overall absorption uniformity.

2.10.3 The absorption uniformity in the forward section of the absorber

In the last section, the absorption distribution in a traditional WGPD is analyzed by using supermode analysis. It pointed out that the absorption uniformity in the forward section and in the rear section is related to different factors. For the design of high power 50 GHz traditional WGPD, in which 2Lc is usually much smaller than the absorber length L, the discussion of absorption uniformity in the forward section (from z=0 μm to z=2Lc) and in the rear section (from z=2Lc to z=L) should be made separately. In this section, the discussion focuses on the absorption uniformity in the forward section, which is followed by the discussion of the absorption uniformity in the rear section in the next section.

In the forward section of the absorber, as discussed in the section 2.10.1, in any traditional WGPD, the absorption uniformity is dominantly affected by the interference between the fundamental supermode and the large gamma supermode. Therefore, the analysis results of a two-supermode traditional WGPD, which has the fundamental supermode and the large gamma supermode excited, can still be applied to the study of absorption in the forward section of any traditional WGPD.

As discussed in the last section, in order to improve the absorption uniformity in any traditional WGPD, the waveguide structure has to be adjusted, so that the peak absorption density $P_{abs,max}$ near the front end can be reduced to be closer to the average absorption density in the forward section. As shown in Equation 2.26, $P_{abs,max}$ is dependent on χ_0, Lc, and Lc/L_{a0}. In the two sets of simulations in the last section, it is already shown that Lc is insensitive to the waveguide structure adjustment. In this case, it is difficult to reduce $P_{abs,max}$ by reducing Lc. For the same two sets of simulations, χ_0 and χ_1 are also simulated and are shown in Figure 2-24, in which χ_0 is also

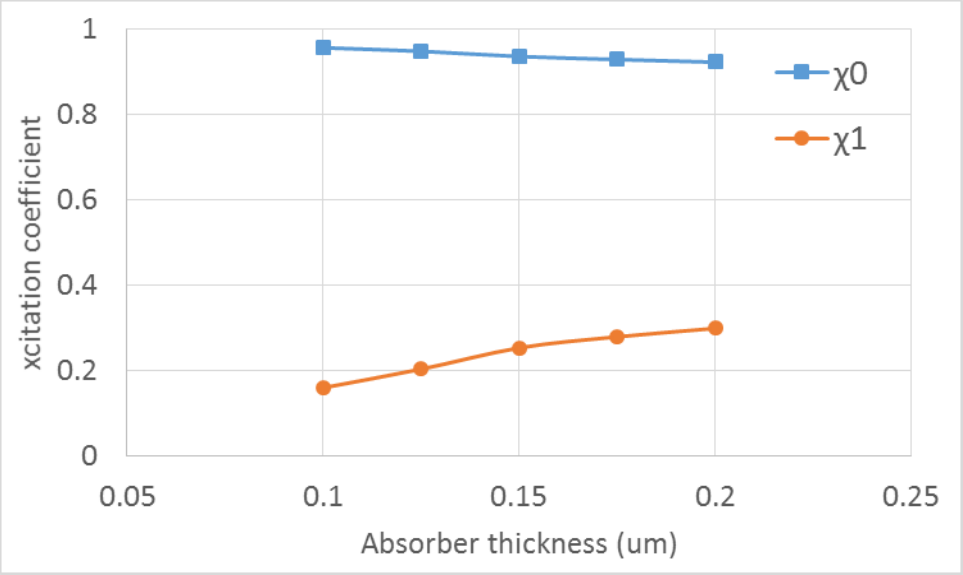

(a)

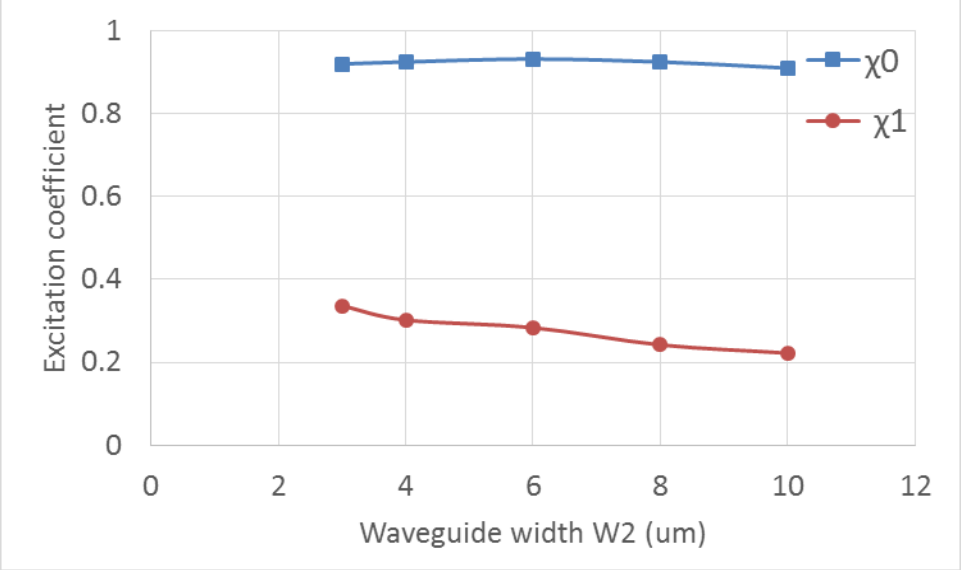

(b)

Figure 2-24 For the two sets of simulation shown in section 2.10.2, the simulated excitation coefficient of the fundamental supermode and the large gamma supermode χ_0 and χ_1 , when the absorber thickness is adjusted (a), and when the waveguide width is adjusted (b). The simulation is done by FIMMWAVE.

insensitive to the waveguide structure adjustment. This is understandable in a traditional WGPD, in which the absorber is usually just a perturbation of the waveguide, and the fundamental supermode always has large field overlap with the 0^{th} order mode of the passive waveguide, and hence small dependence of χ_0 on the waveguide structure. In this case, Lc/L_{a0} becomes the only factor for the discussion of absorption uniformity in the forward section.

In Equation 2.26, Lc/L_{a0} appears in both the linear coefficient and the exponential function in the expression of $P_{abs,max}$, which results in a complicated relation between Lc/L_{a0} and $P_{abs,max}$. In order to visualize this relation, $P_{abs,max}$ is plotted against Lc/L_{a0}, with certain assumptions of the numerical value of χ_0 and Lc. As χ_0 and Lc are part of the linear coefficient of $P_{abs,max}$, any difference between the assumed value and the real value of the two parameters should not change the relation between Lc/L_{a0} and $P_{abs,max}$. Moreover, as Lc is treated as a constant, according to Equation 2.22, the increase of Lc/L_{a0} is equivalent to the increase of confinement factor of the fundamental supermode Γ_0. As shown in Figure 2-25, as Γ_0 increases, L_{a0} decreases and Lc/L_{a0} increases. Along with those changes, $P_{abs,max}$ varies in different manner. When L_{a0} is close to Lc, which corresponds to when Lc/L_{a0} is around 1, $P_{abs,max}$ is not sensitive to the change of Lc/L_{a0}. As L_{a0} decreases, Lc/L_{a0} increases beyond 1, and $P_{abs,max}$ will gradually decrease. However, a traditional WGPD with $Lc/L_{a0}>1$ is not preferred for two reasons. First, L_{a0} will be much smaller than the absorber length L, which will result in smaller absorption efficiency, as discussed in the last section. Second, when L_{a0} is less than Lc, the absorption becomes a faster event than the interference, and the absorption will be very nonuniform. As L_{a0} increases, the reduced Lc/L_{a0} will results in faster reduction of $P_{abs,max}$, which means $P_{abs,max}$ becomes very sensitive to the change of Γ_0.

As discussed in the last paragraph, the reduction of $P_{abs,max}$ and hence the improvement of the absorption in the forward section, can be achieved by the reduction of the confinement factor

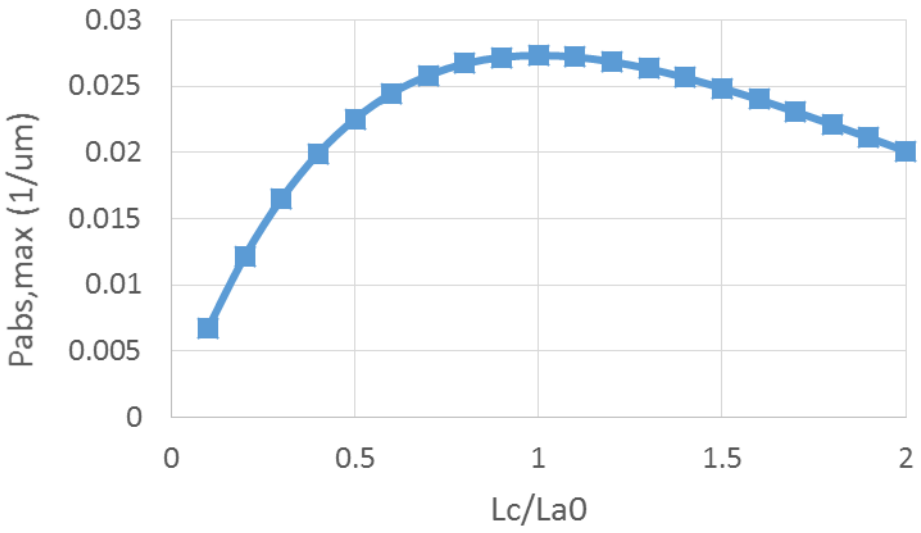

Figure 2-25 The plot of $P_{abs,max}$ against Lc/L_{a0}. χ_0 is assumed to be 0.93, Lc is assumed to be 20 μm.

of the fundamental supermode Γ_0. As shown earlier in this section, χ_0 is insensitive to the waveguide structure change, and the reduction of Γ_0 results in the reduction of $|\chi_0|^2\Gamma_0$. In a two-supermode traditional WGPD, as shown in Equation 2.17, $|\chi_0|^2\Gamma_0 = |\chi_1|^2\Gamma_1$. Therefore, the reduction of $|\chi_0|^2\Gamma_0$ results in the same amount of the reduction of $|\chi_1|^2\Gamma_1$. In a three-supemode traditional WGPD, as shown in Equation 2.18, $|\chi_0|^2\Gamma_0 = |\chi_1|^2\Gamma_1 + |\chi_2|^2\Gamma_2 + 2|\chi_1\chi_2| \iint_{absorber} \Phi_1(x,y)\Phi_2^*(x,y)dxdy$. It is expected that the reduction of $|\chi_0|^2\Gamma_0$ results in the reduction of $|\chi_1|^2\Gamma_1$, although will be at different amount. Similar conclusion can be drawn in traditional WGPD with more supermodes. The reduction of $|\chi_1|^2\Gamma_1$ relates to the reduction of either the excitation coefficient of the large gamma supermode $|\chi_1|$, or the confinement factor of the large gamma supermode Γ_1, or both. In a certain sense, either the reduction of $|\chi_1|$, or Γ_1, or both, is regarded as the suppression of the large gamma supermode. Therefore, the absorption peak in the forward section is expected to be reduced with the suppression of the large gamma supermode. However, when the suppression of the large gamma supermode

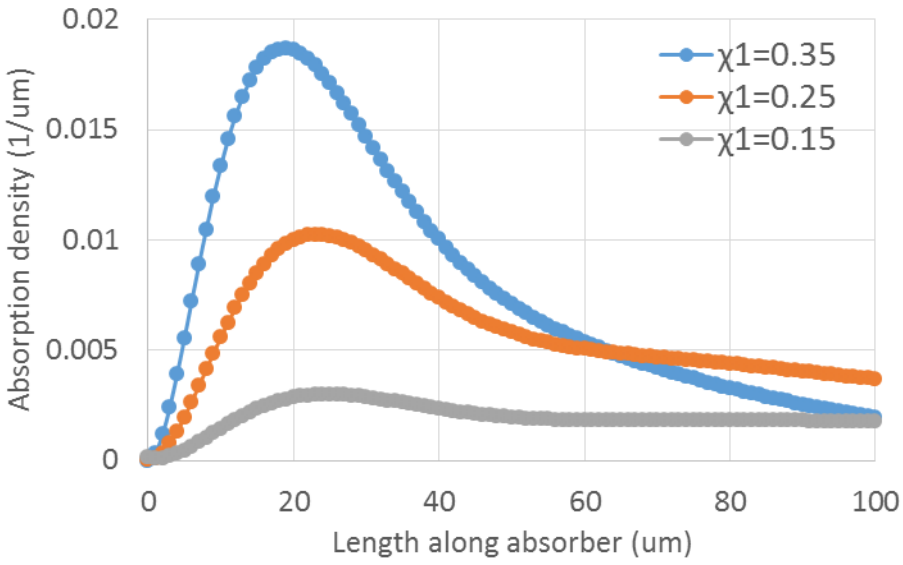

Figure 2-26 The absorption profile of a two-supermode traditional WGPD with the excitation coefficient of the large gamma supermode χ_1 purposely changed.

results in comparable amplitude between the large gamma mode interference term and the higher order mode interference term in the forward section, the above statement no longer stands, because the absorption peak in the forward section relates to both interference terms, instead of the large gamma mode interference term only. This case occurs when the excitation coefficient of the large gamma mode is several times smaller than that of the higher order mode.

It is concluded from the above discussions that the excitation of the large gamma supermode, as well as its interference with the fundamental supermode, should be the studied for the optimization of the absorption uniformity in the forward section of the traditional WGPD. The study of $P_{abs,max}$ shows that the reduction of Γ_0 can effectively suppress the large gamma mode, and improve the absorption uniformity in the forward section. In the following discussion, two simulations are used to verify the above statements concluded from the theoretical analysis. In the first simulation, the statement that reducing the excitation of the large gamma supermode, which effectively suppresses the large gamma supermode excitation, improves the absorption uniformity

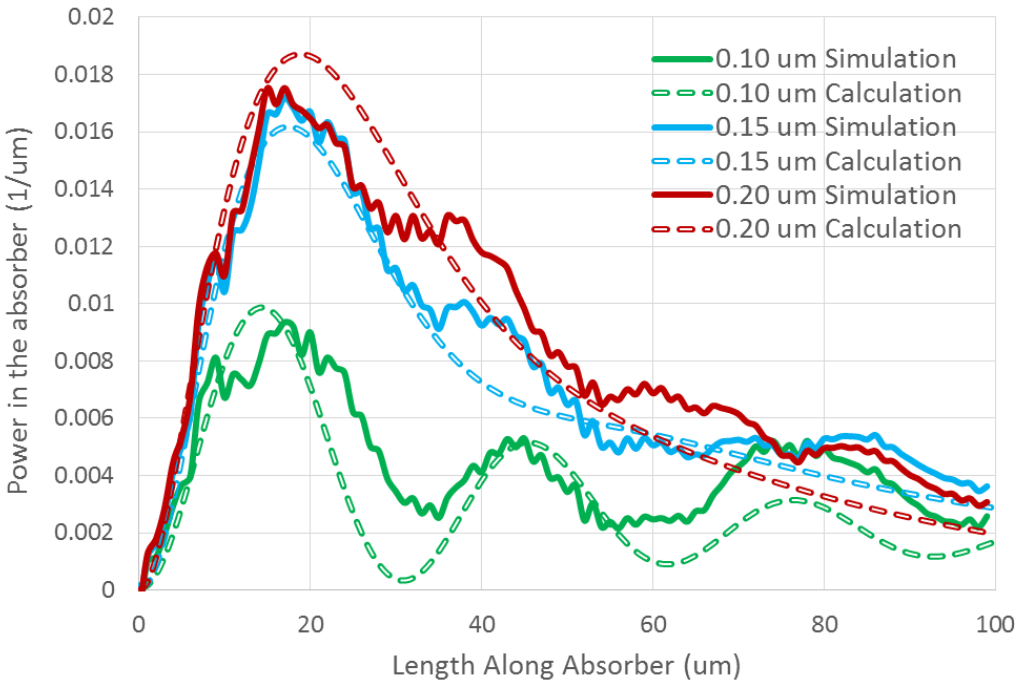

Figure 2-27 The absorption profile of three WGPDs discussed in Figure 2-22. The three WGPDs vary in the absorber thickness. The simulation of absorption profile is done by Beamprop. The calculation of absorption profile is done by using Equation 2-20.

in the forward section is checked. In the second simulation, the statement that the reduction of Γ_0 can effectively reduce the excitation of the large gamma mode and improve the absorption uniformity is checked.

In the first simulation, a two-supermode traditional WGPD's absorption profile is plotted based on Equation 2.20. In order to examine the effect of large gamma supermode excitation on

Table 2-6 For the three WGPDs discussed in Figure 2-27, the simulated Γ_0, χ_1, the absorption peak-to-average ratio (P/A), and the absorption efficiency.

Absorber THK	Γ_0	χ_1	P/A	Absorption efficiency
0.10 μm	0.0058	0.159	2.07	0.434
0.15 μm	0.0162	0.253	2.25	0.775
0.20 μm	0.0356	0.299	2.32	0.853

the absorption in the forward section, χ_1 is purposely assigned with different numerical values in the calculation of $P_{absorber}(z)$. By doing so, it excludes the effects of other parameters' change on the absorption distribution. A few things are also considered along with the adjustment of χ_1. First, $|\chi_0|^2 + |\chi_1|^2 = 1$. This relation makes sure that the two-supermode WGPD simulation is done with constant total power. Second, $|\chi_0|^2 \Gamma_0 = |\chi_1|^2 \Gamma_1$. This relation makes sure the absorption always starts from zero at z=0 μm, which is true for a traditional WGPD with the incident power isolated from the absorber. The calculated absorption profile is shown in Figure 2-26, in which the reduction of χ_1 results in significant reduction of the absorption peak in the forward section of the absorber. Moreover, if the ratio of peak-to-average absorption density is used to characterize the absorption uniformity, it can also be concluded that the reduction of χ_1 results in the improvement of absorption uniformity in a two-supermode traditional WGPD. However, the improvement of absorber uniformity comes at a price of reduced absorption efficiency, this is one major limitation of traditional WGPD, and it will be discussed with more details in the next section.

In the second simulation, in order to examine the effect of reducing Γ_0 on the excitation of the large gamma mode and the absorption uniformity, the absorption profiles of three WGPDs analyzed in Figure 2-22 are plotted by using both Beamprop simulation and the supermode calculation, as shown in Figure 2-27. The simulated and calculated absorption profile make good agreement with each other. The three WGPDs, which vary in the absorber thickness, have the same absorber length of 100 μm. The WGPD with the thinnest absorber shows the lowest absorption peak, at the price of a much smaller absorption efficiency. The simulation results are summarized in Table 2-6, in which the thinner absorber reduces Γ_0, which in turn largely reduces χ_1. As a result, the absorption uniformity in the forward section improves when the absorber becomes thinner, but at a price of reduced absorption efficiency.

The major problem of designing a traditional WGPD with improved absorption uniformity in the forward section is the absorption efficiency reduction, as shown in the above discussion. The cause of the problem is large gamma mode interference. In a traditional WGPD, the large gamma mode interference is the dominant interference in the forward section. In this case, the improvement of the absorption uniformity relies on the suppression of the large gamma mode. However, in a traditional WGPD, as shown in section 2.10.3, the suppression of the large gamma mode always comes along with the reduction of the confinement factor of the fundamental supermode Γ_0, which results in the increase of L_{a0} and the reduction of the absorption efficiency. In chapter 3, the large gamma mode interference becomes a minor interference in the forward section of a novel WGPD, and the above tradeoff between the absorption uniformity and the absorption efficiency is no longer significant. However, for the traditional WGPD, this tradeoff is an issue to be addressed. One way to alleviate this problem is tapering the absorber or waveguide, in which the absorber is designed to be narrow and/or the waveguide is designed to be wide at the front end of the active section, in order to reduce the excitation of the large gamma supermode. As the excited supermodes propagate, although the excitation coefficients of the supermodes are unchanged, the widening of the absorber and/or the narrowing of the waveguide will increase the confinement factor of the excited supermodes, and increase the absorption density, as shown in the Equation 2.20. The following simulation of WGPDs verifies the above statement. The WGPD with 0.15 μm thick absorber used here is already shown in Figure 2-27. This WGPD has a 2 μm wide straight absorber sitting on top of a 4 μm wide straight waveguide. The absorption peaked at z=19 μm. The absorption efficiency is 0.77 when absorber is 100 μm long. The ratio of peak-to-average absorption density is 2.25. If the absorber width is reduced from 2 μm to 1.3 μm, the excitation coefficient of the large gamma mode decreases, which significantly improves the absorption uniformity but at a price of reduced absorption efficiency. In order to improve the absorption uniformity without sacrificing the absorption efficiency, tapering the absorber width and extending the absorber are used to improve

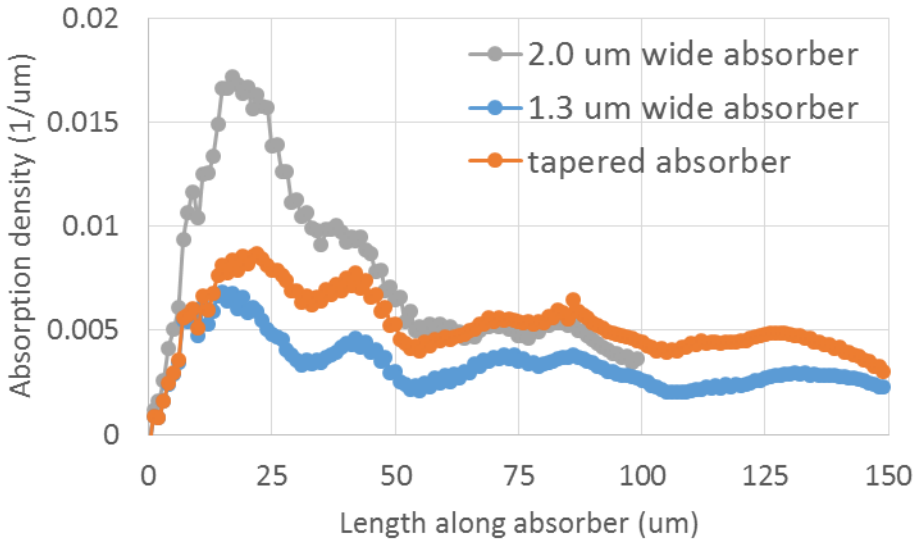

Figure 2-28 The absorption profile of the traditional WGPD with 0.15 μm thick absorber. The waveguide structure is already describe for the use of Figure 2-27. In this plot, the absorber is configured differently. In the first case, its size is 2 μm x 100 μm; in the second case, it is 1.3 μm x 200 μm; in the third case, it is linearly and reversely tapered acrross the 150 μm long length, with the front end width of 1.3 μm and the back end width of 2.7 μm.

the absorption uniformity. The absorber width at the front end is reduced to 1.3 μm, which is then linearly increased to 2.7 μm at the z=150 μm. The simulated absorption profile is shown in Figure 2-28. For the WGPD with the tapered absorber, the absorption efficiency is 0.782, which is close to that in the WGPD with 2 μm x 100 μm absorber. The ratio of peak-to-average absorption density is 1.72, which is 24% lower than that in the straight absorber case. However, in this WGPD with 0.15 μm thick absorber, the improved absorption uniformity in the forward section is at a price of larger absorber area, and hence lower bandwidth. In the above case, the RC bandwidth of the WGPD with 2.0 μm constant width absorber is 70 GHz, while the bandwidth of the WGPD with the tapered absorber is 46 GHz. The degree of this tradeoff between the absorption uniformity and the bandwidth may various in different WGPD, but this tradeoff generally exists in the traditional WGPD.

It is noticed from the work in this chapter, as well as other researchers' work of traditional WGPD [3] [5] [7], that the absorption peak in the forward section of the absorber usually occurs at a distance of between 10 μm and 30 μm away from the absorber front end. For example, as shown in Figure 2-28, in a traditional WGPD made on MUTC2 layer structure, for all three different absorber widths, the absorption peak in the forward section of the absorber is about 20 μm away from the absorber front end. In the design of WGPD, the absorption peak is usually preferred to be much further away from the absorber front end, as the thermal conduction in the longitudinal direction near the front end is worse than the rest of the absorber. As the previous discussion of absorption focuses on the magnitude of the absorption peak in the forward section of the absorber, it is the intent of the following discussion to understand the factors affecting the absorption peak position in the forward section of the absorber in the longitudinal direction.

As pointed out in section 2.10.1, the absorption peak in the forward section of the absorber is a result of the interference of the fundamental supermode and the large gamma supermode, and its position is determined by the period of the interference, which is inversely proportional to the difference of the two supermodes' effective refractive index, $n_{eff,0}$-$n_{eff,1}$. When the waveguide structure is modified, although the supermode analysis can predict the absorption peak position change by calculating the change of ($n_{eff,0}$-$n_{eff,1}$), to my best knowledge, it is difficult to explain why ($n_{eff,0}$-$n_{eff,1}$) responds to the waveguide structure modification in a certain way. Therefore, it is difficult to study the position of the absorption peak in the forward section of the absorber by using supermode analysis.

The waveguide structure of a traditional WGPD can be treated as a vertical coupler waveguide, from which the study of absorption peak positon can be started. Traditionally, a coupler waveguide has an interaction region that has two channel waveguides, separated by a certain distance of the order of the evanescent decay length of the field pattern of the two channel

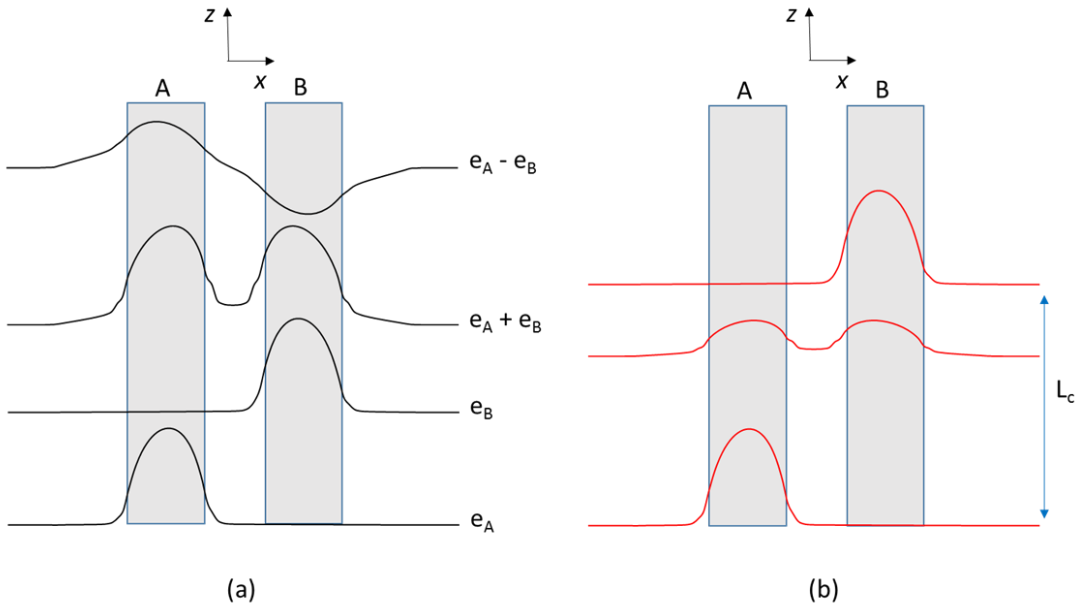

Figure 2-29 Top view of a directional coupler and illustration of coupled modes in the interaction region, within which the refractive index varies in the x direction, and the optical power propagates in the z direction. (a) The field patterns of isolated waveguide A and B, e_A and e_B, as well as the field pattern of symmetric and anti-symmetric mode of a directional coupler with two coupled identical waveguides, $e_A + e_B$ and $e_A - e_B$. (b) A illustration of the power transfer between two coupled waveguides in a directional coupler. Lc is the coupling length.

waveguides, as shown in Figure 2-29 (a). In a coupler waveguide, a prescribed fraction of power in one waveguide is transferred back and forth between the two waveguides within the interaction region, and the power in each waveguide varies periodically, as shown in Figure 2-29 (b). For a traditional WGPD studied in this chapter, a coupler waveguide consists of the lower waveguide and the upper absorber. Any low refractive index layer between the two can be treated as the separation of the coupler waveguide. As the optical power couples into the lower waveguide, when it propagates in the longitudinal direction, it will couple between the waveguide and the absorber in the vertically direction. In this case, similar to the traditional coupler waveguide mentioned above, the optical power in the longitudinal direction in the absorber is expected to have a periodical variation, resulting in peaking of the optical power density. Moreover, along with the power coupling, absorption occurs in the absorber, and attenuates the power coupled into the absorber.

These two factors work together and result in the peaking of the absorption density. Therefore, for the study of the position of the absorption peak in the forward section of the absorber in a traditional WGPD, it is important to study the coupling of the vertical coupler waveguide.

In a traditional coupler waveguide, according to the coupled mode analysis [1], the coupling length Lc can be described as:

$$L_C = \frac{\pi}{\sqrt{C_{AB}C_{BA} + \left[\frac{\pi}{\lambda}(n_A - n_B)\right]^2}} \qquad 2.27.$$

in which

$$C_{AB} = \frac{\omega}{4}\varepsilon_0(n_A^2 - n_3^2)\iint_{S_A}[e_A \cdot e_B^*]\,dS$$

$$C_{BA} = \frac{\omega}{4}\varepsilon_0(n_B^2 - n_3^2)\iint_{S_B}[e_B \cdot e_A^*]\,dS \qquad 2.28.$$

where n_A and n_B are the refractive index of waveguide A and B, n_3 is the refractive index of the background material of waveguide A and B, λ is the wavelength of the optical radiation, ω is the angular frequency of the optical radiation, ε_0 is the dielectric constant of vacuum, e_A and e_B are field patterns of isolated waveguide A and B.

From Equation 2.27 and Equation 2.28, in a directional coupler with the refractive index given for waveguide A and B, as well as for the background material, the coupling length is determined by $\iint_{S_A}[e_A \cdot e_B^*]\,dS$ and $\iint_{S_B}[e_B \cdot e_A^*]\,dS$, which are the overlap of the field pattern of the two isolated waveguide in the region of waveguide A and B. When it comes to a traditional WGPD, the coupling length is determined by the overlap of field pattern of the isolated lower waveguide and the absorber. In another word, the coupling length relates to how the field pattern of isolated lower waveguide and absorber is distributed in its own region, and how it is evanescently

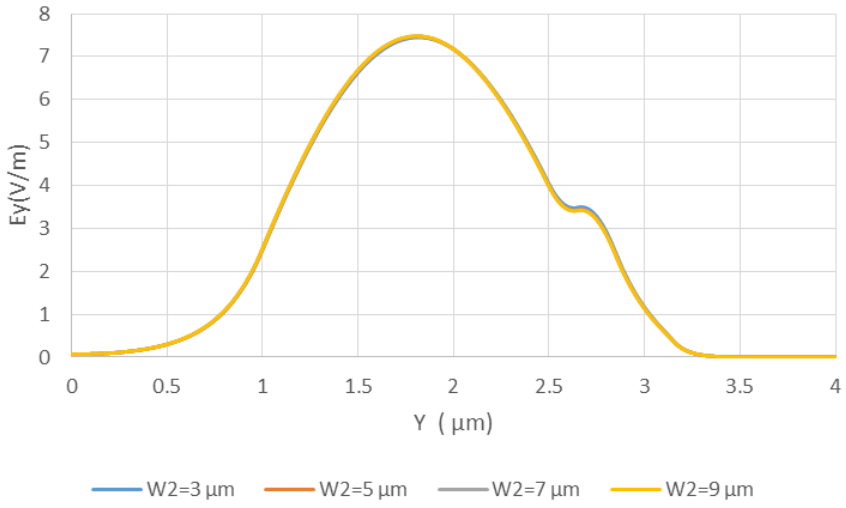

Figure 2-30 The simulated field pattern of the fundamental mode in the y direction (the vertical direction) at x=0 µm. The simulation is done for a traditional WGPD at different waveguide width. The waveguide structure and layer structure are already described in Figure 2-13. The absorber width is fixed at 2 µm.

extends into the other region. The above discussion focuses on establishing a vertical coupler waveguide model for the traditional WGPD, in order to understand the position of the absorption peak. In the following discussion, more detailed study is given to discuss how the waveguide parameters affect the position of the absorption peak.

In the design of a traditional WGPD, it is common to adjust the waveguide width to change the average absorption density. However, it is less known for the relation between the waveguide width and the absorption peak position. In the following discussion, with the waveguide width adjusted in a traditional WGPD, first the field pattern in the vertical direction, which determines the vertical coupling, will be discussed. Then the power distribution in the absorber will be simulated, in order to find the change of coupling length. Last, the absorption distribution will be simulated, in order to observe the change of the absorption peak positon.

When a traditional WGPD is treated as a vertical coupler waveguide, as discussed previously, the position of the absorption peak relates to the coupling length of optical power

between the lower waveguide and the absorber in the vertical direction. As discussed in the last paragraph, the change of coupling length in a traditional WGPD largely depends on the field pattern change in the vertical direction. The field pattern of a waveguide in certain direction is mainly determined by the waveguide dimension in that direction, as well as by the refractive index of the waveguide and its background. Therefore, although the adjustment of waveguide width changes the lower waveguide field pattern in the horizontal direction, it is not expected to introduce large change of field pattern in the vertical direction, which is orthogonal to the direction in which the waveguide dimension changes. Simulation results presented in Figure 2-30 show that, for the simulated cases, the field pattern of the fundamental mode of a traditional WGPD in the vertical direction is quite independent of the waveguide width, which also indicates that large change is not expected for the vertical field pattern in a traditional WGPD. In this case, the coupling length is also expected to be quite independent of the waveguide width in a traditional WGPD.

When a traditional WGPD is treated as a vertical coupler waveguide, as the optical power coupled between the lower waveguide and the absorber, the power distribution in the absorber in the z direction can be used to study the vertical coupling. As shown in Figure 2-31, the power in the absorber is simulated for the traditional WGPDs with various waveguide widths. In order to focus the study on the power coupling, the absorption, which attenuates the coupled power in a realistic case, is turned off in the simulation. From the simulation results, the increase of the waveguide width does not change the first peak position of the power in the absorber, which is fixed at about 25 μm away from the absorber front end. Two changes are observed in Figure 2-31, along with the increase of the waveguide width. One is the reduced magnitude of the power in the absorber, which is due to reduced power density in the lower waveguide. The other is that from the 2^{nd} peak of the power in the absorber, as the waveguide width increases, the peak position becomes further away from the absorber front end. This phenomena is very likely due to the generation of

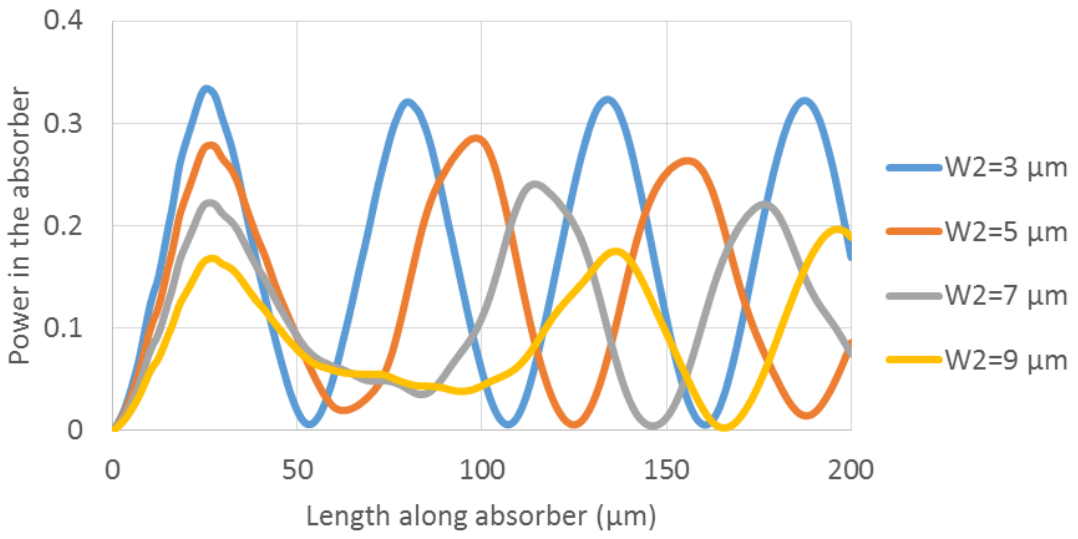

Figure 2-31 The simulated optical power distribution in the absorber layer in a traditional WGPD at different waveguide width. The absorption is turned off in the simulation. The waveguide structure and layer structure are already described in Figure 2-13. The absorber width is fixed at 2 µm. The simulated optical power in the absorber is normalized to the total input optical power.

higher order modes in the lower waveguide, substantial discussion is not given here, as the focus of the discussion is on the position of the 1st power peak position.

The above simulation of power distribution in the absorber shows that the 1st power peak position is independent of the waveguide width. As the absorption density is proportional to the power density in the absorber, it is expected that the 1st absorption peak position will not change too much with the change of waveguide width. From the simulation results shown in Figure 2-32, the 1st absorption peak position is kept at 20 µm away from the absorber front end, when the waveguide width of the traditional WGPD studied above varies from 3 µm to 9 µm. There is a small peak position discrepancy between the simulated power in the absorber in Figure 2-31 and the simulated absorption in Figure 2-32. This is due to the fact that the actual power distribution in the absorber is also affected by the attenuation due to absorption.

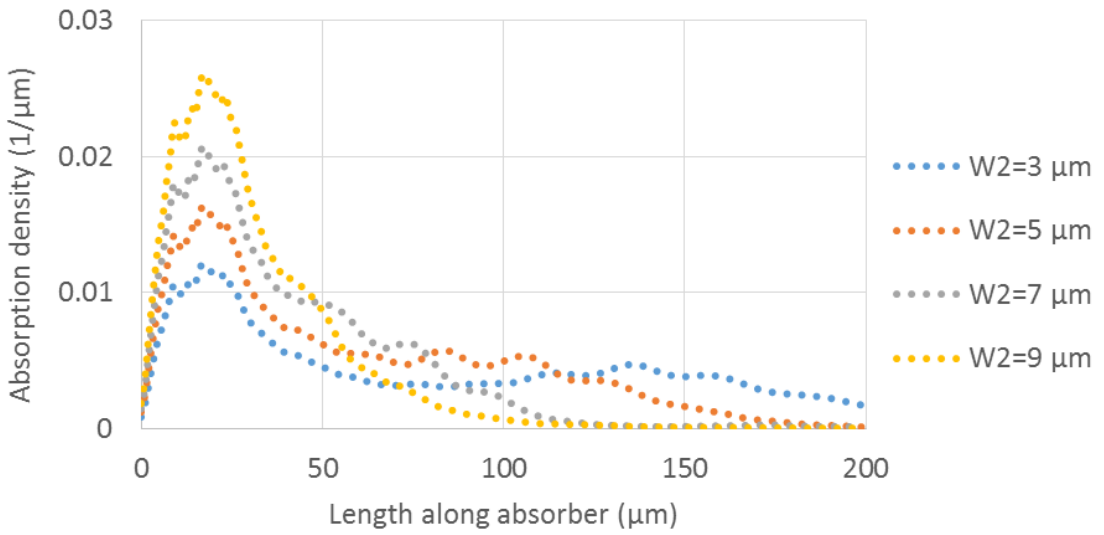

Figure 2-32 The simulated absorption distribution in a traditional WGPD at different waveguide width. The waveguide structure and layer structure are already described in Figure 2-13. The absorber width is fixed at 2 μm.

The above discussion points out that the 1st absorption peak position has small dependence on the waveguide width, due to the fact that power coupling between the lower waveguide and the absorber is quite independent of the waveguide width. Because of the similarity of the reasoning, the same conclusion can also be applied to the relation between the 1st absorption peak position and the absorber width. In this case, it is suggested to change the 1st absorption peak position by adjusting the layer structure, instead of the waveguide structure dimension. Based on the vertical coupler waveguide model, the coupling length can be adjusted by changing the thickness and refractive index of the lower waveguide, absorber, and the separation region between the two. Among which, adjusting the separation region between the lower waveguide and the absorber has the least influence to e_A and e_B, which are the field pattern of the isolated lower waveguide and the absorber in the vertical coupler waveguide model. It only changes the evanescent tail of e_A and e_B. Therefore, the following discussion focuses on adjusting the separation region between the lower waveguide and the absorber, due to its simplicity.

In the above discussion, the separation distance between the lower waveguide and the absorber is zero. In this case, adding a low index layer between the two will reduce the evanescent tail of e_A and e_B, and hence increase the coupling length. This layer, which is added in between two layers that have higher refractive index, is called diluting layer in the following discussion. For traditional WGPD designed on InP substrate, the refractive index of this low index layer can be any number between that of the lower waveguide and InP, and the thickness of this low index layer has to be of the order of the evanescent decay length of e_A and e_B. When the refractive index of this low index layer is smaller, the evanescent decay length of e_A and e_B will be smaller in the direction towards the separation, and thinner low index layer can be used to increase the coupling length. In this case, InP is chosen for the low index layer material in this discussion, in order to minimize the thickness increase of the layer structure, which benefits the wafer growth quality and reduce the carrier transit time.

For traditional WGPD with different thickness of InP diluting layer, the distribution of power in the absorber and absorption density are shown in Figure 2-33. Again, the absorption is turned off in the simulation of the power in the absorber. Different from varying the waveguide dimension, changing the InP diluting layer thickness significantly shifts the peak of power in the absorber away from the absorber front end. For example, change the InP diluting layer thickness from 0 μm to 0.3 μm increases the coupling length from 25 μm to 55 μm. Correspondingly, along with the thickening of the InP diluting layer, the absorption peak (more precisely, the center of the large absorption region) is also shifted away from the absorber front end. It is worth noting that absorption density reduction occurs, when InP diluting layer thickness increases. Generally speaking, any measures that try to push away the absorption peak by increase the coupling length will inevitably reduce the coupled power per length, and hence reduce the absorption efficiency.

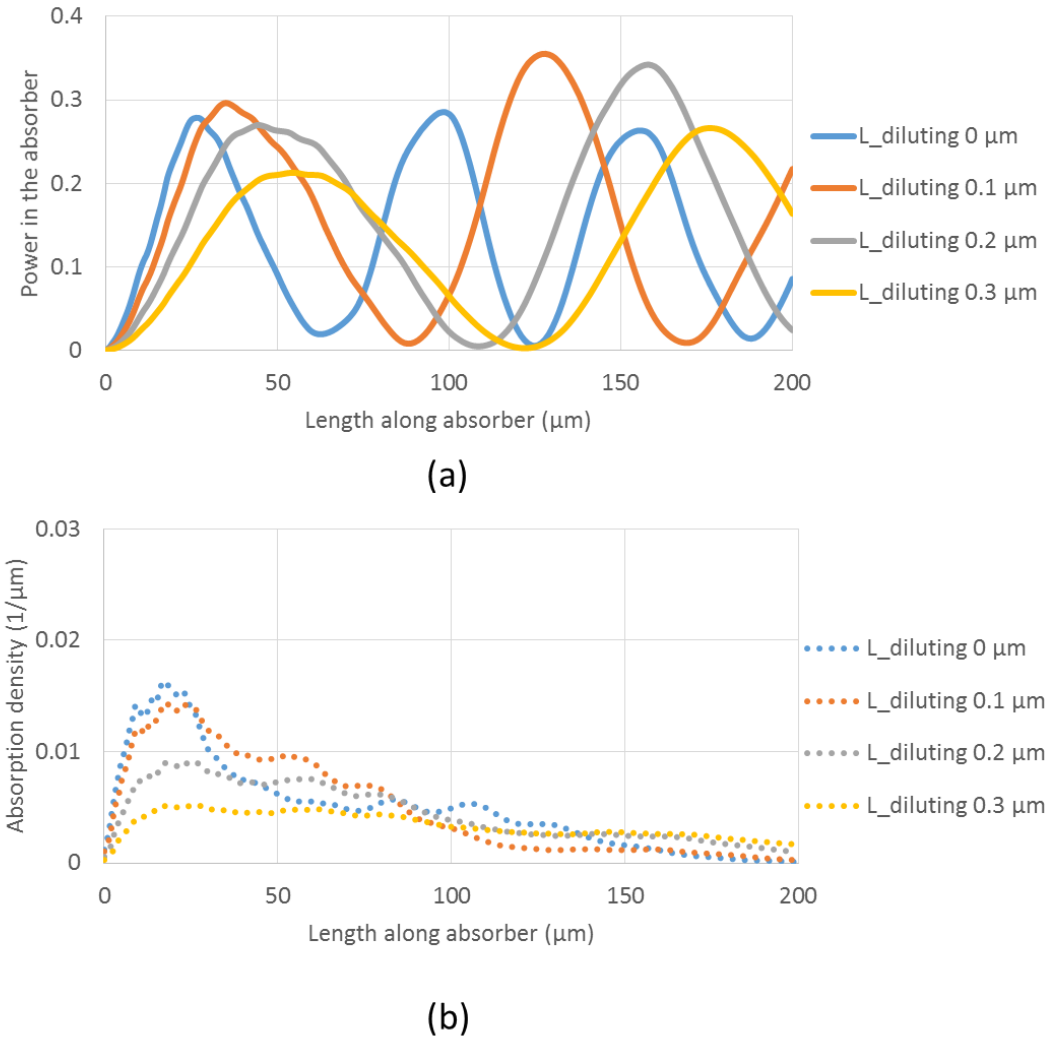

Figure 2-33 the distribution of power in the absorber (a) and absorption density (b) in traditional WGPD with different thickness of InP diluting layer, L_diluting. The absorption is turned off in the simulation of (a). The waveguide structure and layer structure are already described in Figure 2-13. The absorber width is fixed at 2 μm. The waveguide width is fixed at 5 μm.

As have discussed above, the design of high power traditional WGPD requires the excitation reduction of the large gamma supermode, as well as the increase of the distance of the peak absorption position from the absorber front end, in order to improve the absorption uniformity in the forward section. The tradeoff between the absorption uniformity and the bandwidth generally

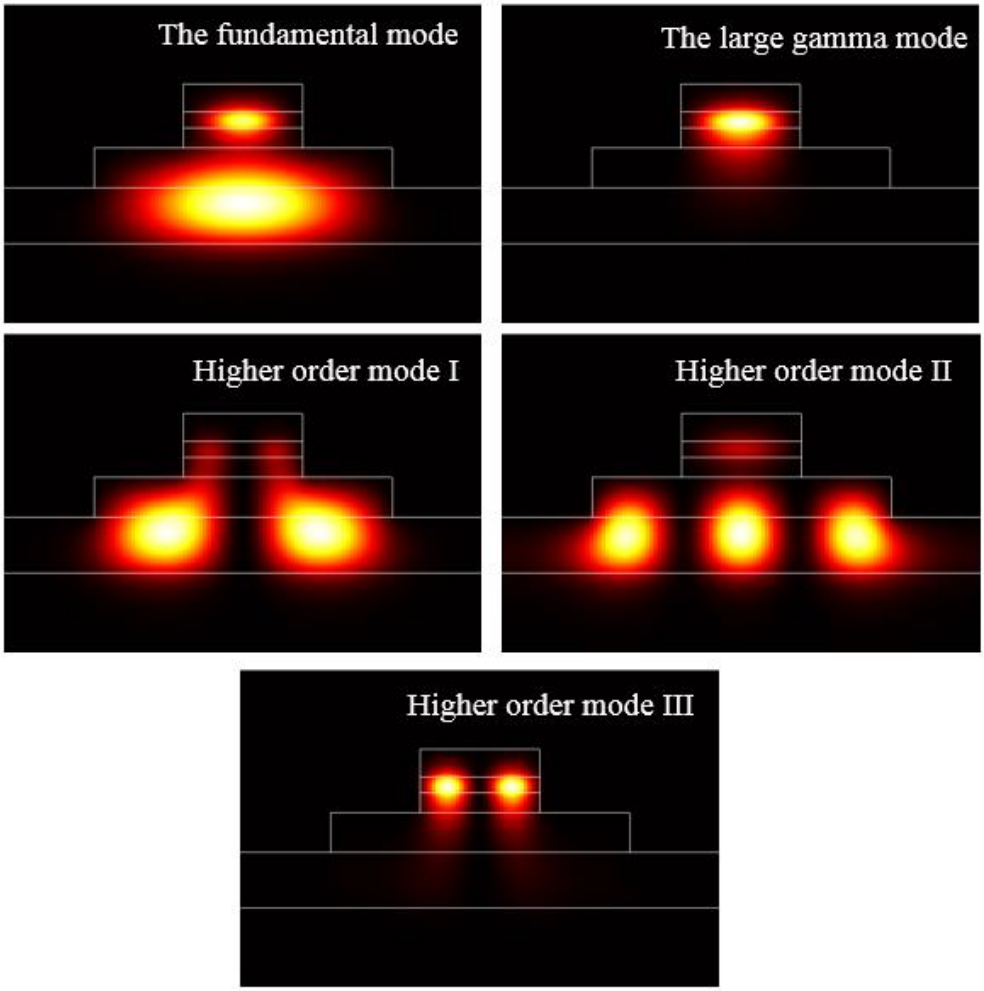

Figure 2-34 The plots of five supermodes in the traditional WGPD shown in Figure 2-13.

exists in the traditional WGPD. As the reduction of the large gamma supermode excitation usually comes along with the reduction of the absorption efficiency, it relies on the absorption in the rear section to keep large absorption efficiency. Therefore, in the next section, how to improve the absorption uniformity in the rear section in a traditional WGPD is studied with supermode analysis.

2.10.4 Higher Order Supermodes and The Absorption Uniformity

Two commonly excited supermodes in a traditional WGPD have been discussed in section 2.10.1, which are the fundamental supermode and the large gamma supermode. As shown in Figure 2-19, in the x direction, the two modes' shape are close to that of the incident radiation pattern,

with only one field peak laterally centered. In the y direction, both supermodes have two field peaks, which locate at the absorber and the waveguide, separately. Higher order supermodes, which have radiation patterns with more variations in the x or y direction than the 0^{th} and 1^{st} supermodes, might also be generated and affect the absorption distribution in a traditional WGPD. Just like the fundamental mode and the large gamma mode, those higher order supermodes will also have power primarily confined in either the absorber or the waveguide, and will be either mode type A or mode type B.

First, it has to be identified what kind of supermodes are beneficial to the absorption uniformity in a traditional WGPD. The following discussion starts from the two-supermode traditional WGPD already shown in section 2.9.2, in which it also has several higher orders supermodes but with very negligible excitation coefficients. In the following simulation, several higher orders modes are selected one at a time, with certain excitation coefficient assumed. The existing two supermodes are kept the same. The absorption profile of this three-supermode WGPD is plotted by using the Equation 2.18. The sum of power of the three modes is normalized to be unity. Three higher orders modes are selected for this simulation, as shown in Figure 2-34. The first one is labeled as mode I, whose electric field in the waveguide in the x direction has one interception point with the x axis (E_x=0). The second one is labeled as mode II, whose electric field in the waveguide in the x direction has two interception points with the x axis (E_x=0). The third one is a type B mode, its field distribution is similar with that of the large gamma supermode, but its electric field in the waveguide in the x direction has one interception point with the x axis (E_x=0). This mode is labeled as mode III. Comparing to other higher order modes, those three higher order modes usually have higher excitation coefficient than other higher order modes, as their radiation patterns in the x and y direction have less variation and will have relatively larger field overlap with the incident radiation pattern. The plots of the three higher order modes, as well as the fundamental

Table 2-7 The real and imaginary part of the effective refractive index n_{eff} of the five supermodes in Figure 2-29, as well as their confinement factor gamma and characteristic attenuation length La at 1.55 μm wavelength .

SUPERMODE	Re（n_{eff}）	Im（n_{eff}）	Gamma	L_a (μm)
The fundamental mode	3.3055	0.0018	0.019	68.6
The large gamma mode	3.2805	0.0390	0.413	3.16
The higher order mode I	3.2972	0.0001	0.001	1234
The higher order mode II	3.2943	0.0010	0.011	123
The higher order mode III	3.2570	0.0324	0.330	3.81

mode and the large gamma mode, are shown in Figure 2-29. The effective refractive index n_{eff}, as well as their characteristic attenuation length La, are shown in Table 2-7. In the x direction, the higher order mode I has very weak power at the center of the waveguide, while the higher order mode II has one power peak at the center of the waveguide. As the absorber sits on top of the center of the waveguide, this power distribution difference in the waveguide results in large gamma difference between the two modes, although both modes are in the same mode group A. While the higher order mode I's gamma is about one tenth of that of the fundamental mode, the higher order mode II's gamma is similar with that of the fundamental mode. The higher order mode III, which belongs to the mode group B, has similar gamma with the large gamma mode. By assuming certain excitation of one of the three higher order modes in the two-mode traditional WGPD shown in section 2.9.2, the effects of the three higher order modes on the absorption distribution can be observed from the power distribution in the absorber plotted based on Equation 2.18, as shown in Figure 2-30.

It is impractical to change the power distribution in the rear section of a traditional WGPD by adding higher order mode I. As pointed out in Equation 2.18, the power in the absorber of a traditional WGPD can be separated into power from individual mode and power from interference

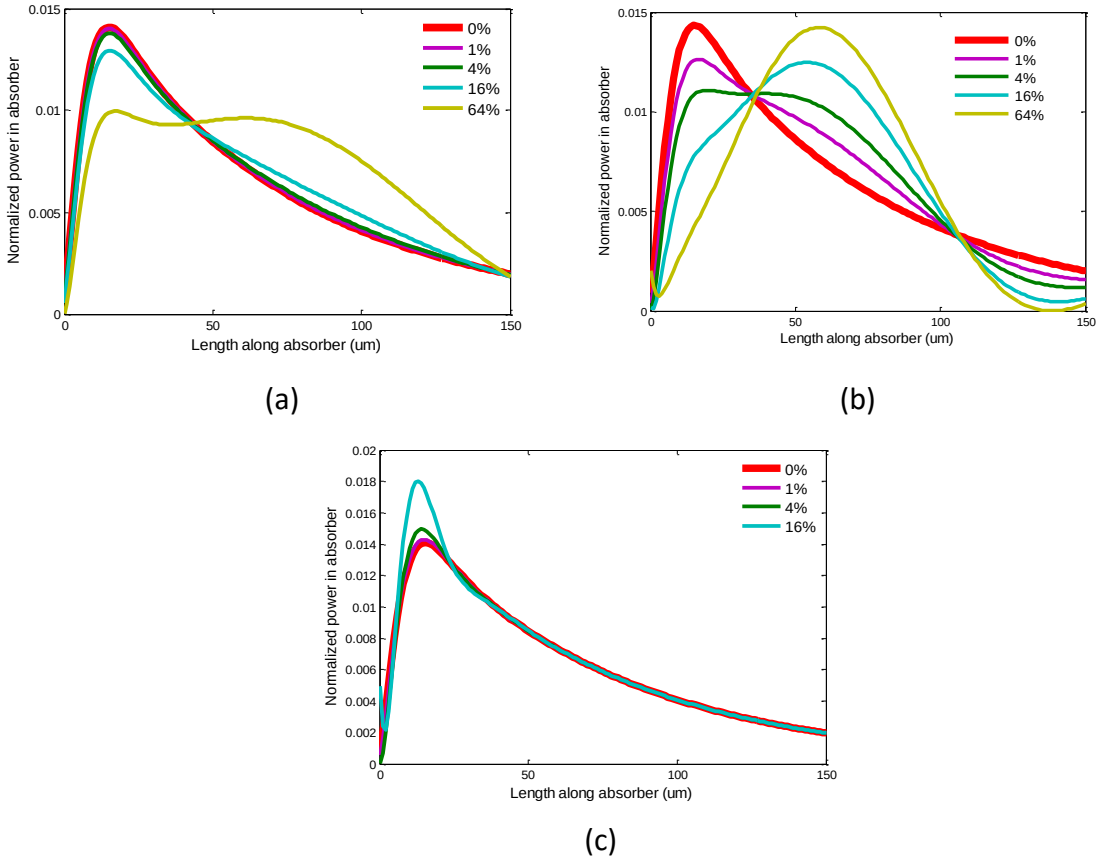

Figure 2-35 The profile of power in the absorber with the addition of higher order mode I (a), mode II (b), and mode III (c). Each simulation considers adding higher order mode accounting for different percentage of the total power. The excitation coefficient of the fundamental mode and the large gamma mode is fixed at 0.9 and 0.15, respectively. The simulated power is normalized by the total power of the three modes.

between two modes, and the contribution from two modes' interference is proportional to the field overlap of the two modes in the absorber. As the field overlap between two modes in the absorber is proportionally to the product of the gamma of the two modes, the higher order mode I, which has much smaller gamma than the fundamental mode, will have small field overlap with the fundamental mode in the absorber. Therefore, the term in Equation 2.18 representing the interference between the fundamental mode and the higher order mode I will have very small magnitude, and will not affect the power in the absorber too much. This is in good agreement with the simulation results in Figure 2-35 (a), in which the light addition of higher order mode I does

not affect the absorption significantly in the rear section of the absorber. There is only one exception case, which is when the higher order mode I excitation coefficient is so high that its interference with the fundamental mode will be very strong, and will compensate the small field overlap between them in the absorber. However, in a realistic traditional WGPD, such large excitation of the higher order mode I is not likely to occur.

The addition of higher order mode III does not change the power distribution in the rear section of a traditional WGPD either. As pointed out in section 2.11.1, in the rear section of a traditional two-mode WGPD, the power of the large gamma mode and the interference between the two modes attenuates a lot. Because of that, the power in the waveguide structure is mainly the power in the fundamental mode, and the absorption distribution in the WGPD follows the exponential decay of the fundamental mode power. Therefore, adding the higher order mode III with large gamma will not change the power distribution in the rear section, which can be observed from the simulation results in Figure 2-35 (c).

The addition of higher order mode II has significant effect on the power distribution in the rear section of a traditional WGPD by interfering with the fundamental mode, as shown in Figure 2-35 (b), in which even very slight addition of the higher order mode II will have visible effect on changing the power distribution in the rear section. This is attributed to two features of the higher order mode II. First, the higher order mode II belongs to the mode group A, and hence has small gamma. While the modes from the mode group B attenuates quickly, the modes from mode group A attenuates much slower and co-exist with the fundamental mode in the rear section. Second, the higher order mode II has similar gamma with the fundamental mode. As the field overlap between two modes in the absorber is proportionally to the product of the gamma of the two modes, comparing to the higher order mode I from the same mode group A, the higher order mode II has larger field overlap with the fundamental mode in the absorber, and hence stronger interference effect with the fundamental mode. In a traditional WGPD, the higher order mode II, as well as the

input radiation pattern and the fundamental mode, have power peak at the center of the waveguide structure in the x direction and simple filed pattern elsewhere. When compares to other higher order modes, this not only results in stronger interference with the fundamental modes, but also results in larger excitation of the higher order mode II. For this reason, the higher order mode II will be the major higher order mode that affect the absorption distribution in a traditional WGPD. If not specifically mentioned, the higher order mode mentioned in the following sections will be the higher order mode II, and will be named the preferred higher order mode.

Therefore, the higher order modes that will be able to help improve the absorption uniformity of a traditional WGPD are the type A modes that has similar confinement factor with the fundamental mode. Those are the preferred higher order supermodes in the discussion of absorption uniformity of the traditional WGPD. When there are more than one higher order modes meets the specifications for the preferred higher order mode, how the absorption uniformity differs from the case with only one preferred higher order mode, will be discussed in the next section.

In the above discussion, it assumes certain excitation of the higher order mode in a two-mode traditional WGPD, without discussing the physical waveguide design that can support the higher order mode. In the following section, three-mode traditional WGPD designs with the higher order mode excited will be studied; its high power performance will be discussed via simulation and experiments.

2.10.5 The absorption uniformity in the rear section and the preferred higher order mode

In a two-mode traditional WGPD, the preferred higher order mode can be generated by the adjustment of several parameters of the waveguide. For WGPD designed for high power applications, some of the adjustments are preferred, while some are not. In the last section, it is pointed out that the preferred higher order mode, which is mode type A and has similar confinement

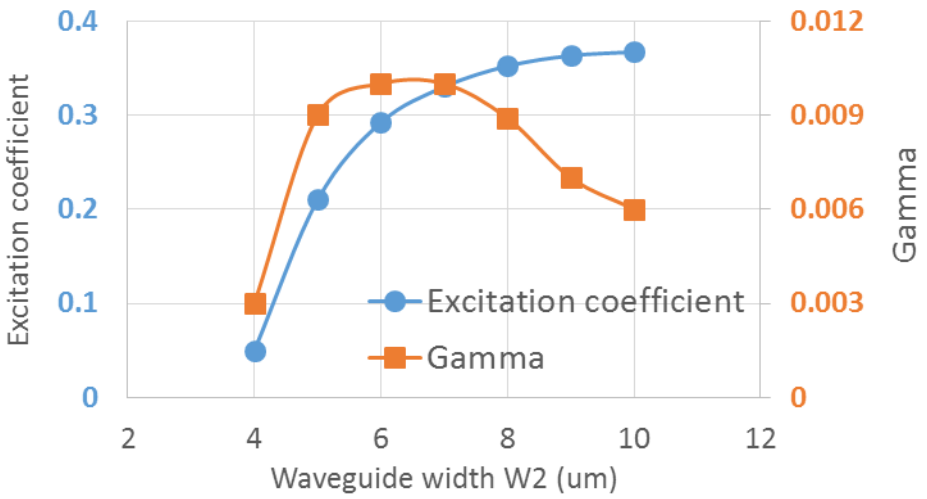

Figure 2-36 The excitation coefficient and gamma of the preferred higher order mode in the traditional WGPD in Figure 2-13. The absorber width W1 is fixed at 2 μm, and the waveguide width W2 varies from 4 μm to 10 μm.

factor with the fundamental mode, helps improve the absorption uniformity in a traditional WGPD. In this section, the goal of waveguide design is to enhance the excitation of the preferred higher order mode, while avoid the excitation of other higher order mode which cannot contribute to or degrade the absorption uniformity.

Theoretically, in order to excite the preferred higher order mode in a traditional WGPD, one can either adjust the incident field, or adjust the refractive index and/or the dimension of the waveguide in the x direction, as the desired higher order mode has field variations in the waveguide in the x direction. In order to focus on the waveguide structure design, the adjustment of the incident field will not be discussed in this study. Adjusting the refractive index of the waveguide is also not considered here, as it not only change the field distribution in the x direction, it may also cause higher order variations of the field pattern in the waveguide in the y direction, which will make the control of power distribution become very complex and difficult. Therefore, it is preferred here to control the preferred higher order mode by adjust the waveguide dimension in the x direction.

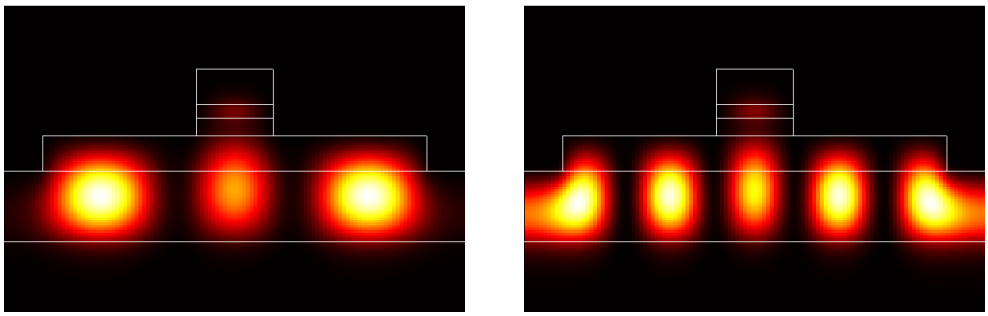

Figure 2-37 The preferred higher order supermode (left) and a second higher order supermode (right) of the WGPD discussed in Figure 2-36. The waveguide width W2 is 10 μm.

In a traditional WGPD, the generation of the preferred higher order mode has to do with the waveguide width. For a given ridge waveguide, certain ridge width is required to generate a higher order mode. When the ridge is too wide, other higher order mode will also be generated. For the traditional WGPD, which has an absorber mesa added on top a ridge waveguide, it is expected to see similar phenomena of higher order mode generation, as the absorber can be treated as only a perturbation to the ridge waveguide. For the traditional WGPD in Figure 2-13, when the absorber width W1 is fixed at 2 μm, and the waveguide width W2 varies between 4 μm and 10 μm, the excitation coefficient and gamma of the preferred higher order mode are simulated, with the results shown in Figure 2-36. Generally speaking, with the widening of the waveguide from 4 μm to 10 μm, first the excitation coefficient of the preferred higher order mode increases very fast, and then the increase slows down as the waveguide get wider. For the gamma of the higher order mode, when the waveguide is narrowed down from 10 μm, the gamma increases first, reaches its peak value at waveguide width of 6 to 7 μm, and drops quickly as the waveguide width keeps reducing. In this sense, for the WGPD shown in Figure 2-13, when the waveguide width is in the range between 6 μm and 8 μm, the preferred higher order mode has large excitation coefficient and large gamma, both of which provide strong interference with the fundamental mode.

The reason that very wide or very narrow waveguide is not good for generating the preferred higher order mode is different, and can be seen from the simulation of the supermode

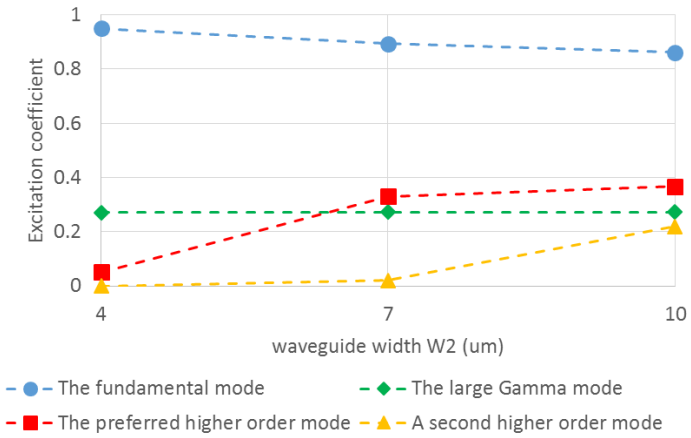

Figure 2-38 The excitation coefficient of the first four dominant modes in three WGPDs shown in Figure 2-31. The waveguide width of these three WGPDs is 4 μm, 7 μm, and 10 μm, respectively.

excitation. The above case is used for the discussion. When the waveguide width is 4 μm, the waveguide structure is too narrow to support the preferred higher order mode well. Therefore, it is not surprising to see in Figure 2-36 that the excitation coefficient and the gamma of the preferred higher order mode is small when the waveguide is only 4 μm wide. When the waveguide width is 10 μm, as shown in Figure 2-37, the waveguide structure is wide enough to support another higher order mode, whose excitation coefficient is comparable to that of the preferred higher order mode. In this case, the power goes into the preferred higher order mode drops, which corresponds to the reduction of excitation coefficient shown in Figure 2-36.

For the three-mode traditional WGPD studied above, the power distribution in the absorber is simulated in WGPD with waveguide width at 4 μm, 7 μm, and 10 um. Based on the above discussion, the three WGPDs have very different excitation of the preferred higher order mode. Figure 2-38 shows the excitation coefficient of the first four dominant modes in the three WGPDs, in which the fundamental mode and the large gamma mode shows only slight change of the excitation coefficient. Meanwhile, when W2 is 4 μm, the excitation of the higher order mode is

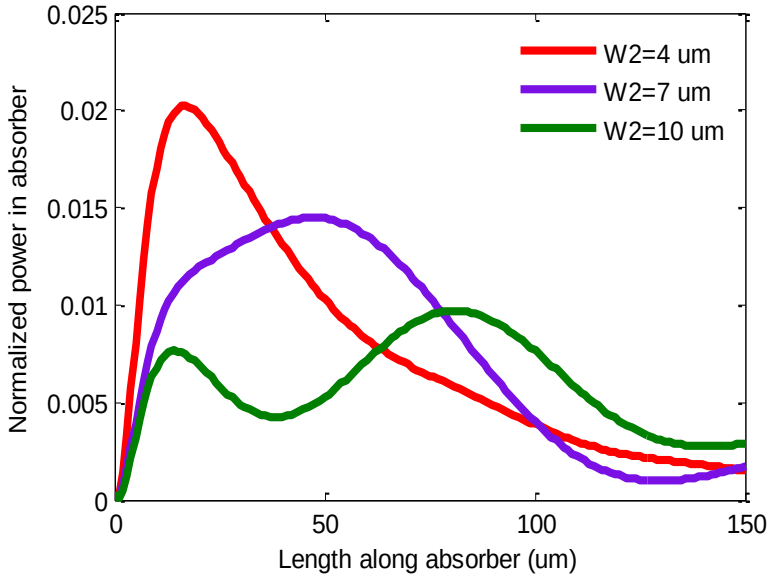

Figure 2-39 The simulated absorption profile of the three WGPDs shown in Figure 2-33.

very weak, and it is the typical case of two-mode traditional WGPD. When W2 is 7 μm, the excitation of the preferred higher order mode becomes large, and it is a case of three-mode traditional WGPD, with the third mode being the preferred higher order mode. When W2 is 10 μm, in addition to the preferred higher order mode, a second higher order mode, which is already shown in Figure 2-38, is also largely excited. This is one of the four-mode traditional WGPD cases. The three traditional WGPDs, which have different number of supermodes excitation, have very different power distribution profile, as shown in Figure 2-39. In the longitudinal direction, in the range of 10 μm to 100 μm from the front end of the absorber, the power distribution in the absorber of the three WGPDs differs a lot from each other. When it is about 10 μm away from the front end of the absorber, there is a turning point in the power distribution profile, which is due to the interference between the fundamental mode and the large gamma mode. This turning point becomes the only peak when W2 is 4 μm, which is a typical feature of the two-mode traditional WGPD, because of the degradation of the interference effect between the two dominant modes.

When W2 is 7 μm, the joining of the preferred higher order mode extends the interference between itself and the fundamental mode substantially, and the power density peaked at about 55 μm. When W2 is increased from7 μm to 10 μm, the absorption efficiency is reduced from 0.82 to 0.64, more absorption density variation exists, and the absorption uniformity degrades. On the one hand, as discussed in section 2.10.1, the absorption efficiency largely depends on the L_{a0}, which is the characteristic attenuation coefficient of the fundamental supermode. Therefore, the reduction of the absorption efficiency can be explained by the increase of L_{a0}, as shown in Figure 2-23. On the other hand, Equation 2.26 describes a local absorption peak due to the interference between the fundamental supermode and the large gamma supermode. In fact, any two-mode interference will generate a local absorption peak. For different interferences, when the effective index differences of the two modes are not the same, the related local absorption peak and amplitude will not be the same, as shown in Equation 2.23 and Equation 2.26. Therefore, for the case with a second higher order supermode, it is easy to generates more absorption variation in the z direction, due to the existence of more interferences. The absorption efficiency reduction and absorption uniformity degradation, which are due to the appearance of multiple preferred higher order modes, can be alleviated by approach such as tapering the waveguide.

In summary, the widening of the waveguide effectively increase the excitation of the preferred higher order mode. With the appearance of the first preferred higher order mode, the absorption uniformity in the rear section improves, due to the existence of the preferred higher order mode interference term. With the appearance of the second or more preferred higher order mode, the co-existence of various higher order mode interference term in the rear section will cause additional absorption variation. Besides that, the appearance of the second or more preferred higher order mode accompanies the reduction of the absorption efficiency. In this case, in the next section, the design of 40 GHz high power traditional WGPD focuses on the waveguide structure with only one preferred higher order mode excited.

2.10.6 The Analysis, Design, and Demonstration of High Power traditional WGPD by Supermode Analysis

In a traditional WGPD, with a given incident optical radiation pattern, the excitation of the large gamma supermode and the preferred higher order supermode relates to the waveguide dimension and the layer structure, which have been briefly discussed in section 2.10.3 and 2.10.5. All the previous discussions are based on the theoretically analysis and simulation. In this section, experimental study is used to work with the previous analysis and design work, in order to verify the supermode analysis results, as well as demonstrate a high power traditional WGPD. The experimental work studies several traditional WGPD with variations of the waveguide dimensions and the layer structure, which include the variation of the absorber width W1, the waveguide width W2, and the absorber thickness. The adjustment of these parameters, which are widely used in many groups in the design of the traditional WGPD, are also adapted in the experimental study in our group. In this section, instead of just providing a recipe of the waveguide dimension and the layer structure for making a high power traditional WGPD, we focus on study how these waveguide parameters' adjustment affects the absorption profile, via changing the supemode excitation. From there, a high power traditional WGPD is designed and demonstrated by using the supermode analysis. Moreover, how to achieve further improvement in the demonstrated WGPD is proposed by using supermode analysis.

The supermodes excitation in a traditional WGPD relates to three items: the layer structure, the waveguide dimension, and the incident radiation pattern. In this section, the discussion starts from a traditional WGPD build on a given layer structure, as shown in Figure 2-13. The incident radiation pattern for the active waveguide structure is assumed to be the fundamental mode of the passive input waveguide. In this case, we focus on discussing how the adjustments of the waveguide width and the absorber width affect the absorption profile, via affecting the excitation of

Table 2-8 The excitation coefficient χ1 of the large Γ mode at various waveguide width W2. The absorber width W1 is fixed at 2 μm.

W2 (μm)	W1/W2	χ_0	χ_1	χ_2
4	0.5	0.953	0.258	0.066
6	0.333	0.965	0.186	0.137
8	0.25	0.959	0.165	0.191

Table 2-9 The excitation coefficient χ_1 of the large Γ mode at various absorber width W1. The waveguide width W2 is fixed at 8 μm.

W1 (μm)	W1/W2	χ_0	χ_1	χ_2
2	0.25	0.964	0.165	0.191
3	0.375	0.940	0.272	0.176
4	0.5	0.928	0.318	0.163

supermodes. Two groups of traditional WGPDs are investigated by both simulation and experiment, in one group the absorber width W1 is varied and the waveguide width W2 is fixed at 8 μm, in the other case the waveguide width W2 is varied and the absorber width W1 is fixed at 2 μm. The study of these two groups of devices shows that the variation of W1 and W2 have similarities and differences on affecting the absorption profile.

First, both groups of devices show the same change of absorption uniformity in the forward section, with the variation of the absorber to waveguide width ratio W1/W2. When W1/W2 is very small, the confinement factor of the waveguide, as well as the confinement factor of the fundamental supermode Γ_0, will become very small. This corresponds to small excitation of the large gamma mode and improved absorption uniformity in the forward section, as discussed in section 2.10.3. The simulation of excitation coefficient of the large gamma supermode and the

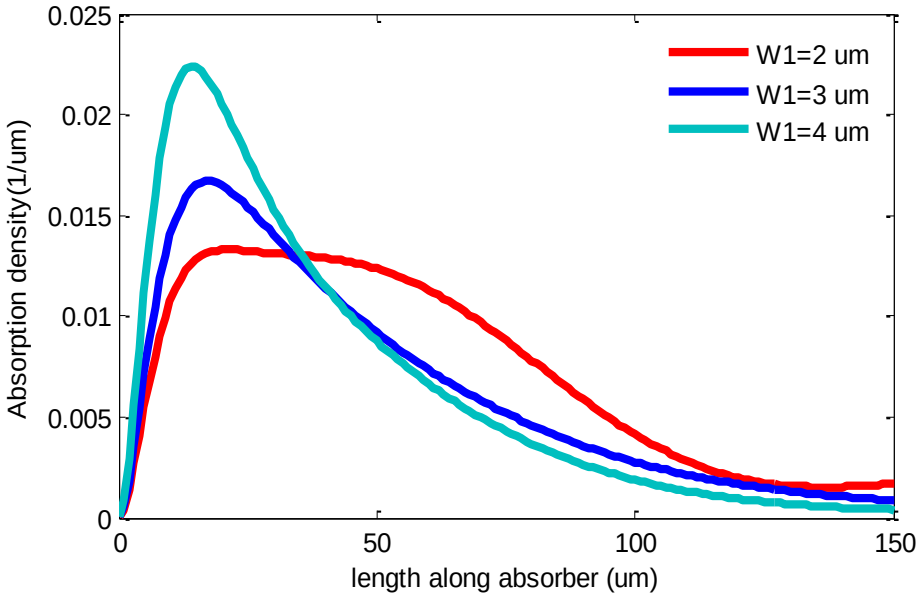

(a)

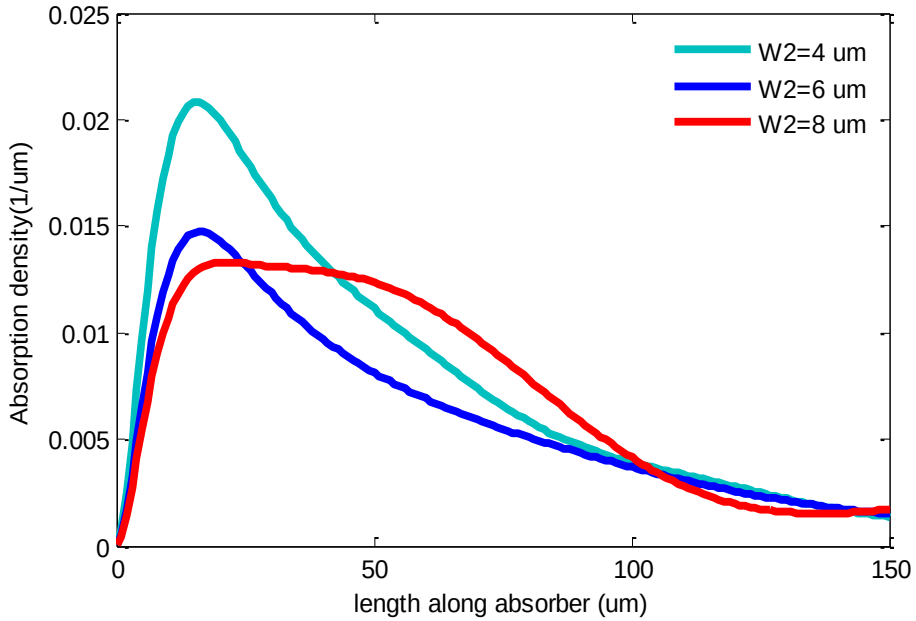

(b)

Figure 2-40 simulated WGPD absorption profile with varied absorber width W1 (W2 is fixed at 8 um) (a), and waveguide width W2 (W1 is fixed at 2 um) (b).

corresponding absorption profile at various W1/W2 agree well with the above prediction. The Fimmwave simulated excitation coefficient of large Γ mode χ_1 is shown in Table 2-8 and Table 2-9, and the Beamprop simulated absorption profile is shown in Figure 2-40. With the widening of the waveguide or the narrowing of the absorber, in the above cases, the simulated excitation coefficient of the large gamma supermode becomes smaller, so does the absorption peak magnitude in the forward section.

Second, both groups of devices show different changes of absorption uniformity in the rear section, with the variation of the absorber to waveguide width ratio W1/W2. As shown in Figure 2-40, the absorption density difference in the rear section is much smaller with the widening of the absorber than with the narrowing of the waveguide. Moreover, χ_2, which is the excitation coefficient of the preferred higher order supermode, also shows smaller change with the widening of the absorber than with the narrowing of the waveguide. The correlation between the absorption uniformity in the rear section and the excitation coefficient of the preferred higher order supermode has been discussed in the last section, which can well explain the phenomena described above. Among all the above simulated cases, when the absorber width is 2 μm, and the waveguide width is 8 μm, the absorption uniformity in the forward section and in the rear section is the best, and is expected to provide the best power handling capability in the experimental test.

The above traditional WGPDs is experimentally presented, with the measured results verifying the discussed waveguide structure effects on the device's power handling capability. In the tested structures, a 3 μm wide passive input waveguide transfers the incident optical radiation into its 0^{th} order mode, which then gradually expands in lateral size in the x direction as it propagates towards the absorber. The tapering of waveguide after the straight input waveguide has to be gentle enough, so that no additional higher order modes are excited and the optical wave propagates with low loss. The epi-layer structure is already shown in Figure 2-13 (b). The devices

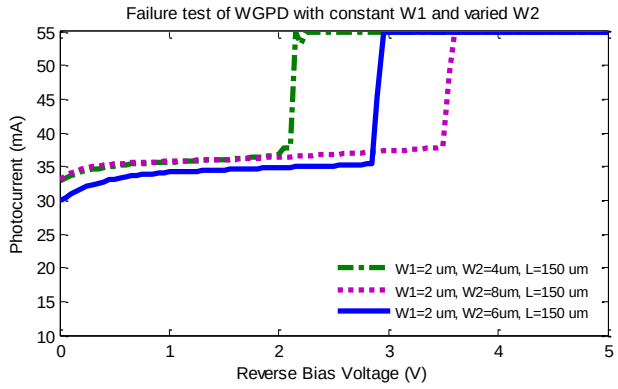

(a)

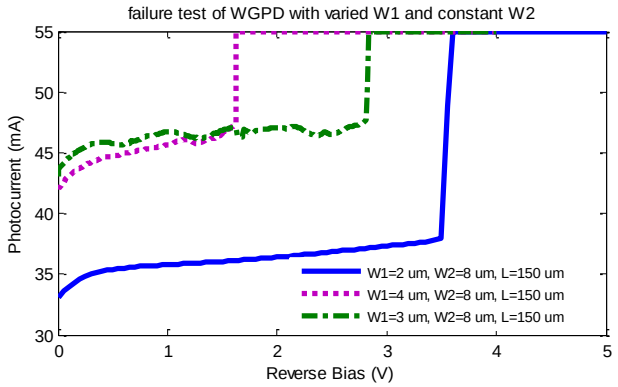

(b)

Figure 2-41 The experimental DC power testing data of WGPD devices with varied waveguide width (a) and varied absorber width (b).

are tested at similar DC photocurrent levels, with the DC bias voltage ramping up. The device-under-test (DUT) is connected to a semiconductor parameter analyzer, which changes the DC bias voltage of the DUT in a sweeping mode. The power handling capability of the DUT is evaluated by the photocurrent bias voltage product at the failure point. The tested devices have similar absorption efficiency at around 0.85. Therefore, the larger the photocurrent bias voltage product is, the higher the device power handling capability will be. From the experimental results shown in Figure 2-41, the widening of the waveguide and the narrowing of the absorber improve the device's power handling capability. This is in good agreement with the conclusion made by the analysis and simulation that smaller W1/W2 ratio corresponds to smaller absorption in the forward section of

the waveguide and higher power handling capability. However, the absorption difference in the rear section between devices is hard to tell from the tested results for two possible reasons. First, the power handling capability in all the devices is dominated by the absorption in the forward section, and the absorption difference in the rear section only contributes to the absorption efficiency. Second, although the absorption is very different in the rear section, the devices discussed here are so long that the actual absorption efficiency will have very small difference.

Although narrow absorber and wide waveguide in a traditional WGPD help improve the power handling capability, the actual practice has several limitations. First, it is limited by the absorption efficiency. If the reduced absorption at the front end cannot be compensated by the absorption increase due to the longer absorber, the total absorption efficiency will drop. Second, the actual absorber width and waveguide width have their own limitations. The absorber is usually wider than 1.5 μm, in order to reduce the ridge sidewall optical scattering induced optical loss, as well as the fabrication difficulty. The waveguide width is usually less than 10 μm. As shown in the last section, very wide waveguide will result in generation of many higher order modes in the waveguide, and it is very likely to degrade the absorption uniformity and power handling capability.

In the following, guided by the supermode analysis, a design of high power traditional WGPD is demonstrated, which is comprehensively compared to other reported traditional WGPD and the ideal WGPD.

The waveguide structure and layer structure of the high power traditional WGPD for this demonstration is shown in Figure 2-42. The demonstrated WGPD have active area of about 300 μm^2, which is expected to have ~45 GHz RC bandwidth. The waveguide and absorber width are well optimized, in order to increase the absorption uniformity in the forward section and in the rear section. As shown in Figure 2-42, the waveguide structure includes tapering of absorber and

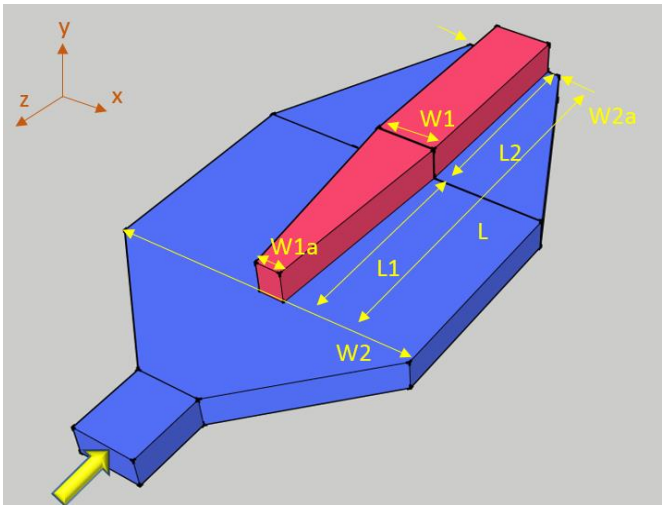

(a)

Layer	Material	Thickness (um)	Index	Type
P-Contact Cap	InGaAs	0.05	3.56	P++
Diffusion Block	InP	0.229	3.17	P+
Absorber	InGaAs	0.2	3.56	P+
Waveguide/MMI	InGaAsP	0.4	3.33	U.I.D
Waveguide/MMI	InGaAsP	0.70	3.33	N
N-Plateau	InGaAsP	0.80	3.33	N+
Substrate	InP			S.I.

absorber

cap

wave guide

(b)

Figure 2-42 The waveguide structure (a) and the MUTC2 layer structure for the demonstration of traditional WGPD by supermode analysis. W1 and W2 is the width of straight absorber and waveguide, W1a is the starting width of the tapered absorber, W2a is the end width of the tapered waveguide. The absorber total length is L, the tapered absorber length is L1, and the straight absorber length is L2.

waveguide, which creates a gentle increase of the ratio of absorber width to waveguide width W1/W2. On the one hand, according to the discussion in section 2.10.3, small W1/W2 at the front end helps reduce the excitation of the large gamma supermode, and hence the reduction of the absorption density in the forward section. Away from the front end of the absorber, the increased W1/W2 of the tapered waveguide structure increases the absorption density, and contributes to

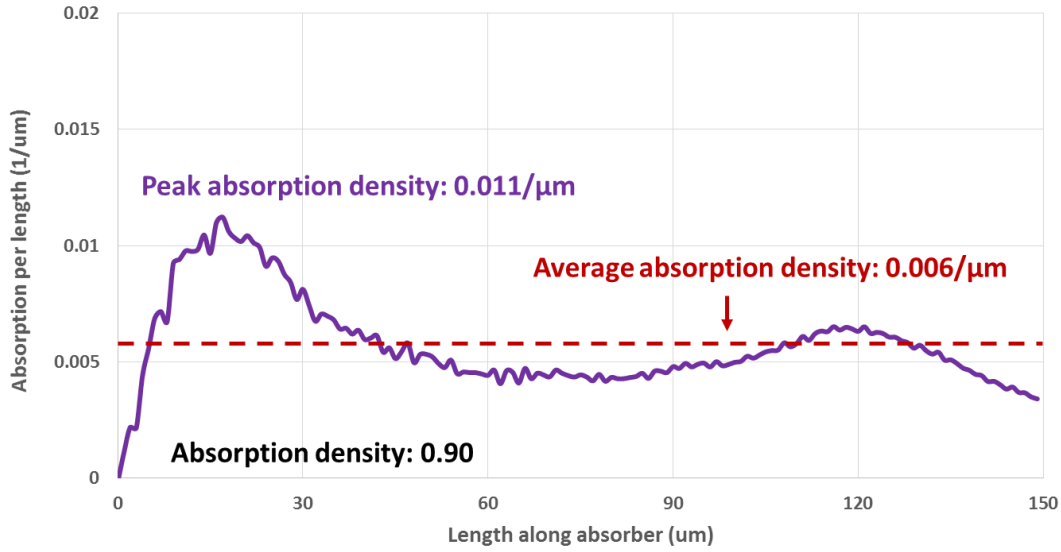

Figure 2-43 The simulated absorption profile of the traditional WGPD for demonstration. The waveguide structure and layer structure are shown in Figure 2-42. The absorber length L is 150 μm. The values of other devices parameters are: L1=75 μm, L2=75 μm, W1=2 μm, W2=8 μm, W1a=1.5 μm, W2a=3 μm.

more uniformly distributed absorption. On the other hand, as discussed in the section 2.10.5, the traditional WGPD with 8 μm wide waveguide has large excitation of the preferred higher order supermode, and hence better absorption uniformity in the rear section.

The detailed description of the demonstrated WGPD, as well as its simulated absorption profile by Beamprop, are shown in Figure 2-43. For the demonstrated WGPD, the simulated absorption density peak-to-average ratio, which is used to characterize the absorption uniformity and relates to the WGPD's power handling capability, is 1.8. This number is usually higher in the reported traditional WGPD, for example, it is 2.2 in [3], and is 2.0 in [4]. This demonstrated WGPD is tested under different optical power level and dc bias voltage. The results are shown in Figure 2-44, in which various lines represent tests at various reverse dc bias voltage. The slope of the line represents the responsivity. When the reverse dc bias voltage is only 1 V, as the optical power increases, the slope gradually reduces, which is due to space charge effect [16]. As the reverse dc

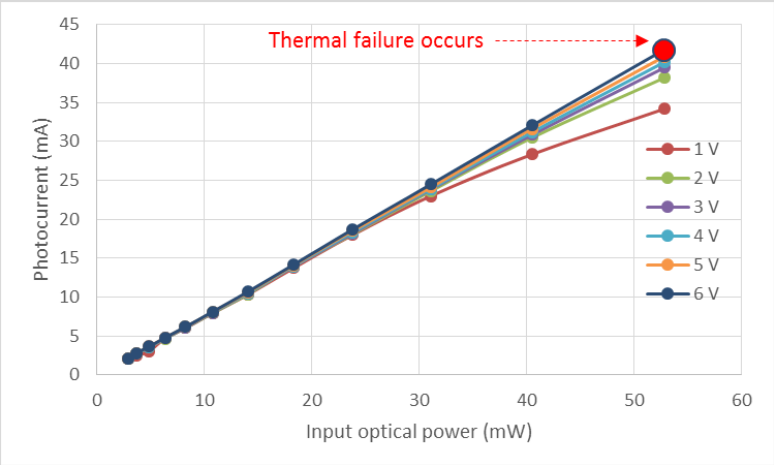

Figure 2-44 The recorded photocurrent generates in the demonstrated WGPD, under different input dc optical power at 1550 nm, which is repeated at dc bias voltage from 1 V to 6 V. The WGPD used is the same with the one shown in Figure 2-31. When the WGPD is biased at 6 V, thermal failure occurs when the input optical power is increased from 41 mW.

bias voltage increases, the responsivity stabilizes at 0.78 A/W. The measured responsivity corresponds to absorption efficiency of 0.62 at 1.55 μm wavelength, which is a little smaller than the simulated absorption efficiency of 0.85. There are several reason accounts for the difference between simulated absorption efficiency and measured absorption efficiency, such as coupling facet reflection, various optical losses in the responsivity measurement, waveguide parameters difference between the simulated WGPD and tested WGPD, and simulation inaccuracy. When the optical power is very high, the high bias voltage causes thermal failure of the WGPD, at which the device becomes shorted. Before thermal failure happens, the demonstrated WGPD generated 32 mA dc photocurrent at -6 V dc bias voltage (the actual voltage drop across the device junction might be a little bit lower), which corresponds to average dissipated electrical power density of about 0.60 mW/μm^2. The power handling capability of the demonstrated WGPD is compared to the other traditional WGPDs, SNPDs, and the ideal WGPD, as shown in Figure 2-45. Based on the collected data, the maximum average power density of the demonstrated WGPDs is larger than that

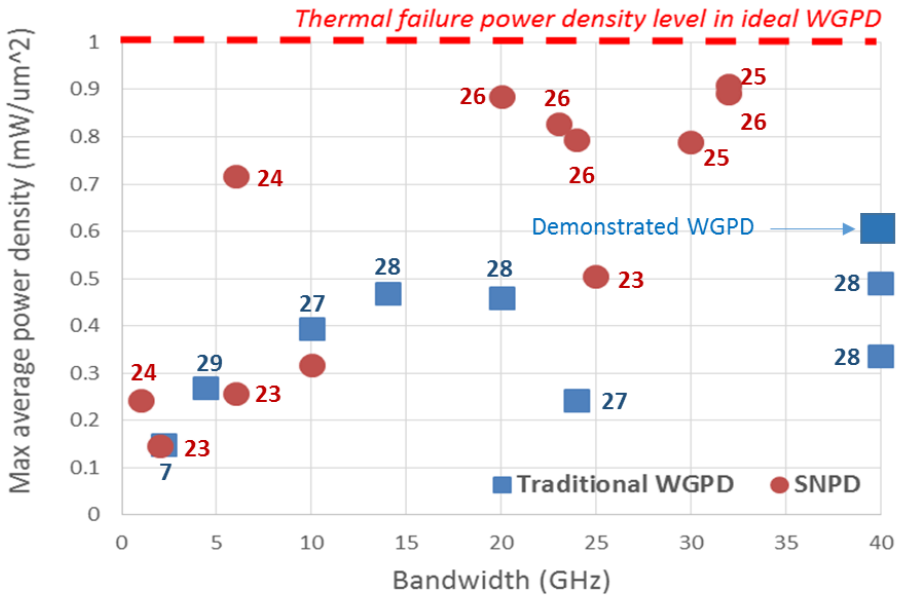

Figure 2-45 The comparison of maximum average dissipated electric power density of the demonstrated WGPD with that of the other traditional WGPD, SNPD, and the ideal WGPD. The bandwidth of the demonstrated WGPD is estimated by using the theoretical capacitance, which is calculated by using 300 μm^2 active area size.

of the other traditional WGPD, which is due to the optimized waveguide design based on the MUTC2 layer structure.

However, the maximum average power density of the demonstrated WGPD is only about ½ of that in an ideal WGPD, which is attributed to several reasons. First, the non-uniform absorption distribution still exists in the demonstrated WGPD, and causes the reduction of power handling capability. According to the discussion in section 2.7.7, at the same total dissipated power, when the power handling capability of a WGPD is limited by the peak local absorption density, the increase of the absorption peak-to-average ratio reduces the power handling capability of a WGPD proportionally from that of an ideal WGPD. Therefore, as the simulated absorption peak-to-average ratio in the demonstrated WGPD is 1.8, theoretically the maximum average power density in the demonstrated WGPD should drop to 0.55 $mW/\mu m^2$, which is close to the measured value 0.60

$mW/\mu m^2$. Second, the heat dissipation condition in the demonstrated WGPD is not ideal, which may result in additional heat accumulation, and account for additional degradation of the power handling capability in the demonstrated WGPD.

In summary, the design of high power traditional WGPD based on the MUTC2 layer structure is analyzed and demonstrated in this section, based on the supermode. The width of the waveguide and the absorber are selected for the reduction of large gamma supermode excitation and the enhancement of the preferred higher order supermode excitation. Moreover, the tapering of the absorber and the waveguide provide more freedom for better absorption uniformity and larger absorption efficiency. The experimental study of the demonstrated traditional WGPD shows better power handling capability than many reported results, which in agree with the smaller absorption peak-to-average ratio in the demonstrated WGPD. However, the demonstrated WGPD still shows smaller power handling capability than an ideal WGPD, which implies the existence of the non-uniform absorption distribution that needs to be further improved.

2.10.7 Further suggestions for improving the power handling capability of the demonstrated WGPD

As the high absorption in the forward section is still one of the major factors that limit the demonstrated WGPD from handling optical power close to an ideal WGPD, it is essential to discuss how to improve the absorption uniformity in the forward section of the demonstrated WGPD. As shown in Figure 2-23 (b), L_{a0}, which is the characteristic attenuation length of the fundamental supermode, is about 60 μm in the demonstrated WGPD. Therefore, L_{a0} is much smaller than the absorber length 150 μm, which will degrade the absorption uniformity, according to the discussion in section 2.10.1. Since there is not too much room left for optimizing the waveguide dimension for better absorption uniformity, adjustment of the wafer layer structure is proposed here for further

improvement of the absorption uniformity of the demonstrated WGPD. As limited by the wafer availability, this part of the research is done through simulation.

Intuitively, the increase of L_{a0} can be achieved by reducing the waveguide confinement factor. What is proposed here is the dilution of the absorber layer index with the addition of lower refractive index layers, which is added between the absorber and the waveguide, in order to further improve the power performance of the demonstrated traditional WGPD. A number of diluted waveguides have been reported in the literature, with different ways of implementation for different purposes. For example, a diluted waveguide was realized by reducing the refractive index difference between the core and the cladding by grading the Al mole fractions [36], in order to increase the transverse mode size in a waveguide laser and improve the coupling efficiency to the optical fiber. An additional lower refractive index InGaAsP layer is added next to the higher refractive index InGaAsP layer in a diluted core waveguide electro-absorption modulator [37], so that the photo-current maximum is separated from the photo-power maximum, and the dynamic range and the maximum power of the modulator was enhanced. A non-absorbing InGaAsP layer is used to dilute the optical confinement factor at the absorber in a conventional straight WGPD [38], in order to enhance the dynamic range and the maximum power of the detector. The proposed approach for improving the power performance of the demonstrated WGPD is along similar idea as [38]. However, the implementation is very different due to the waveguide structure and layer structure difference. The power performance improvement of the conventional WGPD in [38] is achieved by replacing part of the absorber with non-absorbing low refractive index material, which significantly reduces the confinement factor, but comes at the price of longer absorber for the same absorption efficiency. However, the absorber length cannot be increased in the demonstrated WGPD, in order to keep the same bandwidth. Our approach is to include a low refractive index InP diluting layer between the InGaAs absorbing layer and InGaAsP waveguide layer. As shown in Figure 2-46, adding an InP diluting layer in the MUTC2 layer structure can effectively reduce the

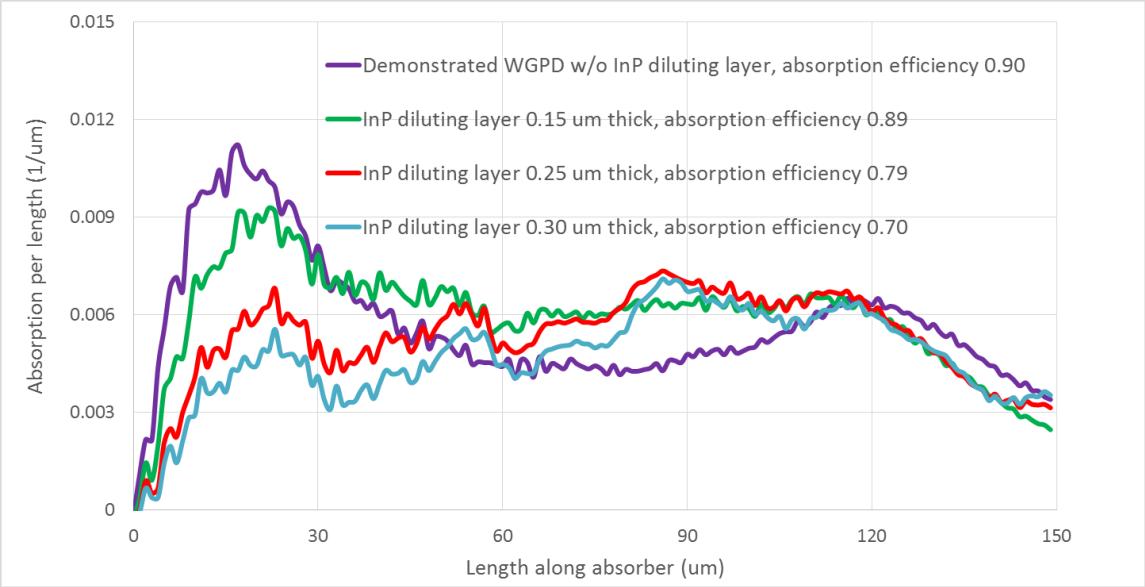

Figure 2-46 The simulated absorption profile of traditional WGPD built on MUTC2 wafer, which InP spacer layer with different thickness added. The simulated waveguide dimension is the same with the demonstrated WGPD simulated in Figure 2.31.

height of 1st absorption peak, which is the major absorption peak in the demonstrated WGPD. However, as the InP diluting layer thickness increases, in the simulation the absorption is kept about the same in the rear section, which improves the absorption uniformity. For example, when 0.25 μm thick InP diluting layer is added, the simulated absorption peak-to-average ratio is reduced from 1.8 to 1.3. However, as shown in Figure 2-46, increased InP diluting layer thickness also leads to reduced absorption efficiency, due to the reduced average confinement factor. The average confinement factor is a term defined as the optical confinement in the absorber layer in a planer waveguide built on a given layer structure, it describes the layer structure's contribution to the confinement factor in a ridge waveguide. The average confinement factor can be obtained by calculating or simulating the confinement factor of the fundamental mode of a WGPD, whose lateral dimension is several times of the wavelength. When 0.30 μm thick InP diluting layer is added in the MUTC2 layer structure, the simulated absorption efficiency drops by 22%, comparing

Table 2-10 The simulated excitation coefficient of various supermodes in the waveguide listed in Figure 2-34.

InP spacer layer thickness(μm)	Excitation of 0^{th} mode	Excitation of 1^{st} mode	Excitation of large Γ mode
0	0.9041	0.3824	0.1915
0.15	0.9528	0.2956	0.1056
0.25	0.9366	0.3107	0.0319

to 12% drop when the InP diluting layer thickness is 0.25 μm. Therefore, from the simulation, when 0.25 μm thick InP diluting layer is added in the MUTC2 layer structure, with bandwidth and absorption efficiency barely affected, the simulated absorption peak-to-average ratio is reduced from 1.8 to 1.3 in the demonstrated WGPD, theoretically it will increase the currently tested maximum thermal failure power density from 0.6 mW/μm^2 to 0.83 mW/μm^2. Although it is still smaller than that for the ideal WGPD, this improved thermal failure power density will make the power handling capability in a traditional WGPD as good as most of the surface normal photodiodes, as shown in Figure 2-45.

The excitation of various supermodes in the waveguide listed in Figure 2-46 is also simulated, as shown in Table 2-10. Comparing the simulated absorption profile and the excitation of the large Γ mode, as the InP diluting layer increases, the reduction of the absorption density in the forward section correlates well with the reduction of the large Γ mode excitation, which agrees with the supermode analysis results.

In summary, the design of the traditional WGPD is guided by the supermode analysis. Suppression of the large Γ supermode is achieved by properly designing the layer structure and waveguide structure. For the demonstrated WGPD with 300 μm^2 active area size, the absorption efficiency is well controlled by adjusting the average confinement factor and the waveguide taper

structure. The lowest simulated absorption density peak-to-average ratio with demonstrated material structures is 1.8, which is smaller than that in many reported traditional WGPD, and indicates improved absorption uniformity. The tested power handling capability of the demonstrated WGPDs is also better than many reported traditional WGPD, as the maximum average power density in the demonstrated WGPD is higher. Compared to the ideal WGPD, the degradation of the power handling capability of the demonstrated WGPD is mainly due to the non-uniform absorption distribution. Future improvement of the absorption uniformity in a WGPD is demonstrated by simulation, which is realized by adding a low refractive index diluting layer. The simulated absorption density peak-to-average ratio can be reduced to as low as 1.3, which represents theoretically a major improvement in the design of WGPD for handling high power.

2.11 Summary

The supermode analysis is introduced to assist the study of absorption uniformity in a traditional WGPD, as well as the design of high power traditional WGPD. The interferences between the fundamental supermode and other supermodes modify the exponential absorption profile of the individual supermode. The optimization of the interferences is the key to improve the absorption uniformity. Different interference affect the absorption uniformity in a traditional WGPD differently in the forward section and in the rear section of the absorber. In the forward section, the large gamma supermode interference has larger amplitude than the higher order supermode interference, and it is the major factor affecting the absorption uniformity. The suppression of the large gamma mode, which can be achieved by reducing the confinement factor of the waveguide structure, can effectively reduce the absorption peak in the forward section, and hence improves the absorption uniformity. In the rear section, the large gamma supermode interference largely attenuates, and the higher order mode interference becomes the major factor affecting the absorption uniformity. In order to improve the absorption uniformity, higher order modes with similar confinement factor with the fundamental mode are preferred. The excitation

coefficient and the number of the preferred higher order modes relate to the waveguide width of the traditional WGPD. When the waveguide is very narrow, there is not any significant excitation of the preferred higher order mode, and the absorption profile in the rear section will follow the exponential decay profile of the fundamental supermode. When the waveguide gets wider, there will be one preferred higher order mode having comparable excitation coefficient with the large gamma supermode, and the absorption uniformity in the rear section will greatly improves from the case without any preferred higher order mode. When the waveguide is so wide that there are more than one preferred higher order supermode, the absorption efficiency will be smaller than the case with just one preferred higher order supermode, and more absorption density variation appears due to the existence of multiple interferences. In this case, approach such as tapering the waveguide can be used to alleviate the absorption efficiency reduction and absorption uniformity degradation.

With the guidance of the supermode analysis, traditional WGPD with the optimized structure demonstrates measured maximum power density of 0.6 $mW/\mu m^2$, which is higher than most of the reported values for WGPD with similar bandwidth. The power handling capability gap between the demonstrated WGPD and an ideal WGPD is also discussed, large waveguide confinement factor due to the MUTC2 wafer is attributed to this gap. A low refractive index diluting layer is proposed to dilute the absorber index in the MUTC2 layer structure. From simulation, a 0.25 μm thick InP diluting layer can reduce the absorption density peak-to-average ratio by 30%, which indicates increase of the theoretical maximum power density by 30% in the demonstrated WGPD, and makes the power handling capability of traditional WGPD as good as most of the surface normal photodiode.

The traditional WGPD structure has some limitations for designing high power WGPD. First, reducing the waveguide confinement factor improves the absorption uniformity in the forward section by suppressing the large gamma supermode, but also reduces the absorption efficiency. Second, the widening of the waveguide improves the absorption uniformity in the rear

section by enhancing the excitation of the preferred higher order mode, but also introduces more absorption variations and absorption efficiency reduction. A different WGPD design, which has very different characteristics of the supermodes and the absorption profile, will be discussed in the next chapter.

2.12 References

[1] W. S. C. Chang, *Fundamentals of Guided-wave Optoelectronic Devices*, Cambridge University Press, Cambridge UK (2010).

[2] C. H. Cox, *Analog Optical Links: Theory and Practice*, NY: Cambridge, New York (2004)

[3] H. Jiang and P. K. L. Yu, "High power waveguide integrated photodiode with distributed absorption," *Microwave Symposium Digest*, vol. 2, pp. 679-682 (2000).

[4] H. Jiang and P. K. L. Yu, "Waveguide integrated photodiode for analog fiber-optics links," *IEEE Trans. Micro. Theory Tech.*, vol. 48, pp. 2604-2610 (2000).

[5] T. S. Liao, *Design of Linear Photodetector for Photonic Antenna Application*, University of California, San Diego (2005).

[6] M. N. Draa, J. Bloch, D. Chen, D. C. Scott, N. Chen, S. B. Chen, X. Yu, W. S. C. Chang, and P. K. L. Yu, "Novel directional coupler waveguide photodiode-concept and preliminary results," *Optics Express*, vol. 18, no. 17, pp. 17729-17731 (2010).

[7] Y. Zhang, Z. Liao, L. Zhao, H. Zhu, J. Pan, and W. Wang, "A high-efficiency high-power evanescently coupled UTC-photodiode," Journal of Semiconductors, vol. 30, no. 4, pp. 1-4, (2009).

[8] J. Klamkin, A. ramaswamy, L. A. Johansson, H. F. Chou, M. N. Sysak, J. W. Raring, N. Parthasarathy, S. P. DenBaars, J. E. Bowers, and L. A. Coldren, "High output saturation and high-linearity uni-traveling-carrier waveguide photodiodes," *IEEE Photonics Technol. Lett.*, vol. 19, no. 3, pp. 149-151 (2007).

[9] N. Michel, V. Magnin, J. Harari, A. Marceaux, O. Parillaud, D. Decoster, and N. Vodjdani, "High-power evanescently-coupled waveguide photodiodes," *IEE Proceedings of Optoelectron.*, vol. 153, no. 4, pp. 199-204 (2006).

[10] M. Seimetz, *High Order Modulation for Optical Fiber Transmission*, Springer series in Optical Sciences (2009).

[11] A. Nespola, T. Chau, M. C. Wu, G. Ghione, "Analysis of failure mechanisms in velocity-matched distributed photodetectors," *IEE Proc. Optoelectron*, vol. 146, no. 1, pp. 25-30 (1999).

[12] N. Duan, X. Wang, N. Li, H. Liu, and J. C. Campbell, "Thermal Analysis of High-Power InGaAs-InP Photodiodes," *IEEE J. Quantum Electron.*, vol. 42, no. 12, pp. 1255-1258 (2006).

[13] T. Yasui, T. Furuta, T. Ishibashi, and H. Ito, "Comparison of power dissipation tolerance of InP/InGaAs UTC-PDs and pin-PDs," *IEICE transactions on electronics E86-C(5),* pp. 864-866 (2003).

[14] K. J. Williams and R. D. Esman, "Design Considerations for High Current Photodetectors," *J. Lightwave Tech*. vol. 17, pp. 1443-1454 (1999).

[15] P. Hill, J. Schlafer, W. Powazinik, M. Urban, E. Eichen, R. Olshansky, "Measurement of hole velocity in n-type InGaAs", *Appl. Phys. Lett*. vol. 50, no. 4, pp. 1260-1262 (1987).

[16] J. P. Barbour, W. W. Dolan, J. K. Trolan, E. E. Martin, and W. P. Dyke, "Space-Charge Effects in Field Emission," *Phys. Rev*. vol. 92, no. 1, p. 45 (1953).

[17] T. Ishibashi, S. Kodama, N. Shimizu, and T. Furuta, "High-speed response of uni-traveling carrier photodiodes," *Jpn. J. Appl. Phys*., vol. 36, pp. 6263-6268 (1997).

[18] T. Ishibashi, H. Fushimi, H. Ito and T. Furuta, "High-power uni-traveling-carrier photodiodes," *Tech. Dig. Int. Topical Meeting on Microwave Photonics*, pp. 75-78 (1999).

[19] D. Woods, *Optoelectronic Semiconductor Devices*, Prentice Hall, New York (1994).

[20] J. Wei, L. Geng, D. G. Cunningham, R. V. Penty, and I. White, "100 Gigabit Ethernet Transmission Enabled by Carrierless Amplitude and Phase Modulation Using QAM Receivers," Optical Fiber Communication Conference (2013).

[21] B. Hoeft, R. Stoy, F. Schröder, A. Reymund, R. Niederberger, O. Mextorf, and S. Werner, "100G Ethernet in the wild – first experiences," *J. of Phys*., vol. 331 (2011).

[22] IEEE 400 Gb/s Ethernet Task Force, "400G SMF PMD Alternatives_A System Vendor's Perspective," San Diego (2014).

[23] N. Duan, N. Li, S. Demiguel, J. C. Campbell, "An InGaAs/InP Photodiode with 600mW RF Output Power," *LEOS Summer Topical Meetings* (2006).

[24] K. J. Williams, D. A. Tulchinsky, and A. Hastings, "High power and high linearity photodiodes," *IEEE Photonics Conference*, (2008).

[25] M. Chtioui, A. Enard, D. Carpentier, S. Bernard, B. Rousseau, F. Lelarge, F. Pmmereau, and M. Achoouche, "InGaAs InP Uni-traveling-carrier photodiodes for high power capability," *Indium Phosphide and related materials* (2008).

[26] Z. Li, H. Pan, H. Chen, A. Beling, and Joe C. Campbell, "High-Saturation-Current Modified Uni-Traveling-Carrier Photodiode with Cliff Layer," *IEEE J. Quantum Electron.*, vol. 46, no. 5, pp. 626 - 632 (2010).

[27] T. Takeuchi, T. Nakata, K. Makita, and T. Torikai, "A high-power and high-efficiency photodiode with an evanescently coupled graded-index waveguide for 40 Gb/s applications," *Optical fiber communication conference and exhibit* (2001).

[28] Y.-S. Wu, J.-W. Shi, P.-H. Chiu, and Wei Lin, "High-Performance Dual-Step Evanescently Coupled Uni-Traveling-Carrier Photodiodes," *IEEE Photon. Technol. Lett*., vol. 19, no. 20, pp. 1682 - 1684 (2007).

[29] J. Klamkin, Y. Chang, A. Ramaswamy, L. A. Johansson, J. E. Bowers, S. P. DenBaars, and L. A. Codren, "Output Saturation and Linearity of Waveguide Unitraveling-Carrier Photodiodes," *IEEE J. Quantum Electron.*, vol. 44, no. 4, pp. 354 - 359 (2008).

[30] D. Wake, “A 1550-nm millimeter-wave photodetector with a bandwidth-efficiency product of 2.4 THz,” *J. Lightwave Technology*, vol. 10, pp. 908-912 (1992).

[31] S. Demiguel, L. Giraudet, L. Joulaud, J. Decobert, F. Blache, V. Coupe, F. Jorge, P. Pagnod-Rossiaux, E. Boucherez, M. Achouche, and F. Devaux, “Evanescently coupled photodiodes integrating a double-stage taper for 40-Gb/s applications-compared performance with side-illuminated photodiodes,” *J. Lightwave Technology*, vol. 20, pp. 2004 - 2014 (2002).

[32] N. Michel, V. Magnin, J. Harari, A. Marceaux, O. Parillaud, D. Decoster, and N. Vodjdani, “High-power evanescently-coupled waveguide photodiodes,” *IEE Proc.-Optoelectron.*, vol. 153, pp. 199-204 (2006).

[33] E. Kapon, J. Katz, and A. Yariv, "Supermode Analysis of Phase-Locked Arrays of Semiconductor-Lasers," *Opt. Lett*., vol. 9, pp. 125-127 (1984).

[34] A. Yariv, and X. K. Sun, "Supermode Si/III-V hybrid lasers, optical amplifiers and modulators: A proposal and analysis," *Opt. Express*, vol. 15, pp. 9147-9151 (2007).

[35] W. S. C. Chang, *Fundamentals of guided-wave optoelectronic devices*, Cambridge University Press, Cambridge, UK (2010).

[36] V. Vusirikala, B. P. Gopalan, S. Kareenahalli, S. A. Merritt, M. Dagenais, C. E. C. Wood, and D. Stone, “GaAs-AlGaAs QW Diluted Waveguide Laser with Low-Loss, Alignment-Tolerant Coupling to a Single-Mode Fiber,” *IEEE Photon. Technol. Lett*., vol. 8, no. 9, pp. 1130 – 1132, (1996).

[37] S. Tan, N. Stoffel, C. Shick, T. McDonald, A. Whitbeck, R. Erdmann, R. J. Michalak, R. Bussjager, I. Shubin, and Paul K. L. Yu, “Design and development of a package for a diluted waveguide electro-absorption modulator,” *SPIE Proceedings*, vol. 6975 (2008).

[38] H. Jiang, J. T. Zhu, A. L. Keliner, P. K. L. Yu, “High-saturation-power waveguide photodetector for analog fiber-optic links,” *SPIE Proceddings*, vol. 2844 (1996).

Chapter 3 High Power Waveguide Photodiode- Analysis, Design and Demonstration

3.1 The limitation of high power traditional WGPD design.

In chapter 2, high power traditional WGPD design and its limitations are studied by using supermode analysis. Approaches that improves the power handling capability in a traditional WGPD are discussed. As discussed in section 2.10.3 and section 2.10.5, the absorption uniformity of a traditional WGPD can be improved by optimizing the waveguide structure, via the suppression of the large Γ supermode and the enhancement of the preferred higher order modes excitation. However, both approaches result in the reduction of the absorption efficiency, which make the tradeoff between the absorption uniformity and the absorption efficiency a key factor limiting the power handling capability that can be achieved in a traditional WGPD. Therefore, further power handling capability improvement requires a better waveguide design than the traditional WGPD designs discussed in Chapter 2.

This chapter investigates a pre-studied novel waveguide structure, directional coupling waveguide photodiode (DCPD) [1] [2], in order to further improve the power handling capability of a traditional WGPD. Some preliminary theoretical study and simulation work of DCPD have been done in our group before the DCPD research work in this dissertation [1] [2], and show that the absorption uniformity and the absorption efficiency can be adjusted with larger flexibility in a DCPD than in a traditional WGPD. Comparing to the reported simulated results in the traditional WGPD [3-6], DCPD achieves relatively uniform simulated absorption distribution. Besides, some preliminary experimental study of DCPD's power handling capability has also been done in the previous studies [1] [2]. The epi-layer structure and waveguide structure of the studied DCPD are shown in Figure 3-1. A maximum photocurrent of about 40 mA at -4 V bias voltage is obtained in the DCPD with about 400 μm^2 active area size. The corresponding power failure density of 0.40

$mW/\mu m^2$ is larger than most reported traditional WGPD with similar active area size [3-6]. The previous study of DCPD reveals the potential of this novel device being a great design of high power waveguide photodiode. However, several issues exist in the previous study of DCPD. First, the analysis and simulation of DCPD in [1] [2] focus on looking for the optimized waveguide dimension for better simulated absorption uniformity, which is similar to the way high power WGPD is designed traditionally. However, there are more waveguide parameters in a DCPD interacting with each other, which complicates the power distribution pattern, thus puts a question mark to the claimed optimized DCPD waveguide structure. Second, there is still a large gap of power handling capability between the DCPD and the ideal WGPD, and the reasons behind that, which needs deeper understanding of this novel and complex waveguide structure, is yet to be discovered. Third, the study of power distribution in [1] [2] did not provide good answers to several important questions, such as how does DCPD differ intrinsically from the traditional WGPD on distributing the optical power, how does these intrinsic difference help improve the absorption uniformity. The lacking of answers to these questions hinders the design of a DCPD with power handling capability exceeds that of the demonstrated traditional WGPD shown in section 2.10.6.

In this chapter, the supermode analysis, which has well performed on analyzing the power distribution in the traditional WGPD in chapter 2, is applied to DCPD. The supermode analysis is used to reveal the intrinsic difference between DCPD and the traditional WGPD on distributing the optical power, from which the understanding of how to optimize the DCPD waveguide structure for better power handling capability is provided. Simulations of supermode excitation and absorption distribution, as well as the relation between them, are used to assist the supermode analysis. A re-designed DCPD with optimized waveguide structure is demonstrated experimentally, whose power handling capability is compared to that of the previous DCPD and the traditional WGPDs. Suggestions are also made for future DCPD study.

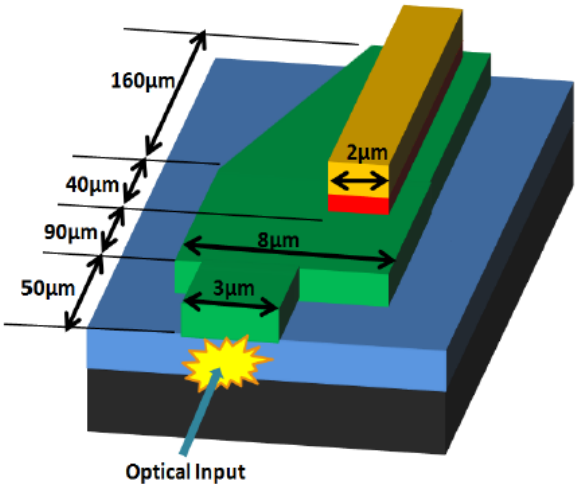

(a)

Layer	Material	Thickness (µm)	λ (nm)	Index	Doping	Type
1	InGaAs	0.05		3.56	2.00E+19	P+
2	InP	0.779		3.21	1.00E+18	P+
3	InGaAsP	0.007	1.00	3.33	1.00E+18	P+
4	InGaAsP	0.007	1.20	3.33	1.00E+18	P+
5	InGaAsP	0.007	1.35	3.42	1.00E+18	P+
6	InGaAs	0.20		3.56	5.00E+17	P
7	InGaAs	0.20		3.56	2.50E+17	P
8	InGaAs	0.20		3.56	1.00E+17	P
9	InGaAs	0.05		3.56	1.00E+16	N-
10	InGaAsP	0.007	1.35	3.42	-	
11	InGaAsP	0.007	1.20	3.33	-	
12	InGaAsP	0.336	1.20	3.33	-	
13	InGaAsP	0.2	1.20	3.33	6.00E+16	N Collector
14	InGaAsP	0.5	1.20	3.33	1.00E+18	N
15	InGaAsP	0.8	1.20	3.33	1.00E+18	N
16	InP	0.25		3.21	3.00E+18	N+
Sub	InP			3.21		

(b)

Figure 3-1 DCPD device (a) and layer structure (b) used in [1] [2].

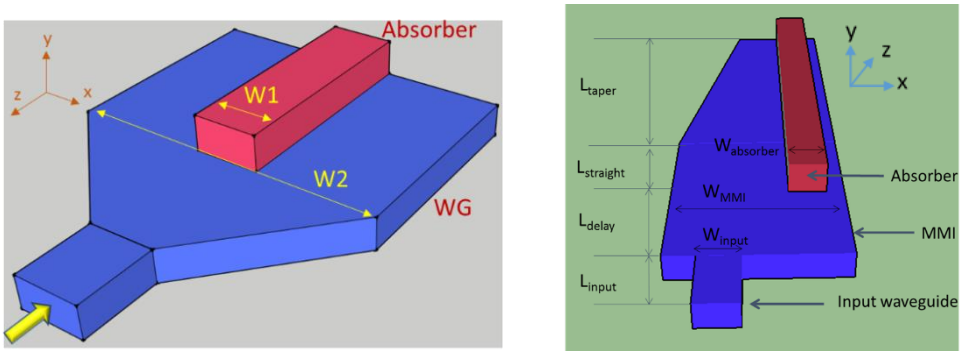

Figure 3-2 Schematic of a traditional WGPD (left) and a DCPD (right).

3.2 Analysis of DCPD

In the discussion below, the orientation of the waveguide structure is defined as follows: the x direction is defined as the lateral direction, which is parallel to the waveguide width direction; the y direction is defined as the vertical direction, which is perpendicular to the wafer substrate; the z direction is defined as the optical power propagation direction, which is along the waveguide length direction. As shown in Figure 3-2, the waveguide structure of a DCPD [1] [2] differs from that of a traditional WGPD in several aspects. First, in the x direction, the input waveguide and the absorber aligns with each other in a traditional WGPD, while there is an offset existing between the two in a DCPD. Second, in the z direction, between the input waveguide and the absorber, a single-mode incident radiation pattern gradually expands in the x direction via an adiabatic taper waveguide in a traditional WGPD, and remains being single-mode when reaching the absorber. In comparison, multiple modes are excited by a single-mode incident radiation pattern at the interface of the input waveguide and the passive MMI, and propagates simultaneously in the passive MMI. Therefore, the optical power pattern reaching the absorber in a DCPD is no longer simply determined by the incident radiation, instead, it is determined by the interaction of the multiple modes excited in the passive MMI. Because of these two differences, the study of the DCPD waveguide structure not only includes the discussion of the absorber width and the waveguide

width, as was done for the traditional WGPD, but also has to include the discussion of the spatial separation between the input waveguide and the absorber in the x direction and in the z direction.

In this chapter, the layer structure of DCPD changes from MUTC1, which is used in the previous DCPD study, to MUTC2, which has reduced doped absorbing layer thickness and are already shown in Figure 2-13. The absorber thickness affects an ideal MUTC WGPD in different aspects, including the thermal conduction, bandwidth, and the absorption efficiency, as discussed in section 2.7.5. Reducing the doped absorbing layer improves the upward thermal conduction. It also increases the transit time limited bandwidth, without affecting the RC time limited bandwidth. Moreover, the simulation also shows the reduced absorber thickness in MUTC2 layer structure will not degrade the absorption efficiency in a DCPD with 150 μm long absorber, which will be shown later in this chapter. Therefore, for the following discussion and the re-designed DCPD analyzed later in this chapter, the MUTC2 layer structure will be used.

3.2.1 The separation between the input waveguide and the absorber in the x direction

As discussed in section 2.9.5, in a traditional WGPD, the large gamma supermode is one of the largely excited supermodes, because of the large spatial overlap between the incident radiation pattern and the large gamma mode in the x direction. In this case, the introduction of certain spatial separation between the input waveguide and the absorber in the x direction, which reduces the spatial overlap between the incident radiation pattern and the large gamma mode, is expected to suppress the excitation of the large gamma supermode in a traditional WGPD. To illustrate that, traditional WGPDs with different delta x, which is the spatial separation between the input waveguide and the absorber in the x direction, are simulated, with the absorption profiles shown in Figure 3-3, and the excitation coefficients of the large gamma mode shown in Table 3-1. On the one hand, it is observed in Table 3-1 that a larger delta x corresponds to reduced excitation of the large gamma mode. In the simulated cases, the excitation coefficient of the large gamma

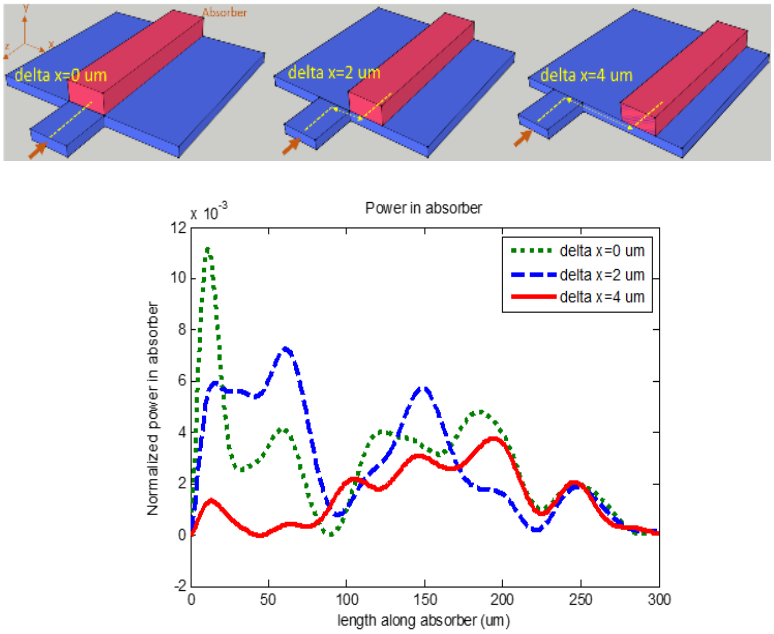

Figure 3-3 The comparison of waveguide structure (a) and absorption profile (b) of WGPD with different delta x, which is the spatial separation delta x between input waveguide and absorber at x direction. The waveguide width is 8 μm, the absorber width is 2 μm, the waveguide and absorber length is 300 μm. The separation between the input waveguide and the absorber is 0 μm, 2 μm, and 4 um, respectively. The layer structure for all three simulated waveguide is shown already in Figure 2.30.

Table 3-1 The excitation coefficient of large gamma mode of the three simulated cases shown in Figure 3-3.

delta x (μm)	excitation coefficient of large Γ mode
0	0.280
2	0.173
4	0.002

mode is significantly reduced when delta x is 2 μm, and becomes negligible when delta x is 4 μm.

On the other hand, it is observed in Figure 3-3 that a larger delta x corresponds to reduced peak

absorption density in the forward section of the absorber. In the simulated cases, when delta x increases from 0 μm to 2 μm, in the first 100 μm long section, the reduced peak absorption density comes along with minimally changed absorption efficiency. However, when delta x increases to 4 μm, as shown in Figure 3-3, although further reduction of peak absorption density is observed, significant drop of the absorption efficiency also occurs in the first 100 μm long section, showing a limitation of reducing the absorption in the forward section by increasing delta x alone. In the next section, a way to break this limitation via the adjustment of other waveguide parameters is discussed.

As discussed in the last paragraph, without changing the dimension of the waveguide and the absorber, introducing some spatial separation between the input waveguide and absorber in the x direction in a traditional WGPD can reduce the absorption density in the forward section, via reducing the large gamma supermode excitation. In the following discussion, a closer look at the excitation of various supermodes in the traditional WGPDs shown in Figure 3-3 is given for better understanding the effects of non-zero delta x.

For the WGPDs shown in Figure 3-3, the excited supermodes are simulated and compared between two different delta x, 0 μm and 4 μm. In Table 3-2, the excitation coefficient and confinement factor of the first five significantly excited supermodes, as well as that of the large gamma mode, are listed. In Figure 3-4, the lateral field distribution of the first three significantly excited supermodes, as well as the large gamma mode and the incident pattern, are shown. From the simulation results, the non-zero delta x has two major effects on the supermode excitation. First, Table 3-2 shows that the large gamma mode excitation is much smaller in WGPD with 4 μm delta x, due to the reduced field overlap between the incident pattern and the large gamma mode, as shown in Figure 3-4. In this case, according to the discussion in section 2.10.3, improvement of the absorption uniformity in the forward section is expected with the reduction of the large gamma

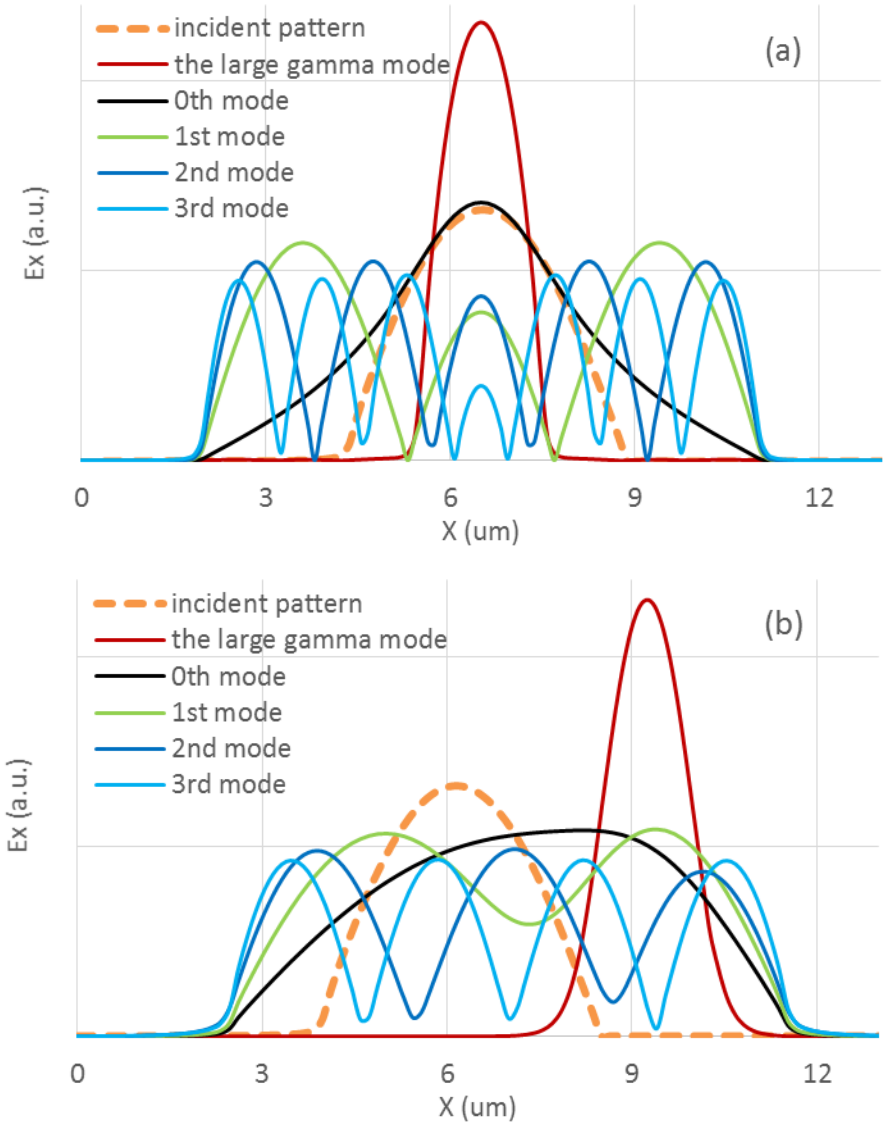

Figure 3-4 The filed plot (the absolute value) in the x direction for the first four major modes, as well as the incident radiation pattern and the large gamma mode, of the WGPDs in Figure 3-3, with delta x equals to 0 μm (a) and 4 μm (b), respectively. The incident radiation pattern is the fundamental mode of the input waveguide.

mode excitation. Second, comparing the excitation coefficients in Table 3-2, it is noted that the power of the incident radiation is more evenly distributed among the significantly excited supermodes in a WGPD with 4 μm delta x, while most of it goes to the 0^{th} order supermode in a

Table 3-2 The excitation coefficient χ and confinement factor Γ of the first 5 major modes and the large gamma mode in two WGPDs shown in Figure 3-3, with delta x equals to 0 μm and 4 μm, respectively.

SUPERMODE	Excitation Coefficient (delta x=0 μm)	Excitation Coefficient (delta x=4 μm)	Confinement factor Γ (delta x=0 μm)	Confinement factor Γ (delta x=4 μm)
0th	0.930	0.340	0.018	0.010
1st	0.200	0.510	0.011	0.011
2nd	0.100	0.430	0.010	0.005
3rd	0.020	0.150	0.006	0.004
4th	0.008	0.110	0.003	0.008
5th	0.001	0.080	0.001	0.007
The large gamma mode	0.280	0.002	0.320	0.310

WGPD with 0 μm delta x. When delta x is 0 μm, the 0th order supermode is dominantly excited, as explained in section 2.9.5. When delta x is 4 μm, the 0th order mode has similar excitation coefficient with the first several significantly excited higher order modes, as their field overlap with the incident pattern is similar in the x direction, as shown in Figure 3-4. Moreover, those significantly excited supermodes not only have similar excitation coefficient, but also have similar confinement factor. As discussed in section 2.9.7, the significant excitation of higher order supermode will increase the absorption density and improve the absorption uniformity in the rear section of the absorber in a traditional WGPD, when the confinement factor of the higher order mode is close to that of the fundamental mode. Therefore, the non-zero offset induces significant excitation of the preferred higher order modes, which can be used to optimize the absorption uniformity in the rear section of the absorber.

From the above discussion, the non-zero delta x is a critical parameter that differentiates a DCPD from a traditional WGPD, as it significantly suppresses the large forward section absorption that is usually observed in a traditional WGPD. This effect is more significant with larger delta x.

However, large delta x will results in inefficient absorption in the forward section of the absorber and reduced absorption efficiency. Once the effect of non-zero delta x is known, the next step will be studying the other waveguide parameters of DCPD, and resolve the issue of inefficient absorption caused by large delta x. .

3.2.2 The separation between the input waveguide and the absorber in the z direction

In the traditional WGPD case discussed in the last section, when delta x is 4 μm, although the large gamma mode is significantly suppressed and the forward section absorption is reduced, there is significant drop of the absorption efficiency in the first 100 μm long of the absorber, and limits the output power that a WGPD can deliver. This problem can be tackled in DCPD by the introduction of delay length, which is a spatial separation between the input waveguide and the absorber in the z direction. In this case, the input waveguide and the absorber in a DCPD is not only separated in the x direction, but also in the z direction, as shown in Figure 3-2.

The idea of delay length in DCPD with a multimode waveguide can be better explained by first taking a look at the optical power distribution in a multimode interference (MMI) coupler, with both ends being abruptly terminated and connected to a number of access single mode waveguide. The power distribution in a MMI coupler has been thoroughly discussed in [7], based on the interference of the propagating modes. By defining L_π as the beat length (i.e. the propagation length in which the phase difference of the two modes is π) between the fundamental mode and the first order mode, it is pointed out that the replicate, the double images, and the mirror of the input field appear at distance z=0, $z=3L_\pi/2$, and $z=3L_\pi$, respectively [7], as shown in Figure 3-5. In this case, in a DCPD, several waveguide parameters can be determined by the interference of the propagating modes. First, in the z direction, the back end of the absorber should be near $z=3L_\pi$, where a mirror single image of the input field appears. As shown in Figure 3-5, when the input field aligns with the MMI region $0<x<W/2$, the absorber separates from the input field laterally and sits

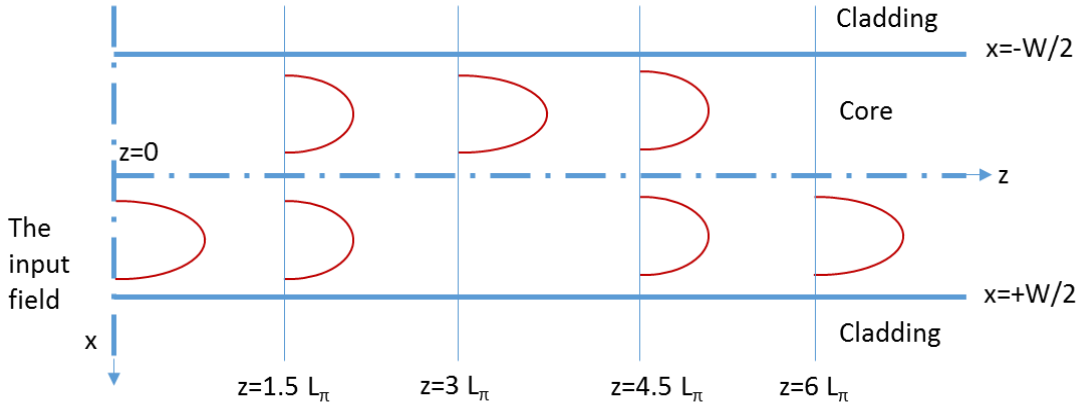

Figure 3-5 Image of the input field at various distances in a multimode interference coupler (MMI). The width of MMI is W. The input field is shown at z=0. It can be decomposed into a summation of all the modes. Each mode has a different phase velocity. The total field profile of the summation of these modes will yield a two-fold image of the input at z=1.5 L_π and at z=4.5 L_π, a mirror single image at z=3 L_π, and a direct single image at z=6 L_π [7].

on top of MMI region $-W/2<x<0$, within which the optical power density increases from z=0, and peaked at $z=3L_\pi$. Considering the monotonic reduction nature of the available optical power in a photodiode in the z direction, having the absorber back end at $z=3L_\pi$ benefits the absorption efficiency and absorption uniformity. Second, in the z direction, the front end of the absorber should be at somewhere between z=0 and z=1.5 L_π. When it is too close to z=0, as already shown in the last section, the absorption in the forward section will be inefficient, as the majority of the optical power stays away from the MMI region $0<x<W/2$, where the absorber locates. When it is too close to $z=1.5L_\pi$, half of the incident optical power will arrive at the absorber front end, and will result in large absorption in the forward section. In the DCPD design, the front end of the absorber is initially set at $z=0.75L_\pi$, with further fine-tuning followed. In this case, the delay length is $0.75L_\pi$, and the absorber length is about $2.25L_\pi$.

In our DCPD study, the dimension of the absorber is set to be 2 μm wide and 200 μm long, which corresponds to about 40 GHz RC bandwidth. As mentioned above, the absorber length

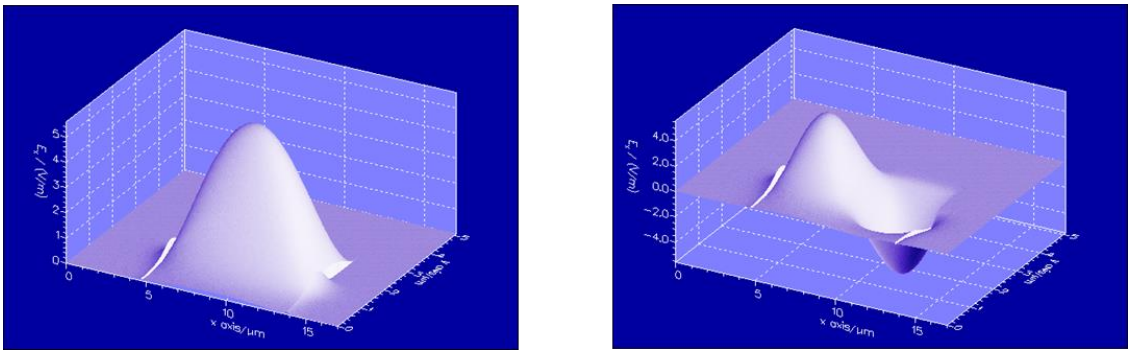

Figure 3-6 The 3D view of the Electrical field of the fundamental mode (left) and the 1st order mode (right). The MMI width is 9 μm, the wavelength λ is 1.55 μm, the layer structure is MUTC2. The effective index of the fundamental mode is 3.30972, the effective index of the 1st order mode is 3.30188, and $\Delta n_{eff,01}$ is 0.0079.

should be about $2.25L_\pi$, and the delay length is $0.75L_\pi$. In this case, L_π is 90 μm, and the delay length is about 70 μm. Please note that the above calculation is based on two assumptions. The first one is that the addition of the absorber mesa onto the MMI does not significantly change the optical distribution in the MMI, which is a reasonable assumption, considering the dimension difference of the MMI and absorber. The justification of this assumption will be done later in this section, by comparing the optical distribution in the right half of the MMI at the absorber side for cases with the absorber and without the absorber. The other assumption is that the absorber and MMI have no taper feature. In the following discussion, first, the relation between L_π and MMI width is simulated, from which the MMI width of a DCPD with a 200 μm long absorber is determined. Second, based on the above known waveguide parameters, the absorption profile of DCPD is simulated, with further fine-tuning followed.

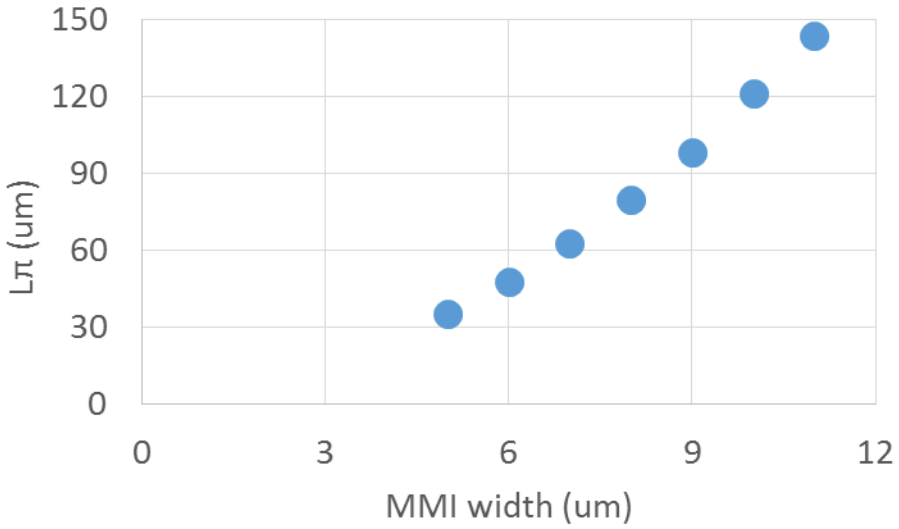

Figure 3-7 The L_π versus MMI width in DCPD. The layer structure is MUTC2.

As mentioned earlier in this section, L_π of a MMI is the propagation length in which the phase difference of the fundamental mode and the first order mode is π, and can be expressed as:

$$L_\pi = \frac{\pi}{\frac{2\pi}{\lambda}\Delta n_{eff,01}} = \frac{\lambda}{2}\frac{1}{\Delta n_{eff,01}} \qquad 3.1$$

where λ is the wavelength of the input optical radiation, $\Delta n_{eff,01}$ is the real part of the effective refractive index difference of the fundamental mode and the first order mode. The two modes are simulated by using Fimmwave software, and L_π is calculated from the simulation results. A 3D view of the two modes is shown in Figure 3-6 in a sample DCPD, and L_π is plotted against MMI width in Figure 3-7. As calculated in the last paragraph, L_π of 90 μm is needed for DCPD with 200 μm long absorber. In this case, MMI width, which should be between 8 μm and 9 μm, can be determined using Figure 3-7.

The relation between L_π and the MMI width shown in Figure 3-7 is checked. On the one hand, the field distribution of the incident optical power in a 9 μm wide MMI is simulated and shown in Figure 3-8, in which the mirrored and the replicated images of the incident radiation field

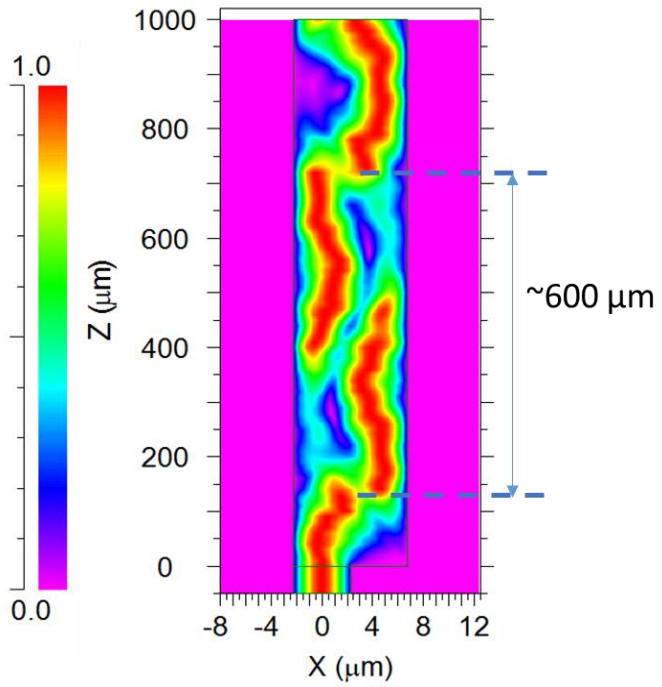

Figure 3-8 The simulated field distribution of the optical power in a 9 μm wide MMI. The layer structure is MUTC2. The simulation is done by Beamprop.

appears at around 300 μm and 600 μm, respectively. In this case, it indicates L_π to be 100 μm. On the other hand, according to Figure 3-7, the calculated L_π is 98 μm in a 9 μm wide MMI, and is very close to the number read from the power distribution in Figure 3-8. Therefore, L_π can be used to help determine the delay length, as well as the MMI width.

According to the earlier discussion in this section, the delay length is initially chosen to be $0.75L_\pi$. When MMI is 9 μm wide, the calculated L_π is 100 μm. In this case, the initial value of delay length should be around 75 μm for the simulation optimization. For DCPDs with delay length differs from 75 μm, the absorption profile, as well as the power distribution in the half of MMI at the absorber side, are simulated and shown in Figure 3-9. These simulation results give plenty of insights into understanding the effects of delay length in a DCPD. First, the DCPD with zero delay length has inefficient absorption in the forward section of the absorber, and results in small absorption efficiency. This issue can be resolved by adding certain delay length, which allows more

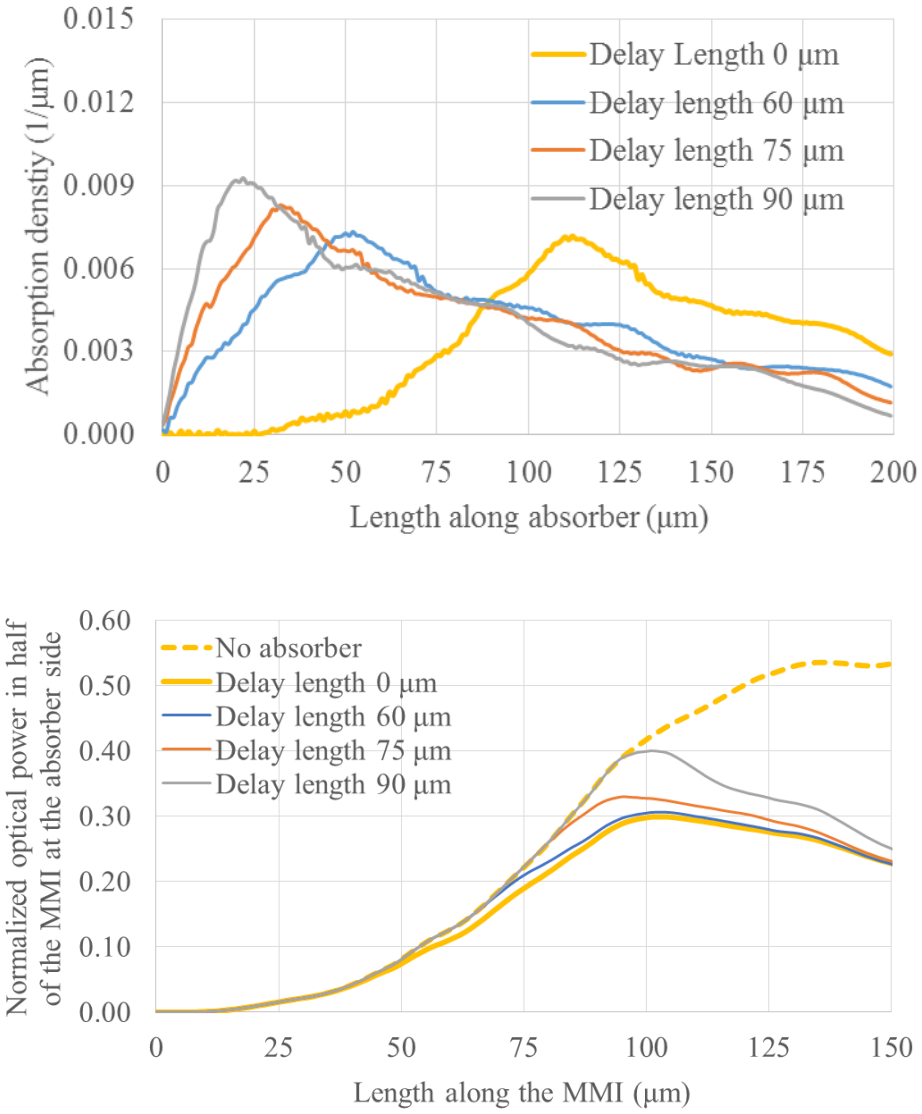

Figure 3-9 Simulated absorption profile (a) and the normalized optical power in half of the MMI at the absorber side, P_h, (b) of DCPD with various delay length. In (a), the absorber is 2 μm x 200 μm, the MMI width is 9 μm, the MMI length is 200 μm plus the delay length. In (b), the simulation is done for the 150 μm long MMI from the MMI front end. In (b), a simulation of DCPD without the absorber is also done for the purpose of comparison. In the x direction, the input waveguide left edge aligns with the MMI left edge, and the absorber aligns to the center of the right half of the MMI.

optical power from the input waveguide reach the absorber forward section. Second, when the delay length is 75 μm, the absorption density monotonically increases from the absorber front end, and peaked at a position that is 35 μm away from the absorber front end, and then decreases afterwards. At this point, adjusting the delay length modifies the absorption profile in the forward section of the absorber. As shown in Figure 3-9 (a), increasing the delay length from 75 μm to 90 μm moves the absorption peak position closer to the absorber front end, and increases the absorption in the forward section of the absorber. In comparison, reducing the delay length from 75 μm to 60 μm moves the absorption peak position further away from the absorber front end, and reduces the absorption in the forward section of the absorber.

The relation between the absorption peak position and the delay length is studied. An observation from Figure 3-9 (a) is that the distance of the absorption peak from the MMI front end, which is the summation of the delay length and the distance of the absorption peak from the absorber front end, is similar in all DCPD variations. In other words, the distance of the absorption peak from the MMI front end is quite independent of the delay length. In order to understand this phenomenon, in Figure 3-9 (b), for the same DCPDs simulated in Figure 3-9 (a), the optical power in the half of the MMI at the absorber side, P_h, is simulated and compared to that of a DCPD without the absorber. In a DCPD, P_h is affected by the lateral optical coupling in the MMI and the absorption. Before the absorber starts, it is not surprising to see that P_h, which increases monotonically, is the same in all DCPD variations. When the absorber starts, within the next 10 μm long section, P_h in DCPDs with various delay length still increases monotonically, and differs little from that in the DCPD without the absorber. This is due to the lateral coupling in the MMI is barely affected by the absorber, and the optical absorption within this short section is rather small. Beyond this 10 μm long section, P_h in DCPDs with various delay length starts to deviate from that in the DCPD without the absorber, because of the accumulated absorption. P_h peaks at certain position, at which power reduction due to the accumulated absorption and the power increase due to the lateral coupling

balance out. After that, P_h starts to drop, because of the monotonic increase of the accumulated absorption. When the delay length is larger, because of the increased power density in the forward section, it requires shorter length to reach certain amount of accumulated absorption that balances out the power increase due to the lateral coupling and enables the peaking of P_h. In this case, it makes sense for what we observed in Figure 3-9 (a) that the distance of the absorption peak positon from the MMI front end appears quite independent of the delay length.

In summary, the MMI of DCPD is substantially studied based on the interference of the supermodes. Once the absorber length is given, by using L_π, the beating length of the fundamental mode and the first order mode, the MMI width and delay length can be determined. It is effective to add delay length to resolve the small absorption efficiency issue in a DCPD with large delta x. Moreover, the absorption near the front end, as well as the absorption peak, is sensitive to the delay length. Therefore, it requires careful optimization of the delay length in a DCPD design.

3.2.3 The MMI width

As briefly mentioned in the last section, for a DCPD with given absorber length, certain beating length L_π of the MMI is required, and certain MMI width is selected so that L_π of the MMI can meet the requirement. In this section, the effects of MMI width on the absorption profile in a DCPD will be studied comprehensively.

In a DCPD, the width of MMI affects both the delta x and the supermode excitation in the MMI, which in turn largely affect the absorption profile. First, the width of the MMI directly relates to the delta x. As shown in Figure 3-2, when the input waveguide aligns with the left half of the MMI, and the absorber sits on top of and aligns with the right half of the MMI, the delta x is one half of the MMI width. In this case, for a very narrow MMI, the delta x will also be small, which is likely to increases the absorption in the forward section of the absorber, based on the discussion in section 3.2.1. On the other hand, when the MMI is too wide, as discussed in section 3.2.2, the

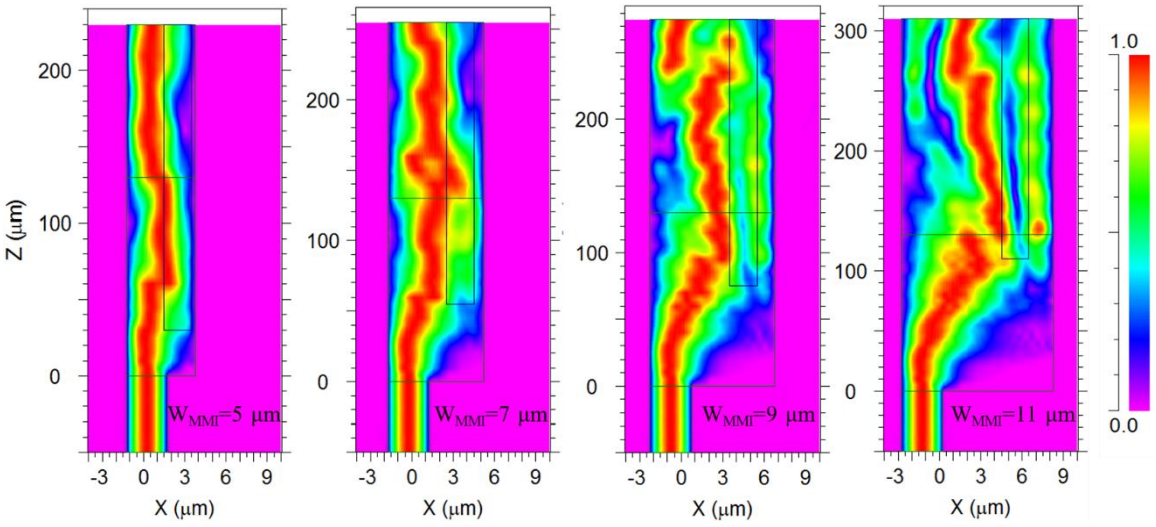

Figure 3-10 The top view of Beamprop simulated field distribution within the MMI in a DCPD with various width MMI. The delay length is set to be 0.75 times of L_π. The value of L_π is shown in Figure 3-7. The absorber, which is 2 μm x 200 μm, is centered on top of right half of the MMI.

resulted large L_π of the wide MMI requires a long absorber to achieve decent absorption efficiency, and reduces the RC limited bandwidth.

DCPD with various MMI width are simulated and studied. In Figure 3-10, the optical field distribution in the MMI of DCPD is simulated at four MMI widths, 5 μm, 7 μm, 9 μm, and 11 μm. In order to study the MMI width's effect on the absorption profile, some other waveguide parameters are determined under certain rules. The absorber is fixed at 2 μm wide and 200 μm long. The delay length is set to be 0.75 times of L_π for all 4 cases, so that when the absorber starts, similar portion of the input power is coupled to the right half of the MMI. The value of L_π is already shown in Figure 3-7. The MMI width is constant in this set of simulations. As shown in Figure 3-10, the input optical power couples into the MMI from the very left edge, and then gradually spreads out as it propagates in the MMI. The wider the MMI is, the more spreading out of the optical power and lower average optical power density will be. Besides, the addition of the absorber mesa changes the optical power distribution in the MMI. Comparing Figure 3-10 with Figure 3-8, with the

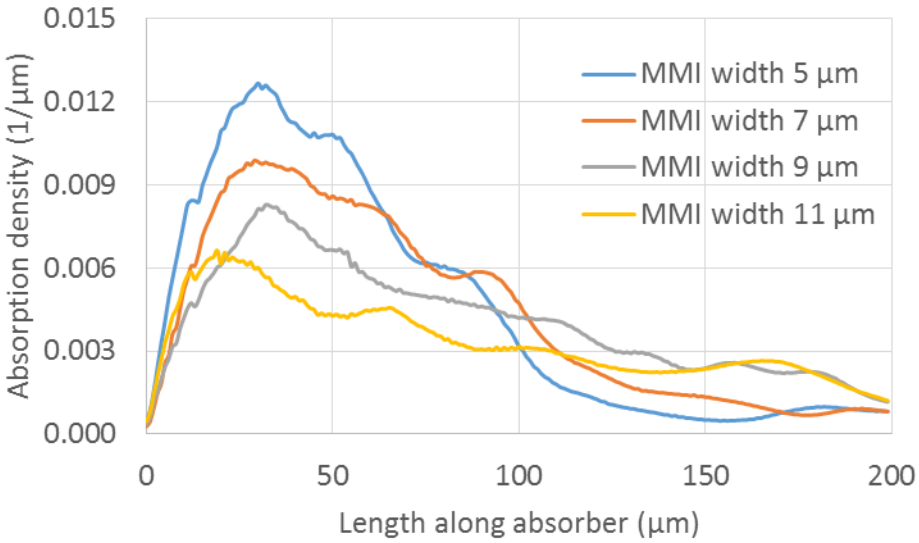

Figure 3-11 The absorption profile of the DCPDs in Figure 3-10.

presence of the absorber mesa, it is noticed that the majority of the optical power in the MMI is kept away from the region under the absorber mesa. This can be explained by the reduced coupling in an asymmetric coupler waveguide structure [8]. This phenomenon actually benefits designing a high power DCPD, as the fact of the absorber being away from the majority of the waveguide power in the x direction reduces the absorption density.

The absorption profile of the four simulated DCPDs are shown in Figure 3-11, with the absorption peak-to-average ratio (P/A) and absorption efficiency shown in Table 3-3. The average power density, as well as the absorption efficiency, is lower in a DCPD with wider MMI, which agrees with the discussion in the last paragraph. Besides, in a DCPD with narrower MMI, the absorption peak near the absorber front end is higher, and results in larger P/A and reduced absorption uniformity. This phenomenon, which also agrees with the discussion in the last paragraph, relates to the delta x and the large gamma supermode excitation, as discussed in section 3.2.1. The position of the absorption peak shown in Figure 3-11 also varies in DCPDs with varied MMI width, and is attributed to the change of two parameters, the MMI width and the delay length. In this section, the study of the MMI width focuses on its effect on the absorption density. Once

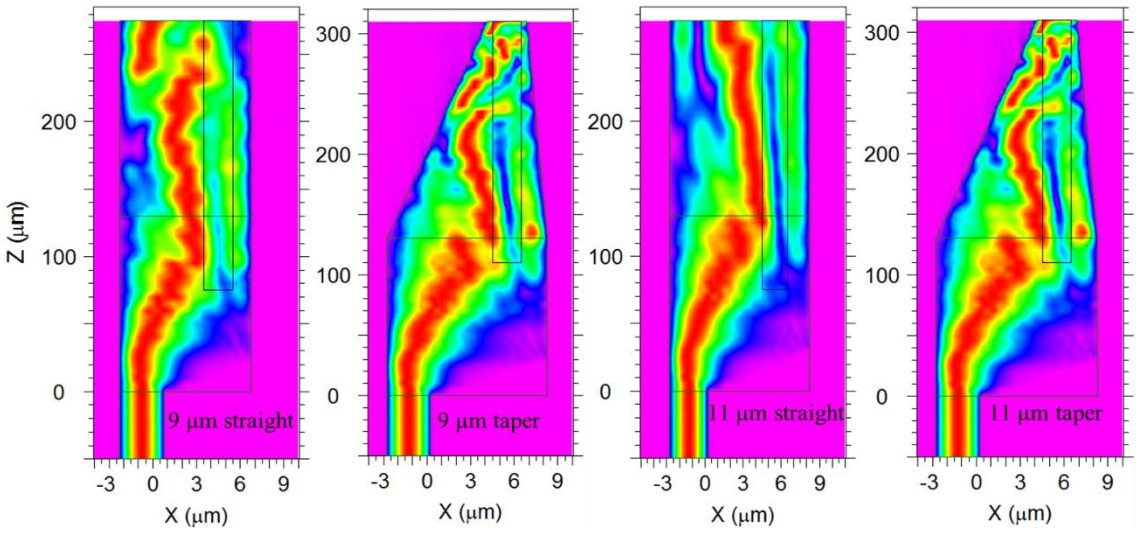

Figure 3-12 The top view of the field distribution in DCPD with straight MMI and tapered MMI. The simulations are done at MMI width of 9 μm and 11 μm, respectively.

Table 3-3 The absorption peak-to average ratio (P/A) and absorption efficiency of the DCPDs in Figure 3-10.

MMI Width (μm)	**5**	**7**	**9**	**11**
P/A	2.72	2.24	2.01	1.92
Absorption efficiency	0.92	0.87	0.82	0.68

the MMI width is set in a DCPD, how to shift the absorption peak positon is controlled by the delay length, as has been discussed in the last section.

The last topic of the discussion of this section is tapering MMI in a DCPD. In the previous DCPD study [1] [2], the MMI is tapered and the width at the back end is very close to that of the absorber, in order to increase the absorption efficiency. In this study, the power distribution and the absorption profile in a DCPD are compared between the straight MMI case and the tapered MMI case, as shown in Figure 3-12 and Figure 3-13. As expected, tapering the MMI pushes the majority of the waveguide power towards to the absorber in the rear section, and causes localized absorption peaks of the absorption profile. When the magnitude of those localized absorption peaks in the rear

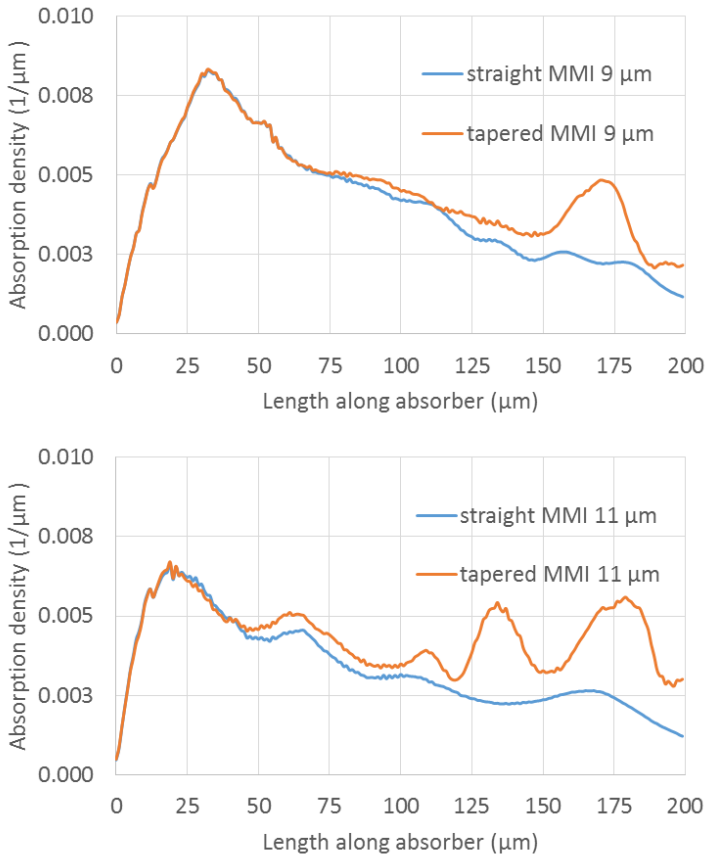

Figure 3-13 The absorption profile of the DCPD with straight MMI and tapered MMI. The simulations are done at MMI width of 9 μm and 11 μm, respectively.

section becomes greater than that of the absorption peak in the forward section, the approach of tapering MMI will degrade the absorption uniformity of DCPD. In the next section, alternative approach will be discussed for increasing the absorption efficiency without degrading the absorption uniformity in a DCPD.

3.2.4 The absorber width

The effects of the absorber area size and the absorber length are already well known in a WGPD. It has pointed out in section 2.1 that the absorber area of a PD relates to the RC time limited bandwidth. For a WGPD, as the optical power propagates along the length direction, the absorber length relates to the absorption efficiency. However, the effect of absorber width of a DCPD is not

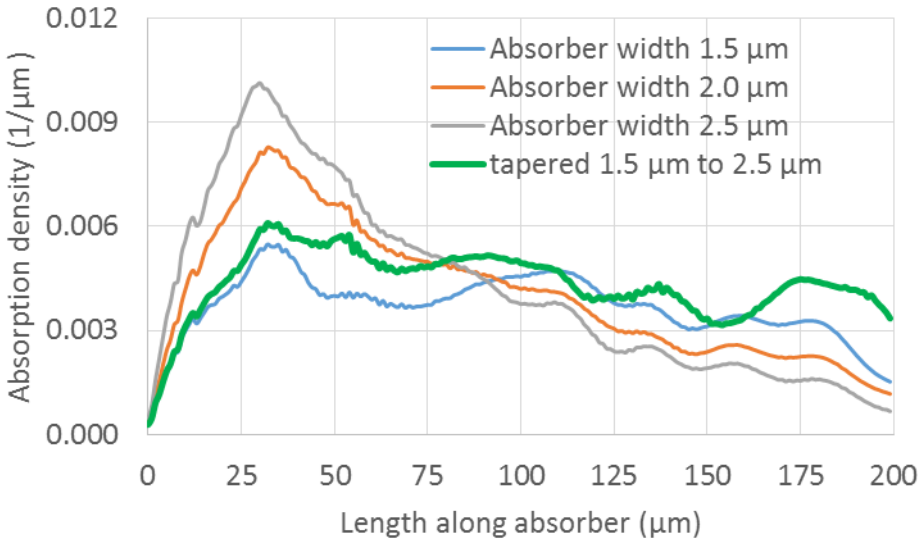

Figure 3-14 The absorption profile of the DCPDs with 4 different absorber width. The first three cases have constant absorber width at 1.5 μm, 2.0 μm, and 2.5 μm, respectively. The fourth case has the absorber linearly widened from 1.5 μm at the front end to 2.5 μm at the back end. The length of the absorber is 200 μm. The delay length is 75 μm. The MMI has constant width of 9 μm and length of 275 μm. The position of the input waveguide and the absorber relative to the MMI is the same with what is shown in Figure 3-10.

quite clear. In this section, the effect of absorber width on the absorption profile of a DCPD is studied.

In general, the absorber width will have two major effects in a WGPD. First, it affects the absorber area, and hence the RC time limited bandwidth. Second, it changes the area overlap between the absorber and the waveguide, which in turn changes the absorption per unit length. The absorption profile of a DCPD with constant width absorber is simulated at three absorber width, 1.5 μm, 2.0 μm, and 2.5 μm, as shown in Figure 3-14. The major difference of the 3 cases is the absorption density in the first 100 μm long absorber, with the wider absorber resulting in significantly larger absorption density, due to the larger area overlap between the absorber and the waveguide. Another difference of the absorption density appears in the second 100 μm long

absorber, with the wider absorber resulting in slightly smaller absorption density, due to the smaller available optical power in this section.

Improving the absorption efficiency without degrading the absorption uniformity is important for any photodiode. In the previous DCPD design, the approach of tapering the MMI is used to improving the absorption efficiency, but at a price of degraded absorption uniformity in the rear section of the absorber, as shown in Figure 3-13. The approach of tapering the absorber is proposed in this study, in order to increase the absorption efficiency of a DCPD, without degrading the absorption uniformity. The absorber is linearly widened from 1.5 μm at the front end to 2.5 μm at the back end, while the length is leave unchanged. In this case, the total area of the reverse-tapered absorber is still the same with that of the 2 μm x 200 μm straight absorber. Such a reverse-tapered absorber will reduce the absorption density in the forward section of the absorber, via the reduction of area overlap between the absorber and the MMI. Meanwhile, the slight widening of the absorber in the rear section, and hence the increase of area overlap between the absorber and the MMI, can increase the absorption density in the rear section of the absorber. In this case, the absorption is the forward section and the rear section is more balanced, and the absorption uniformity is improved without sacrificing the absorption efficiency. Moreover, as shown in Figure 3-15, the slight widening of the absorber in the rear section barely changes the optical distribution in the MMI, comparing to the significant change of optical distribution in a tapered MMI, which has been identified in the last section as the major cause of absorption uniformity degradation. The absorption profile of the DCPD with absorber widened from 1.5 μm to 2.5 μm is shown in Figure 3-14. Comparing to the absorption profile of DCPD with 1.5 μm constant width absorber in Figure 3-14, it shows increased absorption efficiency and very similar absorption uniformity. Comparing to the absorption profile of DCPD with tapered MMI in Figure 3-13 (a), it shows that tapering the absorber is a better approach for increasing the absorption efficiency, as it will not degrade the

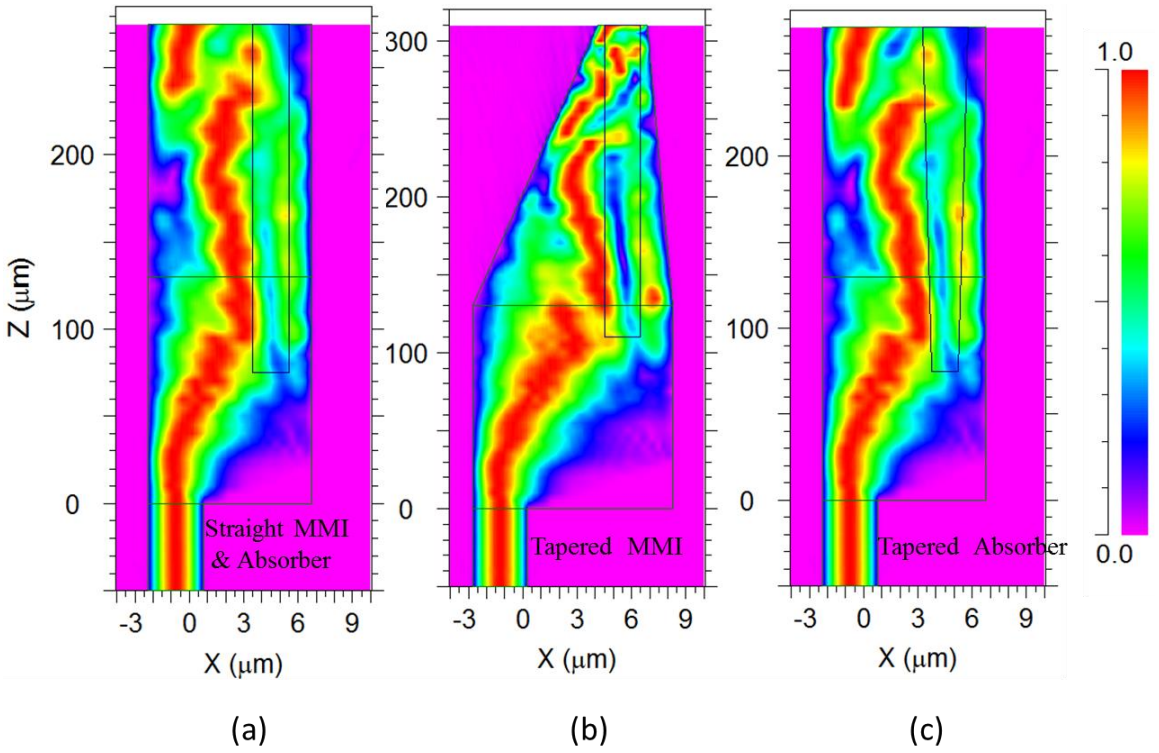

Figure 3-15 The optical field distribution in the MMI of DCPDs. The simulated DCPDs have the width of MMI and absorber vary differently in the z direction. In (a), both the MMI and the absorber have constant width. In (b), the absorber has constant width, and the MMI is linearly tapered from 9 μm to 3 μm in the last 170 μm long region. In (c), the MMI has constant width, and the absorber is linearly widened from 1.5 μm at the front end to 2.5 μm at the back end. Other than that, all 3 DCPDs have the same waveguide parameters. The delay length is 75 μm, the MMI width is 9 μm.

absorption uniformity.

3.2.5 The comparison between DCPD and the traditional WGPD

In the previous discussions of section 3.2, we have substantially discussed various waveguide parameters of DCPD. Some of the waveguide parameters, such as the delta x and the delay length, are unique to the DCPD and are not included in other WGPD. Some of the general waveguide parameters, such as the waveguide width and the absorber width, have also been

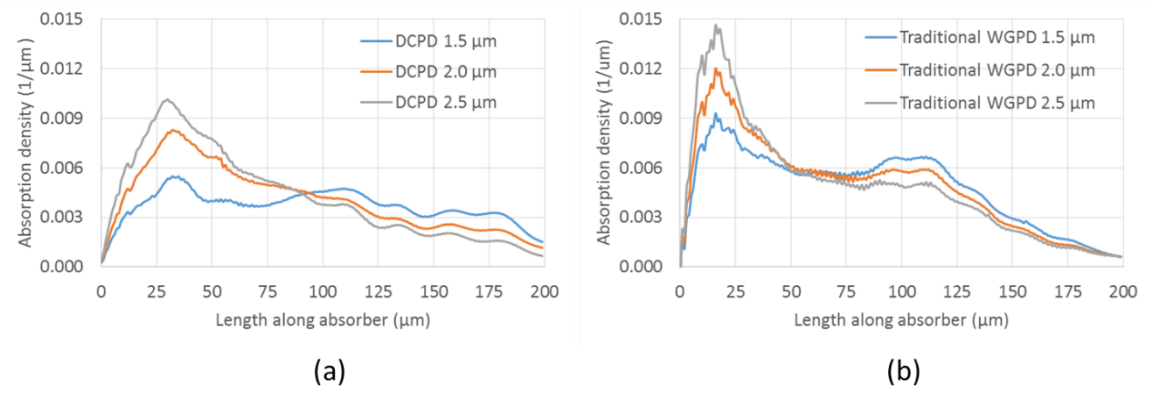

Figure 3-16 The absorption profile of a DCPD and a traditional WGPD with varied absorber width of 1.5 μm, 2.0 μm, and 2.5 μm. The waveguide width of both are fixed at 9 μm. The description of the DCPD structure is already shown in Figure 3-14. The description of the traditional WGPD structure is already shown in Figure 2-13.

discussed in the traditional WGPD in chapter 2 for their effects on the absorption profile. Therefore, in this section, the effects of the waveguide width and the absorber width on the absorption profile will be compared for the two important WGPDs discussed in this dissertation, the traditional WGPD and the DCPD.

For a given optical distribution in a waveguide with fixed width, the absorber width determines the area overlap between the absorber and the waveguide, which in turn changes the absorption per unit length. In this case, when it is near the absorber front end, where the available optical power are about the same, the absorption per unit length will be proportional to the absorber width. When it is further away from the absorber front end, where the available optical power becomes less in the wide absorber case, the absorption per unit length will no longer be proportional to the absorber width, and may even become inversely proportional to the absorber width. The above discussion is based on an assumption that the absorber width variation does not significantly change the optical distribution in the waveguide, which is usually true when the waveguide width is several times larger than the absorber width.

As shown in Figure 3-16, for a DCPD and a traditional WGPD with the same waveguide width of 9 μm, the comparison of absorption profile at various absorber width of 1.5 μm, 2.0 μm, and 2.5 μm show the absorber width effects that agree well with the discussion in the last paragraph. In this case, the absorption uniformity of both WGPD structure will be benefited from the adoption of reverse-tapered absorber discussed in section 3.2.4, with reduced absorption in the forward section and enhanced absorption in the rear section.

For a WGPD with a fixed width absorber, the waveguide width, plus the incident radiation pattern, determines the optical power distribution in the waveguide. In general, the waveguide width affects the average optical power density and the number of supported supermodes, and the incident radiation pattern affects the optical power distribution and the supermodes excitation. Although the supported supermodes may be the same in a traditional WGPD and a DCPD that have the same waveguide width, the number of excited supermodes is smaller in a traditional WGPD than that in a DCPD, due to the delta x difference discussed in section 3.2.1. As a result, for the two WGPDs with the same waveguide width, even when the average optical power density may be the same, the actual optical power distribution may be very different.

The absorption profile of a DCPD and a traditional WGPD, which have the absorber width fixed at 2 μm and the waveguide width varies, are shown in Figure 3-17. The corresponding average absorption density in the first 100 μm long absorber section and the peak-to-average absorption density ratio (P/A) of the whole device are shown in Figure 3-18. The calculation of the average absorption density does not use the whole absorber length, as the rear section absorption is not very efficient in the simulated cases. Those comparison at various waveguide width of 5 μm, 8 μm, and 11 μm show some similarity and difference of optical power distribution in the two WGPDs. First of all, for both WGPD structure, the larger the waveguide width is, the smaller the average absorption density will be. This observation is in good agreement with the discussion in the last

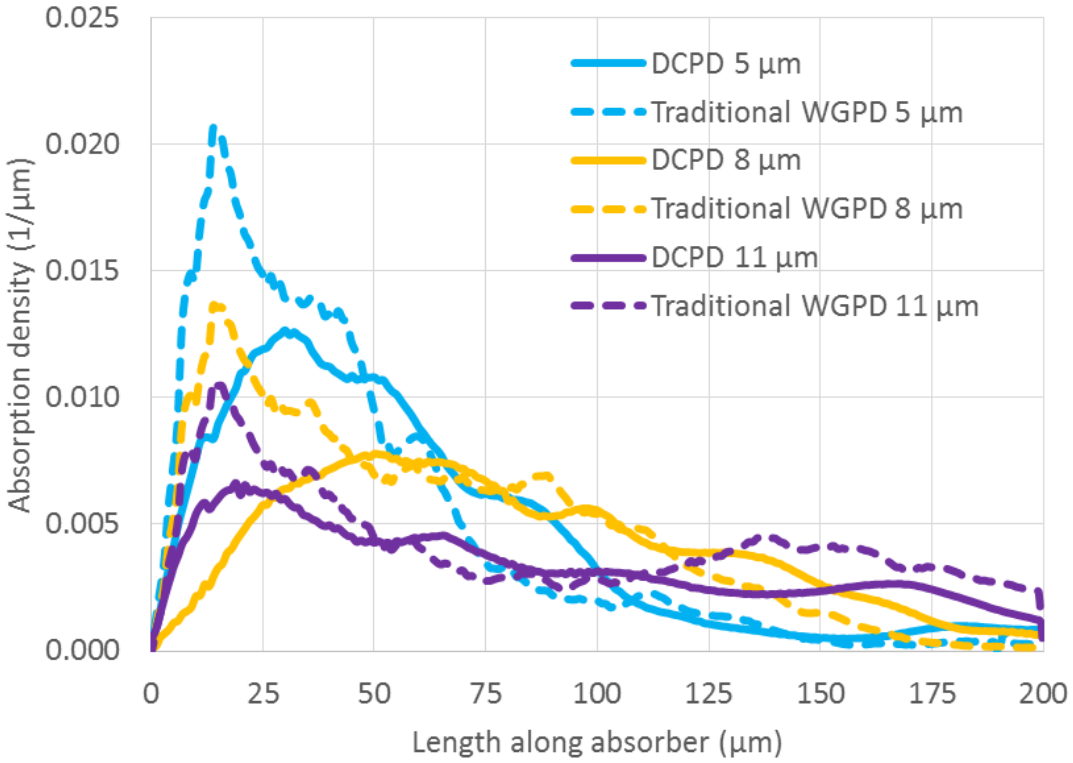

Figure 3-17 The absorption profile of a DCPD and a traditional WGPD with varied waveguide width of 5 μm, 8 μm, and 11 μm. The waveguide has no taper feature. The absorber width of both devices is fixed at 2 μm. The description of the DCPD structure is already shown in Figure 3-10. The description of the traditional WGPD structure is already shown in Figure 2-13.

paragraph that the waveguide width determines the average optical power density. In this case, widening the waveguide is effective to reduce the average absorption density in both WGPD structures. Second, in the first 100 μm long of the absorber, when the two WGPDs have the same waveguide width, the average absorption density of the DCPD is smaller than that of the traditional WGPD. According to Figure 3-18, for the average absorption density in the first 100 μm long of the absorber, it is about the same in a DCPD with 5 μm wide waveguide and in a traditional WGPD with 8 μm wide waveguide. Similarly, it is about the same in a DCPD with 8 μm wide waveguide and in a traditional WGPD with 11 μm wide waveguide. The above observations show that the absorption in the forward section is less crowded in a DCPD than in a traditional WGPD. Third,

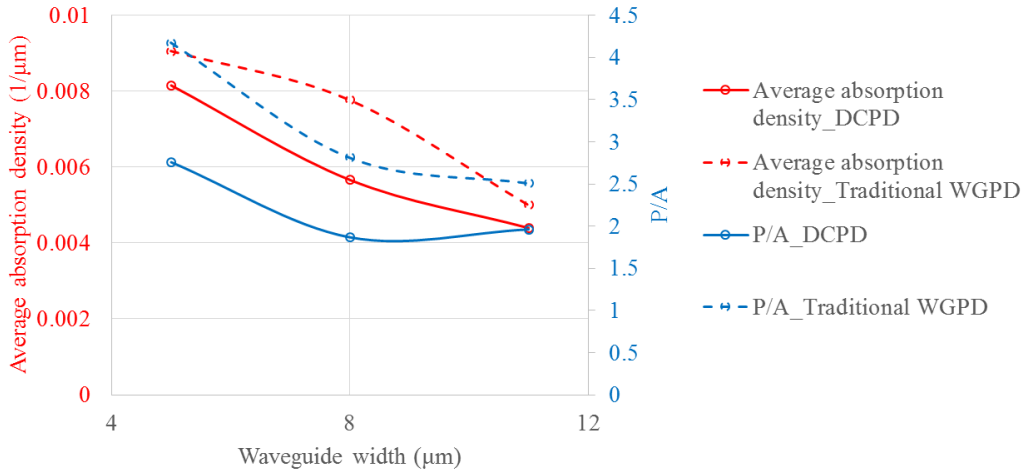

Figure 3-18 For the DCPD and the traditional WGPD simulated in Figure 3-17, the average absorption density of the first 100 μm long absorber section, and the peak-to-average absorption density ratio (P/A) of the 200 μm long absorber section.

when the waveguide width is the same, the absorption uniformity, which is characterized by P/A, is better in the DCPD than in the traditional WGPD. According to the supermode analysis in chapter 2, the absorption uniformity relates to the suppression of the large gamma mode and the enhancement of the preferred higher order mode, which have to rely on the optimization of the waveguide dimension in a traditional WGPD. However, in a DCPD, the large gamma mode excitation is suppressed by the intrinsic feature of the delta x, leaving the excitation of a number of preferred higher order modes. Therefore, better absorption uniformity is observed in the simulated DCPD case.

3.2.6 Summary

In summary, in order to gain a deeper understanding of this novel waveguide structure from the previous study, the waveguide structure of DCPD is analyzed in this section with the assistance of supermode analysis, Four important waveguide parameters are analyzed, they are the delta x, the delay length, the MMI width, and the absorber width. The supermode analysis shows the large

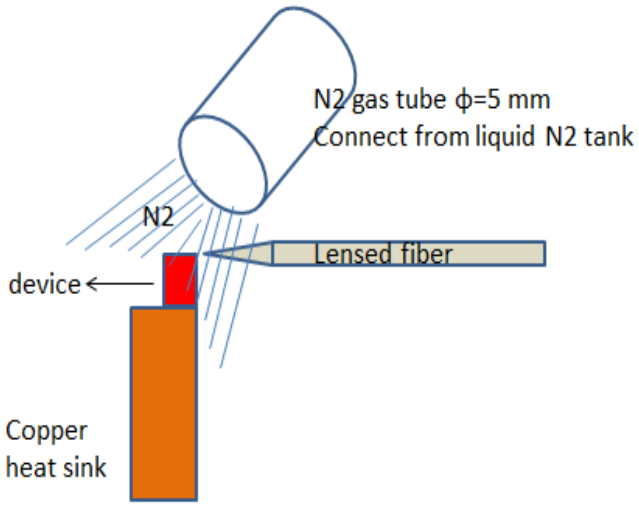

Figure 3-19 The DC optical power handling test setup.

forward section absorption density is less an issue in a DCPD than in a traditional WGPD, due to the delta x related suppression of the large gamma supermode. The large delta x will also results in inefficient absorption in the forward section and small absorption efficiency, which can be resolved by adding some delay length between the input waveguide and the absorber in the z direction. For a given absorber length, the beating length L_π is used to determine the delay length, as well as the MMI width. Tapering of the MMI down to as narrow as the absorber, which is used to increase the absorption efficiency in the previous DCPD study [1] [2], is pointed out to degrade the absorption uniformity. To resolve this issue, reverse-tapering the absorber is proposed to increase the DCPD absorption efficiency while maintaining the absorption uniformity. In the following discussion, a re-designed DCPD is introduced, based on the above discussion. The power handling capability of the re-designed DCPD, as well as its variances, will be experimentally studied.

3.3 Demonstration of high power DCPD

In order to study DCPD experimentally and demonstrate its high power handling capability, DCPDs are fabricated and measured on a MUTC2 epitaxial wafer, which differs from the MUTC1

epitaxial wafer used in [1] [2]with the much thinner absorbing layer. Traditional WGPD devices are also fabricated on the same wafer for comparison. The fabrication of DCPD is done by using photo-lithography and wet etching. The wafer is lapped down to ~100 μm thick and is cleaved into arrays, which then are mounted on a copper mount with thermal conductive Epoxy. The optical test of DCPD is performed in an ambience with low moisture and low temperature, which is created by gently blowing cool and dry N_2 gas around the mounted device, as shown in Figure 3-19. The thermal conductive copper mount and the low temperature N_2 gas ambience help the thermal dissipation in the device-under-test (DUT). The DUTs are aligned with a lensed SMF fiber with 2.5 μm diameter spot size of the near field. A reverse bias voltage is applied to the DUT, and the generated current is monitored by a current meter. At a given input optical power level and bias voltage, the current is recorded when the reading from the current meter is stable and maximized. As the dark current of the fabricated DCPD is of the ~nA order, the recorded current is considered as the photocurrent. In the power handling capability test, the above measurement is done with incremental input optical power until thermal failure occurs in the DUT. The optical power handling capability is characterized by the maximum average power density, which is calculated by dividing the product of the bias voltage and the highest recorded photocurrent by the absorber area size of the DUT.

Figure 3.20 shows the pictures of a thermally failed DCPD and traditional WGPD, in which the damaged absorber region is 80 μm long in the DCPD, while it is 12 μm long in the traditional WGPD. Although the damaged occurs around the absorber front end in both devices, the thermal failure is more localized in the traditional WGPD than in the DCPD. Very localized high temperature or thermal damage, which is related to the localized high absorption density, commonly shows up in a region that is close to the absorber front end in traditional WGPDs [1], [9], [10]. Therefore, it is important for the high power WGPD design to avoid the localized peak absorption near the absorber front end. The more extended damaged region in DCPD shown in

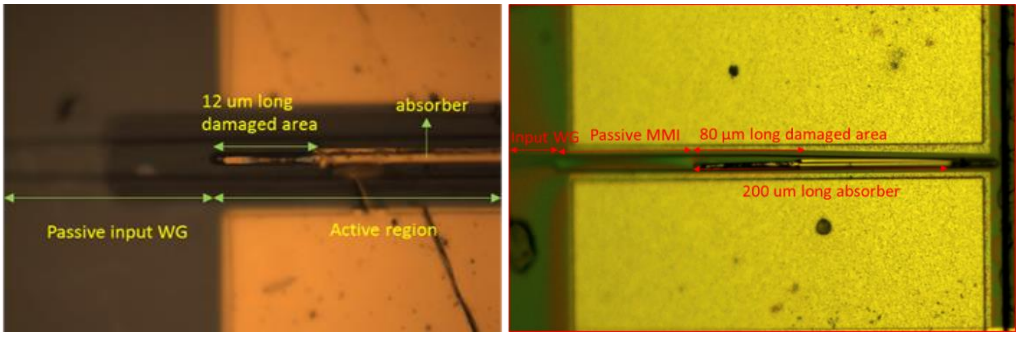

Figure 3-20 The picture of thermally failed traditional WGPD (a) and DCPD (b) during DC optical power handling test. Both devices are fabricated on the same MUTC2 wafer and are tested under the same condition. The traditional WGPD has 8 μm wide waveguide, the DCPD has 7 μm wide MMI.

Figure 3-20 indicates that DCPD design is able to not only spread the majority of the absorption in a wider range, but also pushes the absorption peak further away from the absorber front end. In this case, DCPD shows potential of being a good high power WGPD design. In the following discussion, the power handling capability test is done at DCPD with several kinds of waveguide parameter variations, the testing results are substantially discussed, and high power DCPD design is demonstrated and compared to other photodiode designs.

In the previous DCPD study [1] [2], the device performances with different absorber width and MMI width are discussed, with the delay length fixed at 90 μm for all cases. As discussed in section 3.2.2, the delay length plays an important role in adjusting the absorption density in the forward section of the absorber, which in turn affects the high power handling capability significantly. As shown in Figure 3-21, the delay length is varied in a DCPD with 9 μm wide MMI and 2 μm wide absorber, the responsivity is tested at incremental dc photocurrent until reaching the device thermal failure. While the responsivity is about the same for all three devices, the maximum photocurrent generated in the DCPD with 60 μm delay length is twice of that in the DCPD with 100 μm delay length. Please note the suggested delay length, which is $0.75*L_{\pi}$, is 75 μm for a

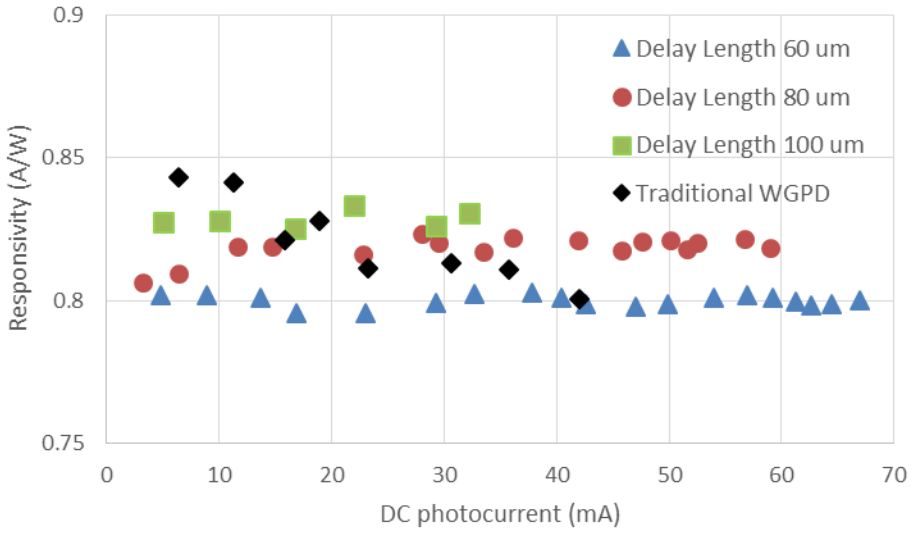

Figure 3-21 The dc optical power handling test of three DCPD devices with varied delay length, in comparison with the traditional WGPD device fabricated with the same waveguide dimension and the same layer structure with DCPD. The device responsivity is recorded at incremental dc photocurrent, and the recording stops right before the thermal failure of the tested devices. The tests are done under 4 volts reverse bias voltage. The DCPD waveguide parameters are as follows, the MMI width is 9 μm, the absorber is 2 μm wide, and 200 μm long.

DCPD with a 9 μm wide MMI, as discussed in section 3.2.2. The test results shown in Figure 3-21 indicates that the power handling capability can be improved in a DCPD with delay length being smaller than the suggested value, and can be degraded in a DCPD with delay length greater than the suggested value. Smaller delay length not only reduces the forward section absorption density, but also moves the absorption peak further away from the absorber front end, as discussed in section 3.2.2. Therefore, the power handling capability of the previous studied DCPD [1] can be improved by the optimization of the delay length. Moreover, the power handling capability of DCPD is compared to a traditional WGPD in Figure 3-21, with the two compared devices having the same dimension of the absorber and the waveguide. It shows that DCPD has better power handling

capability than the traditional WGPD, when the delay length is close or slightly less than the suggested value.

In the last paragraph, for a given waveguide (MMI) width, the delay length's effect in a DCPD is experimentally explored. In this paragraph, DCPD is compared to the traditional WGPD for their power handling capability at various waveguide width. As discussed in section 3.2.3 and section 3.2.5, the waveguide width determines the average power density in both the DCPD and the traditional WGPD, and the DCPD spread the optical power more evenly than the traditional WGPD, when the two have the same waveguide width. In this case, one the one hand, better power handling capability is expected in a DCPD, when it is compared to that in a traditional WGPD with the same width. On the other hand, better power handling capability is expected in a DCDP with larger waveguide width than that with smaller waveguide width. Both of the above predictions based on simulation agree with the experimental results shown in Figure 3-22. It is worth noting that the improvement of the power handling capability of DCPD with MMI width increasing from 7 μm to 9 μm is small, which indicates the existence of other factors other than the MMI width related average optical power that affect the power handling capability. As discussed in section 2.7.7, the power handling capability of a WGPD with non-uniform optical power distribution will be smaller than that of an ideal WGPD, even when the average optical power density of the two are the same. This reduction of the power handling capability is proportional to P/A. Therefore, it is very likely that when the MMI width increases from 7 μm to 9 μm, the P/A increases. This increase of P/A will affect the power handling capability in an opposite direction to what the reduction of the optical power density will do.

The DCPD with reverse-tapered absorber is also fabricated and tested, with its power handling capability shown in Figure 3-22. The effect of tapering the absorber is discussed in section 3.2.4, which points out that the adjustment of the absorber width effectively change the absorption

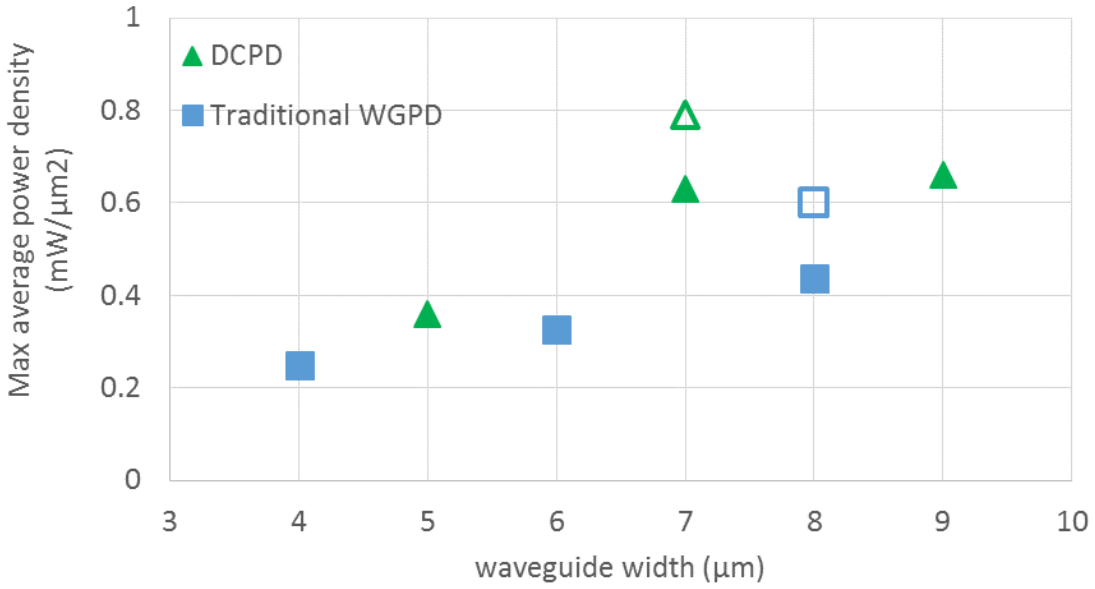

Figure 3-22 The maximum average absorption density of the DCPD and the traditional WGPD at various waveguide width. For the data points with solid marker, the absorber has constant width of 2 μm, and length of 150 μm. For the data points with empty marker, the absorber is reverse-tapered, as described in Figure 2-38. The data for the traditional WGPD with constant width absorber is collected from Figure 2-36. The 150 μm long absorber has two sections with equal length. The first 75 μm long section has the width linearly widened from 1.5 μm at the front end to 2 μm at the back end, and the second 75 μm long section has the width fixed at 2 μm. The waveguide width of the first section is fixed for both the DCPD and the traditional WGPD, and the waveguide width of the second section is linearly tapered down to 3 μm in the traditional WGPD, and is kept constant width in the DCPD. The delay length of DCPD with 5 μm, 7 μm, and 9 μm wide MMI is 35 μm, 45 μm, and 60 μm, respectively.

per unit length, and is a good approach to improve the absorption uniformity in a WGPD. Therefore, tapering absorber is applied to both DCPD and traditional WGPD, and experimental results in Figure 3-22 show significant improvement of the power handling capability by tapering the absorber. As the measured responsivity is very close between the reverse-tapered absorber device and the straight absorber device, it can be deduced that the reverse-tapered absorber increases the power handling capability via reducing the peak absorption density, or P/A.

Table 3-4 The measured responsivity (A/W) of the DCPD and traditional WGPD that have different absorber lengths. The two types of WGPD, which have reverse-tapered absorber, are already shown in Figure 3-22. The waveguide width of the DCPD and the traditional WGPD is 7 μm and 8 μm, respectively. The absorber has two sections. The first 75 μm long section has the width linearly widened from 1.5 μm at the front end to 2 μm at the back end, and the second section has the width fixed at 2 μm. The waveguide width of the first section is fixed for both the DCPD and the traditional WGPD, and the waveguide width of the second section is linearly tapered down to 3 μm in the traditional WGPD, and is kept constant width in the DCPD.

Absorber Length (μm)	DCPD	Traditional WGPD
100	0.42	0.65
150	0.76	0.78
200	0.79	0.79

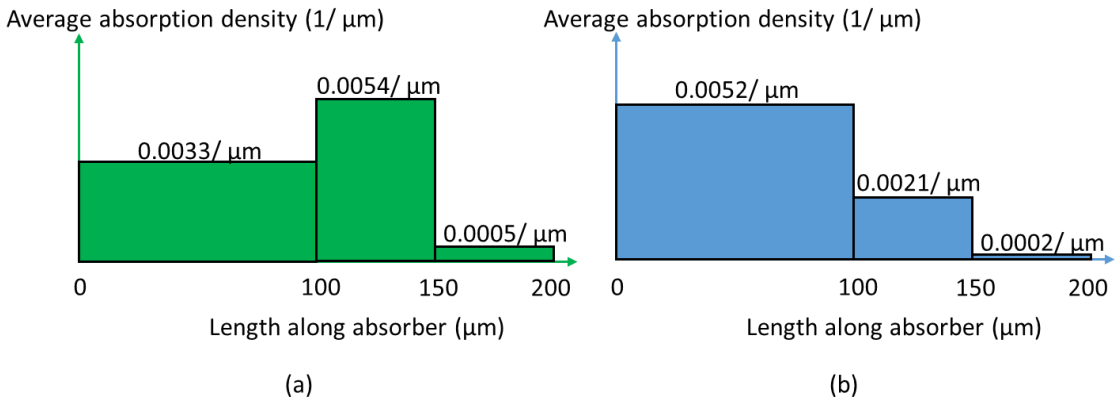

Figure 3-23 The average absorption density in different sections of the DCPD (a) and the traditional WGPD (b) that are tested and shown in Table 3-4.

In the above discussion, the overall absorption uniformity in the entire absorber is studied. In the following discussion, the absorption uniformity in different sections of the absorber is experimentally studied. In the experiment, DCPDs with the same waveguide dimension but different absorber lengths are fabricated in the same round, and are tested under the same condition. The three absorber lengths are 100 μm, 150 μm, and 200 μm. The responsivity and the power

handling capability of these DCPDs are tested and compared. Similar experimental study is also done for traditional WGPDs. Assuming the same material and fabrication quality for all tested devices, and the same optical launching and coupling condition, the tested results allow us to look deeper into the absorption in different sections of the absorber in a WGPD. The responsivity test results are shown in Table 3-4, which show very different absorption density in different sections, as shown in Figure 3-23. The average absorption density of each section is calculated by dividing the absorption efficiency in each section by the section length. The absorption efficiency of the first 100 μm is obtained from the responsivity of the device that has 100 μm long absorber. The absorption efficiency of the next 50 μm is obtained from the responsivity difference of the devices with 150 μm long absorber and the device with 100 μm long absorber. The absorption efficiency of the last 50 μm is obtained from the responsivity difference of the devices with 200 μm long absorber and the device with 150 μm long absorber. From the results in Figure 3-23, it is shown that the DCPD and the traditional WGPD have very different absorption distribution along the absorber. On the one hand, the average absorption density of the first 100 μm section is 2.5 times of that of the next 50 μm section in the traditional WGPD, while this ratio is only 0.60 in the DCPD. It is noticed that this ratio of 0.60 is not obvious from the simulation results in Figure 3-17, in which this ratio is greater than 0.60. The explanation is given as follows. First, the measured ratio of 0.60 is for a DCPD with reverse-tapered absorber, while what is shown in Figure 3-17 is for constant width absorber. The reverse-tapered absorber will result in absorption density reduction in the forward section, as shown in Figure 3-14. Second, the setting of delay length is different for the two cases. The ratio of 0.60 is measured in a DCPD with delay length smaller than 0.75 $L\pi$, while what is shown in Fig. 3.17 has delay length equals to 0.75 $L\pi$. This delay length difference will affect the forward section absorption density, as discussed in section 3.2.2. Because of the above two reasons, what is simulated in Figure 3-17 does not contradict to what is measured here. On the other hand, the average absorption density of the first 100 μm section is about 60% higher in the

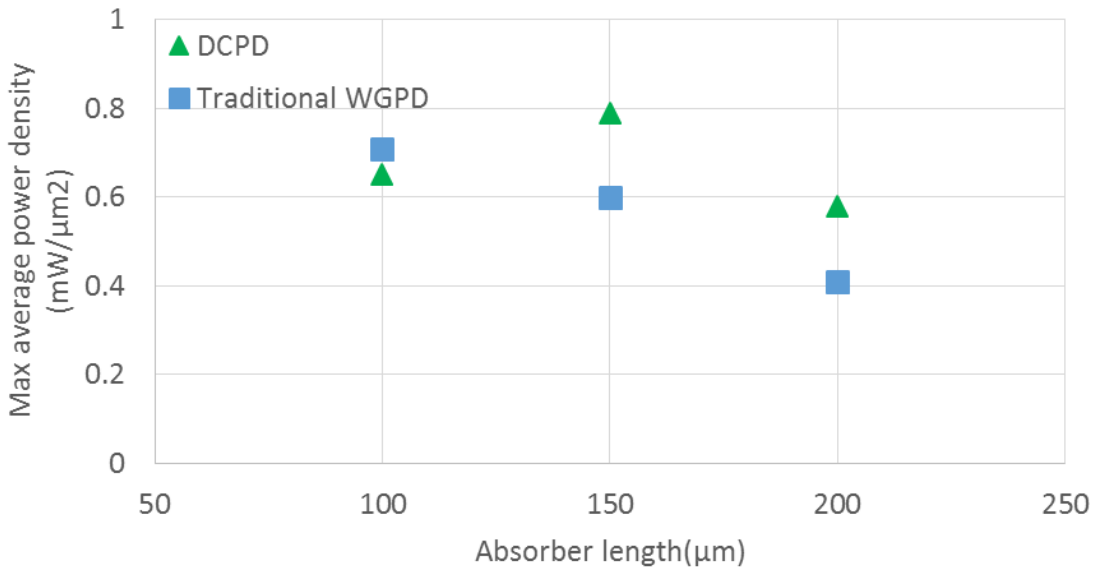

Figure 3-24 The maximum average power density of the DCPD and the traditional WGPD at various absorber length. The tested devices are the same with those shown in Table 3-4.

traditional WGPD than that in the DCPD, the average absorption density of the next 50 μm section is 160% higher in a DCPD than that in a traditional WGPD, and the average absorption density of the last 50 μm is very low in both devices. From the above comparison, it is shown that the absorption is more suppressed in the first 100 μm section in the DCPD than in the traditional WGPD, the high average absorption density section is further away from the absorber front end in the DCPD than in the traditional WGPD, and most of the absorption completes in the first 150 μm long absorber in both devices. It is worthy to note that the simulated average absorption density shown in Figure 3-18 is about 30% to 40% higher than the measured average absorption density shown in Figure 3-23. This difference is due to the combined effects of several factors, including the coupling reflection at the input waveguide facet, various optical losses in the responsivity measurement, waveguide parameter difference between the simulated WGPD and the tested WGPD, and simulation inaccuracy. Based on these observations, the power handling capability difference of the two kinds of WGPDs, which is represented by the maximum average absorption density, can

be predicted. The power handling capability tests are done for the devices shown in Table 3-4, and the related maximum average power density are shown in Figure 3-24. As mentioned at the beginning of this section, the maximum average power density of a WGPD is calculated by dividing the product of the bias voltage and the highest recorded photocurrent by the absorber area size. In this case, the power handling capability depends on how efficient and how uniform the absorption is across through the whole absorber area. In the following discussion, the tested results of the power handling capability of various devices shown in Figure 3-24 will be discussed. First, the drop of the maximum average power density of the 200 μm long absorber case relates to the inefficient absorption in the last 50 μm long absorber section, as shown in Figure 3-23. To resolve this issue, approaches that can reduce the average absorption density in the first 150 μm long absorber section can be used, such as adding a low refractive index InP diluting layer, increasing the waveguide width, and reducing the absorber width. It is worthy to note again that the selection of absorber dimension has to consider both the power handling capability and the bandwidth. Second, when the absorber length increases from 100 μm to 150 μm, the maximum average power density increases in the DCPD, and decreases in the traditional WGPD. As the power handling capability depends on how efficient and how uniform the absorption is across through the absorber area, it indicates the tested DCPD's absorption is less efficient and uniform in the first 100 μm long absorber section than in the next 50 μm long absorber section, while it is the opposite for the tested traditional WGPD. This difference relates to how the two WGPD structures differ in exciting the modes and distributing the optical power in the waveguide. For the tested traditional WGPD, the optical power couples mostly into the fundamental mode, whose characteristic attenuation length is less than 100 μm, as shown in Figure 2-23. Even though the large gamma mode interference and the higher order mode interference adjust the exponential decay distribution of the fundamental mode power, most of the absorption will occur within the first 100 μm long absorber section, leaving less total available absorption in the next 50 μm long absorber section. For the tested DCPD,

the optical power couples into a larger number of modes than in the traditional WGPD, the characteristic attenuation length of these excited supermodes varies, and the absorption distributes more extensively in the z direction. As shown in Table 3-2, when the two WGPDs has similar waveguide width, there are more excited modes in the DCPD, the confinement factor of most of which is several times smaller than that of the fundamental mode in the traditional WGPD. This explains why the majority of the absorption happens in the first 100 μm long absorber section in the traditional WGPD, and it is more extensive in DCPD. Moreover, the re-designed DCPD purposely reduces the forward section absorption by using small delay length, which pushes the majority of the absorption further away from the absorber front end, as shown in Figure 3-9. In this case, it is understandable that the absorption efficiency and uniformity is better in the next 50 μm long absorber section in DCPD. The above explanations are based on assumptions of the same material and fabrication quality for all devices, and the same optical launching and coupling condition. Third, comparing to the maximum average power density in the traditional WGPD, it is 8.5% lower in the DCPD when the absorber is 100 μm long, and it is 32% higher in the DCPD when the absorber is 150 μm long. The better power handling capability performance in a DCPD with 150 μm long absorber relates to the more suppressed absorption in the forward section in the re-designed DCPD, which is achieved by reverse-tapered absorber and reduced delay length. In summary, comparing to the tested traditional WGPDs, the tested DCPDs effectively reduce the absorption in the forward section, and push the majority part of the absorption further away from the absorber front end. This difference of the absorption distribution in the tested DCPD and the traditional WGPD agrees well with the observations from the damage distribution in Figure 3-20.

In the previous discussion of this section, experimental studies have been done to several DCPD variations, which are also compared to their traditional WGPD counterparts. These studies have shown good agreements between the simulations and the testing results for the absorption distribution, and verify the power handling capability of the re-designed DCPD outperforms that

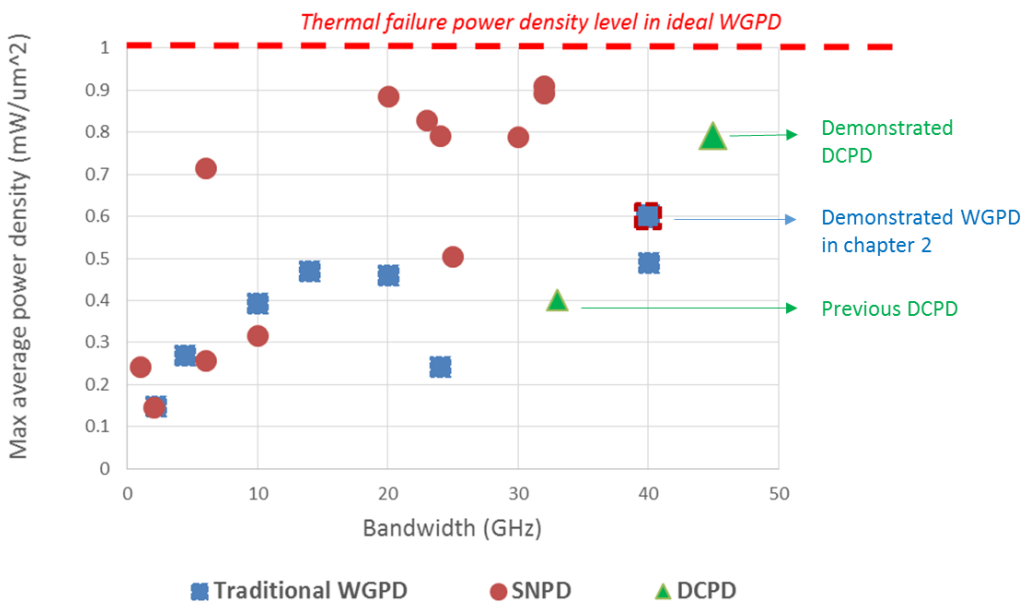

Figure 3-25 The comparison of the failure power density between the demonstrated DCPD and other reported WGPDs. The unlabeled WGPDs and SNPDs listed in the plot are the same with the one in Figure 2-40. For the demonstrated DCPD, the absorber has two sections. The first 75 μm long section has the width linearly widened from 1.5 μm at the front end to 2 μm at the back end, and the second section has the width fixed at 2 μm. The MMI width is 7 μm.

of the traditional WGPD in several cases. Comparing to the pre-studied DCPD [1], the improved power handling capability of the re-designed DCPD is attributed to several factors. First, based on the study in section 2.10.7, the adoption of layer structure that has smaller average waveguide confinement factor can reduce the overall absorption density, and benefit the high power WGPD design. In the re-designed DCPD, the reduction of the average waveguide confinement factor is achieved by reducing the absorber thickness from 0.65 μm in the previous DCPD to 0.20 μm. Second, the MMI width is optimized for the given absorber length, as discussed in section 3.2.3. Third, the absorber is properly tapered to improve the absorption uniformity. Fourth, the delay length is reduced to further reduce the absorption peak in the forward section. Last, the power handling capability test of the re-designed DCPD is in a more constant low temperature and dry

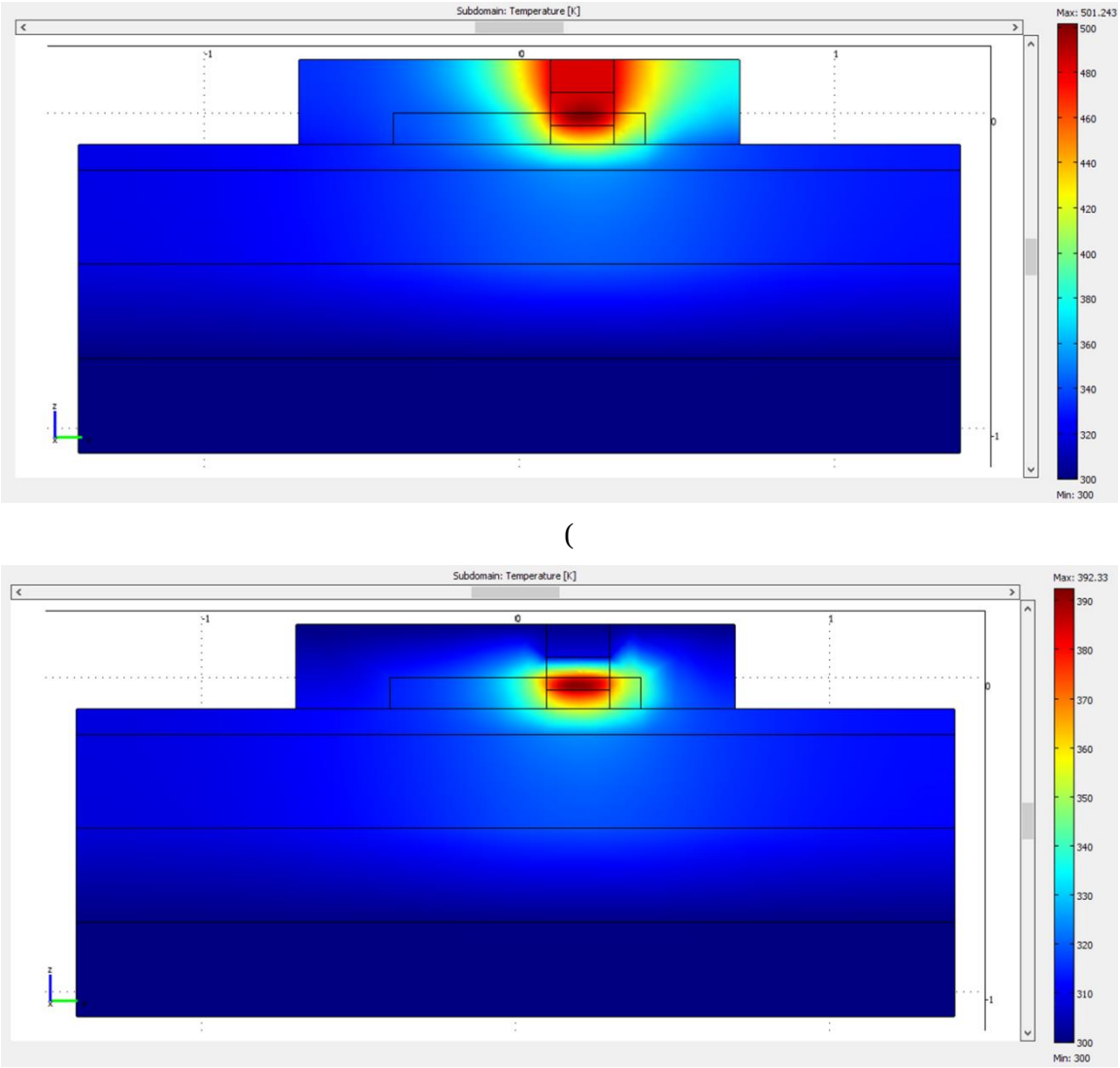

Figure 3-26 The simulated thermal distribution of the DCPD with bottom heat sink only (a), and with both bottom and top heat sink (b). The area of the heat source, which has the highest temperature in the two figures, is 2 μm wide, and 0.4 μm high. The heat density of the heat source is 2 mW/ μm^3.

ambience. In Figure 3-25, the power handling capability of a selected re-designed DCPD is demonstrated and compared to that of the previous DCPD, the traditional WGPD demonstrated in chapter 2, and some other traditional WGPDs from the literatures. For the re-designed DCPD with absorber area size close to 300 μm^2, at -4 V dc bias, the highest recorded photocurrent is 59.2 mA,

which corresponds to a maximum average power density of 0.79 mW/μm^2. Based on the collected data, the maximum average power density of the demonstrated DCPD is larger than that of the previous DCPD, and other traditional WGPDs, including the experimentally demonstrated traditional WGPD in Chapter 2. Although it is still smaller than that for the ideal WGPD, this demonstrated maximum average power density represents a big improvement of the power handling capability of WGPD whose bandwidth is close to 50 GHz.

There is still a gap of power handling capability between the demonstrated DCPD and the ideal WGPD, as shown in Figure 3.-25. In order to narrow down this gap, a suggestion is made here for the future DCPD study. In the previous discussion of DCPD, we have been focusing on discussing how to make the heat generation more uniform, and have not paid too much attention to the heat dissipation. As the limiting factor of the power handling capability for the re-designed DCPD is the heat accumulation induced device thermal failure, it is expected that when the heat dissipation inside the device is improved, the thermal failure current level will be increased. For the tested DCPD, the heat sink is at the bottom side (the substrate side), and the air is at the top side. In this case, the generated heat will have poor upwards dissipation, and it can be improved by improving the thermal conductivity of the top side ambience, such as adding a heat sink. As

shown in Figure 3-26, by adding a top heat sink to the current DCPD design, the highest temperature inside the DCPD will be 20% lower.

3.4 Summary

In this chapter, the supermode analysis is applied to analyze DCPD, which is a previously studied novel WGPD design in our group. The DCPD is re-designed, with the guidance of the theoretically analysis and simualtions. DCPD variations are fabricated and tested, and good agreements are obtained between the simulations and the testing results for the absorption distribution. The power handling capability of the demonstrated DCPD is greater than that of the previous DCPD, and other traditional WGPDs.

From the supermode analysis and simulation of the DCPD, deeper understandings are gained. Four important waveguide parameters are analyzed and simulated for better absorption uniformity in a DCPD. They are the delta x, the delay length, the MMI width, and the absorber width. The supermode analysis shows the forward section absorption density in a DCPD can be smaller than that in a traditional WGPD, due to the delta x related suppression of the large gamma supermode. The large delta x will also results in inefficient absorption in the forward section and small absorption efficiency, which can be resolved by adding some delay length between the input waveguide and the absorber in the z direction. For a given absorber length, the beating length L_π is used to determine the MMI width, as well as the delay length. Tapering of the MMI down to as narrow as the absorber, which is used to increase the absorption efficiency in the previous DCPD study, is point out to degrade the absorption uniformity. To resolve this issue, tapering the absorber is proposed to increase the DCPD absorption efficiency while maintains the absorption uniformity.

There are several major differences between the re-designed DCPD and the traditional WGPD. First, the suppression of the large gamma supermodes in the DCPD is effectively achieved by the offset in the x direction, without sacrificing the absorption efficiency. In comparison, the suppression of the large gamma supermodes in the traditional WGPD relies on the adjustment of the waveguide dimension or the layer structure, while with limited effect, it usually also results in the reduction of the absorption efficiency. Because of this difference, the absorption density in the forward section can be much easier controlled in DCPD than in traditional WGPD. Second, the preferred higher order modes, which improve the absorption uniformity in the rear section of the absorber, are excited more easily in DCPD than in traditional WGPD. Because of these two major differences, good absorption uniformity and great power handling capability can be achieved in the re-designed DCPD.

Comparing to the pre-studied DCPD [1], the improved power handling capability of the re-designed DCPD is attributed to several factors. First, in the re-designed DCPD, the reduction of

the average waveguide confinement factor is achieved by reducing the absorber thickness. Second, the MMI width is optimized for the given absorber length, as discussed in section 3.2.3. Third, the absorber is properly reverse-tapered to improve the absorption uniformity. Fourth, the delay length is reduced to further reduce the absorption peak in the forward section. Last, the power handling capability test of the re-designed DCPD is in a more constant low temperature and dry ambience.

Various waveguide parameters are optimized for a high power DCPD design, which demonstrates measured maximum power density of 0.79 $mW/\mu m^2$, with ideal RC bandwidth being close to 50 GHz. This demonstrated DCPD shows better power handling capability than that of any other traditional WGPDs with similar bandwidth, including the experimentally demonstrated traditional WGPD in Chapter 2, and the previously studied DCPD.

With the deeper understandings of how to design high power DCPD, and the demonstration of great power handling capability in the re-designed DCPD, the DCPD can meet the high power high bandwidth requirement for the next generation high speed Ethernet network.

3.5 References

1. M. N. Draa, J. Bloch, D. Chen, D. C. Scott, N. Chen, S. B. Chen, X. Yu, W. S. C. Chang, and P. K. L. Yu, "Novel directional coupler waveguide photodiode-concept and preliminary results," *Optics Express*, vol. 18, no. 17, pp. 17729-17731 (2010)

2. M. N. Draa, *High Power High Linearity Waveguide Photodiodes: Measurement, Modeling, and Characterization for Analog Optical Links*, University of California, San Diego (2010).

3. H. Jiang and P. K. L. Yu, "Waveguide integrated photodiode for analog fiber-optics links," *IEEE Trans. Micro. Theory Tech.*, vol. 48, no. 12, pp. 2604-2610 (2000).

4. N. Michel, V. Magnin, J. Harari, A. Marceaux, O. Parillaud, D. Decoster, and N. Vodjdani, "High-power evanescently-coupled waveguide photodiodes," *IEE Proceedings of Optoelectron.*, vol. 153, no. 4, pp. 199-204 (2006).

5. T. S. Liao, P. Mages, P. K. L. Yu, "Investigation of the high power integrated uni-traveling carrier and waveguide integrated photodiode," Proceedings of IEEE MTT-S Digest, pp. 155-158 (2003).

6. J. Klamkin, A. ramaswamy, L. A. Johansson, H. F. Chou, M. N. Sysak, J. W. Raring, N. Parthasarathy, S. P. DenBaars, J. E. Bowers, and L. A. Coldren, "High output saturation and high-linearity uni-traveling-carrier waveguide photodiodes," *IEEE Photonics Technol. Lett.*, vol. 19, no. 3, pp. 149-151 (2007).

7. W. S. C. Chang, *Fundamentals of Guided-Wave Optoelectronic Devices*, Cambridge University Press, Cambridge, UK (2010).

8. W. S. C. Chang, *Principles of Lasers and Optics*, Cambridge University Press, Cambridge, UK (2005).

9. J. E. Bowers, M. Piels, A. Ramaswamy, and T. Yin, "High Power Waveguide Ge/Si Photodiodes," *Annual meeting of the Electrochemical Society*, vol. 33, no. 6, pp.729-738 (2010).

10. S. D. McDougall, M. J. Jubber, O. P. Kowalski, J. H. Marsh and J. S. Aitchison, "GaAs/AlGaAs waveguide pin photodiodes with non-absorbing input facets fabricated by quantum well intermixing," *Electron. Lett*., vol. 36, no. 8, pp. 749 – 750 (2002).

Chapter 4 Cascaded optical band pass filter in Radio-over-Fiber link

4.1 Introduction

In a fiber optic link, the optical loss of fiber has to be considered when the transmission distance is tens of kilometers and beyond, due to the limited transmitter optical power and receiver sensitivity. Due to the inherent low optical loss in the standard single mode fiber SMF28, wavelength around 1550 nm is preferred in the long distance fiber optic link, even though the fiber dispersion characteristic is stronger than using other wavelengths. However, for amplitude modulated signals with double sidebands (DSB), the received signal power will suffer from the periodical variation, because the fiber dispersion results in different phase shifts between the lower sideband (LSB) and upper side band (USB) of the DSB. This phenomenon is called power fading. Although other modulation schemes that do not involve amplitude modulation, such as phase modulation, frequency modulation, and polarization modulation, do not suffer from power fading, the corresponding modulator and detector usually require more complex hardware than the amplitude modulation scheme. Therefore, for a cost-effective design of fiber optic link, amplitude modulation is usually preferred. In a long distance fiber optic link, the fiber dispersion accumulates over long fiber and can lead to very strong power fading. In order to solve the power fading issue, various techniques have been proposed, such as using dispersion compensation fiber (DCF) for pre-compensation or post-compensation [1], and adopting optical single sideband (OSSB) modulation technique [2] [3]. The effect of DCF approach is very fiber length and signal frequency dependent, and limits its applications in resolving the power fading issue. In contrast, by suppressing one of the two sidebands, the OSSB approach addresses the root causes of problems,

and is more versatile than the DCF approach. Therefore, OSSB modulation has found wide use in fiber optic link to address the power fading issue.

Multiple techniques have developed to implement OSSB, including optical heterodyning [4] [5], OSSB modulator [6]-[9], and optical filtering [10] [11] [12]. Among them, optical filtering method is most cost effective. Optical heterodyning achieves OSSB modulation by combining two optical carriers of different wavelength. The two optical carriers have to be generated either from two different lasers, or within the one single laser that operates in two modes. Therefore, the deployment of optical heterodyning leads to issues of cost or even availability. One relatively simple design of OSSB modulators uses a dual-electrode Mach-Zehnder modulator that is driven by electrical signals with a 90 degree phase shift. Other designs of OSSB modulators also use electrical signals with a 90 degree phase shift to drive either multiple modulators in series or in parallel. However, those OSSB modulators rely on non-standard electrical designs, and could also lead to issues of cost and fractional signal bandwidth. In contrast, optical filtering uses the narrow bandpass optical filters that are widely adopted in the dense wavelength division multiplexing (DWDM) systems, and hence becomes a more preferred approach for OSSB modulation.

The power fading drawback can be largely alleviated when narrow bandpass optical filters are adopted, which have been demonstrated via different optical filter schemes [10] [11]. However, the majority of these filtering approaches also reduces the optical modulation index *m*, due to the loss of half of the signal power. In practice, dispersion-managed transmission which maintains a high optical modulation index, while keeping low distortion level, is preferred for the sake of large CNR [13]. This chapter proposes and demonstrates a novel yet practical approach of cascading four identical off-the-shelf 100 GHz DWDM optical bandpass Fabry-Perot filters into the fiber link, which not only largely minimizes the power fading effect, but also enhances *CNR* and maintains the distortions at a low level. The distortions are further characterized and compared between links

using single filter and cascaded filter respectively, which provides insight on how the cascaded filter maintains the linearity while mitigates the power fading.

4.2 Power fading effect in a long distance fiber optic link

For intensity modulated signals with double sidebands (DSB), because the fiber chromatic dispersion results in different phase shifts accrued, after a long propagation distance, between the lower sideband (LSB) and upper side band (USB) of the DSB, the signal power generated in the receiver suffers from the periodical variation. This phenomenon is called power fading. In the following discussion, the two factors, chromatic dispersion and DSB modulation, are briefly discussed.

Chromatic dispersion is caused by the fact that single mode glass fibers transmit light of different wavelengths at different speeds. There are two major types of chromatic dispersion that cause power fading: material dispersion and waveguide dispersion. Material dispersion is caused by the dependence of light speed on the optical frequency, via the variation of the optical frequency dependent refractive index of a homogenous material. Besides material dispersion, there is waveguide dispersion in an optical fiber, due to the fact that the fiber mode profile, which determines the amount of the fields overlap between core and cladding, depends strongly on the optical frequency resulted from the waveguide dimension and refractive index profile. As the refractive index of the core and cladding of fiber is different, the light travels at different speed in the two sections of fiber. The permissible modes will be discrete, and meet the boundary condition at the interface, with speed somewhere between the two speeds. Therefore, the optical frequency dependent fiber mode profile will result in optical frequency dependent light speed in a fiber, and causes waveguide dispersion.

In a DSB modulation, the optical carrier at an optical frequency f_c is modulated by a signal frequency of f_s, and produces two sidebands at optical frequencies of (f_c-f_s) and (f_c+f_s), respectively. Because of the material dispersion and waveguide dispersion of single mode fiber, when

transmitting through a single mode fiber, the two sidebands, which have different optical frequencies and travel at different speeds, will accrue different phase relative to the optical carrier. This phase difference $\Delta\varphi_s$ is a function of the subcarrier frequency, the transmission distance over the fiber, and the dispersion characteristic of the fiber. When the optical carrier and the two sidebands are detected by a square law photodetector, the USB and LSB beat with the optical carrier simultaneously and generate the detected electrical signal. In this case, the phase difference of the two sidebands causes the amplitude cancelling of the detected electrical signal, and causes power fading.

The discussion of power fading in this chapter is restricted to subcarrier fiber optic link, which differs to baseband fiber optic link in that the data is multiplexed to a subcarrier frequency before modulating an optical carrier, instead of directly modulates an optical carrier. In this case, f_c refers to the subcarrier frequency. In a subcarrier fiber optic link, multiple subcarriers with different frequency can be used for different communication channels with respective occupation of occupies a different portion of the optical spectrum, instead of surrounding the center frequency of the optical carrier in a baseband fiber optic link. By doing so, the interference between different signals can be minimized in a subcarrier fiber optic link. Besides, complex modulation can be implemented more cost-effectively in a subcarrier fiber optic link than in a baseband fiber optic link. In order to maximize the spectrum efficiency, complex modulation is used in which both the amplitude and phase of the carrier are modulated. Comparing to applying complex modulation to the optical carrier in the baseband fiber optic link with the high cost optical components, subcarrier multiplexing in a subcarrier fiber optic link is carried out with low cost electrical components. Therefore, subcarrier fiber optic link is preferred in the long distance fiber optic link, in which high spectrum efficiency is desired cost-effectively, and is the main focus area of this chapter. For the baseband fiber optic link, the influence of chromatic dispersion mainly relates to the pulse broadening and inter-symbol interference, and will not be discussed in this study.

Power fading can be mathematically described as [14]:

$$P_{RF} \propto cos^2(\frac{\pi LD\lambda^2 f_s^2}{c}) \qquad 4.1.$$

where P_{RF} is the detected RF signal power at the receiver, c is the velocity of light, λ is the optical carrier wavelength, L is the fiber length, f_s is the subcarrier frequency, and D is the fiber dispersion parameter.

From Equation 4.1, it can be seen that at a transmission distance of an integral number of $\frac{c}{2D\lambda^2 f_s^2}$, the power of a received signal with two double sidebands that have equal amplitude will become zero. In a subcarrier fiber optic link, the fast growing data speed discussed in chapter 1 requires large frequency of subcarrier f_s, which in turn will greatly reduce the transmission distance at which the power fading occurs. For example, when a 25 Gbps digital data in the form of baseband signal multiplexes with a subcarrier frequency, in order to avoid the spectrum overlap with the optical carrier, the subcarrier frequency has to be larger than 12.5 GHz. In this case, when the optical carrier wavelength is 1550 nm, in a single mode fiber whose D is 17 ps/nm/km at 1550 nm wavelength, the received signal power will be reduced by half at transmission distance as short as 11.8 km, and will be reduced to zero at a transmission distance as short as 23.6 km. Therefore, in a high speed fiber optic link, the fading effect can be very strong at a relatively short transmission distance.

4.3 Traditional Optical Bandpass Filter

Because the fading effect results from the accrued phase difference between two sidebands, suppressing one sideband can largely alleviate the power fading effect. The suppressing of one sideband can be obtained by filtering one of the sidebands of a DSB signal, with the adoption of optical bandpass filter, which at the same time keep the optical carrier and the other sideband from being affected in an ideal case.

4.3.1 Introduction of filter transfer function

The characteristics of an optical filter can be defined completely by the complex-valued transfer function H(ω), which describes an optical filter's impulse response of the amplitude and phase on the input signal $E_{in}(\omega)$. If H(ω) is known, then the output signal of the filter, $E_{out}(\omega)$, can be found simply as a product of the input signal and the filter transfer function.

Several characteristics of an optical filter have to be considered in the design. The first one is the insertion loss, which is defined as the optical loss in the passband of the filter, and affects the system power budget. The second one is the sharpness, which describes the steepness of the filter edges, and is mainly responsible for the attenuation of filtered signals. The third one is the spectral structure, such as the ripple and flatness inside the passband, the shape of the roll-off away from the passband edge, and the side lobes outside the passband. The spectral structure is mainly responsible for distortions. The fourth one is filter bandwidth, which is defined as the frequency range where the amplitude falls below 3 dB. The fifth one is the crosstalk, which relates to the rejection of the out-of-band signals. The above five characteristics relate to the magnitude response of an optical filter. Of equal importance is the phase response, which is responsible for the distortion expressed as the narrowing or broadening of pulse. If the magnitude response is known or measured for a given filter, the phase response can be derived using a linear transformation known as the Hilbert transform [15] [16].

Optical bandpass filters with three different transfer functions are simply discussed below, they are Bessel filter, Butterworth filter, and Elliptic filter. Bessel filters are designed to have flat group-delay characteristics, so that there is no ringing in the impulse responses [17] [18]. Butterworth filters are designed to have an amplitude response characteristic that is as flat as possible in the passband [17] [18]. The elliptical filter has an extremely large sharpness, which makes it ideally suited for filter design cases where there must be severe attenuation in frequencies just entering the stopband of the filter [17] [18]. The response of magnitude, phase, and group delay

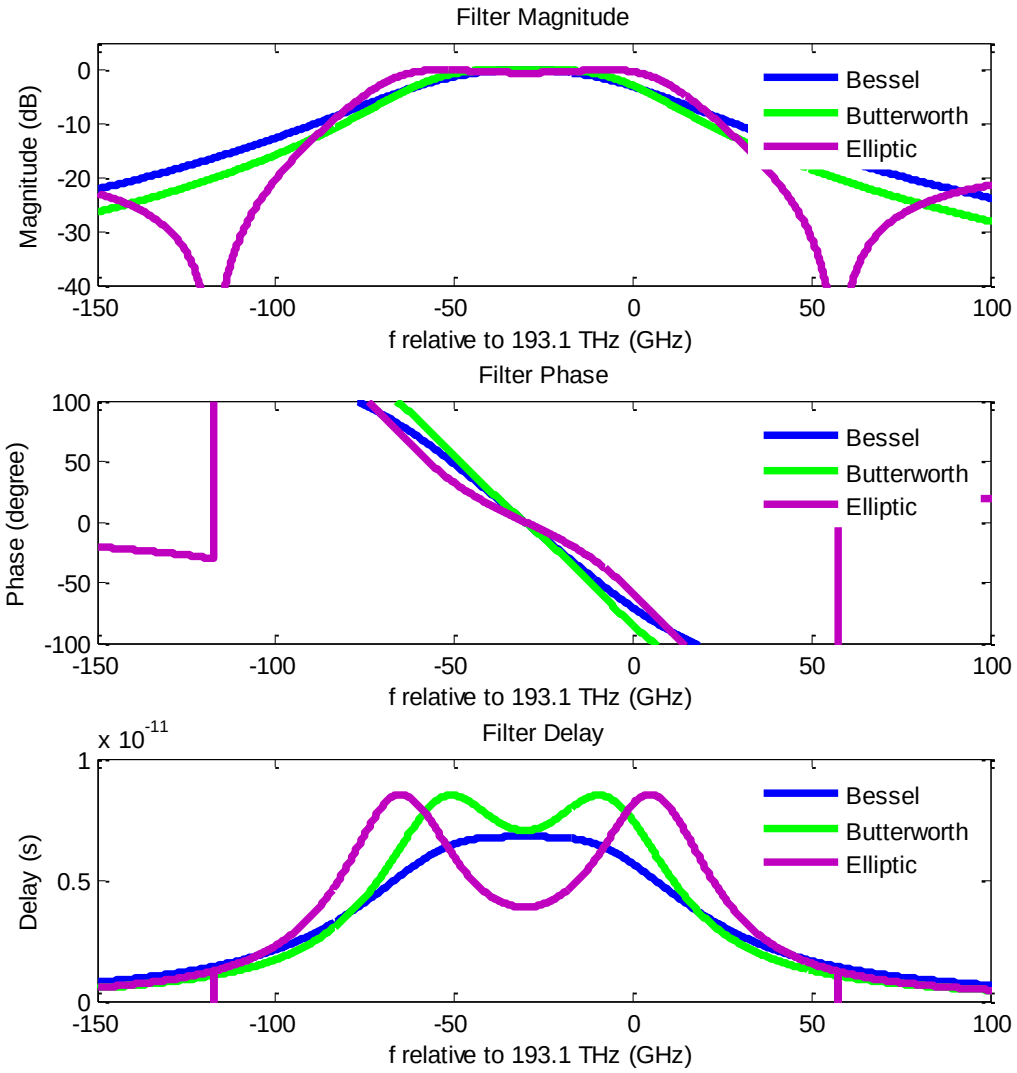

Figure 4-1 Transfer functions of various band pass filters, including Bessel, Butterworth, and Elliptic [18]. The filter bandwidth is 64 GHz, the filter center frequency is 193.07 THz. The filter order is 2.

of the three filters are compared in Figure 4-1 [18]. For optimistic optical single side band (OSSB) transmission, fast and linear filter roll-off is desirable, especially for high speed signal transmissions. In this chapter, Bessel optical bandpass filter is used because it has the smallest delay different over the band among the three kinds of optical bandpass filters, and will introduce least

pulse distortion, as shown in Figure 4-1. However, the Bessel optical bandpass filter has relatively slow filter roll-off, which will result in small attenuation of the targeted sideband. Therefore, the design of optical bandpass filter with fast and linear roll-off becomes an important research subject.

4.3.2 CNR

OSSB using optical filtering, which has proved to alleviate fading effect, usually also causes the reduction of optical modulation index *m*, as half of the signal power was filtered out. However, since *m* is referenced to the carrier power, it can be enhanced if the carrier power can be preferentially attenuated in the process. This can be realized if the filter has fast roll-off.

According to Equation 4.2 [19] below, theoretically, *CNR* is proportional to m^2, and the enhancement of *CNR* with larger m is especially more significant in a relative intensity noise (*RIN*) dominated link. Thus, the adoption of the fast roll-off filter not only minimizes the power fading effect, it can potentially improve the *CNR* performance. It should be noted that although operating the carrier wavelength λ deep into the roll off slope may achieve larger m, more distortion may be generated when the filtering shape becomes nonlinear. In this case special consideration should be given in the design of the filter so as to maintain a low distortion level while keep a large *m* and *CNR*.

$$CNR = \frac{\frac{1}{2}(mI_0)^2}{B_e\left(2eI_0 + n_{th}^2 + RIN \times I_0^2\right)} \qquad 4.2.$$

where I_0 is the average received photocurrent. B_e is the noise power bandwidth, which is usually 4 MHz, as defined by analog NTSC television channels standard. The thermal noise of the receiver is $B_e n_{th}^2$, and the shot noise is $2B_e eI_0$, where the e is the electron charge [19].

4.3.3 Magnitude response induced pulse distortion in an optical bandpass filter

The distortion due to both magnitude response and the phase response of the optical bandpass filter can be studied with the help of the Taylor's series expansion. For example, the magnitude transfer function of an optical bandpass filter can be expanded using Taylor's series as

$$H(f)=A_0+A_1(f-f_0)+A_2(f-f_0)^2/2+\cdots \quad 4.3.$$

where f_0 is the center frequency of an optical signal pulse, and A_n (n=0, 1, 2, ⋯) are the Taylor's series coefficients in dB. The magnitude transfer function of the optical filter in linear unit can be written as

$$H(f)=\exp(a_0+a_1(f-f_0)+a_2(f-f_0)^2/2+\cdots) \quad 4.4.$$

where a_n (n=0, 1, 2, ⋯)= $A_n\log(10)/10=0.23A_n$.

According to [20], when a Gaussian shape optical pulse transmits through an optical filter, the 1st order Taylor's series coefficient a_1 determines the gain or loss of the optical pulse transmitting through the optical filter, and does not give rise to the distortion. Meanwhile, the 2nd order Taylor's series coefficient a_2 determines the narrowing or broadening of the pulse resulted from the nonlinear magnitude transfer function. In this case, the 1/e width of input pulse, T_{in}, and the 1/e width of the output pulse, T_{out}, can be related as

$$\frac{T_{out}}{T_{in}}=(1-\frac{a_2}{{T_{out}}^2})^{1/2} \quad 4.5.$$

where the contribution of higher order terms of a_n (n>2) to the signal pulse width is neglected. The output pulse may be narrowed or broadened, depends on the sign of a_2. The larger the absolute value of a_2 is, the greater the pulse width will be changed. Therefore, small a_2 is desired for the linear operation of the optical bandpass filter.

4.4 Cascaded optical bandpass filter

4.4.1 Introduction of cascaded optical bandpass filter

In the previous discussion of section 4.3, single optical bandpass filter with Bessel transfer function is introduced. Besides, the potential effects of optical bandpass filter on a fiber optic link's

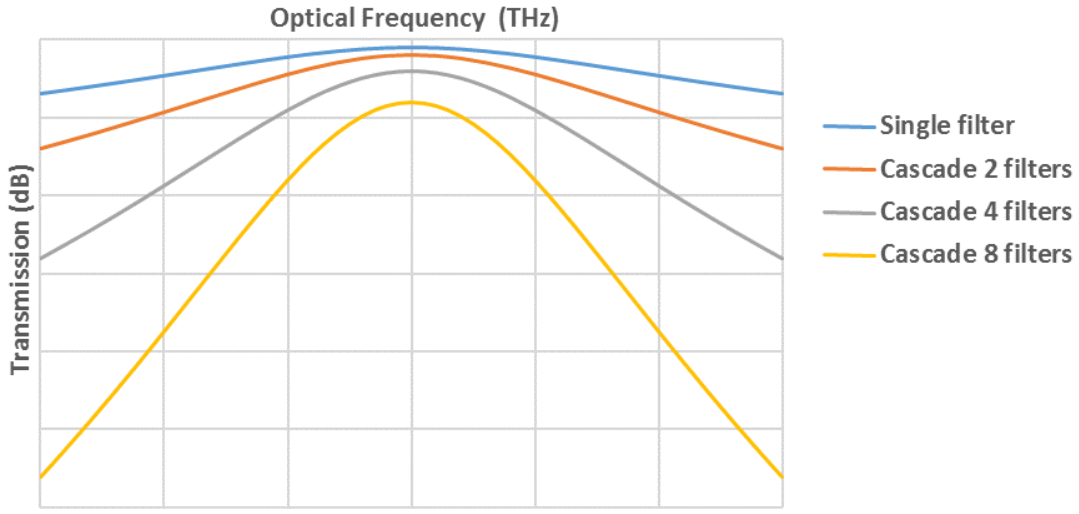

Figure 4-2 An illustration of the magnitude response of various cascaded filters and a single filter. The single filter is an optical bandpass filter with Bessel transfer function. The cascaded filter has multiple identical single filters spliced together in series.

CNR and distortions are introduced. It is pointed out that a single Bessel optical bandpass filter has relatively slow filter roll-off, comparing to optical bandpass filters with either Butterworth or Elliptic transfer function. In this section, cascaded optical bandpass filter with Bessel transfer function is proposed to improve the roll-off band sharpness. How the cascaded filter differs from the single filter on affecting the link CNR and distortion, as well as the physical explanations for these differences, will be studied.

In the cascaded filter discussed in this section, multiple identical filters are connected in series, via splicing the pigtail fiber of the optical port of every two filters. The magnitude response (in dB) of a cascaded filter is the sum of the magnitude response (in dB) of each individual filter, plus the fiber splicing loss. A comparison of the magnitude response of various cascaded filters and a single filter is shown in Figure 4-2. In the passband, due to the filter insertion loss and fiber splicing loss, the more filters are cascaded together, the larger the insertion loss of the cascaded filter will be. In the roll-off band, the filter sharpness is proportional to the number of filters in series. Therefore, when the number of filters in series is considered, there is a tradeoff between the

filter insertion loss and filter sharpness. In this chapter, how the filter sharpness affects the link CNR and linearity in the application of power fading suppressing is focused. The filter insertion loss can be compensated by increasing either the laser source power or the optical amplifier power. This approach may affect the link CNR and linearity, as it changes the operation conditions of the laser or the optical amplifier [17] [19].

As mentioned in section 4.3.2, when an optical bandpass filter is used for power fading suppression, in order to avoid the CNR reduction, certain attenuation of optical carrier power is required. In this case, the optical carrier wavelength moves away from the filter passband and into the roll-off band. As the roll-off band sharpness of a cascaded filter is greater than that of a single filter, for the same optical carrier power attenuation, the optical carrier wavelength will be closer to the passband in the cascaded filter case than in the single filter case. In another word, CNR can be enhanced similarly in both the cascaded filter case and the single filter case, however, the optical carrier has to align with the two types of filter differently.

As mentioned in section 4.3.3, when the nonlinear magnitude transfer function of an optical bandpass filter is expanded with the Taylor's series expansion, the 2^{nd} order Taylor's series coefficient a_2 determines the narrowing or broadening of an optical pulse transmitting through the filter, and small absolute value of a_2 is desired for the linear operation of the optical bandpass filter. When an optical filter is used for power fading suppression, as discussed above, when the filter sharpness varies, in order to get the same link CNR, the optical carrier has to align with the filter differently, and results in very different a_2. Therefore, different distortion level introduced by the filter is expected for different filter sharpness, which will be discussed in the following section.

4.4.2 Demonstration of cascaded optical bandpass filter

In this section, optical bandpass filter is experimentally explored to resolve the CNR degradation issue while minimizing the related distortions. As discussed in section 4.3.1, optical

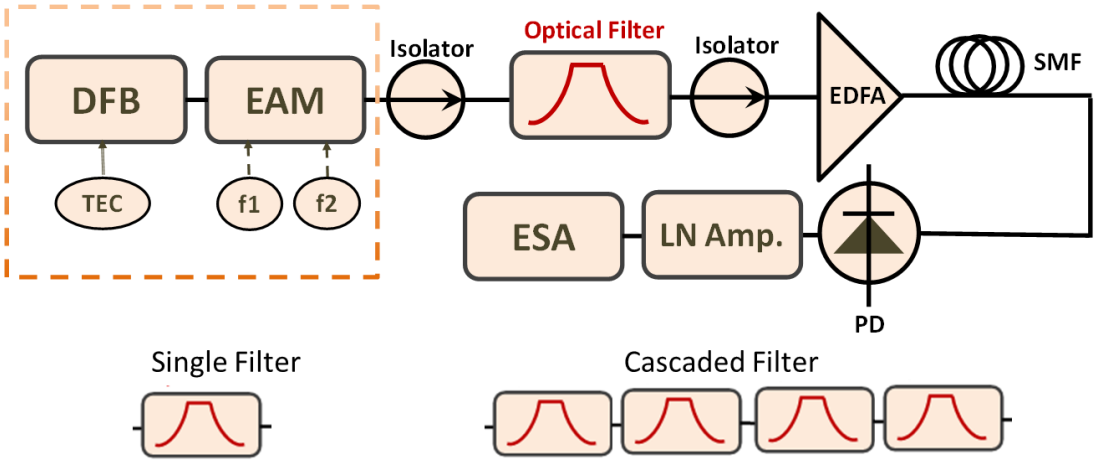

Figure 4-3 Optic link performance measurement setup with single filter and cascaded filter.

bandpass filter with Bessel shape transfer function has relatively linear but slow roll-off. Therefore, a method of cascading four identical Bessel optical bandpass filter is proposed to obtain fast filter roll-off, in order to combat with the power fading effect while minimize the distortions introduced by the filter [13].

At the initial demonstration stage, we cascade four identical off-the-shelf 100 GHz optical bandpass filters, which have Bessel transfer function for the magnitude response. The wavelength of the filter passband center aligns to ITU Grid DWDM channel 55, which is 1533.47 nm. In order to test the effects of this cascaded optical bandpass filter on two most critical fiber optic link performances, CNR and linearity, a measurement setup is built, as shown in Figure 4-3. On the transmitter side, an electro-absorption modulated laser EML (CyOptics LIM10X) transmitter is used, in which a DFB laser with temperature control (TEC) generates continuous wave (CW) laser at 1533.47 nm, when the temperature is set at 17.5°C. The laser wavelength corresponds to ITU Grid DWDM channel 55, which aligns well with the wavelength of the optical filter's passband center. The laser wavelength shifts with the TEC setting temperature at about 0.08 nm/°C within the temperature range of 10 °C to 50 °C. In the measurement, fine adjustment of the laser

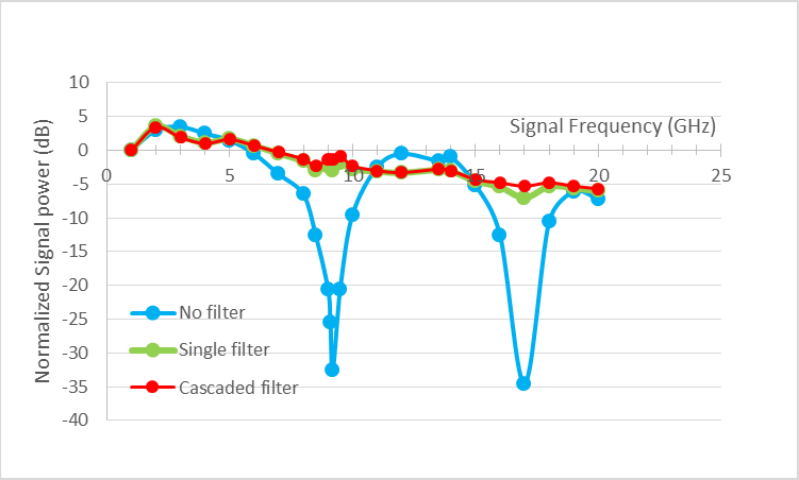

Figure 4-4 Measured dispersion response versus signal frequency through 40 km SMF-28 fiber.

wavelength is achieved by changing the TEC temperature setting of the EML, and this is used to optimize the link CNR and linearity performance. The RC bandwidth of the transmitter is about 10 GHz. The optical output port of the optical transmitter connects to the cascaded optical bandpass filter, via an optical isolator for suppressing optical back-reflection induced laser RIN noise. The optical output of the optical bandpass filter, which is amplified by an EDFA, transmits through certain length of standard single mode fiber, and reaches the optical receiver. The EDFA output power is set at a low level of 5 dBm, in order to avoid the Stimulated Brillouin Scattering (SBS) effect induced degradation of noise and distortion [21]. An optical isolator is also placed between the EDFA and fiber for the same purpose of suppressing optical back-reflection induced laser RIN noise. The photodiode (PD) re-generates the signal, which is characterized in an electrical spectrum analyzer (ESA). In our test, the power of generated electrical signal in the PD is weak, due to the limited EDFA output power and fiber attenuation over the long fiber. Therefore, the regenerated electrical signal is amplified by a broadband linear low noise amplifier (LN Amplifier), which benefits accurate characterization of the CNR and distortions in the ESA.

First, the suppression of fading effect is tested. In this test, 40 km long standard single mode fiber is used. A single tone with frequency ramped up from 1 GHz to 20 GHz drives the EML

on the transmitter side, and the power of the amplified re-generated signal at the same frequency is recorded. The same test was done for three cases, which are without filter, with single filter, and with cascaded filter. During the test, the wavelength of the optical carrier roughly aligns to the right edge of the passband, so that the suppression of one sideband occurs in two filter cases. The test results are plotted in Figure 4-4, which shows that the suppression of signal power due to fading effect is as large as 30 dB in the no filter case. In contrast, it is only about 1 dB in the single filter case, and it becomes negligible in the cascaded filter case. The reduction of the signal power in the cascaded filter case in Figure 4-3 is due to the RF frequency dependent loss. In this case, both the cascaded filter and single filter works approximately the same on suppressing the fading effect. Please note, the suppression of fading effect largely depends on the alignment of the optical carrier and the filter in spectrum. Any filter that causes large difference of amplitude between the two sidebands can suppress the fading effect, however, filters may behave very differently on affecting the link CNR and linearity, which will be discussed in the following discussion.

Second, the change of optical modulation index m, as well as the resulted change of the CNR, are tested. In this test, the LN amplifier is removed to reflect the original optical modulation index. Optical modulation index m is an important parameter in fiber optic link, especially for analog applications. On the one hand, large m is desirable for large CNR, according to Equation 4.2. On the other hand, large m more likely causes large nonlinearity in a nonlinear link, especially for modulator with nonlinear transfer curve. Generally speaking, as long as the link linearity meets the required specifications, large m is desired. When an optical carrier and two sidebands transmit through an optical bandpass filter, depends on the spectrum alignment of the optical carrier and the filter, the sidebands and the optical carrier may be attenuated at different amount, and results in complex change of m, which can be calculated with the recorded average photocurrent I_0 and the detected single tone signal power P_f, based on Equation 4.6.

$$m = {I_{ac}}/{I_0} = \left. 2\sqrt{(\frac{2P_f}{R_L})} \right/ I_0 \qquad 4.6.$$

where I_{ac} is the ac current generated in the PD, R_L is the load impedance of the ESA.

Table 4-1. The comparison of m. When there is no optical filter, the wavelength of the optical carrier is 1533.47 nm. When an optical filter is used without carrier suppression, the wavelength of optical carrier in the single filter case and cascaded filter case is 1533.74 nm and 1533.72 nm, respectively. When there is carrier suppression, the wavelength of optical carrier in the single filter case and cascaded filter case is 1533.88 nm and 1533.80 nm, respectively. When there is carrier suppression, the optical carrier is attenuated by about 5 dB in both single filter case and the cascaded filter case. f_s=10 GHz, I_0=5 mA.

m (without optical filter)	12.2%
m (with optical filter and w/o carrier suppression)	6.10%
m (with optical filter and with carrier suppression)	18.0%

When the optical carrier aligns to the passband of an optical filter, one of the DSBs is suppressed, and the power of the other DSB and the optical carrier is unchanged, comparing to m in the case without filter, m is reduced by 3 dB. In this case, CNR will be reduced by 6 dB, according to Equation 4.2. When the optical carrier aligns to the somewhere in the roll-off band, not only one sideband is suppressed, but also the optical carrier is attenuated. In this case, there will be less reduction of m and CNR, or even the enhancement of the two. As shown in Table 4.1, when the wavelength of the optical carrier is tuned in both the single filter case and the cascaded filter case, the optical carrier is attenuated by about 5 dB, and m of 18.0% can be obtained, comparing to m of 12.2% in the case without any optical filter, and m of 6.1% in the case with one sideband

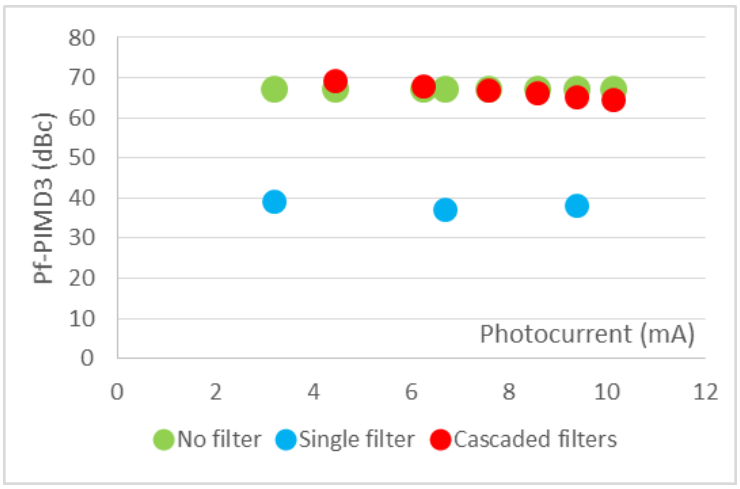

Figure 4-5 Measured distortion versus photocurrent at the detector for two 10 GHz RoF channels (f1=10 GHz, f2=10.11 GHz) through 10 km SMF-28 fiber.

suppression only. This enhancement of m results in enhancement of CNR by 3.5 dB, comparing to when there is no filter used.

Although both the single filter and the cascaded filter can achieve similar fading suppression and CNR enhancement in our test, they performs differently at the introduced distortions. In our two-tone test, the power difference between the fundamental tone and the third order intermodulation tone (IDM3) is tested at different photocurrent levels. IDM3 is studied here as it is very close to the fundamental tone in the spectrum and cannot be filtered out. A comparison is done between the no filter case, the single filter case, and the cascaded filter case. In order to separate the transmitter and receiver's distortion contributions from those of the filters, all the distortion measurements were done with the same m of 0.22. In this study, P_f-P_{IMD3}, the power difference of the fundamental tone and the IDM3 distortion, is tested at different photocurrent levels, as shown in Figure 4-5. P_f-P_{IMD3} measures the dynamic range due to the IMD3 distortion at a specific modulation index and without a noise reference. Comparing to the no filter case, while more than 20 dB reduction of the dynamic range is observed by using single filter, and only a small decrease is observed by using cascaded filter. Therefore, by optical carrier suppression, the

cascaded filter is able to enhance the CNR without degrading the linearity performance, while the single filter degrades the 3rd order linearity significantly.

In order to explain the different linearity performance between the two filters that are operated at optical carrier suppression, how the optical carrier and the two sidebands are aligned with the filter magnitude response curve is studied. When the optical carrier is suppressed by a bandpass filter, it aligns with somewhere in the roll-off band, instead of the low-loss passband. The attenuation of the optical carrier depends on two factors, the steepness of the roll-off, and the spectral distance between the optical carrier and the passband edge. When the roll-off is not steep enough, in order to obtain large attenuation of the optical carrier, the spectral distance between the optical carrier and the passband edge has to be large. In other words, the optical carrier has to move further into the roll-off band. In this case, depends on the subcarrier frequency f_s, the remaining sideband will be very likely away from the linear passband and move into the nonlinear roll-off band. The nonlinearity difference between the single filter case and the cascaded filter case, which is observed in Figure 4-5, will be analytically discussed in the following discussion.

According to the above discussion, in the case when an optical filter is applied to suppress the power fading effect without degrading the link CNR, the nonlinearity of an optical filter arises from the fact that the remaining sideband overlaps with the nonlinear band of the filter in spectrum. Any filter's nonlinear transfer function T(f) can be expanded with Taylor's series expansion around certain sideband optical frequency f_B.

$$T(f) = T(f_B) + \sum_{n=1}^{\infty} \frac{T^{(n)}(f)|_{f=f_B}}{n!}(f - f_B)^n \qquad 4.7.$$

In our case, in which the LSB is suppressed and the remaining USB carries the modulation information, $f_B = f_c + f_s$, where f_c is the optical frequency of the optical carrier, and f_s is the RF frequency of the subcarrier. Assume a signal f_m is superimposed on the subcarrier frequency f_s, then

$$T(f_B + f_m) = T(f_B) + \sum_{n=1}^{\infty} \frac{T^{(n)}(f)|_{f=f_B}}{n!}(f_m)^n \quad 4.8.$$

Please note, in most subcarrier fiber optic links, a baseband signal usually multiplexes with the subcarrier, instead of superimposes on it. However, for the benefits of nonlinearity analysis, superposition is used here. When the signal f_m contains two tones at different frequency f_1 and f_2,

$$f_m = f_0[\sin(2\pi f_1 t + \varphi_1) + \sin(2\pi f_2 t + \varphi_2)] \quad 4.9.$$

where f_0 is the amplitude of the signal, φ_1 and φ_2 are the phase of the two tones, respectively. In this case, the transfer function of an optical filter can be written as

$$T(f) = T(f_B) + \sum_{n=1}^{\infty} \frac{T^{(n)}(f)|_{f=f_B}}{n!}(f_0)^n[\sin(2\pi f_1 t + \varphi_1) + \sin(2\pi f_2 t + \varphi_2)]^n \quad 4.10.$$

In order to explore the nonlinearity related to an optical filter, in the subcarrier fiber optic link, the optical filter is assumed to be the only nonlinear source, other components, such as the modulator, the fiber, and the photodetector, are assumed to be ideally linear. In this case, the photocurrent I_d generated in the photodetector is [22]:

$$\begin{aligned} I_d &= P_L t_{ist} T(f) R_d \\ &= P_L t_{ist} R_d \left\{ T(f_B) + \textstyle\sum_{n=1}^{\infty} \frac{T^{(n)}(f)|_{f=f_B}}{n!}(f_0)^n[\sin(2\pi f_1 t + \varphi_1) + \sin(2\pi f_2 t + \varphi_2)]^n \right\} \end{aligned} \quad 4.11.$$

where P_L is the laser power, t_{ist} is the total optical insertion loss between the laser to the photodetector, R_d is the responsivity of the photodetector.

By separating the orders that we are interested, we can obtain dc, the fundamental signal, the second order distortions, the third order distortions, and other higher order distortions. The fundamental signal is

$$P_{f_1} = T'(f)|_{f=f_B} f_0 \sin(2\pi f_1 t + \varphi_1) \tag{4.12.}$$

For the third-order intermodulation signals, due to the symmetry, only one frequency, $2f_1$-f_2 for example, needs to be examined. The lowest polynomial order involving this frequency is the third order. By following the trigonometrical identities,

$$\begin{aligned}
&[\sin(2\pi f_1 t + \varphi_1) + (sin2\pi f_2 t + \varphi_2)]^3 \\
&= [\sin(2\pi f_1 t + \varphi_1)]^3 + [\sin(2\pi f_2 t + \varphi_2)]^3 \\
&+3[\sin(2\pi f_1 t + \varphi_1)]^2 \sin(2\pi f_2 + \varphi_2) \\
&+3[\sin(2\pi f_2 t + \varphi_2)]^2 \sin(2\pi f_1 t + \varphi_1)
\end{aligned} \tag{4.13.}$$

$$\begin{aligned}
&[\sin(2\pi f_1 t + \varphi_1)]^2 (sin2\pi f_2 t + \varphi_2) \\
&= \frac{1 - \cos[2(2\pi f_1 t + \varphi_1)]}{2} (sin2\pi f_2 t + \varphi_2) \\
&= \frac{(sin2\pi f_2 t + \varphi_2)}{2} - \frac{sin[2\pi(2f_1 + f_2) + (2\varphi_1 + \varphi_2)]}{4} + \\
&\frac{\sin[2\pi(2f_1 - f_2) + (2\varphi_1 - \varphi_2)]}{4}
\end{aligned} \tag{4.14.}$$

The third order intermodulation distortion at frequency $2f_1$-f_2 can be obtained.

$$P_{(2f_1-f_{2)}} = \frac{T'''(f)|_{f=f_B}}{8}(f_0)^3 \sin[2\pi(2f_1 - f_2) + (2\varphi_1 - \varphi_2)] \quad 4.15.$$

Therefore, the third-order distortion limited dynamic range, P_f-P_{IMD3}, which is the power difference between the fundamental tone and the third order intermodulation distortion, can be expressed as:

$$\left[P_{f_1} - P_{(2f_1-f_{2)}}\right](dB) = 10\log\left\{T'(f)|_{f=f_B} f_0 \Big/ \frac{T'''(f)|_{f=f_B}}{8}(f_0)^3\right\} \quad 4.16.$$

And the difference of this dynamic range in the cascaded filter case and in the single filter case can be written as:

$$\left\{\left[P_{f_1} - P_{(2f_1-f_{2)}}\right]\right\}(dB)|_{cascaded\ filter} - \left\{\left[P_{f_1} - P_{(2f_1-f_{2)}}\right]\right\}(dB)|_{single\ filter}$$
$$= 10\log\left\{\frac{[T'(f)|_{f=f_{B1}}/T'''(f)|_{f=f_{B1}}]|_{cascaded\ filter}}{[T'(f)|_{f=f_{B2}}/T'''(f)|_{f=f_{B2}}]|_{single\ filter}}\right\} \quad 4.17.$$

In general, the magnitude response (in dB) of multiple filters can be added to each other when they are cascaded, which means larger insertion loss in the passband, as well as larger steepness in the roll-off band. In this studied case, when 4 identical Bessel bandpass filter cascaded together, comparing to the single filter, the magnitude response still has Bessel transfer function, the insertion loss in the passband increases from 0.4 dB to about 2.2 dB, and the steepness is about 4 times of that in a single filter. Please note, for the cascaded filter in this study, the insertion loss includes not only the cumulative insertion loss from each individual single filter, but also the inter-connection loss between filters resulted from the fiber splicing. The increased insertion loss of a

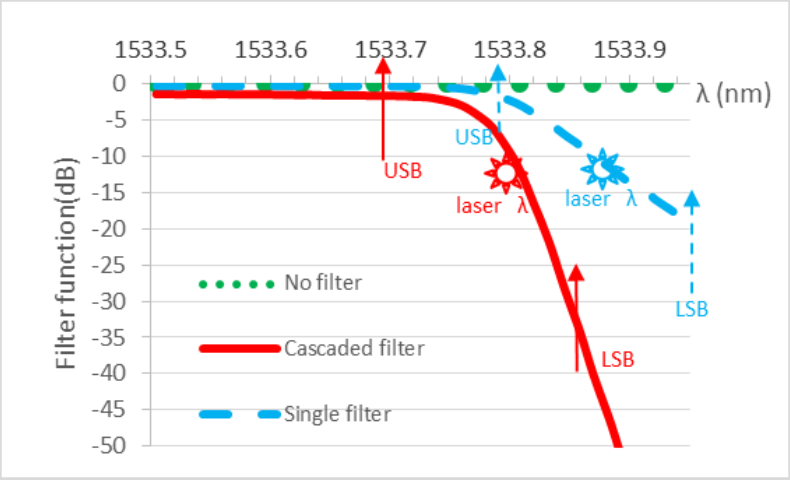

Figure 4-6 The Spectral structure of the cascaded filter and the single filter around the right edge of the passband.

cascaded filter can be compensated by a low noise figure EDFA. A comparison of roll-off of a single filter and a cascaded filter is done, as shown in Figure 4-6. In this comparison, the optical modulation index m of 18% is set to be the same for both filters. Because of the difference of the roll-off steepness, in order to achieve the same m of 18%, the optical carrier has to be attenuated by 5 dB, and the optical carrier wavelength has to align with the two filters' transfer function differently. As shown in Figure 4-6, because of the difference of roll-off band steepness, the optical carrier aligns to the cascaded filter at a spectrum position that is much closer to the passband edge than the single filter. The wavelength of the optical carrier is 1533.77 nm and 1533.87 nm in the cascaded filter case and single filter case, respectively. As a result, when f_s is 10 GHz, while optical wavelength of the upper sideband (USB) is 1533.69 nm in the cascaded filter case, and is still in the passband, in the single filter case it is 1533.79 nm, and is already at the passband edge. As f_s increases, the USB in the single filter case will move further away from the passband edge, and into the roll-off band.

As shown in Equation 4.17, the third order limited dynamic range difference between the single filter and the cascaded filter can be predicted by the 1st derivative and 3rd derivative of the

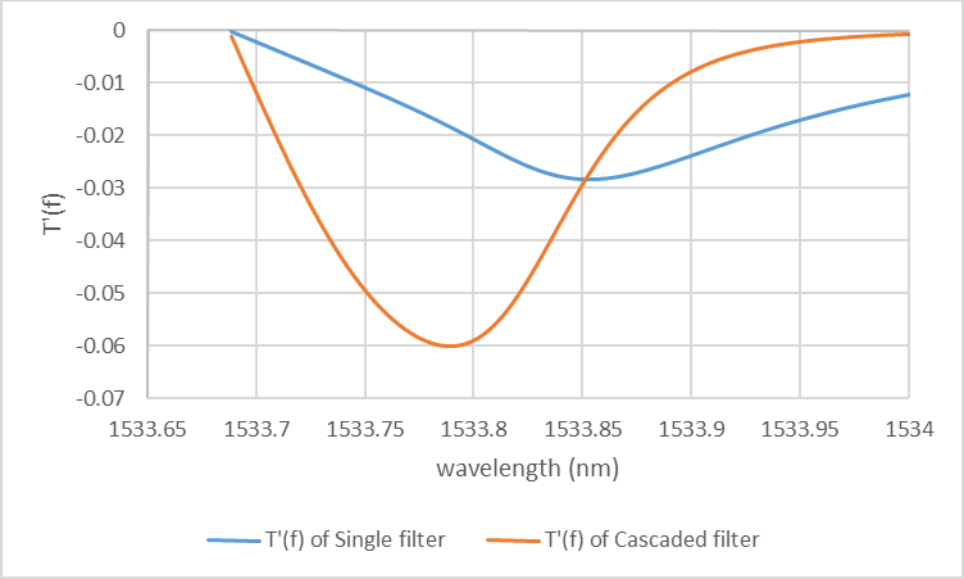

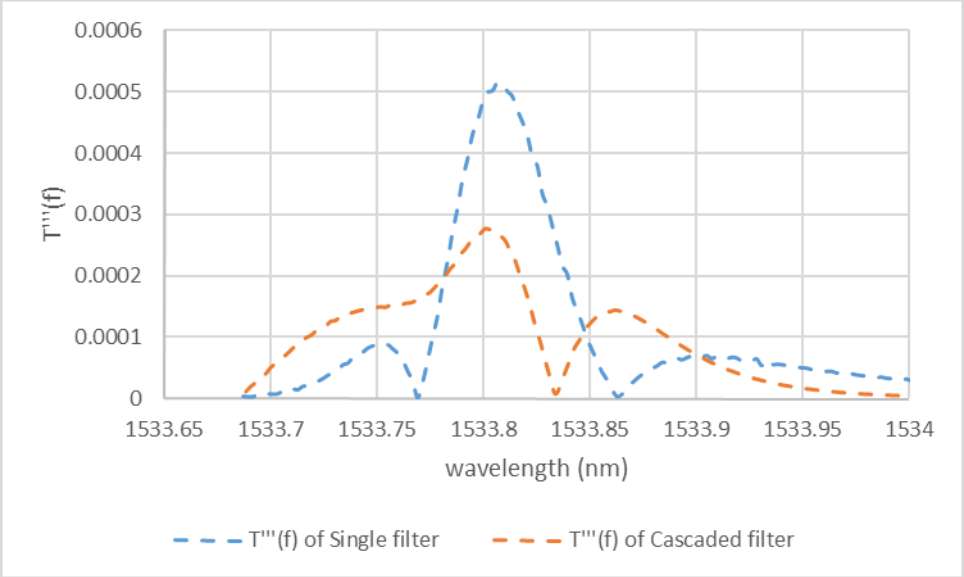

Figure 4-7 The 1st derivative (a) and 3rd derivative (b) of the transfer function of the single filter and cascaded filter shown in Figure 4-6. The plot starts from the passband right edge wavelength of 1533.68 nm.

corresponding filter transfer function, which are shown in Figure 4-7, at the corresponding remaining sideband position. In Figure 4-7, starting from the passband ridge edge wavelength of

1533.68 nm, the magnitude of the 1st derivative of the transfer function T'(f), which accounts for the steepness of the roll-off band, is larger in the cascaded filter. Starting from the passband ridge edge , the 3rd derivative of the transfer function T'''(f) is larger in the cascaded filter. However, when it is more than 1 nm away from the passband right edge, the cascaded filter shows smaller T'''(f) than the single filter. In this case, the nonlinearity difference of the two filters depends on not only the filter transfer function, but also the alignment of the remaining sideband (USB in this study) with the transfer function. In the case when both filters achieve similar effects of power fading suppression and CNR improvement, because of the difference of the roll-off band steepness, the USB of the two filter are at different positions in spectrum. As shown in Figure 4-6. The optical wavelength of the USB for the single filter case and the cascaded filter case is 1533.79 nm and 1533.69 nm, respectively. In this case, as shown in Figure 4-7, the magnitude of T'(f) of the cascaded filter and the cascaded filter at the corresponding USB position is 0.004 and 0.018, respectively, and the magnitude of T'''(f) of the cascaded filter and the cascaded filter at the corresponding USB position is 5.6×10^{-6} and 4×10^{-4}, respectively. The above observations show that the USB in the cascaded filter case aligns to a relative linear and flat section of the transfer curve, and the USB in the single filter case aligns to a nonlinear and steep section of the transfer curve. Based on Equation 4.7, the third order distortion limited dynamic range in the cascaded filter case will be about 12 dB higher than that in the single filter case. Therefore, both the experiment and analysis show more linear operation of the cascaded filter than the single filter, when they are used for suppressing the power fading effect and enhancing the link CNR.

4.5 Summary

In summary, we have proposed and demonstrated the incorporation of cascaded optical bandpass filter in a RoF link can significantly improve the link performance. As a cost-effective approach, it not only eliminates the power fading effect, but also improves *CNR* without worsening the 3rd inter-modulation distortions. By comparing the RoF links with single and cascaded optical

bandpass filter, we show that the latter can significantly improve the link performance, which is attributed to its flat linear bandpass region and fast frequency response roll-off. As this approach relies on flat passband and fast response roll-off, further enhancement of the third order distortion limited dynamic range can be achieved when the optical bandpass filtering shape is optimized.

Portions of chapter 4 appear in “Cascaded Optical Band Pass Filters in Radio-over-Fiber Link”, IEEE EDSSC, Hongkong (2013), Dingbo Chen, Chen-Kuo Sun and Paul K. L. Yu, and “Optical Band Pass Filters in High Linearity Radio-over-Fiber Link”, IEEE AVFOP, San Diego (2013), Dingbo Chen, Chen-Kuo Sun and Paul K. L. Yu.

4.6 References

[1] A. Lebedev, J. J. Vegas Olmos, M. Lglesias, S. Forchhammer, I. Tafur Monroy. "A novel method for combating dispersion induced power fading in dispersion compensating fiber," *Opt. Express,* vol. 21, pp. 13617-13625 (2013).

[2] E. Vourc'h, B. Della, D. L. Berre, D. Herve, "Millimeter-wave power –fading compensation for WDM fiber-radio transmission using a wavelength-self-tunable single-sideband filter," *IEEE Trans. Micro. Theory Tech.*, vol. 50, no. 12, pp. 3009-3015 (2002).

[3] A. Narasimha, X. Meng, C. F. Lam, M. C. Wu, and E. Yablonovitch, "Maximizing spectral utilizing in WDM systems by microwave domain filtering of tandem single sidebands," *IEEE Trans. Micro. Theory Tech.*, vol. 49, no. 10, pp. 2042-2047 (2001).

[4] L. A. Johansson and A. J. Seeds, "Millimeter-wave modulated optical signal generation with high spectral purity and wide-locking bandwidth using a fiber-integrated optical injection phase-lock loop," *IEEE Photonics Technol. Lett.,* vol. 12, no. 6, pp. 690-692 (2000).

[5] D. Wake, C. R. Lima, and P. A. Davies, "Optical generation of millimeter-wave signals for fiber-radio systems using a dual-mode DFB semiconductor laser," *IEEE Trans. Micro. Theory. Tech*., vol. 43, no. 9, pp. 2270–2276 (1995).

[6] G. H. Smith, D. Novak, and Z. Ahmed, "Technique for optical SSB generation to overcome dispersion penalties in fibre-radio systems," Electron. Lett., vol. 33, no. 1, pp. 74-75 (1997).

[7] B. Davies, and J. Conradi, "Hybrid modulator structures for subcarrier and harmonic subcarrier optical single sideband," *IEEE Photonics Technol. Lett.*, vol. 10, no. 4, pp. 600-602 (1998).

[8] M. Izutsu, S. Shikama, and T. Sueta, "Integrated optical SSB modulator/frequency shifter," *IEEE J. Quantum Electron*., vol. 17, pp. 2225-2227 (1981).

[9] E. Vergnol, F. Devaux, D. Tanguy, and E. Pénard, "Integrated lightwave millimetric single side-band source: Design and issues," IEEE J. Lightwave Technol., vol. 16, no. 7, pp. 1276–1284 (1998).

[10] J. Park, W. V. Sorin, and K. Y. Lau, "Elimination of the fibre chromatic dispersion penalty on 1550 nm millimetre-wave optical transmission," *Electron. Lett*., vol. 33, pp.512-513 (1997).

[11] H. Toda, T. Yamashita, K. Kitayama, and T. Kuri, "A DWDM MM-wave fiber-radio system by optical frequency interleaving for high spectral efficiency," Micro. Phototics, pp. 85–88 (2001).

[12] E. Vourch, D. Le Berre, and D. Hervé, "Lightwave single sideband wavelength self-tunable filter using an InP:Fe crystal for fiber-wireless systems," *IEEE Photonics Technol. Lett.*, vol. 14, no. 2, pp. 194-196 (2002).

[13] D. B. Chen, C. K. Sun, and P. K. L. Yu, "Cascaded Optical Band Pass Filters in Radio-over-Fiber Link," *IEEE International Conference on Electron Devices and Solid-State Circuits*, Hongkong (2013).

[14] N. J. Gomes, P. P. Monteiro, A. Gameiro, *Next Generation wireless communications using radio over fiber*, John Wiley & Sons, Hoboken, New Jersey (2012).

[15] M. Asghari, H. & Azaña J, "All-optical Hilbert transformer based on a single phase-shifted fiber Bragg grating: design and analysis," *Opt. Lett*., vol. 34, pp. 334-336 (2009).

[16] N. Q. Ngo and Y. Song, "On the interrelations between an optical differentiator and an optical Hilbert transformer," *Opt. Lett*., vol. 36, pp. 915-917 (2011).

[17] C. K. Madsen and J. H. Zhao, *Optical Filter Design and Analysis*, John Wiley & Sons, Hoboken, New Jersey (1999).

[18] A. V. Oppenheim and R. W. Schafer, *Digital Signal Processing*. Englewood Cliffs, NJ: Prentice-Hall, New Jersey (1975).

[19] W. S. C. Chang, *RF photonic technology in optical fiber links*, Cambridge University press, Cambridge, UK (2002).

[20] K.P. Ho, L.K. Chen, and F. Tong, "Modeling of waveform distortion due to optical filtering," *Quantum Elect*., vol. 6, no. 2, pp. 223-226 (2000).

[21] E. Lichtman, R. G. Waarts, and A. A. Friesem, "Stimulated Brillouin scattering excited by a modulated pump wave in single-mode fibers," *J. Lightwave Technol*., vol. 7, pp. 171-174 (1989).

[22] X. Xie, *High Power Peripheral Coupled Waveguide Electro-Absorption Modulator for Analog Fiber-Optic Link Applications*, University of California, San Diego (2007).

Chapter 5 Conclusion and Future Work

This dissertation has advanced the design of waveguide photodiode via the supermode analysis, and demonstrated the utility of cascade bandpass optical filters in a radio-over-fiber (RoF) link. The research in this dissertation is one small part of the overall physical understanding and technology development for the high speed fiber optic link.

5.1 Summary

Waveguide photodiode has been investigated quite some time by the analog communications community to provide better power handling capability [1] [2] [3]. As the required bandwidth kept increasing, an increasing photocurrent is needed in a reduced absorber area, all of which challenges the traditional WGPD designs. The traditional approach to analyze and design WGPD starts from adjusting the waveguide dimension to monitor and then optimize the profile of waveguide confinement factor in the longitudinal direction, which suppresses any local absorption peak and eventually evens out the absorption distribution [2] [4] [5]. It works for the WGPD that does not need a large bandwidth, as small waveguide confinement factor can be used to reduce the absorption peak density as well as the average absorption density. However, when the required bandwidth increases, small waveguide confinement factor reduces the absorption efficiency, and WGPD with larger confinement factor has to be used, leading to higher absorption peak and reduced absorption uniformity. In this case, the traditional WGPD design method, which is based on adjusting the waveguide confinement factor, runs into a dilemma. On the one hand, the large power handling capability requires small waveguide confinement factor. On the other hand, the large bandwidth-efficiency product requires a large waveguide confinement factor. Therefore, the primary motivation behind this dissertation is to study the power distribution in a WGPD from an angle that is different from focusing on the waveguide confinement factor, and provide a better

design of high power WGPD for the fiber optic link that requires aggregate speed of more than 100 Gbps.

First, the supermode analysis of WGPD is developed and applied to study the absorption uniformity in a traditional WGPD. Instead of focusing on optimizing the waveguide confinement factor profile in the longitudinal direction, the supermode analysis studies how every excited supermode in a traditional WGPD, as well as the interference between two supermodes, affect the absorption uniformity. The above knowledge is then used to guide the design of layer structure and waveguide dimensions. The interferences between the fundamental supermode and other supermodes modify the exponential absorption profile of the individual supermode. The optimization of the interferences is the key to improve the absorption uniformity. In the forward section, the interference between the fundamental supermode and the large gamma supermode is the major factor affecting the absorption uniformity. In this case, the absorption uniformity in the forward section of the absorber can be improved by suppressing the large gamma supermode. This can be achieved by reducing the confinement factor of the waveguide structure. One side effect is that the suppression of the large gamma supermode reduces the absorption density in the forward section, and will also reduce the absorption efficiency. This is intrinsic in the design of a traditional WGPD. In the rear section, the excitation of the higher order supermodes with similar confinement factor with the fundamental mode are preferred, as they interfere with the fundamental supermodes and improve the absorption uniformity. Certain waveguide width is required for supporting the preferred higher order modes, which will increase the absorption density in the rear section of the absorber from the case without any preferred higher order mode, and hence improve the absorption uniformity. As the waveguide becomes wider, more preferred higher order modes will be excited. In this case, the absorption efficiency will drop, and the absorption uniformity in the rear section of the absorber will degrade, due to the existence of multiple inter-modal interferences with different coupling lengths. In this case, approaches such as tapering the waveguide can be used to

alleviate the absorption efficiency reduction and absorption uniformity degradation. The above supermode analysis looks into the physical connection between the waveguide structure and the absorption uniformity in a traditional WGPD, in order to improve the power handling capability and reveal the related limitations.

Aided by the supermode analysis, traditional WGPD with the optimized structure demonstrates measured maximum power density of 0.6 $mW/\mu m^2$, which is higher than most of the reported power density values for WGPD with similar bandwidth. In order to further improve the power handling capability, a 0.25 μm thick InP diluting layer is proposed to dilute the absorber index in the present layer structure, and increases the theoretical maximum power density by 30% in the demonstrated WGPD. The overall design renders the power handling capability of traditional WGPD as good as most of the surface normal photodiode. However, the supermode analysis also points out that the traditional WGPD structure has some limitations for designing high power WGPD. The improvement of the absorption uniformity largely relies on the suppression of the large gamma supermode, which usually comes along with the reduction of the absorption efficiency, especially when the required bandwidth is high.

In order to overcome the absorption uniformity issue related to the large gamma supermode, the supermode analysis is also applied to DCPD, a different WGPD design that is pre-studied in our group. From the supermode analysis and simulation of the DCPD, deeper understandings have been gained. It is found out that the large gamma mode is largely suppressed in DCPD, because of the offset between the input waveguide and the MMI in the lateral direction. In this case, the improvement of the absorption uniformity in a DCPD is not compromised by the tradeoff between the absorption uniformity and the absorption efficiency, in contrast to the traditional WGPD. The offset between the input waveguide and the MMI in the lateral direction will also result in inefficient absorption in the forward section and small absorption efficiency, which can be resolved by adding some delay length between the input waveguide and the absorber in the z direction. For

a given absorber length, the beating length L_π is used to determine the MMI width, as well as the delay length. Tapering of the MMI down to as narrow as the absorber, which is used to increase the absorption efficiency in the previous DCPD study, is point out to degrade the absorption uniformity. To resolve this issue, inversely tapering the absorber, instead of tapering the MMI, is proposed to increase the DCPD absorption efficiency while maintaining the absorption uniformity.

There are several major differences between the re-designed DCPD and the traditional WGPD. First, the suppression of the large gamma supermodes in the DCPD is effectively achieved by the offset in the lateral direction, without sacrificing the absorption efficiency. In comparison, the suppression of the large gamma supermodes in the traditional WGPD relies on the adjustment of the waveguide dimension or the layer structure, while it usually also results in the reduction of the absorption efficiency. Because of this difference, the absorption density in the forward section can be much easier controlled in DCPD than in traditional WGPD. Second, the preferred higher order modes, which improve the absorption uniformity in the rear section of the absorber, are excited more easily in DCPD than in traditional WGPD. Because of these two major differences, better absorption uniformity and greater power handling capability can be achieved in the re-designed DCPD.

Comparing to the pre-studied DCPD, the improved power handling capability of the re-designed DCPD is attributed to several factors. First, in the re-designed DCPD, the reduction of the average waveguide confinement factor is achieved by reducing the absorber thickness. Second, the MMI width is optimized for the given absorber length. Third, the absorber is properly reverse-tapered to improve the absorption uniformity. Fourth, the delay length is reduced to further reduce the absorption peak in the forward section.

The DCPD is re-designed, with the guidance of the theoretically analysis and simualtions. DCPD variations are fabricated and tested, and good agreements are obtained between the simulations and the testing results for the absorption distribution. The power handling capability of

the demonstrated DCPD is greater than that of the previous DCPD, and other traditional WGPDs. Various waveguide parameters are optimized for a high power DCPD design, which demonstrates measured maximum power density of 0.79 mW/μm^2, with the RC time limited bandwidth being close to 50 GHz. This demonstrated DCPD shows better power handling capability than that of any other traditional WGPDs with similar bandwidth, including the experimentally demonstrated traditional WGPD in Chapter 2, and the previously studied DCPD.

Besides, we have proposed and demonstrated the incorporation of cascaded optical bandpass filters in a ROF link can significantly improve the link performance. As a cost-effective approach, it not only eliminates the power fading effect, but also improves *CNR* without worsening the 3rd inter-modulation distortions. By comparing the RoF links with single and cascaded optical bandpass filters, we show that the latter can significantly improve the link performance, which is attributed to its flat linear bandpass region and fast frequency response roll-off. As this approach relies on flat passband and fast response roll-off, further enhancement of spur-free-dynamic range can be achieved when the optical bandpass filtering shape is optimized.

5.2 Suggestions for Future Work

While the work in this dissertation has achieved some good progress on high power photodiode, there are some further study that could move the design to the next level. The following lists several areas of future work which are closely related to the investigations in this dissertation.

Properly combining the supermode analysis and the traditional power distribution based analysis can improve the design of high power WGPD. The application of supermode analysis is limited to a straight WGPD with constant cross-section. However, as the required bandwidth increases, in order to achieve efficient absorption in a reduced absorption area and improve the absorption uniformity, the dimension of the waveguide and the absorber will be adjusted in the longitudinal direction [2] - [5]. In this case, the assumption of constant cross-section does not hold, and the accuracy of supermode analysis of such a WGPD will be reduced. In contrast, the traditional

power distribution based analysis, such as the Beam Propagation method (BPM), can handle the analysis of such waveguide structure well. In this case, it will be a more powerful tool of designing waveguide by combining the mode based analysis and the power distribution based analysis.

A multiphysics analysis of the high power WGPD will also improve the analysis accuracy. When a WGPD is operated under high power, multiple simultaneous physical phenomena coexist in the waveguide and affect the power distribution. For example, the study in this dissertation analyzes the power distribution in a WGPD with the pre-defined refractive index profile, which is treated as temperature independent. However, when large photocurrent generates in a reversely biased WGPD, the resulted excessive heating will cause some change to the temperature-dependent refractive index, i.e., thermal-optic effect, of the semiconductor materials. The thermal-optic effect has not gained much attention in the traditional study of WGPD. Therefore, when there is large amount of heat generated in a WGPD, and especially when the heat generation is not evenly distribution through the waveguide, the interplay between the heat generation and the power distribution may change the absorption uniformity. In this case, the analysis of power distribution will be more accurate in a Multiphysics analysis.

As the growing high speed communication system requires photodetector bandwidth beyond 50 GHz, it is essential to study DCPD with smaller active area size, which reduces the RC time limited bandwidth. Currently, DCPD works fine when the absorber length is comparable with the coupling length between the dominant modes in the MMI. With the given layer structure, the DCPD works best when the absorber is 2 μm wide, 100 μm to 200 μm long, which corresponds to RC time limited bandwidth of between 25 to 50 GHz. Although the approach of increasing the depletion region thickness can increase the RC time limited bandwidth, it would reduce the transit time limited bandwidth and affect the total photodiode bandwidth. Moreover, increased depletion region thickness also increases the required bias voltage, and hence can cause further heat dissipation across the junction. In this case, the study of power handling capability of DCPD with

absorber length less than 100 μm is important, which requires reducing the MMI width in order to have large absorption efficiency. However, as the MMI gets narrower, the spatial separation between input waveguide and absorber in the lateral direction would also get narrower, which would make the DCPD to behave more like the traditional WGPD. In this case, it increases the excitation of large confinement mode and reduces the power handling capability. One alternative approach is changing the refractive index profile of the DCPD, but it requires the knowledge of material and waveguide, with the considerations of various performances of the DCPD.

Good thermal dissipation capability is essential for both traditional WGPD and DCPD, in order to improve the power handling capability. The improvement of power handling capability due to improved upwards thermal dissipation has been experimentally approved in SNPD [6], however, similar research in WGPD is yet to be done. Moreover, in WGPD, the thermal dissipation can be improved from both vertical and lateral direction. The study of which direction of thermal dissipation is more critical is also important. Besides, III-V materials with improved thermal conductivity can be used for WGPD, as the InP and InGaAsP used in current traditional WGPD and DCPD have relatively poor thermal conductivity. Improving the thermal dissipation provides another angle different from improving the absorption uniformity for the high power WGPD design.

5.3 References

[1] C. H. Cox, *Analog Optical Links: Theory and Practice,* NY: Cambridge, New York (2004)

[2] H. Jiang and P. K. L. Yu, "Waveguide integrated photodiode for analog fiber-optics links," *IEEE Trans. Micro. Theory Tech.,* vol. 48, pp. 2604-2610 (2000).

[3] K. J. Williams and R. D. Esman, "Design Considerations for High Current Photodetectors," *J. Lightwave Tech*. vol. 17, pp. 1443-1454 (1999).

[4] H. Jiang, J. T. Zhu, A. L. Keliner, P. K. L. Yu, "High-saturation-power waveguide photodetector for analog fiber-optic links," *SPIE Proceddings*, vol. 2844 (1996).

[5] N. Michel, V. Magnin, J. Harari, A. Marceaux, O. Parillaud, D. Decoster, and N. Vodjdani, "High-power evanescently-coupled waveguide photodiodes," *IEE Proc.-Optoelectron.,* vol. 153, pp. 199-204 (2006).

[6] Z. Li, Y. Fu, M. Piels, H. Pan, A. Beling, J. E. Bowers, and J. C. Campbell, "High-power high-linearity flip-chip bonded modified uni-traveling carrier photodiode," *Optics Express*, vol. 19, no. 26, pp. 385 – 390 (2011).